



Hybrid systems for highly efficient and stable perovskite solar cells

Camille Geffroy

► To cite this version:

Camille Geffroy. Hybrid systems for highly efficient and stable perovskite solar cells. Polymers. Université de Bordeaux, 2018. English. NNT : 2018BORD0370 . tel-02500484

HAL Id: tel-02500484

<https://theses.hal.science/tel-02500484>

Submitted on 6 Mar 2020

HAL is a multi-disciplinary open access archive for the deposit and dissemination of scientific research documents, whether they are published or not. The documents may come from teaching and research institutions in France or abroad, or from public or private research centers.

L'archive ouverte pluridisciplinaire **HAL**, est destinée au dépôt et à la diffusion de documents scientifiques de niveau recherche, publiés ou non, émanant des établissements d'enseignement et de recherche français ou étrangers, des laboratoires publics ou privés.

THÈSE PRÉSENTÉE

POUR OBTENIR LE GRADE DE

DOCTEUR DE

L'UNIVERSITÉ DE BORDEAUX

ÉCOLE DOCTORALE DES SCIENCES CHIMIQUES

SPÉCIALITÉ : POLYMÈRES

Par Camille GEFROY

Systèmes hybrides pour cellules solaires à pérovskite stables à haut rendement

Hybrid systems for highly efficient and stable perovskite solar cells

Sous la direction de : Pr. Georges HADZIIOANNOU
co-directeurs : Pr. Hiroshi SEGAWA et Pr. Thierry TOUPANCE

Soutenue le 12 Décembre 2018

Membres du jury :

M. MAGLIONE Mario
M. BOLINK Henk
M. VEENSTRA Sjoerd
M. HADZIIOANNOU Georges
M. SEGAWA Hiroshi
M. TOUPANCE Thierry
M. CLOUTET Eric

Directeur de Recherche, CNRS-ICMCB
Professeur, Universidad de Valencia
Directeur de Recherche, Solliance
Professeur, Université de Bordeaux
Professeur, University of Tokyo
Professeur, Université de Bordeaux
Directeur de Recherche, CNRS-LCPO

Président
Rapporteur
Rapporteur
Examineur
Examineur
Examineur
Invité

Remerciements

Ces trois années de recherche sont le fruit d'un travail collaboratif. Je souhaite exprimer ma gratitude à l'ensemble des personnes ayant contribué à ce projet.

Je remercie mon directeur de thèse le Pr. Georges Hadziioannou qui m'a donné l'opportunité d'effectuer ma thèse dans son équipe au Laboratoire de Chimie des Polymères Organiques. Merci pour votre foi en ce projet, votre exigence et votre soutien. Je remercie mon co-directeur de thèse le Pr. Thierry Toupance pour m'avoir accompagné depuis mon stage de fin d'étude jusqu'à la fin de cette thèse. Merci pour votre investissement, votre fiabilité et vos encouragements. Je remercie mon co-encadrant le Dr. Eric Cloutet pour sa disponibilité au quotidien, ses conseils et sa grande patience lorsqu'il a été question de chimie. Je vous remercie tous pour votre confiance, pour m'avoir laissé une grande liberté dans ce projet, pour m'avoir envoyé au bout du monde compléter et présenter mes travaux de recherche et pour votre indéfectible soutien.

Je remercie mon co-directeur de thèse le Pr. Hiroshi Segawa pour m'avoir accueilli dans son laboratoire au RCAST à l'université de Tokyo. Je remercie le Pr. Satoshi Uchida qui m'a suivi durant mon premier séjour. Merci au Dr. Ludmila Cojocar de m'avoir transmis tout son savoir-faire sur les cellules planes. Je remercie le Pr. Takeru Bessho pour m'avoir encadré durant mon second séjour, pour son expertise, son enthousiasme communicatif et ces nombreux brainstormings. Je remercie le Dr. Samy Almosni, mon acolyte franco-versaillais, pour m'avoir guidé au RCAST. Merci pour les partages de tes trucs & astuces autour des pérovskites, pour le décryptage des subtilités de la vie tokyoïte et pour les duos enflammés pour faire face au mal du pays. Enfin je remercie l'équipe NextPV du RCAST pour leur accueil et pour avoir facilité mon intégration. Cette collaboration, en plus d'avoir été une expérience personnelle riche, a pleinement contribué à la réussite du projet.

Je remercie l'ensemble de mes collègues du LCPO qui ont collaboré à ce projet. Merci aux Dr. Eftychia Grana et Dr. Muhammad Mumtaz pour les synthèses de polymères, aux Dr. Tindara Verduci et Dr. Anirudh Sharma pour leur expertise en XPS et UPS. Je remercie l'équipe ElorPrintTec pour mettre à disposition des équipements de qualité. Je remercie tous les B8ers que j'ai pu solliciter pendant ces trois ans, qu'il s'agisse de conseils, de services, de problèmes techniques ou simplement de partager de bons moments. Je remercie spécialement mes chers collègues de bureau Geoffrey, Solène et Daniele. Merci pour votre oreille attentive, votre bonne humeur et votre humour sans égal. Grâce à vous, aucun des jours de ma thèse ne fut triste.

Je remercie mes amis, Gauvin pour avoir été un pilier et un moteur, les copains de CBP qui malgré la distance sont toujours présents. Enfin je remercie ma famille. Merci de m'avoir toujours encouragée et soutenue dans ces longues études loin de la maison.

Content

Résumé.....	9
Abbreviations.....	21
Symbols	23
General Introduction	25
References.....	28
Chapter 1 Background	29
1 Photovoltaic generalities.....	30
1.1 Principle.....	30
1.2 Efficiency measurement.....	31
1.3 Solar spectrum.....	32
1.4 Photovoltaic technologies	33
2 Perovskite material	35
2.1 Structure & Composition.....	35
2.2 Opto-electronic properties.....	36
2.3 Deposition technics	37
2.4 Working principle	39
3 Perovskite solar cells	40
3.1 Evolution towards 20 % efficiency	40
3.2 Over 20 % efficiency perovskite solar cells	43
3.2.1 n-i-p Mesoscopic solar cells.....	43
3.2.2 n-i-p Planar solar cells	44
3.2.3 p-i-n Inverted solar cells	44
3.3 Current and future challenges.....	45
3.3.1 Reliability of device performances	45
3.3.2 Device sustainability	45
4 Hole transporting materials for perovskite solar cells	46
4.1 Highly efficient HTMs	47
4.1.1 Inorganic HTMs.....	47
4.1.2 Metal-organic complex HTMs	47
4.1.3 Organic molecular HTMs	48
4.1.3.1 Spiro-like HTMs	48
4.1.3.2 Thiophene-based HTMs.....	50
4.1.3.3 Triphenylamine-based HTMs	51

4.1.3.4	Aza-based HTMs	52
4.1.3.5	Carbazole-based HTMs	53
4.1.4	Polymer HTMs	54
4.1.4.1	Thiophene-based polymer HTMs	55
4.1.4.2	Triphenylamine-based polymer HTMs	56
4.2	Dopant-free HTMs	57
	Conclusion	62
	References	63
Chapter 2	Perovskite Solar Cell Fabrication	73
1	Introduction	74
2	n-i-p Planar perovskite solar cells	74
2.1	Fabrication steps of planar perovskite solar cells	74
2.2	Optimizations of the process	75
2.2.1	TiO ₂ blocking layer	75
2.2.2	TiO ₂ post treatments	79
2.2.3	Perovskite process	81
2.3	Reference PV performances of planar perovskite solar cells	87
3	Mesoscopic perovskite solar cells	88
3.1	Fabrication of mesoscopic perovskite solar cells	88
3.2	Reference PV performances of mesoscopic perovskite solar cells	89
4	Inverted Perovskite Solar Cells	90
4.1	Fabrication steps	90
4.2	Optimizations of the process	90
4.3	Reference PV performances of planar perovskite solar cells	94
	Conclusion	96
	References	97
Chapter 3	Functionalized-Polyvinylcarbazoles as Hole Transporting Materials	99
1	Introduction	100
2	Properties of the PVK derivatives	102
2.1	Thermal analyses	102
2.2	Solubility	104
2.3	Opto-electronic properties	104
2.4	Charge transport properties	106
3	PVK derivatives as HTM in planar perovskite solar cells	109
3.1	Preliminary results	109
3.2	Case of PVK-[N(PhOCH ₃) ₂] ₂	111
3.2.1	Photovoltaic performances	111

3.2.2	Interfacial energetics	115
3.2.3	Stability	118
4	PVK-[N(PhOCH ₃) ₂] ₂ as HTM in mesoscopic perovskite solar cells	120
5	Dopant-free PVK-[N(PhOCH ₃) ₂] ₂ HTM in planar PSCs.....	127
	Conclusion	130
	References.....	131
Chapter 4 Polyelectrolytes in Perovskite Solar Cells.....		133
1	Introduction.....	134
1.1	Potential use as hole transport material.....	135
1.2	Potential use as dopant for spiro-OMeTAD	135
1.3	Potential use as dopant for the perovskite	138
2	Properties of the polyelectrolytes.....	140
2.1	Solubility	140
2.2	Opto-electronic properties.....	140
3	Polyelectrolytes as alternative dopants to LiTFSI for spiro-OMeTAD	142
3.1	Preliminary results.....	142
3.1.1	Solubility	142
3.1.2	HOMO level	142
3.1.3	Perovskite solar cells	143
3.2	PVBI-TFSI and tBP doped spiro-OMeTAD	147
3.2.1	Photovoltaic performances	147
3.2.2	Understanding of the doping mechanism.....	155
3.2.3	Thin film properties	165
3.2.4	Passivation effect of PVBI-TFSI	170
3.2.5	Stability	176
4	Polyelectrolytes as dopants for the perovskite.....	178
	Conclusion	181
	References.....	182
Chapter 5 PEDOT:PSTFSI Hole Transporting Material Towards Semi-Transparent Inverted Perovskite Solar Cells		187
1	Introduction.....	188
2	PEDOT:PSTFSI as an alternative to PEDOT:PSS	190
2.1	Properties of PEDOT:PSTFSI thin films	190
2.2	Integration of PEDOT:PSTFSI in perovskite solar cells.....	194
3	Towards semi-transparent perovskite solar cells.....	197
	Conclusion	203
	References.....	204

General Conclusion & Perspectives	205
Experimental Details	209
1 Syntheses of polymers	209
1.1 Materials.....	209
1.2 Syntheses and characterizations	209
1.2.1 Synthesis of poly[N3,N3,N6,N6-tetrakis(4-methoxyphenyl)-9-vinylcarbazole-3,6-diamine] (PVK-[N(PhOCH ₃) ₂] ₂)	209
1.2.1.1 Synthesis of poly(9-vinylcarbazole) (PVK, 7.0 kg/mol):	209
1.2.1.2 Synthesis of poly[(3,6-dibromo)-9-vinylcarbazole] (PVK-Br ₂)	210
1.2.1.3 Synthesis of PVK-[N(PhOCH ₃) ₂] ₂ (11.7 kg/mol).....	211
1.2.2 Synthesis of poly[(3,6-di- <i>tert</i> -butyl)-9-vinylcarbazole] (PVK-(tBu) ₂ , 8.5 kg/mol)	212
1.2.3 Synthesis of poly[(3,6-dimethoxy)-9-vinylcarbazole] (PVK-(OCH ₃) ₂ , 12.4 kg/mol) .	213
1.2.4 Synthesis of poly(1-butyl-3-vinylimidazolium iodide) (PVBI-I)	216
1.2.4.1 Synthesis of 1-vinyl-3-butyl-imidazolium iodide synthesis (VBI-I)	216
1.2.4.2 Synthesis of poly(1-butyl-3-vinylimidazolium iodide) (PVBI-I)	216
1.2.5 Synthesis of poly(1-butyl-3-vinylimidazolium bis(trifluoromethylsulfonyl)-imide) (PVBI-TFSI)	217
1.2.6 Synthesis of Poly(1-butyl-3-vinylimidazolium bis(trifluoromethylsulfonyl)imide)- <i>b</i> -poly(9-vinylcarbazole) (PILS(TFSI)- <i>b</i> -PVK)	218
1.2.7 Synthesis of poly[4-styrenesulfonyl(trifluoromethylsulfonyl) imide] potassium salt (PSTFSI-K).....	219
1.2.8 Synthesis of PEDOT:PSTFSI	220
1.3 Methods	220
2 Fabrication of perovskite solar cells	221
2.1 n-i-p planar perovskite solar cells.....	221
2.1.1 Materials.....	221
2.1.2 Fabrication steps	221
2.1.3 APTES grafting to TiO ₂ surface.....	222
2.2 Mesoscopic perovskite solar cells	222
2.2.1 Materials.....	222
2.2.2 Fabrication steps	222
2.3 p-i-n Inverted perovskite solar cells	224
2.3.1 Materials.....	224
2.3.2 Fabrication steps	224
2.4 Methods	225
References.....	228

Résumé

- **Introduction & Objectifs**

La consommation énergétique mondiale a considérablement augmenté durant ces dernières années principalement à cause de l'accroissement de la population mondiale et d'une forte industrialisation. Cette demande énergétique a jusqu'à présent été satisfaite par l'exploitation de ressources fossiles primaires, telles que le pétrole, le charbon et le gaz naturel. Cependant, notre dépendance en ces ressources a conduit d'une part à leur raréfaction, et d'autre part à une dégradation de l'atmosphère provoquée par les fortes émissions de CO₂. Les conséquences climatiques sont nombreuses, et il est donc urgent de développer de nouvelles solutions de production et de stockage de l'énergie étant à la fois efficaces, durables et compétitives avec les technologies existantes.

Les sources d'énergie renouvelable ont les avantages d'être inépuisables et plus respectueuses de l'environnement. Elles regroupent notamment le solaire, l'hydroélectricité, la biomasse, l'éolien et la géothermie. Le solaire apparaît comme une alternative intéressante de par son accessibilité et sa large disponibilité. Les cellules photovoltaïques sont traditionnellement composées de silicium cristallin. Ce type de cellule est le plus commercialisé aujourd'hui avec des rendements de conversion d'énergie jusqu'à 25 %.

Afin d'atteindre de plus hauts rendements et/ou de réduire les coûts, d'autres types de cellules solaires ont été développées. Parmi elles, les cellules à base de pérovskite organométallique ont attiré l'attention par la rapide progression de leurs rendements, de 3 % à 23 % en moins de 10 ans. Grâce à ces hautes performances, la disponibilité des matériaux et une fabrication peu coûteuse par voie liquide, les cellules solaires à base de pérovskite sont une alternative intéressante aux cellules à base de silicium. Cependant quelques challenges restent à relever, comme la fabrication des cellules performantes à grande échelle et l'amélioration de la stabilité des dispositifs, tout en gardant leur prix attractif. En effet, la pérovskite est sensible à l'humidité, aux variations de température et au rayonnement UV. La stabilité des cellules peut aussi être altérée par d'autres composants de la cellule comme le matériau transporteur de trous. Néanmoins, il a été montré qu'intégrer des polymères à ces dispositifs pouvaient améliorer leur stabilité mais aussi leur performance.

Dans ce contexte, cette thèse vise à améliorer la stabilité et les rendements de conversion énergétique des cellules solaires à pérovskite en développant de nouveaux systèmes impliquant des polymères pour le transport de trous. Des polymères ont été spécifiquement synthétisés et étudiés

pour chacune des principales architectures de cellules à pérovskite (Figure 1). Les résultats les plus importants sont brièvement décrits ci-dessous.

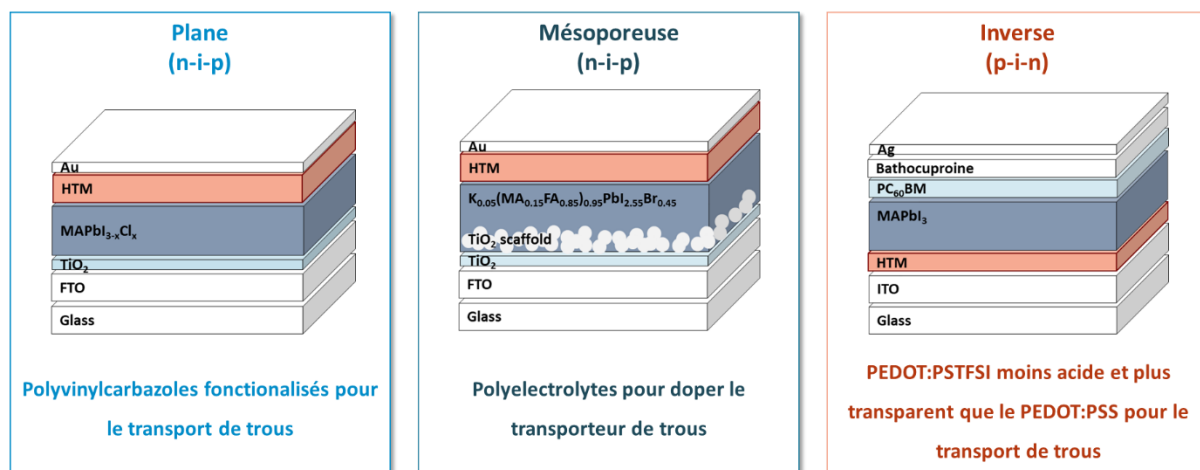


Figure 1. Représentation des trois architectures étudiées et des polymères testés dans chacune d'elles. Le FTO et l'ITO correspondent aux électrodes transparentes, le HTM au transporteur de trous, le TiO_2 , et le PC_{60}BM aux transporteurs d'électrons, $\text{MAPbI}_{3-x}\text{Cl}_x$, MAPbI_3 et $\text{K}_{0.05}(\text{MA}_{0.15}\text{FA}_{0.85})_{0.95}\text{PbI}_{2.55}\text{Br}_{0.45}$ aux pérovskites et, Ag et Au aux électrodes métalliques.

• Cellules de référence

La première partie du projet a consisté à fabriquer trois types de dispositifs en utilisant des transporteurs de trous standards. L'objectif était d'obtenir des rendements assez hauts, stables et reproductibles pour pouvoir évaluer les performances de nos nouveaux polymères. Les rendements (PCE) de références sont reportés dans le Tableau 1. Le courant de court-circuit (J_{sc}), la tension de circuit ouvert (V_{oc}), le facteur de forme (FF) et l'indice d'hystérèse (HI) sont utilisés pour comparer les performances des cellules. Notons que pour une cellule sans hystérèse, HI est égal à 0, qu'un HI positif représente un PCE supérieur pour le scan $V_{oc} \rightarrow J_{sc}$ que pour le scan $J_{sc} \rightarrow V_{oc}$, et inversement.

L'hystérèse dans les cellules planes est assez grande comparée à la littérature. L'optimisation des méthodes de dépôt, des traitements de surface de TiO_2 et des formulations de la solution de pérovskite ont été nécessaires pour réduire l'hystérèse. Le meilleur rendement obtenu avec ces cellules est de 15.99 %. Un meilleur rendement de 18.44 % avec une légère hystérèse a été obtenu dans les cellules mésoporeuses. Cette amélioration est due à la couche mésoporeuse de TiO_2 qui aide à l'extraction des électrons, à la composition de la pérovskite et au dopage des matériaux. L'ajout de LiTFSI et $\text{Mg}(\text{TFSI})_2$ dans le TiO_2 et de K^+ dans la pérovskite modifient favorablement les propriétés énergétiques des matériaux pour notre application. Enfin, un meilleur rendement de 12.23 % a été

obtenu dans les cellules inverses avec une hystérèse raisonnable, mais relativement plus faible que l'état de l'art.

Tableau 1. Meilleures performances obtenues pour les cellules de référence plane, mésoporeuse et inverse.

Cellule	Scan	J_{sc} $mA.cm^{-2}$	V_{oc} V	FF	PCE %	HI
Plane	$V_{oc} \rightarrow J_{sc}$	20.61	1.08	0.72	15.99	0.37
Mésoporeuse	$V_{oc} \rightarrow J_{sc}$	22.45	1.10	0.73	18.44	0.04
Inverse	$J_{sc} \rightarrow V_{oc}$	21.68	0.88	0.63	12.23	-0.13

- Polyvinylcarbazoles fonctionnalisés pour le transport de trous dans les cellules planes**

Un premier projet a été dédié à l'étude de polymères à base de polyvinylcarbazole (PVK) pour le transport de trous dans les cellules planes ou mésoporeuses. Souvent employés en électronique organique, les PVKs ont l'avantage d'avoir de bonnes propriétés de transport de charge, d'être hydrophobes, disponibles et abordables. Notre stratégie a été de synthétiser puis de fonctionnaliser des PVKs avec différents groupements dans le but d'améliorer leurs propriétés optoélectroniques, leur caractère filmogène, leur solubilité ou leur conductivité. Les synthèses de ces matériaux, présentées en Figure 2, se font au maximum en 3 étapes, à partir de matériaux et de méthodes bon marché. La purification des polymères se fait simplement par extraction Soxhlet.

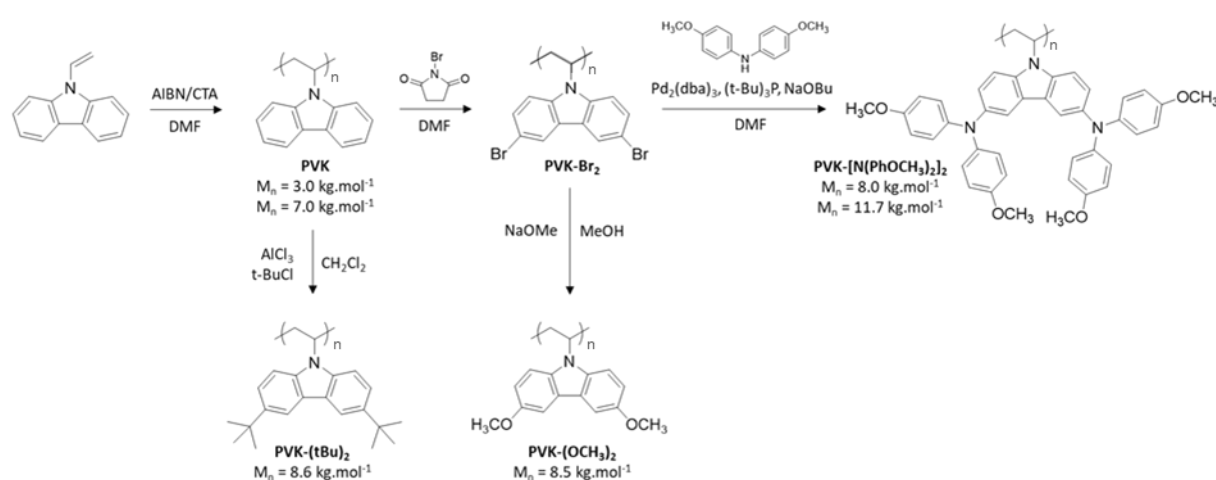


Figure 2. Voies de synthèses des dérivés de PVK étudiés.

Les propriétés de ces polymères ont été comparées au conducteur de trous de référence, le spiro-OMeTAD dopé par le bis(trifluorométhanesulfonyl) imide de lithiumlithium (LiTFSI) et la *tert*-butylpyridine (tBP) (Figure 3).

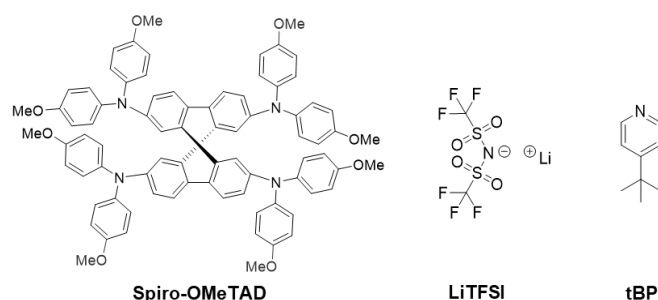


Figure 3. Structures chimiques du spiro-OMeTAD, du sel de lithium et de la *tert*-butylpyridine.

Tous les polymères sont stables thermiquement, avec des températures de transition vitreuses (T_g) et de dégradation élevées, et sont solubles dans le chlorobenzène pour ne pas altérer la pérovskite lors du dépôt par voie liquide (Tableau 2). En revanche, seul le PVK-[N(PhOCH₃)₂]₂ possède une HOMO compatible avec l'architecture de nos cellules et une mobilité de trous élevée, supérieure d'un ordre de grandeur à celle du spiro-OMeTAD. Notons que pour le spiro-OMeTAD et ce dernier polymère, le dopage a permis d'augmenter leur mobilité de trous de deux ordres de grandeurs et est donc essentiel pour améliorer les propriétés de transport de charges.

Tableau 2. Propriétés thermiques, solubilité, propriétés optoélectroniques et mobilité de trous des polymères comparés au matériau de référence le spiro-OMeTAD.

	T_g	Temp. de dégradation ^a	Solubilité dans le chlo- robenzène	E_g^b	E_{HOMO}^c	E_{LUMO}^d	μ après dopage ^e
	°C	°C		eV	eV	eV	cm ² /V.s
PVK	203	402	+	^g	- 5.75	^g	1.37 ± 0.37 E-06
PVK-(OCH₃)₂	219	366	+	3.25	- 5.52	- 2.17	7.79 ± 0.87 E-07
PVK-(tBu)₂	^f	416	+	3.50	- 5.64	- 2.14	3.69 ± 0.52 E-07
PVK- [N(PhOCH₃)₂]₂	222	419	+	3.00	- 5.23	- 2.23	1.67 ± 0.32 E-03
Spiro- OMeTAD	^g	420	+	3.10	- 5.20	- 2.10	1.42 ± 0.61 E-04

^a 10% de perte massique ; ^b à partir des spectres d'absorption et d'émission ; ^c par spectroscopie photoélectronique ; ^d $E_{LUMO} = E_{HOMO} + E_g$; ^e mobilité des trous du matériau dopé au LiTFSI et à la tBP ; ^f pas de T_g entre 0 et 250°C ; ^g non mesuré.

Par la suite, le spiro-OMeTAD a donc été remplacé par le PVK-[N(PhOCH₃)₂]₂ dans les cellules planes. Les performances des cellules sont présentées dans le Tableau 3. Un rendement maximal de 14.05 % a été obtenu en utilisant le PVK-[N(PhOCH₃)₂]₂ comme transporteur de trous. Les cellules à base de PVK-[N(PhOCH₃)₂]₂ sont plus reproductibles que celles à base de spiro-OMeTAD avec une efficacité moyenne comparable à celle du spiro-OMeTAD et une hystérèse plus faible, probablement dû à la meilleure mobilité de trous du PVK-[N(PhOCH₃)₂]₂.

Tableau 3. Meilleures performances et performances moyennes des cellules solaires planes à base de spiro-OMeTAD ou de PVK-[N(PhOCH₃)₂]₂.

	Meilleur scan	J _{sc} mA.cm ⁻²	V _{oc} V	FF	PCE %	HI	PCE moy ^a %
Spiro-OMeTAD	V _{oc} → J _{sc}	20.61	1.08	0.72	15.99	0.37	11.66 ± 3.13
PVK-[N(PhOCH₃)₂]₂	V _{oc} → J _{sc}	22.07	0.95	0.67	14.05	0.30	11.30 ± 1.95

^a Moyenne sur 30 cellules.

De plus, la durée de vie des cellules planes a été considérablement améliorée en utilisant le PVK-[N(PhOCH₃)₂]₂. En Figure 4 sont représentées les efficacités des cellules au cours du temps, stockées en atmosphère inerte, en salle sèche ou en dessiccateur. Dans tous les cas, les cellules à base de polymère sont plus stables que celles à base de spiro-OMeTAD.

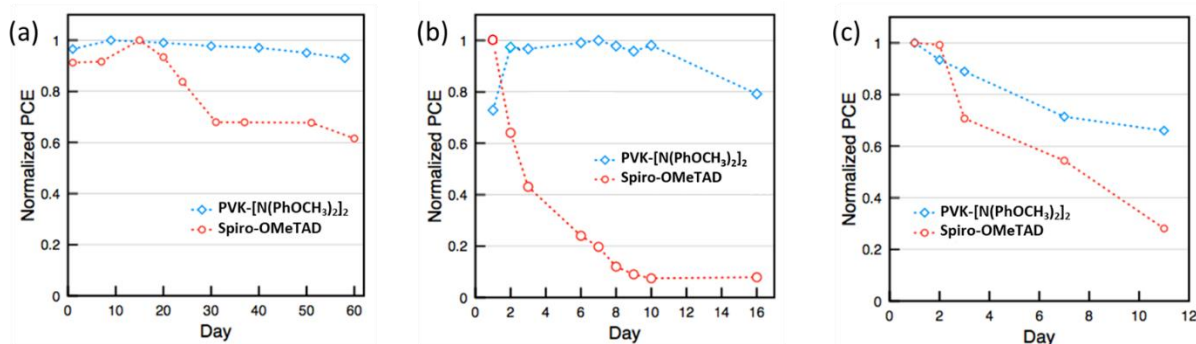


Figure 4. Evolution des efficacités des cellules stockées a) en boîte à gants (N₂), b) en salle sèche (humidité < 2%) et c) en dessiccateur (humidité ≈ 20%).

L'amélioration de la stabilité des cellules pourrait s'expliquer par la meilleure qualité de film obtenue avec le polymère. En effet, les images de la surface des films par microscopie à force atomique (AFM) et les images des cellules en tranche par microscopie électronique à balayage ont montré la présence

de trous dans le cas du spiro-OMeTAD (Figure 5a, b). De plus, la mesure d'angle de contact d'une goutte d'eau sur la surface des films indique que le polymère est plus hydrophobe que le spiro-OMeTAD (Figure 5c). Il est possible que le PVK-[N(PhOCH₃)₂]₂ agisse comme une barrière hydrophobe, protégeant la pérovskite de l'humidité ambiante et ainsi améliorant sa durée de vie.

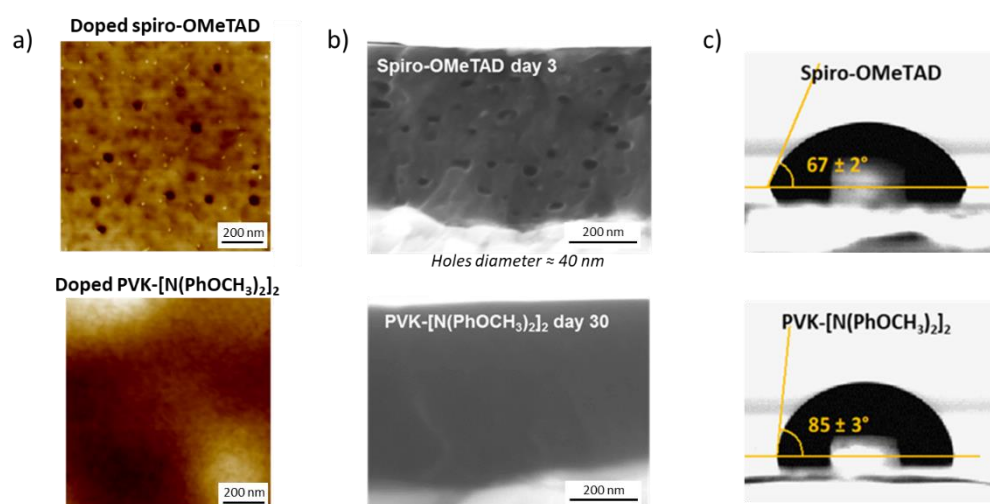


Figure 5. a) Topographie de la surface des films de spiro-OMeTAD et PVK-[N(PhOCH₃)₂]₂ par AFM. b) Vue en tranche des cellules solaires par MEB. c) Angle de contact d'une goutte d'eau sur les films.

Introduit dans les cellules mésoporeuses, le V_{oc} des cellules à base de PVK-[N(PhOCH₃)₂]₂ était remarquablement bas. Ce problème a pu être résolu en modifiant à l'interface la composition de la pérovskite en déposant du MAI, et donc en modifiant localement les niveaux d'énergies de la pérovskite de manière plus favorable à l'extraction des trous. Un meilleur rendement de 17.17 % a pu être atteint.

Enfin, le PVK-[N(PhOCH₃)₂]₂ a été testé sans dopants dans des cellules planes. Pour compenser la perte des propriétés de transport induits par les dopants, une fine couche de PVK-[N(PhOCH₃)₂]₂ et une couche d'oxyde de molybdène entre le transporteur de trou et l'électrode ont été utilisés. Un meilleur rendement de 10.63 % a été obtenu, comparable aux performances du spiro-OMeTAD.

- **Polyélectrolyte pour cellules mésoscopiques**

Un second projet a été dédié à l'utilisation de polyélectrolytes dans les cellules mésoscopiques. Les polyélectrolytes synthétisés sont présentés en Figure 6. Leurs propriétés pour une potentielle application en tant que transporteur de trous, dopant pour transporteur de trous ou dopant pour pérovskite ont été étudiées.

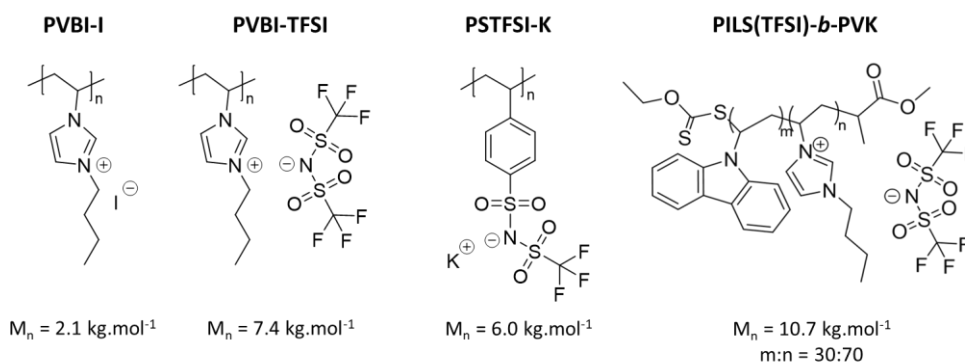


Figure 6. Structure chimique et masse molaire des polyélectrolytes utilisés comme dopant.

Parmi ces polyélectrolytes, le PVBI-TFSI a montré des résultats intéressants pour le dopage du spiro-OMeTAD. Le PVBI-TFSI a été utilisé en remplacement du LiTFSI. De par ses longues chaînes, il est supposé ne pas migrer comme le LiTFSI à travers les différentes couches de la cellule et ainsi améliorer sa stabilité.

Le dopage du spiro-OMeTAD a d'abord été mis en évidence en atmosphère inerte par un changement de couleur de la solution du transparent au rouge orangé après addition du PVBI-TFSI et suivi par spectroscopie d'absorption UV-visible (Figure 7). Ainsi, on constate la présence d'espèces oxydées à l'ajout du PVBI-TFSI, leur disparition après ajout de la tBP et une réapparition après exposition de la solution finale à la lumière.

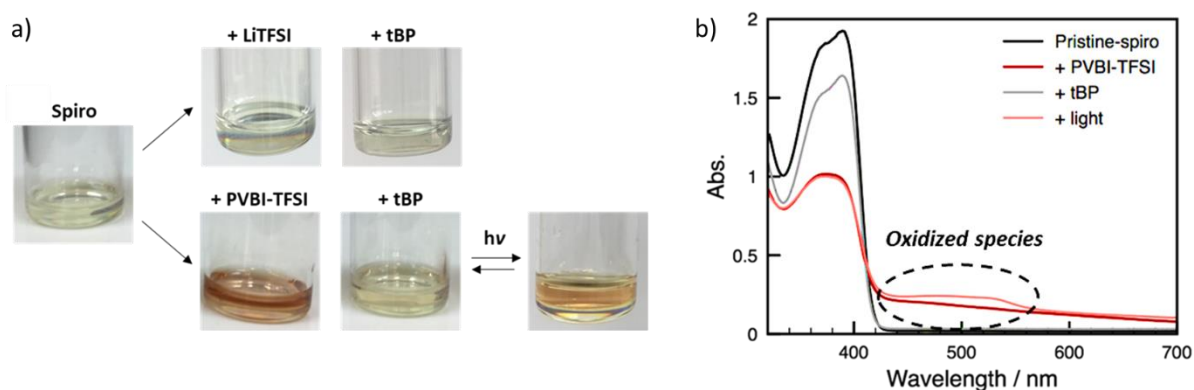


Figure 7. a) Changement de couleur des solutions de spiro-OMeTAD préparées en atmosphère inerte. b) Suivi de ces changements de couleur par spectroscopie d'absorption.

Un mécanisme a été proposé afin d'expliquer ces observations (Figure 8). La première réaction implique le partage du proton le plus acide de l'imidazole du PVBI-TFSI avec un des azotes du spiro-OMeTAD. Par résonance magnétique nucléaire des protons (RMN ^1H), cette interaction se traduit par un élargissement des signaux associés aux protons aromatiques (voisins de l'azote) du spiro-OMeTAD

et d'un déplacement plus important du proton acide de l'imidazole. La deuxième réaction est l'interaction préférentielle du proton de l'imidazole avec l'azote de la tBP qui serait réversible après exposition à la lumière. En effet, à l'ajout de la tBP, les signaux des protons aromatiques du spiro-OMeTAD retrouvent leur définition initiale. L'interaction PVBI-tBP semble moins forte qu'avec le spiro-OMeTAD puisqu'aucun élargissement des signaux de la tBP n'a été observé. Enfin, la dernière réaction est la déprotonation de l'imidazole par le spiro-OMeTAD pour former un carbène. Néanmoins, aucun carbène n'a pu être identifié par RMN ^{13}C en solution.

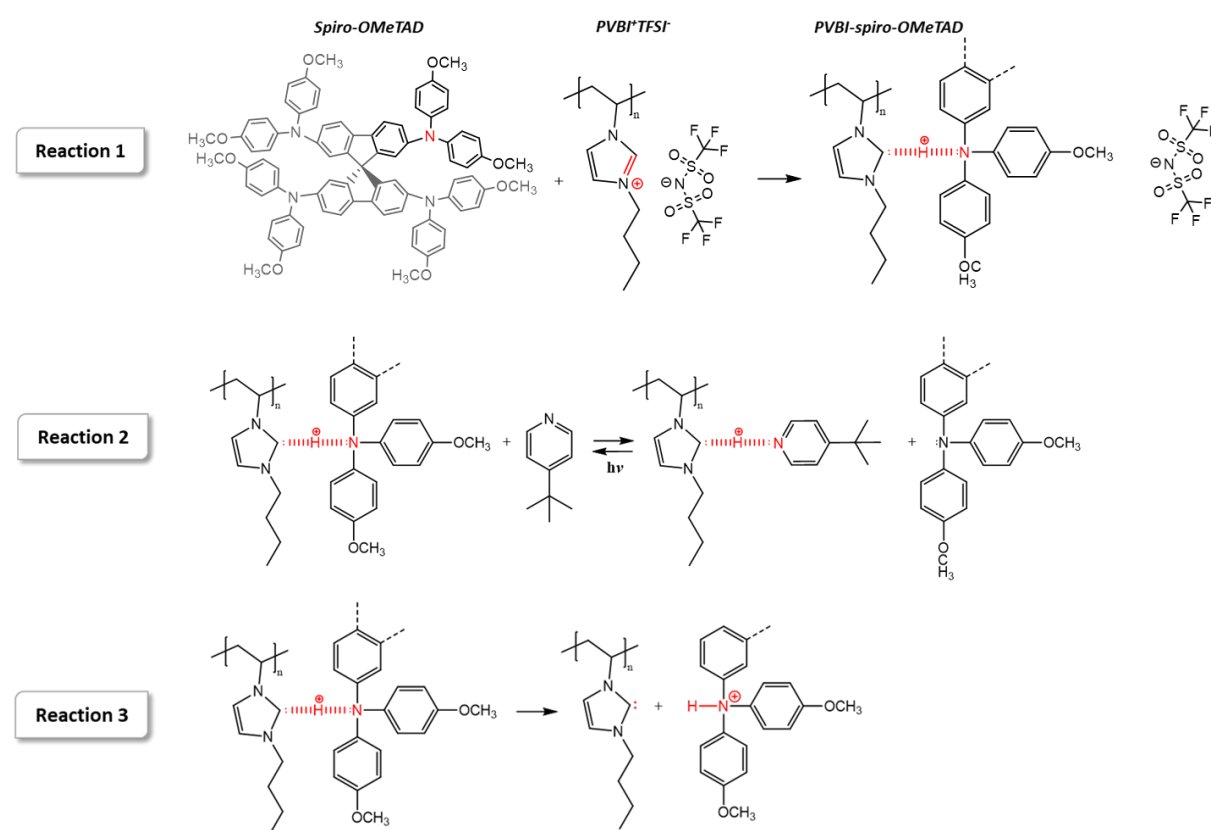


Figure 8. Mécanisme de dopage du spiro-OMeTAD par le PVBI-TFSI et influence de la tBP et de la lumière.

Des mesures de spectroscopie photoélectronique UV sur des films de spiro-OMeTAD non dopés et dopés au PVBI-TFSI fabriqués entièrement en atmosphère inerte ont été réalisées. Sous l'effet du dopage au PVBI-TFSI, la HOMO du spiro-OMeTAD se rapproche du niveau de Fermi, tandis que son travail de sortie et son potentiel d'ionisation augmentent (Figure 9). Ces observations prouvent que l'oxygène n'intervient pas dans le mécanisme de dopage.

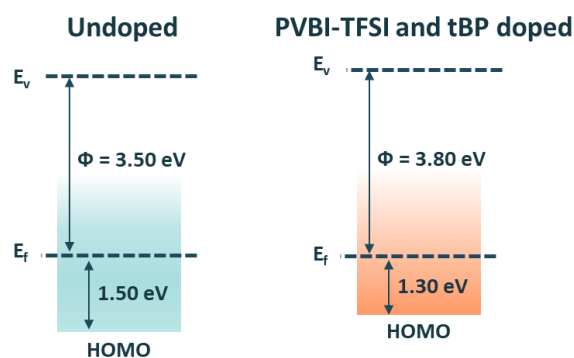


Figure 9. Diagramme de bande du spiro-OMeTAD non dopé (gauche) et dopé au PVBI-TFSI et à la tBP (droite).

La conductivité des films de spiro-OMeTAD dopés au PVBI-TFSI et à la tBP a été comparée à celle du spiro-OMeTAD standard dopé au LiTFSI et à la tBP (Tableau 4). Le remplacement du LiTFSI par le PVBI-TFSI améliore considérablement, de deux ordres de grandeur, la conductivité du film. Notons que la conductivité du spiro-OMeTAD dopé au PVBI-TFSI est également influencée par la concentration en tBP et l'exposition à la lumière.

Tableau 4. Comparaison de la HOMO et de la conductivité du spiro-OMeTAD en fonction des dopants.

	Conductivité ^a
	S/cm
Spiro-OMeTAD	$2.5 \pm 0.2 \text{ E-06}$
Spiro-OMeTAD + LiTFSI + tBP	$1.1 \pm 0.2 \text{ E-05}$
Spiro-OMeTAD + PVBI-TFSI + tBP	$1.9 \pm 0.5 \text{ E-03}$

^a Moyenne sur 4 films.

Intégré dans des cellules solaires mésoporeuses, le spiro-OMeTAD dopé au PVBI-TFSI a sensiblement augmenté l'efficacité des cellules tout en réduisant l'hystérèse (Tableau 5). Ainsi, une meilleure efficacité de 20.4 % a été obtenue, soit 2 % de plus qu'avec le LiTFSI avec une très bonne reproductibilité. Cette amélioration peut être due à une réduction des recombinaisons à l'interface perovskite/spiro-OMeTAD et à un bon équilibre d'extraction de charges induits par une haute conductivité et un meilleur alignement des bandes d'énergie.

Tableau 5. Meilleures performances et performances moyennes des cellules mésoscopiques à base de spiro-OMeTAD dopé au LiTFSI ou au PVBI-TFSI.

Dopant	Meilleur scan	J_{sc} $mA.cm^{-2}$	V_{oc} V	FF	PCE %	HI	PCE moy ^a %
LiTFSI	$V_{oc} \rightarrow J_{sc}$	22.45	1.10	0.73	18.44	0.04	17.59 ± 0.54
PVBI-TFSI	$J_{sc} \rightarrow V_{oc}$	23.04	1.16	0.76	20.35	-0.01	19.75 ± 0.57

^a Moyenne sur 20 cellules.

La stabilité des cellules reste à discuter. En effet, en fonctionnement continu, les cellules dopées au PVBI-TFSI ont une efficacité qui décroît plus rapidement qu'avec le LiTFSI (Figure 8a). Cependant, en exposant alternativement les cellules à la lumière, les cellules à base de PVBI-TFSI semblent avoir une meilleure photosensibilité et une meilleure stabilité (Figure 8b). Enfin, en mesurant l'efficacité des cellules stockées dans l'obscurité en atmosphère sèche pendant plusieurs jours, les cellules à base de PVBI-TFSI se stabilisent après 10 jours et le restent jusqu'à un mois en conservant 92 % de son efficacité initiale (Figure 8c).

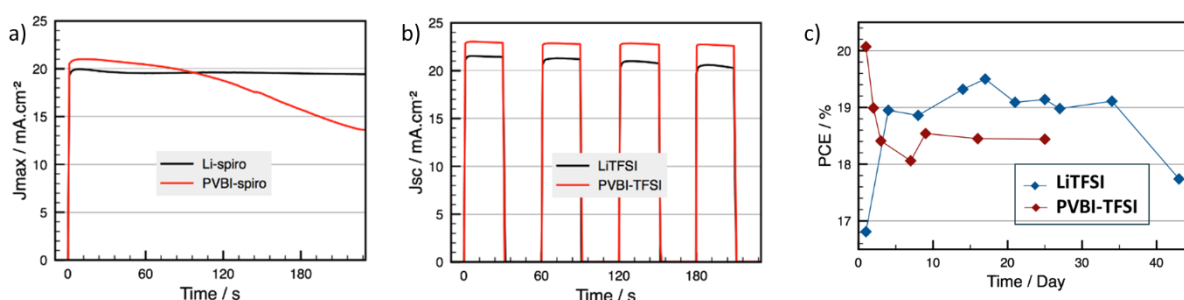


Figure 10. a) Suivi de la puissance maximale délivrée par les cellules. b) Suivi du J_{sc} des cellules en alternant exposition à la lumière et obscurité. c) Evolution de l'efficacité des cellules.

• Complexes de PEDOT pour le transport de trous dans les cellules inverses

Le PEDOT:PSTFSI a été choisies pour remplacer le PEDOT:PSS comme conducteur de trous dans les cellules inverses pour sa plus grande transparence et pour son caractère moins acide qui ne risque pas d'altérer l'électrode d'ITO (Figure 11).

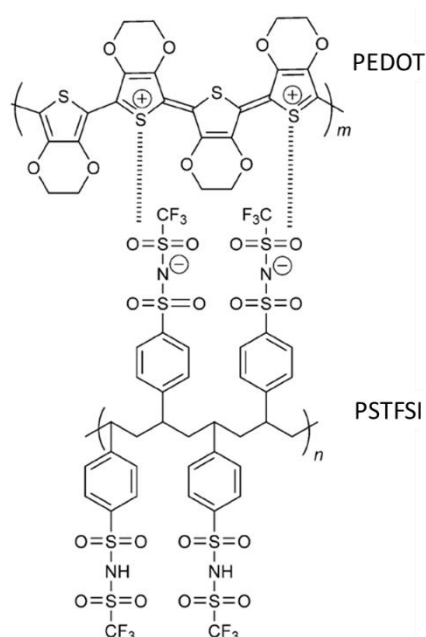


Figure 11. Structure chimique du PEDOT:PSTFSI.

Néanmoins, les films de pérovskite formés sur le PEDOT:PSTFSI semblent de moins bonne qualité, avec de plus petits grains observés par AFM. De plus, la conductivité du PEDOT:PSTFSI est d'environ 225 S/cm, inférieure à celle du PEDOT:PSS d'environ 780 S/cm. Ainsi les efficacités des cellules qui en résultent n'ont pu surpasser celles des cellules de référence au PEDOT:PSS notamment à cause d'un J_{sc} très faible (Tableau 6).

Tableau 6. Meilleures performances et performances moyennes des cellules inverses à base de PEDOT:PSS ou PEDOT:PTFSI.

	Meilleur scan	J_{sc} $mA.cm^{-2}$	V_{oc} V	FF	PCE %	HI	PCE moy ^a %
PEDOT:PSS	$J_{sc} \rightarrow V_{oc}$	21.68	0.88	0.63	12.23	-0.13	10.09 ± 0.91
PEDOT:PSTFSI	$J_{sc} \rightarrow V_{oc}$	10.24	0.86	0.58	5.26	-0.13	4.26 ± 0.63

^a Moyenne sur 8 cellules.

• Conclusion

Ces travaux de thèse visent à répondre à certains challenges pour le développement des cellules solaires à pérovskite, soit l'amélioration des efficacités et de la stabilité des dispositifs. La stratégie a été de remplacer des transporteurs de trous et un des dopants pour le transporteur de trous connus pour dégrader les cellules par des matériaux polymères plus stables.

Dans le premier projet, le spiro-OMeTAD a été remplacé par des dérivés de PVK, hydrophobes, stables chimiquement et thermiquement et relativement bon marché. Des rendements comparables au spiro-OMeTAD ont été obtenus avec le PVK-[N(PhOCH₃)₂]₂ dans les cellules planes et mésoporeuses. Le dopage des transporteurs de trous reste essentiel pour atteindre de hautes efficacités. Pour mieux comprendre les mécanismes de transfert de charge et l'influence de la modification de la composition de la pérovskite, il serait intéressant d'étudier les propriétés énergétiques de l'interface pérovskite/transporteur de trou.

Le deuxième projet a été dédié au remplacement du LiTFSI par des polyélectrolytes afin de doper plus efficacement le spiro-OMeTAD, de limiter la migration des dopants dans le dispositif et d'éviter l'exposition des cellules à l'oxygène. Le PVBI-TFSI s'est montré le plus efficace dans les cellules mésoporeuses avec un rendement maximal de 20.4 %, supérieur de 2 % à celui du LiTFSI, et une hystérèse négligeable. Les perspectives de ce travail se portent sur la compréhension des effets de la lumière et de la *tBP* sur le mécanisme de dopage et leur lien avec les réactions photo-réversibles observées durant le fonctionnement des cellules.

Finalement, nous avons montré que des matériaux polymères fonctionnels pouvaient améliorer la viabilité des cellules solaires à pérovskite, *i.e.* leurs performances et leur stabilité à travers des procédés accessibles. La fonctionnalisation spécifique et contrôlée de matériaux polymères offre des possibilités infinies de progrès pour les cellules solaires à pérovskite.

Abbreviations

a-Si	Amorphous silicon
AFM	Atomic force microscopy
ALD	Atomic layer deposition
APTES	3-Aminopropyltriethoxysilane
bl-TiO ₂	Titanium dioxide blocking layer
c-Si	Crystalline silicon
BCP	Bathocuproine
BDT	Benzo[1,2-b:4,5-b']-dithiophene
CB	Conduction band
CIGS	Copper indium gallium selenide
CRP	Controlled radical polymerization
CZTS	Copper zinc tin sulphide
DMF	Dimethylformamide
DMSO	Dimethylsulfoxide
DSC	Dye-sensitized solar cell
EQE	External quantum efficiency
ETL	Electron transporting layer
ETM	Electron transporting material
FA	Formamidinium
FF	Fill factor
FTIR	Fourier transform infrared
FTO	Fluorine tin oxide
GBL	γ -Butyrolactone
HI	Hysteresis index
HOMO	Highest occupied molecular orbital
HTL	Hole transporting layer
HTM	Hole transporting material
I-V	Current-voltage
IPA	Isopropyl alcohol
IPCE	Incident-photon-to-electron conversion efficiency
ITO	Indium tin oxide
LiTFSI	Lithium bis(trifluoromethanesulfonyl)imide
LUMO	Lowest unoccupied molecular orbital
MA	Methylammonium
mono-Si	Monocrystalline silicon
mp-TiO ₂	Mesoporous titanium dioxide
NMP	N-methyl-2-pyrrolidone
NMR	Nuclear magnetic resonance
NREL	National Renewable Energy Laboratory
OPV	Organic photovoltaic
PC ₍₆₀₎ BM	(6,6)-Phenyl C61 butyric acid methyl ester
PCE	Power conversion efficiency
PESA	Photoelectron spectroscopy in air
PEDOT	Poly(3,4-ethylenedioxythiophene)
PIL	Poly(ionic liquid)
PILS(TFSI)- <i>b</i> -PVK	Poly(1-butyl-3-vinylimidazolium bis(trifluoromethylsulfonyl)imide)- <i>b</i> -poly(9-vinylcarbazole)

PL	Photoluminescence
poly-Si	Polycrystalline silicon
PSC	Perovskite solar cell
PSS	Polystyrene sulfonate
PSSC	Perovskite-sensitized solar cell
PSTFSI(K)	Poly(4-styrenesulfonyl(trifluoromethylsulfonyl)imide) (potassium)
PV	Photovoltaic
PVBI-I	Poly(1-butyl-3-vinylimidazolium iodide)
PVBI-TFSI	Poly(1-butyl-3-vinylimidazolium bis(trifluoromethylsulfonyl)imide)
PVK	Poly(9-vinylcarbazole)
PVK-[N(PhOCH ₃) ₂] ₂	Poly[N3,N3,N6,N6-tetrakis(4-methoxyphenyl)-9-vinylcarbazole-3,6-diamine]
PVK-(OCH ₃) ₂	Poly[(3,6-dimethoxy)-9-vinylcarbazole]
PVK-(tBu) ₂	Poly[(3,6-di- <i>tert</i> -butyl)-9-vinylcarbazole]
RAFT	Reversible addition fragmentation chain transfer
RH	Relative humidity
SCLC	Space-charge-limited current
SEC/GPC	Size exclusion chromatography / Gel permeation chromatography
SEM	Scanning electron microscopy
spiro-OMeTAD	2,2',7,7'-Tetrakis(N,N-di-p-methoxy-phenylamine)-9-9'-spirobifluorene
ss-PSSC	Solid-state perovskite-sensitized solar cell
tBP	<i>tert</i> -Butylpyridine
TGA	Thermogravimetric analyses
THF	Tetrahydrofuran
TiAcAc	Titanium diisopropoxide bis(acetylacetonate)
TPA	Triphenylamine
UPS	Ultraviolet photoelectron spectroscopy
VB	Valence band
VBM	Valence band maximum
XPS	X-ray photoelectron spectroscopy
XRD	X-ray diffraction

Symbols

d	<i>m</i>	Thickness
E _f	<i>eV</i>	Fermi energy level
E _g	<i>eV</i>	Energy bandgap
E _v	<i>eV</i>	Vacuum energy level
ε		Permittivity / Dielectric constant
ε ₀		Vacuum permittivity = 8.854 10 ⁻¹²
F	<i>V.m⁻¹</i>	Electric field
γ	<i>m^{1/2}.V^{-1/2}</i>	Field dependence mobility
I _{sc}	<i>A</i>	Short-circuit current
J	<i>A.m⁻²</i>	Current density
λ	<i>m</i>	Wavelength
M _n	<i>g.mol⁻¹</i>	Molar mass
μ	<i>m².V⁻¹.s⁻¹</i>	Mobility
P	<i>J.s⁻¹</i>	Power
q	<i>A.s</i>	Elementary charge = 1.602 10 ⁻¹⁹
r	<i>m</i>	Radius
R _q	<i>m</i>	Roughness (root mean squared)
R _s	<i>Ω</i>	Series resistance
R _{sh}	<i>Ω</i>	Shunt resistance
σ	<i>S.m⁻¹</i>	Conductivity
t		Tolerance factor
T _g	<i>°C</i>	Glass transition temperature
V _{oc}	<i>V</i>	Open-circuit voltage
Φ	<i>eV</i>	Work function
Φ _λ	<i>m⁻².s⁻¹</i>	Spectral photon flux

General Introduction

The constant growth of the population associated to strong industrialization development dramatically intensified world energy consumption. This energetic crisis is considered as one of the most serious challenges our society has to face today. As depicted on Figure 1 world energy consumption is accentuated by Asia and especially by China, where energy demand has risen together with economic growth.¹ In the past years, primary fossil resources such as oil, coal and gas, have been extensively exploited as energy sources. Their increasing scarcity pushed the cost production up. Moreover, this reliance on fossil fuels has considerably altered the Earth's atmosphere through high emission of CO₂. This contributed to the increase in the greenhouse effect and climate imbalance such as melting of the ice, sea levels rise, floods, typhoons... Since energy needs are estimated to double from 574 EJ (in 2017) to over 1100 EJ by 2050, it is urgent to develop alternative sources of pollution-free renewable energy.¹ In order to insure future energy needs, important efforts have been devoted to production and storage solutions competitive with conventional energy sources, *i.e.* efficient, cost-effective, and environmentally friendly.

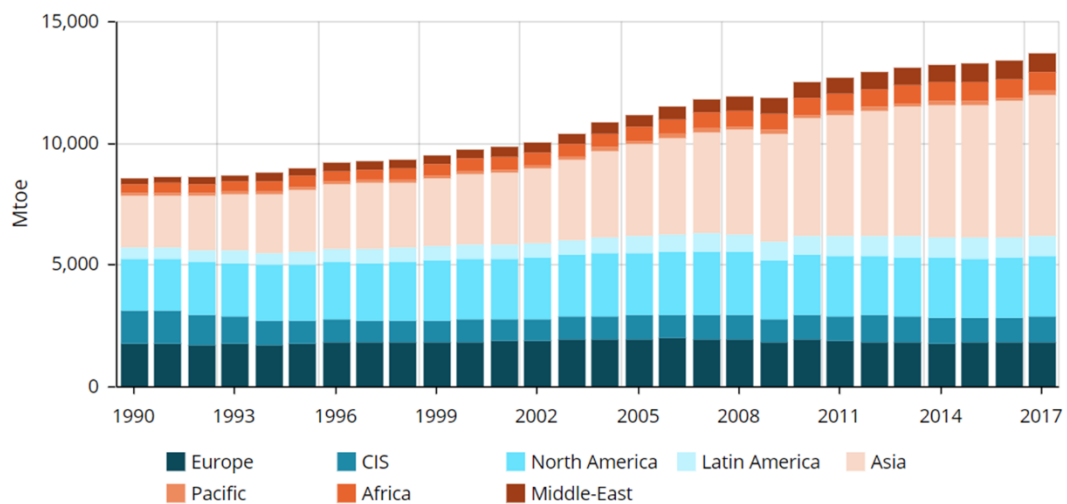


Figure 1. Annual world energy consumption from 1990 to 2017.¹

Today's candidates include solar power, wind power, hydropower, geothermal power and tidal power. Harnessing solar energy to produce electricity has been proven to be one of the most promising solutions. Indeed, annual potential solar energy received on Earth was estimated to be

1575 – 49837 EJ according to the region of the world, by the United Nations Development Programme in 2000, which is largely above one year of world energy consumption (574 EJ or 13.7 Gtoe).¹⁻² It was estimated that this amount of energy could be delivered by solar panels exhibiting 20 % efficiency distributed on 0.4 % of the Earth's surface. Such efficiency has already been successfully achieved in several photovoltaic devices owing to intensive research efforts on the understanding of the photovoltaic (PV) effect, the investigation of novel materials and optimization of processes. The first solar cells developed and the most commercialized today are based on crystalline silicon. As an available material showing an average 20 % efficiency and available material, silicon-based modules represent 90 % of the PV market in the world.

Thereby, PV systems have become attractive solutions for energy transition, to the extent to be the world's fastest growing energy generation technology. Growing within the past years of 30-40 % per year, 1.7 % of the energy production is provided by PV systems at present. This trend is not expected to slow down in the future considering research advances, government actions (financial support, CO₂ emission taxes), and general awareness about environmental concern.

On the research side, several PV systems have been elaborated since the silicon solar cell breakthrough. The one gathering the most attention today by way of impressive efficiency progress is based on organometal halide perovskite material. The gradual understanding of the specific properties of such material together with careful optimization of devices have risen power conversion efficiencies from 3 % to over 22 % within only 9 years. Relying on high PV performances, available materials and cost-effective solution processability, perovskite solar cells are expected to compete with crystalline silicon solar cells in the next years. On this way, important challenges are animating the scientific community: enhancing the efficiency of large scale devices and increasing their lifetime while keeping their price attractive. Indeed, perovskite materials can be altered by moisture, temperatures and UV light. Degradation of the perovskite can also be induced by other components of the solar cells such as the organic hole transporting material which helps charge collection at the perovskite interface. On the other hand, combined to polymers, these devices have already shown enhancement of stability together with performances.

In this context, this thesis broadly focuses on enhancing stability and power conversion efficiency of perovskite solar cells by introducing novel polymers as hole transporting layer or as additive in the hole transporting layers. The three main perovskite structures (mesoporous n-i-p, planar n-i-p and inverted planar p-i-n) were considered according to the specific properties the polymeric materials could bring to the systems.

The First Chapter is dedicated to a description of the state-of-the-art perovskite solar cells and particularly the hole transporting materials developed for this application. Chapter 2 gathers methods to fabricate perovskite solar cells based on conventional materials and areas of optimizations. These solar cells are taken as reference in the following parts. In Chapter 3 are introduced poly(9-vinylcarbazole)-based polymers as hole transporting materials in n-i-p PSCs. Chapter 4 focused on polyelectrolytes and in particular, their potential to be alternative dopants for hole transporting materials in mesoscopic perovskite solar cells. Finally, Chapter 5 is dedicated to inverted p-i-n perovskite solar cells and their potential to be integrated as semi-transparent device in window panels. This implied the introduction of a PEDOT derivative highly transparent and conductive.

References

1. Enerdata Global Energy Statistical Yearbook 2018. <https://yearbook.enerdata.net/total-energy/world-consumption-statistics.html> (accessed September 2018).
2. Council, U. N. d. P. a. W. E. *Energy and the challenge of sustainability*; 2000.

Chapter 1

Background

In Chapter 1 is presented an overview of the background knowledge necessary for the understanding of the manuscript. This includes a general description of photovoltaic effect and technologies, a focus on the evolution and the current challenges of perovskite solar cells and finally, a review of hole transporting materials developed for this application.

1 Photovoltaic generalities

Photovoltaic (PV) effect is the direct conversion of light energy into electricity. This was first observed by Edmond Becquerel in 1839 who recorded electrical current between two platinum electrodes immersed in a liquid electrolyte when exposed to sunlight. A century later, Bell Telephone laboratories realized the first solar cell and the first solar module based on silicon. At this time, the costly technology was mostly considered to supply spacecraft. Through further research, PV technology got more affordable. Thus, after the 70's oil crisis, PV devices were recognized as energy source of interest for terrestrial applications. Today, silicon-based modules lead the PV market owing to the availability of the active material, their rather high power conversion efficiency (PCE) up to 20 %, their relatively long lifetime and their cost-effective process.

1.1 Principle

PV effect occurs in semiconducting materials which have the ability to absorb light and release electrons that can be collected and used as electricity. Upon illumination, electrons from the valence band are excited into the conduction band of the semiconductor. Photoexcited charge carriers are separated through an asymmetrical device that drives them in opposite and preferred directions. The asymmetry in the device is traditionally achieved by a p-n junction, i.e. an interface between a p-type and an n-type semiconductor (Figure 2). When such materials are in contact, excess of charge carriers in the doped semiconductors recombine, creating a depletion region composed of positive and negative ions in the n-type and in the p-type material, respectively. Upon illumination, these ions specifically attract photogenerated charge carriers at the interface and in the bulk.

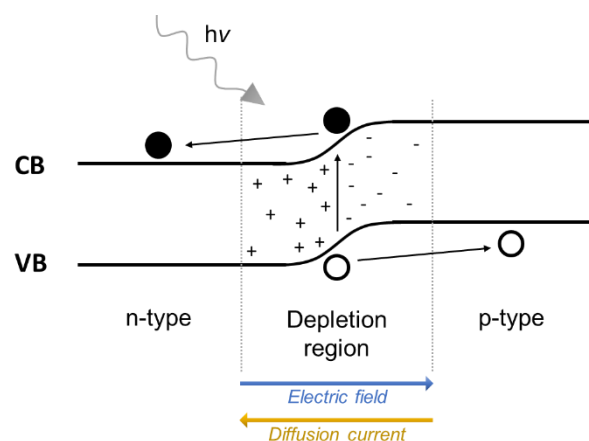


Figure 2. Charge carrier separation at the p-n junction.

1.2 Efficiency measurement

Performance of PV devices is evaluated by the PCE, which is calculated from PV characteristics extracted from current-voltage (I-V) curves (Figure 3a). The short-circuit current (I_{sc}) represents the current produced when no voltage is applied to the device. Generally, current (I) is expressed as current density (J). The open-circuit voltage corresponds to the voltage produced when no current is flowing through the device. Therefore, series resistance R_s and shunt resistance R_{sh} can be defined as the inverse of the slope at $V = V_{oc}$ and at $J = J_{sc}$ respectively. The fill factor (FF) gives an indication on the quality of the system by comparing the ideal power (P_{ideal}) the device could generate to the maximum power (P_{max}) that it is actually achieving. FF can be defined by the Equation 1.

$$FF = \frac{I_{max} V_{max}}{I_{sc} V_{oc}} = \frac{P_{max}}{P_{ideal}} \quad (1)$$

Therefore, the PCE is defined as the ratio of the maximum power delivered by the device on the power provided by the incident light (P_{inc}), as given in Equation 2.

$$PCE = \frac{FF I_{sc} V_{oc}}{P_{inc}} = \frac{P_{max}}{P_{inc}} \quad (2)$$

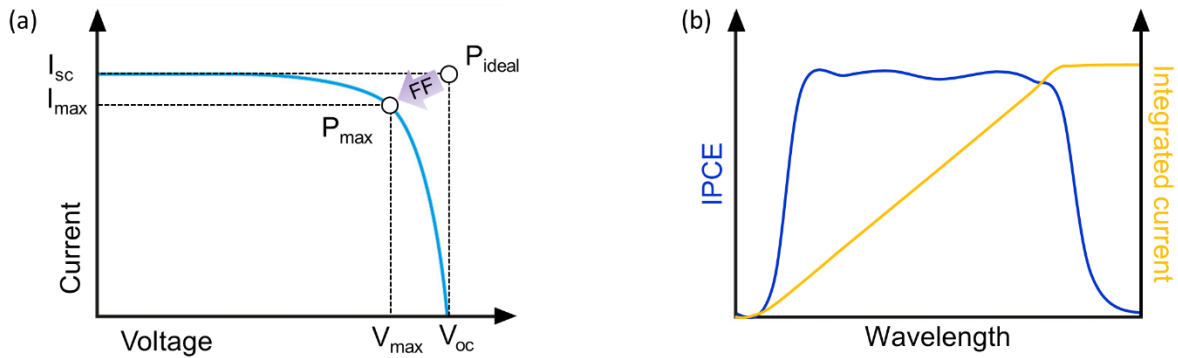


Figure 3. (a) I-V curve of a solar cell under illumination and (b) IPCE curve.

Incident-photon-to-electron conversion efficiency (IPCE) or external quantum efficiency (EQE) is a complementary characterization of solar cells giving the ratio between collected charge carriers and incident photons received at the surface of the solar cell for a defined wavelength (Figure 3b). Moreover, J_{sc} can be calculated by integration of IPCE curve through the Equation 3:

$$J_{sc} = q \int_{\lambda_1}^{\lambda_2} EQE(\lambda) \Phi_{\lambda} d\lambda \quad (3)$$

where q is the electric charge, $\lambda_2 - \lambda_1$ is the wavelength step, and Φ_λ is the spectral photon flux. Thereby, IPCE are also used to verify validity of information given by I-V curves by comparing J_{sc} .

1.3 Solar spectrum

Conditions to record I-V curves have been standardized. The solar simulator should emit the air mass 1.5 (AM1.5) spectrum representing solar spectrum received by mid-latitude regions with an incident angle of 48° to the ground. The incident power is assumed to be 100 mW.cm^{-2} . The AM1.5 spectrum is represented on Figure 4a.

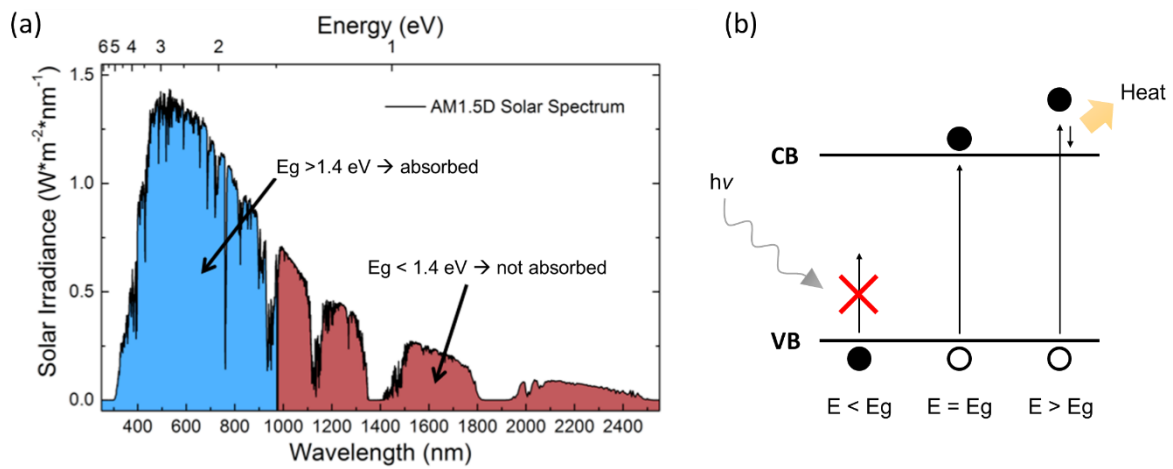


Figure 4. (a) Parts of solar radiation spectrum a typical semiconductor with a bandgap of 1.4 eV can absorb. (b) Energy conditions for a semiconductor to absorb radiations.

Consequently, to generate high photocurrent, maximum of the solar irradiance has to be absorbed by the semiconductor. The ability of the semiconductor to absorb photon energy is defined by its energy bandgap (E_g) defined by the energy difference between its conduction band (CB) and its valence band (VB). Photons of lower energy than the bandgap cannot be absorbed because of the lack of states for electrons at this energy value. On the other hand, photons of higher energy than the bandgap can be absorbed. Electrons are excited from the valence to high energy state where they rapidly go back to the conduction band releasing thermal energy (Figure 4b). Therefore, there is a threshold excitation energy to reach for the semiconductor to absorb. Excitation doesn't need to be excessively high since excess of energy is converted into thermal losses.

The theoretical maximum efficiency of a solar cell made of one p-n junction is stated at around 33.7 % by the Shockley-Quiesser limit and represents a bandgap of 1.34 eV in standard conditions. Only multiple junction solar cells, constituted of a stack of semiconducting materials absorbing different region of the solar spectrum can overpass this limit.

1.4 Photovoltaic technologies

Over years, several PV technologies have been developed in addition to crystalline silicon (c-Si) solar cells. They are often classified in term of generations (Figure 5). The first generation refers to crystalline silicon solar cells, the second includes solar cells based on inorganic thin films, and the third gathers emerging technologies and new concepts. Evolution of PV performances of these technologies is reported by the National Renewable Energy Laboratory (NREL) and illustrated on Figure 6.¹

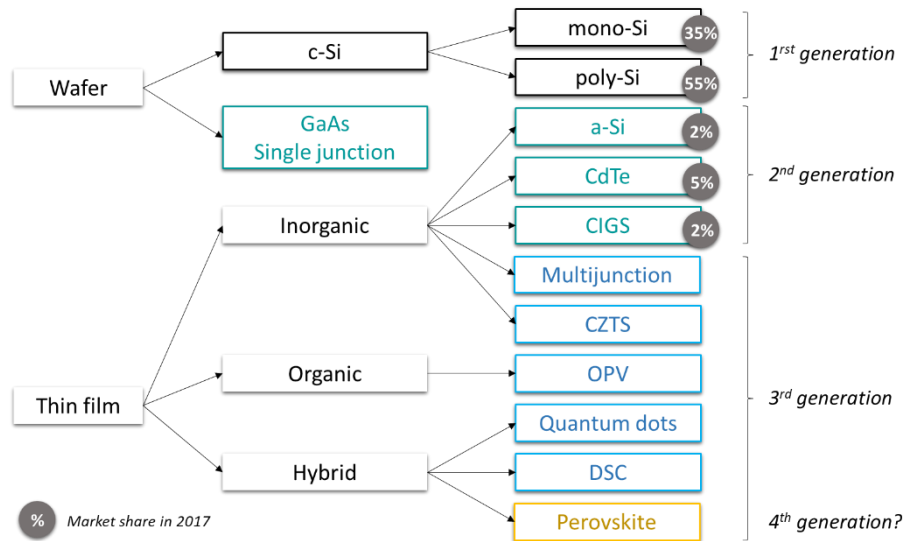


Figure 5. Classification of PV technologies and their market share.

c-Si solar cells are a mature technology that now dominates the PV market. They are made of p-doped and n-doped monocrystalline silicon (mono-Si) or polycrystalline silicon (poly-Si) wafers, assembled to form a p-n junction. At lab scale, record efficiency of 26.7 % was achieved employing mono-Si vs. 22.3 % for poly-Si solar cells.² Taking advantage of research advances and microelectronics industry feedbacks, manufacturing has been optimized to fabricate affordable modules of poly-Si that exhibit PCE around 20 %. c-Si PV market was still growing in 2017 while the module price continued to decrease.³ However, as we can see on the NREL chart, no significant breakthrough has been reported since the 90's, making the PCEs stagnated. Moreover, industrial processes include environmental unfriendly and energy guzzling steps such as high temperatures (> 1100°C) and high pressures.

Inorganic thin film technologies from the second generation were first developed to rival the price of c-Si solar cells, notably by employing less material. They mainly gather hydrogenated amorphous silicon (a-Si), gallium arsenide single junction (GaAs), cadmium telluride (CdTe) and copper indium

gallium selenide (CIGS) solar cells. The direct bandgap of these materials (1.0-1.8 eV) allows high PV performances with less matter. In term of efficiency, a-Si knew very little progress in the past 20 years, while CdTe and CIGS technologies compete at lab scale with c-Si module efficiency.¹ However, the toxicity of the CdTe and CIGS devices slowed their penetration into the PV market. On the other hand, although high efficiency of up to 29 %, GaAs single junction cells application for terrestrial application is limited by their high cost.⁴

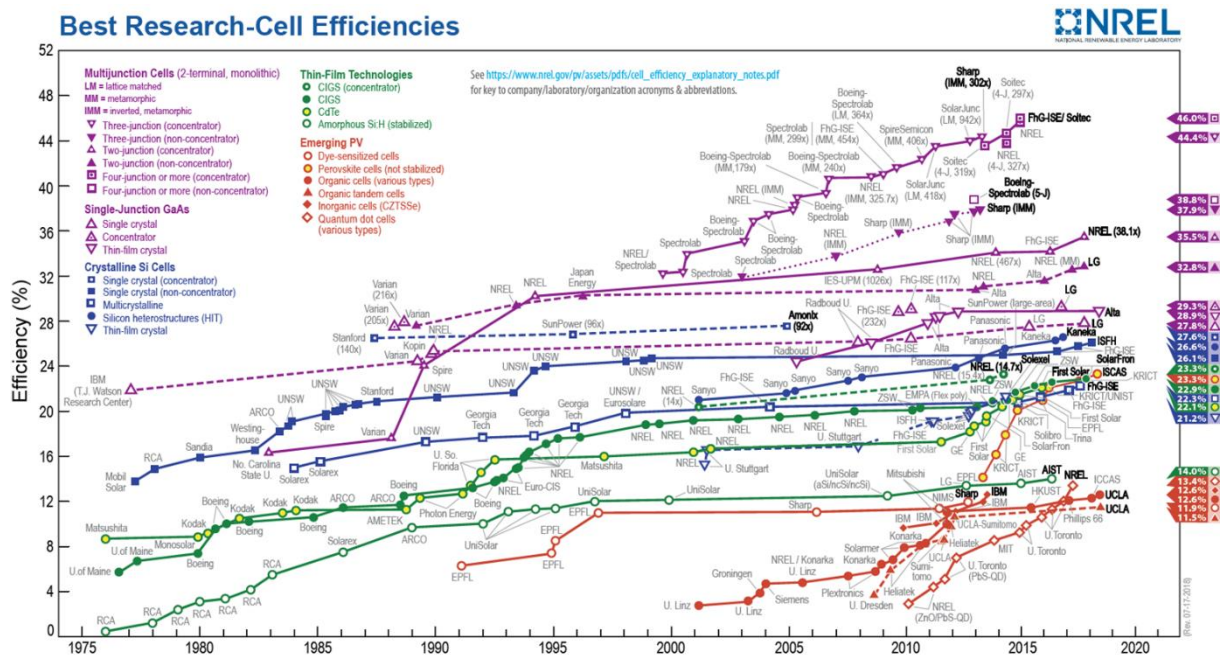


Figure 6. Amelioration efficiency of PV technologies reported by NREL on September 2018.¹

Third generation solar cells include ongoing development PV technologies: copper zinc tin sulphide (CZTS), organic photovoltaics (OPVs), dye-sensitized solar cells (DSCs), quantum dots solar cells, perovskite solar cells (PSCs), tandem and multijunction cells. Some of these new concepts such as III-V multijunction cells achieved record efficiency of 46 %.² However, they are saved for space application due their high cost. Others, like OPVs or DSCs, have received interest for their facile and low-cost production, and their compatibility with flexible devices, although generally associated to low stability and low efficiency. Recently, worldwide attention gathered around PSCs. PSCs emerged from DSCs, where the organic or metallo-organic dye absorber was replaced by perovskite material. Rapidly, performances of PSCs overtook that of DSCs to achieve today 22.6 % efficiency (22.1 % certified data).⁵ This novel high-efficiency low-cost PV technology could be foreseen as the fourth generation solar cells.

2 Perovskite material

2.1 Structure & Composition

Perovskites are a type of material defined by the same crystal structure as calcium titanium oxide (CaTiO_3). The mineral was discovered in 1839 in the Ural Mountains of Russia and was dedicated to the mineralogist Perovski, from where it takes its name. Perovskites are described as ABX_3 structures, where A and B are cations, A being larger than B, and X an anion bonding to both. In the cubic structure, X anions form a network of octahedrons. B is located at the centre of each octahedron while A is at the centre of cuboctahedrons formed between the octahedrons (Figure 7).

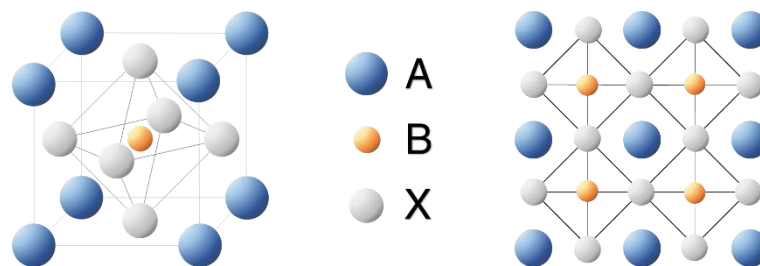


Figure 7. Cubic perovskite crystalline structure.

The phase stability of the 3-dimensional (3D) crystal can be predicted by the Goldschmidt's tolerance factor (t). It gives an indication on the compatibility of the compounds to form a stable perovskite crystal according to their size. It is defined by Equation 4, where r_A , r_B and r_X are the radii of A, B and X, respectively.

$$t = \frac{r_A + r_X}{\sqrt{2} (r_B + r_X)} \quad (4)$$

In the ideal packed cubic structure, $t = 1$. In the case of hybrid organic inorganic perovskites, a cubic lattice is assumed when $0.8 \leq t \leq 1$. If $t < 0.8$, perovskite distortion can lead to tetragonal, trigonal, rhombohedral or hexagonal phases. For $t > 1$, the 3D perovskite structure will change for 2-dimensional (2D) structure, where A cations are located between B-X octahedrons.⁶

The perovskites used for photovoltaic applications are organometal halide perovskites. Many compositions have been investigated for photovoltaic applications.⁶ In 3-dimensional (3D) perovskites, the cation A is generally methylammonium CH_3NH_3^+ (MA) or formamidinium $\text{NH}_2\text{CH}=\text{NH}_2^+$ (FA). Additional small cations like Li^+ , Na^+ , K^+ , Cs^+ or Rb^+ can eventually be incorporated to the crystal. Typical centred cation B is a metal like lead. Some examples of lead-free perovskite were also explored, especially tin-based perovskite to reduce the toxicity of the compound.⁷ The

anion X is a halide I^- , Br^- or Cl^- that can migrate throughout the crystal via vacancies.⁸ Several mixed cations, mixed metals and mixed halides perovskite structures have also been investigated. Such perovskites have generally cubic or tetragonal structures in ambient conditions, which can be modified by temperature variations. For instance, the tetragonal MAPbI₃ exhibit transformation to cubic and then to orthorhombic phase when decreasing the temperature. On the other hand, FAPbI₃ perovskite keeps its trigonal phase even at high temperature.⁹

Low-dimensional perovskites have also attracted attention for PV applications. Their structures are generally defined as $(RNH_3)_2A_{n-1}M_nX_{3n+1}$ and $R(NH_3)_2A_{n-1}M_nX_{3n+1}$, and are illustrated in Figure 8.¹⁰ Such structures can be elaborated by incorporating larger organic molecules than in 3D ones between inorganic layers, that force the perovskite to organize in 2D layers. Although 2D perovskites were proved to be considerably more stable than 3D ones toward atmosphere, high temperatures and illumination, their larger bandgap and low hole mobility leads to lower PCEs, making them less attractive for PV applications. Therefore, only 3D perovskite materials are considered in this work.

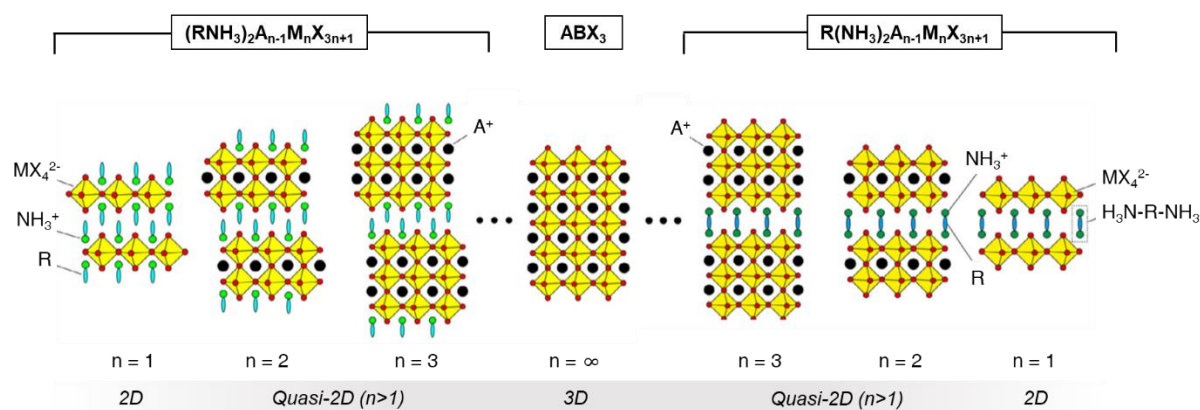


Figure 8. Perovskite structures from 2D ($n=1$) to 3D structures ($n=\infty$).³

2.2 Opto-electronic properties

Organolead halide perovskites have a broad absorption range of visible light and low exciton binding energy (≈ 16 meV) allowing high photoconversion rate.¹¹ Moreover, they present excellent ambipolar charge transport properties with a high hole and electron mobility of 5-12 and 2-10 $cm^2 \cdot V^{-1} \cdot s^{-1}$ respectively.¹² MAPbI₃ perovskite is commonly taken as reference perovskite material. It has been widely studied owing to its large bandgap, broad absorption range and long carrier diffusion length around 100 nm. Nonetheless, its 1.5 eV bandgap can be optimized in order to maximize absorption in the visible region. As the bandgap is particularly dependent to the B-X bond, it can be tuned through composition engineering by modifying X or B, or even A which affects B-X-B bond length and angle. The electronic properties of some examples of perovskite materials are depicted in Figure 9.

Thereby, FAPbI₃ perovskite has a lower energy bandgap and a broader absorption range than MAPbI₃. Also, the larger size of the FA⁺ cation compared to MA⁺ increases the tolerance factor of the perovskite which makes it more stable towards temperature variations. Similar bandgap reduction can be observed by replacing part of Pb²⁺ by Sn²⁺.¹⁴ On the other hand, by substituting part or full of iodide by bromide ions, perovskite bandgap is significantly enlarged resulting in lower absorption and higher V_{oc}.¹⁵ Incorporation of chloride into the perovskite preparation led to a remarkable improvement of charge carrier diffusion length up to 1 μm and also a better stability. Interestingly, X-ray diffraction (XRD) analysis of final perovskite film revealed a Cl⁻ ratio of only 3-4 % to I⁻ when 40 % were introduced.¹⁶ Most of chloride is suggested to sublime while the remaining one is unconverted and thus, doesn't integrate perovskite crystal. Enhanced diffusion length was attributed to the restructuration of the crystal during chloride evaporation.¹⁷ Finally, it was reported that MAPbI_{3-x}Cl_x perovskite thin film has similar absorption, photoluminescence decay lifetime and energy levels as MAPbI₃. Introduction of small quantities of additional cations also afford tuning of energy bands of the perovskite. Modifications of the perovskite result from the different size of the elements that will take different places in the crystal.¹⁸

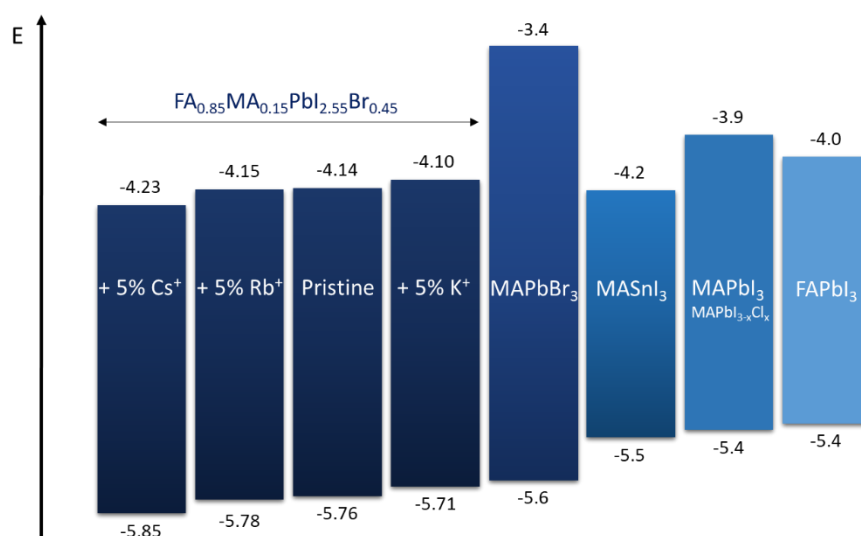


Figure 9. Energy diagram of perovskite materials of different compositions.

2.3 Deposition technics

General reaction forming ABX₃ perovskite can be described as AX + BX₂ → ABX₃. Several deposition methods have been optimized according to the substrate and the composition of the perovskite, to form high quality layers with few defects, high crystallinity, homogeneous covering and good reproducibility. Film fabrication routes include solution and vapour processing in one or several steps, and hybrid vapour-solution deposition (Figure 10).

To prepare MAPbI₃ perovskite thin film, solution processing is the most prominent technic. Sequential deposition was traditionally employed. PbI₂ layer was deposited from solution, usually by spin coating in DMF, and annealed. Then, MAI was added to convert PbI₂ film into MAPbI₃ either by dipping PbI₂ film directly into MAI solution, or by spin coating a MAI solution in isopropanol (IPA), by vapour-assisted deposition, or by thermal evaporation. Perovskite crystallization was finally achieved by thermal annealing.

Generally, one-step solution deposition of PbI₂ and MAI leads to poor quality perovskite layers due to the faster crystallization of PbI₂ as compared to MAI. To retard PbI₂ crystallization, additives or additional solvents like DMSO can be added to the mixture.¹⁹ High quality films were also obtained by replacing PbI₂ by PbCl₂.²⁰ Besides, anti-solvent quenching method consists in dropping an anti-solvent like chlorobenzene during the spin coating of the perovskite precursor solution.²¹ As the anti-solvent cannot solubilize MAI nor PbI₂, perovskite crystallization is triggered. This method is particularly popular for the deposition of high quality multiple cation and multiple halide perovskites.

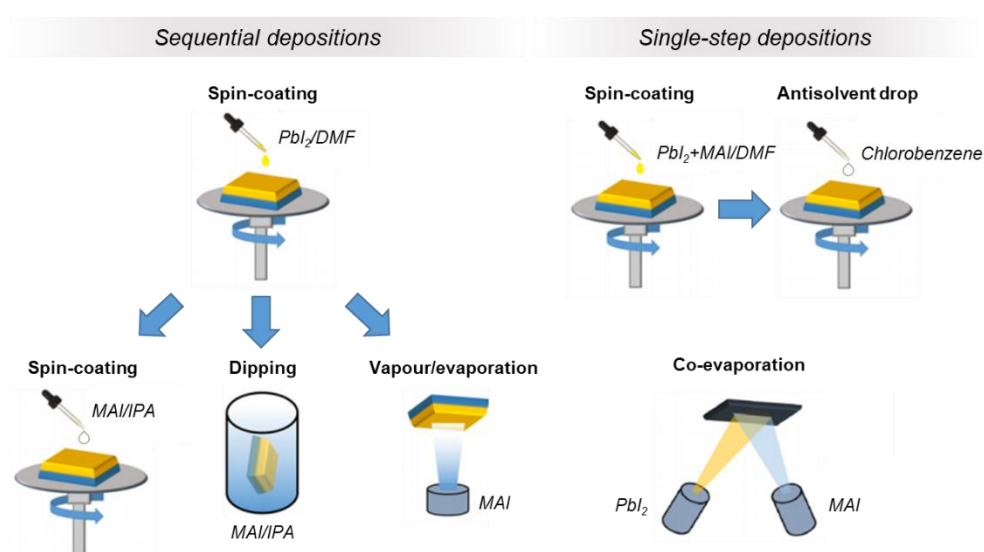


Figure 10. Examples of sequential and single-step deposition routes to make MAPbI₃ perovskite thin films.

Vapour deposition routes were adapted for perovskite materials in order to reduce perovskite defects and improve device reproducibility. First example described the formation of MAPbI_{3-x}Cl_x via the co-evaporation of PbCl₂ and MAI with few defects and complete covering of the planar substrates.²⁰ To form MAPbI₃, PbI₂ and MAI can also be successively evaporated.²² However, it is more tedious to incorporate multiple cations and halides.²³

The deposition methods described above are convenient to develop high quality perovskite thin film at lab scale but are not compatible with industrial processes, especially evaporation steps which require low vacuum level (10^{-5} mbar) and elevated temperatures (350°C for PbCl_2). Thus, scalable processes such as doctor blading, spray coating, or slot-die coating have also been considered.

2.4 Working principle

Generally, perovskite solar cells are described as p-i-n or n-i-p junction solar cells, where the intrinsic perovskite absorber i is stacked between an n-type and a p-type material forming selective contacts. Although the processes of charge generation to collection in PSCs has not totally been overcome, the operating mechanism can be simply described. Light is absorbed into the perovskite material. Electrons of the valence band are excited generating electron-hole pairs also called excitons. Charges are immediately separated due to the low exciton binding energy of the perovskite. Free holes and electrons diffuse into the perovskite until they reach selective contacts, where they are extracted. A carrier at the wrong selective contact is blocked and cannot be extracted. This simplified mechanism is illustrated in Figure 11 and is valid in the open circuit condition. Undesirable charge-transfer processes, i.e. recombinations of photo-generated charge carriers, can also occur into the perovskite layer and at the interfaces.

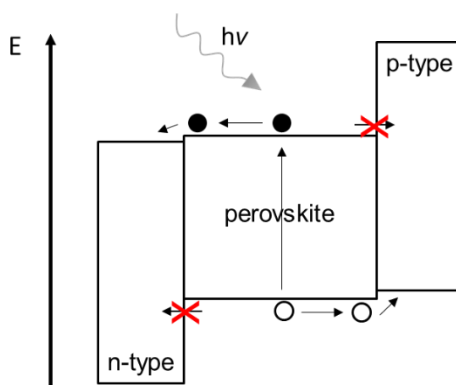


Figure 11. Energy diagram of PSCs and charge generation and collection mechanisms.

Based on this mechanism, some requirements for optimal operation of PSCs can be defined. To maximize sun light absorption, perovskite bandgap has to be close to 1.3-1.4 eV. To limit charge recombinations into the perovskite layer, long charge carrier diffusion length and high quality perovskite film, i.e. continuous with few defects, are required. Energy levels of selective contacts have to be well-aligned with those of the perovskite to limit energy loss and facilitate charge extraction. Selective materials must have high carrier mobility to limit series resistance in the device.

Finally, materials on the illuminated side of the device have obviously to be as transparent as possible for optimal photoconversion.

As previously mentioned, PCE is maximized with high FF, J_{sc} and V_{oc} . Optimal FF is obtained by minimizing series resistance in the device and increasing conductivity of the selected materials. On the other hand, hole and electron extracting rates ruled the photocurrent. Maximum V_{oc} is theoretically determined by the energy difference between the LUMO or the conduction band of the n-type material and the HOMO or valance band of the p-type material. Experimental V_{oc} never reaches this maximum because it is affected by the generation and dissociation probability of excitons, and by the charge recombinations.

3 Perovskite solar cells

3.1 Evolution towards 20 % efficiency

The PSC evolution has been punctuated by series of important breakthroughs. The first perovskite-sensitized solar cells (PSSCs) were reported in 2009 by Kojima *et al.* Similar architecture as DSCs was employed (Figure 12). The perovskite material was used as a dye, coated on a mesoporous scaffold and immersed in a liquid electrolyte. Based on MAPbI_3 , PCE of up to 3.1 % was measured, while 3.8 % was achieved using MAPbBr_3 .²⁴ However, the device lifetime was very short due to the decomposition of the perovskite crystal into the liquid electrolyte. To overcome perovskite degradation, Park *et al.* introduced in 2012 solid-state perovskite-sensitized solar cells (ss-PSSCs) replacing the iodine/iodide-based liquid electrolyte by the solid hole transporter spiro-OMeTAD (Figure 12). PCE was improved to 9.7 %.²⁵ Going further, Cho *et al.* introduced the first hole-transporter-free PSCs. A monocrystalline perovskite film was grown through cavitation-triggered asymmetric crystallization to suppress grain boundaries and associated defects and traps. $\text{FTO}/\text{TiO}_2/\text{MAPbBr}_3/\text{Au}$ PSCs gave PCE of up to 6.5 %. It was also the first planar, i.e. mesoporous-layer-free, PSC reported.²⁶

Alternative scaffold to TiO_2 was introduced by Snaith *et al.*, who demonstrated that PCE can be enhanced to 10.9 % by coating the $\text{MAPbI}_{3-x}\text{Cl}_x$ perovskite on an inert Al_2O_3 scaffold, showing that photogenerated electrons can be also transported through the perovskite material.²⁷ In 2013, they modified the device architecture by forming thick perovskite film into the Al_2O_3 scaffold (Figure 12) which yielded improved PCE of 12.3 %. This proved the ambipolar conductivity properties of the perovskite crystal, able to generate, separate and transport charge carriers. Later, it was also found

that Al_2O_3 scaffold actually improved the stability of PSCs toward UV-light compared to TiO_2 .²⁹ Seok *et al.* equalled 12.3 % PCE by introducing colourful mixed halides $\text{CH}_3\text{NH}_3\text{PbI}_{3-x}\text{Br}_x$.¹⁵

Polymers introduction in PSCs as hole or electron transporters started on May 2013. PTAA was introduced by Seok *et al.* as HTM.³⁰ A best PCE of 12.0 % was reported, which was comparable at that time to the highest PCE reported in DSSCs (12.1 %).³¹ Following, Snaith *et al.* showed that they can improve the PCE of PSCs from 10.2 to 11.7 % by depositing a fullerene mono-layer on the TiO_2 scaffold. It was suggested that the fullerene inhibits electron injection to the TiO_2 where the electron transport is slower.³²

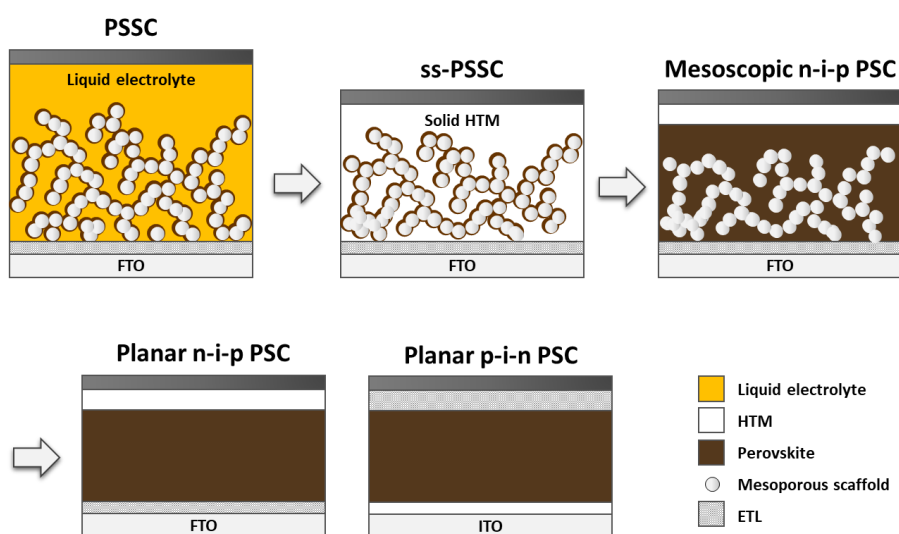


Figure 12. Schematic representation of the evolution of PSC architectures. From left to right: perovskite-sensitized solar cell, solid-state PSSC, n-i-p mesoporous PSC, n-i-p planar PSC and p-i-n inverted planar PSC.

On July 2013, Grätzel *et al.* optimized a sequential spin-coating deposition method to prepare perovskite films.³³ This method was previously reported by Mitzi *et al.* 15 years ago.³⁴ The improved perovskite morphology led to PCE as high as 15 %. On September 2013 was reported planar heterojunction PSC by Snaith *et al.* $\text{MAPbI}_{3-x}\text{Cl}_x$ layer was formed by dual-source vapour deposition on top of a compact TiO_2 layer, without using a mesoporous scaffold (Figure 12). The record PCE achieved was 15.4 %.²⁰ $\text{MAPbI}_{3-x}\text{Cl}_x$ perovskite was found more appropriate than MAPbI_3 for planar devices due to its longer charge diffusion length than MAPbI_3 (1 μm vs. 100 nm).³⁵

At the same period, the first inverted p-i-n planar structure was reported by Chen *et al.* (Figure 12). PEDOT:PSS on ITO substrate and fullerene derivatives were respectively employed to collect holes and electrons. They reached a best PCE of 3.90 %.³⁶ Few months later, on December 2013, Bolink *et al.* described another example of inverted PSCs, incorporating an interlayer of poly-TPD between PEDOT:PSS and the perovskite as electron-blocking layer. The PCE was improved to 12.0 %.³⁷ This

breakthrough significantly simplified the fabrication of PSCs by suppressing high temperature process of the inorganic compact layer and mesoporous scaffold, and opened the way to flexible and portable devices. On October 2013, Mathews *et al.* optimized ZnO low-temperature deposition process on ITO-PET flexible substrate. PSCs exhibited 2.6 % efficiency.³⁸

First step toward large scale perovskite solar modules was realized by Di Carlo *et al.* on January 2014. They fabricated perovskite solar modules composed of 5 cells connected in series for a total active area of 16.8 cm². A maximum PCE of 10 % was recorded employing P3HT as hole conductor.³⁹

On July 2014, Spiccia *et al.* introduced a one-step fast deposition-crystallization process also called anti-solvent method. It resulted in highly crystalline perovskite layers affording PCE of 16.2 %.²¹ At the same time, Seok *et al.* reported record PCE of 16.5 % (16.2 % certified data) through solvent engineering. DMF was replaced by γ -butyrolactone and DMSO while chlorobenzene anti-solvent was substituted by toluene resulting in extremely uniform perovskite films.¹⁹

First replacement of MA⁺ by FA⁺ cation was realized by Baikie *et al.* on December 2013. FA based perovskites have a broader absorption range and thus have the potential to increase photocurrent of PSCs. However, due to difficult preparation, FAPbI₃ based PSCs lead to only 4.3 % PCE.⁴⁰ Mixing FA and MA to form MA_{0.6}FA_{0.4}PbI₃ afforded an easier preparation of perovskite films and PCE reached up to 14.9 %.⁴¹ To further improve PCEs, Seok *et al.* on January 2015 included bromide to the mixed cation perovskite. Bromide based perovskites allow to reach higher photovoltage but narrower absorption range than iodide based perovskite. Through compositional engineering, they reported PCE of 18.4 % (17.9 % certified data), making MA_{0.15}FA_{0.85}PbBr_{0.45}I_{2.55} one of the reference perovskite material for PSCs.⁴²

Planar bulk heterojunction PSCs were reported on April 2015 by Masi *et al.* PC₆₁BM was mixed to the MAPbI₃ perovskite active layer to help to electron extraction. They obtained improved PCE of 15.0 %.⁴³

On June 2015, the first PSC exceeding 20 % efficiency, published by Seok *et al.* 20.2 % PCE (20.1 % certified data), was achieved by optimizing the 2-step deposition process for FAPbI₃ perovskite crystal. The strategy involved the incorporation of DMSO into the PbI₂ precursor solution to form PbI₂-DMSO films. FAI was then more easily inserted into the PbI₂ layer via intramolecular exchange between DMSO and FAI.⁴⁴

3.2 Over 20 % efficiency perovskite solar cells

Three main PSC architectures have been introduced: mesoscopic and n-i-p planar and p-i-n inverted. Different routes addressing specific issues have been explored to achieve high efficiency in each kind of device.

3.2.1 n-i-p Mesoscopic solar cells

Improvement of mesoscopic solar cells mainly resulted from the optimization of the perovskite layer. Best composition of perovskite material is still under investigations. Seok *et al.* reported the beneficial effects resulting in an excess of PbI_2 in MAPbI_3 perovskite. It was found that PbI_2 reduced hysteresis and ion migration, leading to PCEs up to 19.8 %.⁴⁵ On the other hand, Park *et al.* realized PSCs exhibiting best PCE of 20.4 % with an excess of MAI in MAPbI_3 . A MAI layer has been suggested to be formed at the grain boundaries, which suppress recombinations and improve charge extraction through ionic-conducting pathways.⁴⁶ The composition of $\text{FA}_{1-x}\text{MA}_x\text{Pb}(\text{I}_{1-x}\text{Br}_x)_3$ was also studied. Hagfeldt *et al.* reached efficiency as high as 20.7 % and 20.8 % for $\text{MA}_{0.33}\text{FA}_{0.67}\text{Pb}(\text{I}_{0.83}\text{Br}_{0.17})_3$ and “ $\text{MA}_{0.15}\text{FA}_{0.81}\text{Pb}(\text{I}_{0.83}\text{Br}_{0.15})_3$ ” compositions, respectively.⁴⁷ Triple cation perovskite was introduced by Grätzel *et al.* by adding 5% cesium to form $\text{Cs}_{0.05}(\text{MA}_{0.17}\text{FA}_{0.83})_{0.95}\text{Pb}(\text{I}_{0.83}\text{Br}_{0.17})_3$. Cs^+ improved stability of the perovskite as well as PCE to 21.2 %.⁴⁸ They further proposed rubidium doped perovskite. The best system was based on quadruple cation perovskite, including Rb^+ , Cs^+ , MA^+ , and FA^+ , and reached 21.8 % PCE.⁴⁹ Segawa *et al.* introduced potassium as more available dopant (than Rb^+ and Cs^+) for the perovskite. Best PCE of 20.3 % was obtained thanks to a better energy band alignment and few defects into the perovskite.⁵⁰ A more original additive to the perovskite was incorporated by Grätzel *et al.* They mixed PMMA polymer to the perovskite precursor solution to improve crystallization of the perovskite. It resulted in PCE as high as 21.6 %.⁵¹

Improvements of deposition technics also afforded to overtake 20 % efficiency. Grätzel *et al.* reported 20.8 % efficiency by depositing the perovskite through sequential spin-coating deposition, while they obtained 20.5 % efficiency by treating perovskite layer under vacuum after spin-coating deposition.⁵² Record PCE published today was obtained by Seok *et al.* Perovskite layer was deposited by two-step spin-coating. Originality comes from iodide ions which were obtained by dissolving I_2 into isopropyl alcohol through oxidation of isopropyl alcohol to acetone. They achieved impressive PCE of 22.6 % efficiency (22.1 % certified data).⁵

Although main advances focused on the perovskite layer, investigations around selective materials also played a part in PSCs progress. Since it was reported that additives, such as lithium bis(trifluoromethanesulfonyl)imide salt (LiTFSI) and tert-butylpyridine (tBP), present in the conventional spiro-OMeTAD hole transporting layer could be detrimental for the device stability,

novel HTMs and additives were investigated.⁵³ Thereby, over 20 % PCE devices have been realized replacing conventional spiro-OMeTAD HTM by small molecules, metal organic compounds, or polymers.⁵⁴

3.2.2 n-i-p Planar solar cells

Planar architecture emerged from simplification of mesoscopic devices. Besides, planar TiO₂-based devices generally suffer from large hysteresis. The slow electron transport of the TiO₂ layer creates charge accumulation at the TiO₂/perovskite interface. This was overcome in mesoscopic devices by the larger TiO₂/perovskite interface which multiplies the sites where electron extraction is possible. Therefore, hysteresis reduction and elimination of charge trapping have constituted a serious challenge in n-i-p planar PSCs progress.

Perovskite morphology has been improved using HI as additive to the MAPbI_{1-x}Cl_x precursor solution, leading to 19.1 % PCE.⁵⁵ Grain size was increased and interface was passivated by introducing Pb(SCN)₂ in the MAPbI₃ precursor solution, resulting in PCE of 19.5 %.⁵⁶ Ko *et al.* prepared niobium-doped TiO₂ layer through low temperature process and UV exposure. Compatible with flexible devices, UV-Nb-TiO₂ layer had enhanced conductivity and better band alignment than conventional TiO₂, leading to 19.6 % PCE.⁵⁷ SnO₂ has also been reported as good alternative to TiO₂. Combining spin coating and chemical bath deposition techniques, Hagfeldt *et al.* reported PCE as high as 20.8 % with especially high V_{oc} of 1.18 V.¹⁸ Choi *et al.* demonstrated that charges trapped at perovskite grain boundaries induces degradation of the device, and showed that replacing TiO₂ by C₆₀ could reduce charge trapping and enhanced PCE to 20.4 %.⁵⁹ To improve electron extraction at the TiO₂/perovskite interface, Chang *et al.* modified TiO₂ surface with an ionic liquid of superior conductivity. It was also found to form a better base for perovskite growth that led in devices to 19.6 % PCE.⁶⁰ All of these advances were reported to reduce hysteresis in the device.

3.2.3 p-i-n Inverted solar cells

Inverted planar p-i-n PSCs are preserved from the use of metal oxide which limit electron extraction and corrosion of the perovskite layer by additives present in the upper HTM. Choi *et al.* introduced thin layer of molybdenum oxide between graphene electrode and PEDOT:PSS HTM to dope the graphene and improve contact between graphene and PEDOT:PSS. It resulted in 18.8 % PCE.⁶¹ Optimizing the HTL by replacing the traditional PEDOT:PSS by PTAA polymer, Huang *et al.* reached PCE of 18.3 %.⁶² Through insertion of a PS interlayer at the perovskite/C₆₀ interface, they succeeded in overtaking 20 % PCE.⁶³ Success of inverted PSCs resulted from high efficiencies obtained through optimizations of ETL and HTL together with electrodes in the prospect of fully printed low-cost PSCs.

3.3 Current and future challenges

3.3.1 Reliability of device performances

Together with efficiency improvements came out questions about reliability of the reported performances. These questions arose from anomalous hysteresis in J-V curves of PSCs, which would lead in over or under-estimation of device performance. Hysteresis behaviour is affected by speed and voltage direction of the scan. Three acceptable reasons producing hysteresis have been identified: the ferroelectricity of the perovskite material, ion migration in the perovskite material and charge accumulation, or unbalanced charge extraction, at the perovskite interfaces. It has been shown that hysteresis in PSCs could be explained by a ferroelectric diode model.⁶⁴ Polarization of the device could generate migration of ions and defects toward perovskite interfaces and create hysteresis.⁶⁵ Finally, insufficient charge transport rates at one of the perovskite interface could also induce charge accumulation and hysteresis.⁶⁶ Although in some cases J-V hysteresis has totally been overcome, it is still present in many devices. For more transparency of the reported data, it has been recommended, if not mandatory, to communicate conditions of J-V curves measurements, PV performances recorded from both scan directions, and solar cell area. It has been shown that solar cells smaller than 0.1 cm² could undergo optical artefacts affecting J-V measurements and leading to overestimation of J_{sc} .⁶⁷

3.3.2 Device sustainability

PSC as sustainable technology has first sustained scepticism due to the high sensitivity of the perovskite material to moisture and humidity. Although composition engineering and deposition technics have improved chemical and thermal stability of the perovskite, preparation conditions, such as temperature and relative humidity, were found to considerably affect device reproducibility and thus, have to be perfectly controlled. Moreover, overcoming preparation and encapsulation issues, decomposition of the perovskite layer can be induced by other constituents of the device, like the HTM or the ETM. The additives incorporated to the spiro-OMeTAD HTM in n-i-p devices has been especially pointed to promote perovskite degradation. Therefore, efforts on the perovskite material, preparation conditions and stability of selective layers have to be pursued, since long-term stability is a necessary requirement toward commercialization.

Sustainability of a technology also relies on availability of the materials which is often closely related to their price. Hopefully, lead is abundant on Earth, and some optimistic cost analysis demonstrated yet that traditional PSCs could compete existing technologies such as c-Si solar cells for an efficiency greater than 12 % and a lifetime of 15 years.⁶⁸ Cost reduction is further expected for replacement of expensive FTO and ITO conductive oxides, low-cost and low-temperature printable process and the

use of cheaper ETMs and HTMs than fullerene derivatives, spiro-OMeTAD or PTAA that are still largely employed in PSCs.

Finally, the incontestable toxicity of ionic lead constitutes a stumbling block for development of PSCs, from industrialization to recycling phase. Industrial use of lead is strongly regulated by international organisations such as the Restriction of Hazardous Substances of the European Union.⁶⁹ Moreover, in case of leakage or deterioration of a module, the solubility of perovskite in water could rapidly spread lead contamination and be detrimental for the environment. Although great progress in the substitution of lead by alternative elements like tin have been achieved, the efficiencies of the corresponding devices cannot rival yet with organolead-halide PSCs.

4 Hole transporting materials for perovskite solar cells

HTM remains an essential component of highly performing PSCs. The main role of the HTM is to collect and transport photo-generated holes from the perovskite to the electrode. To maximize PSC efficiency, ideal HTMs should have the following specific properties: a HOMO level or valence band energy compatible with the valence band energy of the perovskite, a high hole mobility, a good film-forming ability, a good photochemical and thermal stability, a low light absorption in the visible and near-IR regions of the solar spectrum, and a cost-effective process.

Owing to its suitable HOMO level, wide band gap, good solubility and film-forming, **spiro-OMeTAD** is the most popular and the most efficient organic HTM for regular PSCs. This 3D molecule is composed of a spiro-fluorene core substituted with four N,N-dimethoxyphenylamine groups (Figure 13). Spiro-OMeTAD was used for the first time in DSCs.⁷⁰ It was later introduced in PSCs. Replacing the liquid electrolyte, device lifetime was considerably extended.²⁵ However, due to the lack of π - π interactions, spiro-OMeTAD suffers from relatively low conductivity and low hole mobility. Therefore, chemical dopants such as LiTFSI salt and tBP, were successfully employed to p-dope spiro-OMeTAD. In PSCs, it resulted in higher PV performances and a reduction of carrier recombination at the interface in PSCs. Record PCE achieved employing spiro-OMeTAD is 21.3 %.⁷² Nonetheless, chemical dopants were reported to induce degradation of device materials by inducing ion migration and by bringing moisture into the device in the case of hygroscopic materials.⁵³ Last but not least, spiro-OMeTAD is an expensive molecule which necessitates tedious and costly purification processes which makes it inappropriate for mass production.

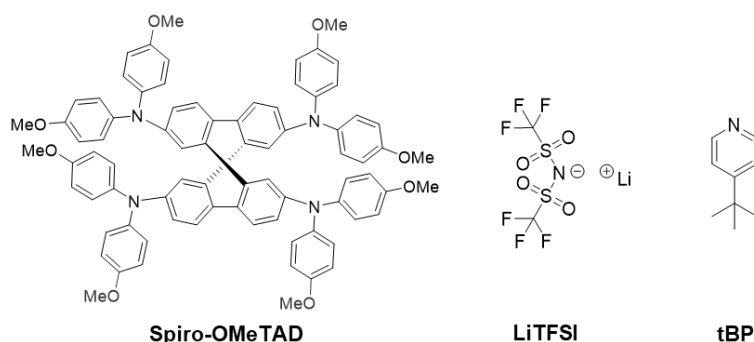


Figure 13. Chemical structure of spiro-OMeTAD HTM, and LiTFSI and tBP dopants.

Thereby, inspired from the specific structure of spiro-OMeTAD and learning from pointed instability issues, novel materials were synthesized paying particular attention to doping needs, cost of synthetic routes, chemical and thermal stability, and hygroscopicity of the materials.

4.1 Highly efficient HTMs

Here are reported examples of HTMs that gave over 18 % power conversion efficiency in mesoscopic, n-i-p planar or p-i-n inverted structure. If not mentioned, HTMs are doped.

4.1.1 Inorganic HTMs

Inorganic p-type semiconducting materials are interesting candidates as HTM for PSCs due to their good chemical stability and low cost. Moreover, they present good charge properties that often doesn't require the use of dopants. They are generally deposited from solvents able to dissolve the perovskite, and thus have mostly been studied for inverted PSCs. Materials studied include copper iodide (CuI),⁷³ nickel oxide (NiO),⁷⁴ Cu:NiOx,⁷⁵ and doped $\text{Li}_x\text{Mg}_y\text{Ni}_{1-x-y}\text{O}$.⁷⁶

Nickel oxide (**NiO**), owing to its high transmittance and appropriate VB, has been the most studied inorganic HTM in inverted PSCs. It was first introduced by Tang *et al.* in 2014 who demonstrated that PCE of 7.6 % can be achieved through low-temperature solution processing.⁷⁴ Seok *et al.*, via pulsed laser deposition of nanostructured NiO film, dramatically promoted PCE to 17.3 %.⁷⁷ Best efficiency reported was realized by Liu *et al.* who reached 18.8 % PCE combining NiO to nitrogen-doped reduced graphene oxide (**NiO:N-RGO**).⁷⁸

4.1.2 Metal-organic complex HTMs

Copper-based materials were the first inorganic HTMs employed in PSCs. Copper thiocyanate (**CuSCN**) is intrinsically p-doped and thus is conductive enough to be employed without additives. It was first introduced in TiO_2 -based PSCs in 2014. CuSCN was deposited by drop casting and PSCs exhibited only 6.4 % PCE.⁷⁹ Owing to device optimization, Grätzel *et al.* reported on November 2017 remarkable PCE of 20.4 % employing CuSCN as HTM.⁸⁰ On the other hand, in inverted PSCs, CuSCN demonstrated PCE up to 16.6 %.⁸¹

Various copper phthalocyanine compounds (**CuPc**) were studied as HTM or even as dopant for HTM (Figure 14).⁸² Tetrafluorotetracyanoquinodimethane-doped copper phthalocyanine-3,4',4'',4'''-tetra-sulfonated acid tetra sodium salt (**TS-CuPc:F4TCNQ**) was developed by Liao *et al.* PCE up to 16.1 % were achieved in inverted PSCs. Used as intermediate layer between spiro-OMeTAD and the top electrode, impressive PCE of 20.2 % was reached.⁸³ Recently, nickel phthalocyanine (**NiPc**) have also been tested as HTM for n-i-p PSCs. Despite high mobility and low cost, thermal evaporation process and relatively lower PCE (12.1 %) cannot compete with the CuPc derivative.⁸⁴

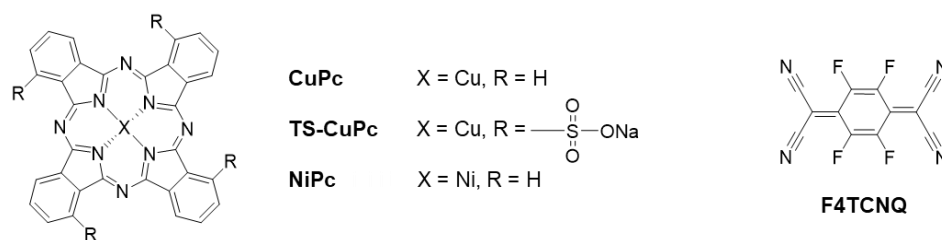


Figure 14. Chemical structures of metal-organic complexes.

4.1.3 Organic molecular HTMs

A larger range of organic HTMs have been developed for n-i-p and p-i-n PSCs. Despite generally lower hole mobility and stability than inorganic HTMs, organic HTMs offer broader access to specific properties inherent to the whole device through chemical modifications or doping. Thereby, best performing PSCs at present include organic HTMs.

4.1.3.1 Spiro-like HTMs

The effect of the 3D geometry of spiro-OMeTAD was studied by Hagfeldt *et al.* who replaced the spiro-bonded fluorenes of spiro-OMeTAD by C-C (**H11**) and C=C (**H12**) bonded fluorenes (Figure 15). They observed that the hole mobility decreased together with the perpendicular arrangements, and was minimal for H12. However, film-forming was improved. A compromise between both led to PCE of 19.8 % employing H11 as HTM.⁸⁵ Insertion of phenyl (**V859**) or thiophene (**V862**) groups in the two fluorene units of spiro-OMeTAD was carried out by Getautis *et al.* (Figure 15). Both HTMs were synthesized through cost-effective process. High hole mobility of the materials resulted in highly efficient PSCs exhibiting 19.5 and 20.0 % with V859 and V862 respectively.⁸⁶

Several examples of modified cores based on fluorenes were investigated. Sun *et al.* prepared via two-step reaction two novel HTMs, where one of the carbon bond of the two fluorenes of spiro-OMeTAD was broken. **HT1** fluorene was substituted with methoxy groups while **HT2** fluorene was substituted with N,N-dimethoxyphenylamine groups (Figure 15). The extended 3D structures improved film formation and enhanced hole mobility, leading to high PCE of 17.2 and 18.3 % for HT1

and HT2, respectively.⁸⁷ Nazeeruddin *et al.* changed the spiro-fluorene core of spiro-OMeTAD to dissymmetric fluorene-thiophene core (Figure 15). It was found that the thiophene groups interact with iodide of the perovskite at the interface enhancing hole transfer. **FDT**-based PSCs achieved excellent PCE of 20.2 %, over the reference spiro-OMeTAD PSCs.⁸⁸

Spiro[fluorene-9,9'-xanthene] (SFX) based HTMs **X59** and **X60** were simply synthesized via two-step synthetic route (Figure 15). **X59** was found to reduce hysteresis and extend device lifetime while **X60** had a high hole mobility and conductivity. Similar PCE of 19.8 % were obtained for both HTMs. It was at this time the first example of easily synthesized HTMs exhibiting comparable PV performance to the conventional spiro-OMeTAD.⁸⁹ More original structures combining SFX and triphenylamine groups were tested by the same group. **X54** and **X55** are highly distorted oligomers made in one-pot synthesis allowing good solubility in organic solvents. **X55** presented higher hole mobility, better film-forming and deeper HOMO level, yielding to high 20.8 % PCE.⁹⁰

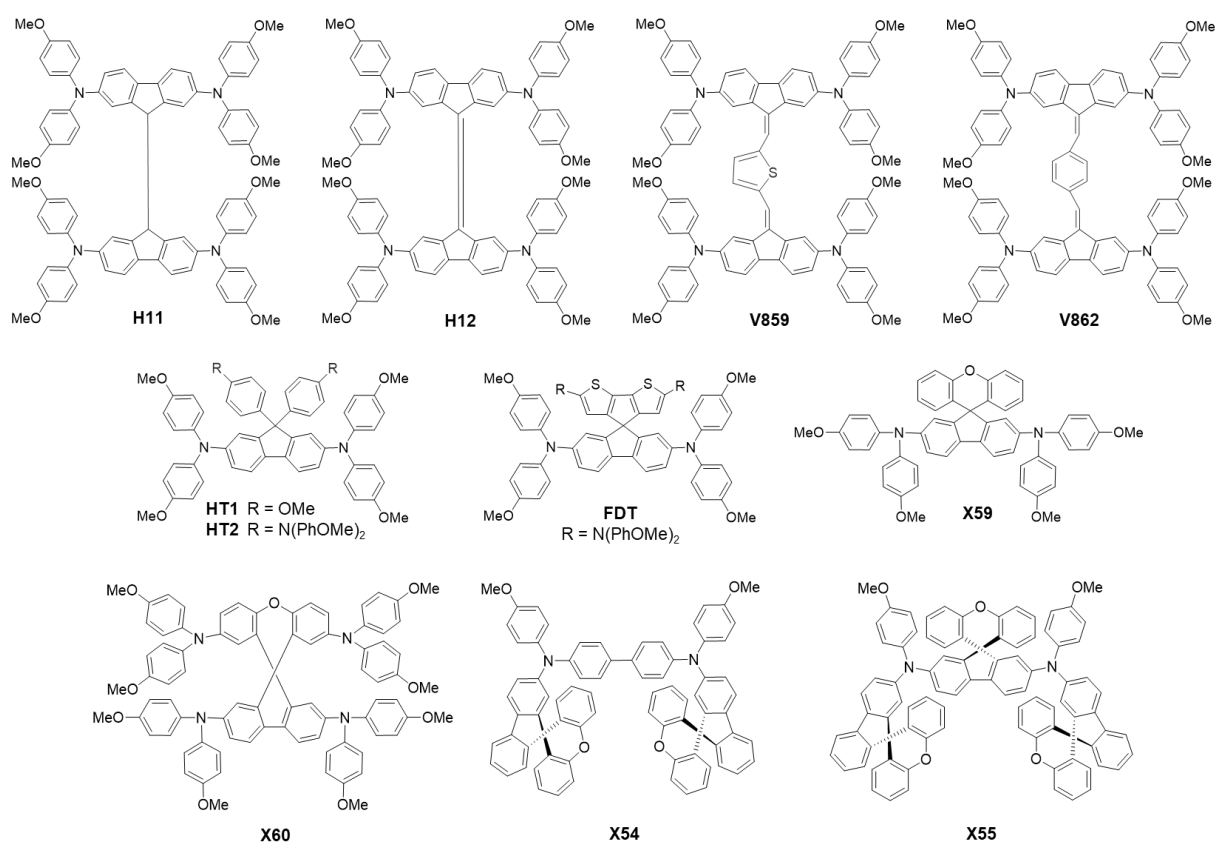


Figure 15. Chemical structures of spiro-like HTMs.

4.1.3.2 Thiophene-based HTMs

Thiophene groups have been successfully used to modify spiro-OMeTAD. These thiophene modified HTMs can reach relatively high PCE through simplified and cheapest synthesis, and can extend lifetime of the devices.

Recently, Zhang *et al.* reported cost-effective **Z25** and **Z26** based on thiophene core functionalized with methoxy groups which improved solubility of the materials (Figure 16). Moreover, introduction of double bonds in Z26 planar flattened the molecule, improving the conjugation effect and thus, the conductivity. Remarkable PCE of 20.1 % was obtained with Z26, vs. 16.9 % for Z25 and 20.6 % for spiro-OMeTAD.⁹¹

Nazeeruddin *et al.* studied the influence of alkyl length ending groups on anthra[1,2-b:4,3-b':5,6-b'':8,7-b'']tetrathiophene- (ATT-) based HTMs by comparing **ATT-OMe**, **ATT-OBu**, **ATT-OHe** and **ATT-Ode** (Figure 16).⁹² When increasing alkyl length, solubility of the materials was improved, hole conductivity was reduced while energy levels were unchanged. Thus, best PCE of 18.1 % was obtained employing ATT-OMe, while lowest PCE of 9.7 % was obtained using ATT-Ode.

Nazeeruddin *et al.* also developed benzotrithiophene (BTT) HTMs. **BTT-1** was functionalized with diphenylamine groups, **BTT-2** with triphenylamine groups and **BTT-3** with carbazoles endowed with diphenylamine groups (Figure 16). BTT-3 had the deepest HOMO level of -5.4 eV and the highest conductivity, leading to high PCE of 18.2 %, which was competitive with spiro-OMeTAD devices.⁹³

Phenothiazine-based HTMs were recently reported by Grätzel *et al.* Phenothiazines were either linked to dimethyltriphenylamine (**Z28**), ethyl carbazoles (**Z29**), or dimethoxytriphenylamine moieties (**Z30**). Z30 was found to be the best combination for hole transport affording PCE of 19.2 %, vs. 17.8 % for Z28 and 14.7 % for Z29.⁹⁴

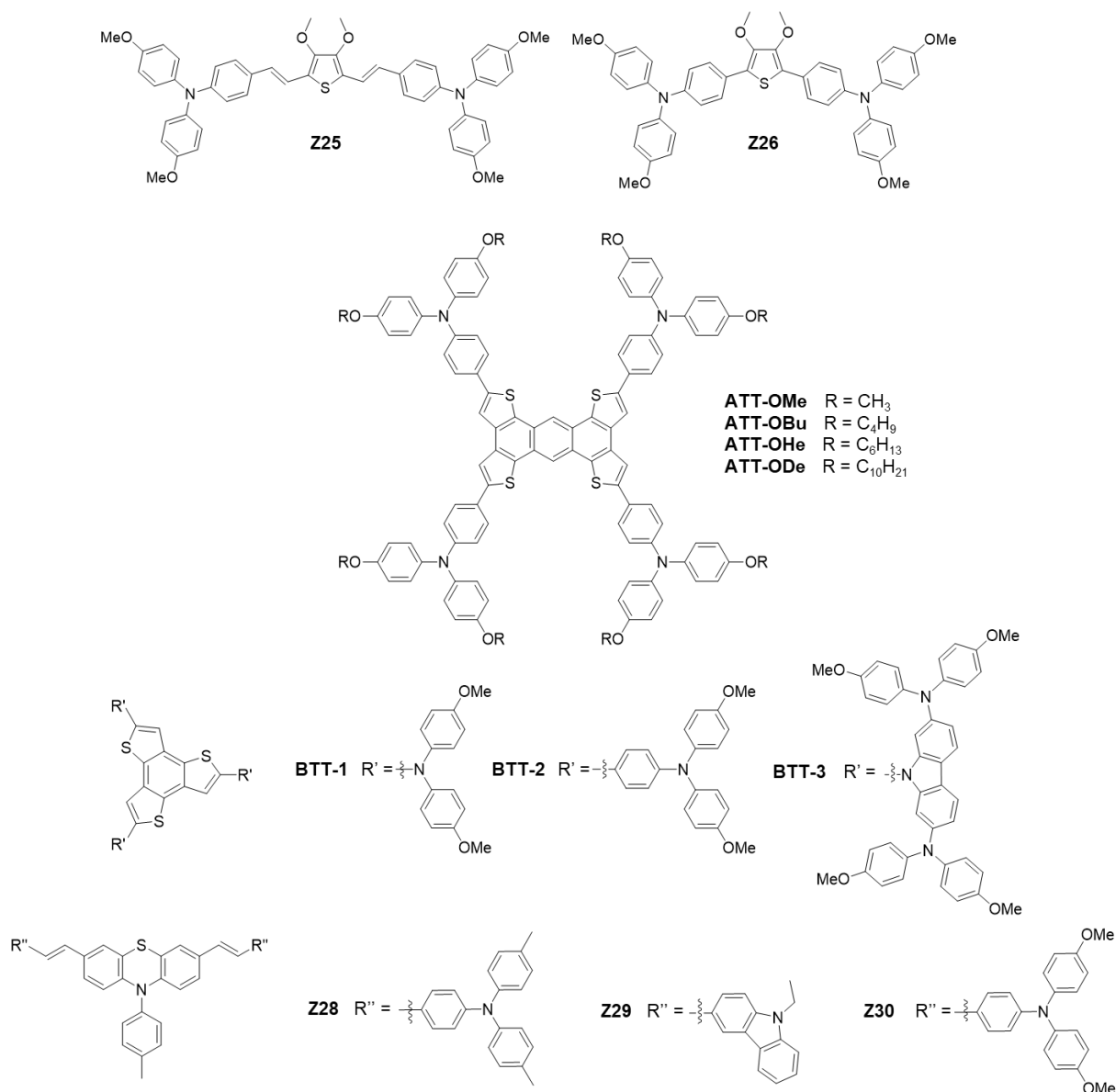


Figure 16. Chemical structures of thiophene-based HTMs.

4.1.3.3 Triphenylamine-based HTMs

Triphenylamine units are often present in HTMs due to good thermal and light stability, low ionic potential, and good solubility. Hole transmission is possible via positively charged vacancies. The nitrogen of TPA attracts electrons of aromatic rings through inductive effect, while its lone pair electrons are distributed to the aromatic rings. Inductive effect being weaker, aromatic rings became electron rich due to the p- π conjugated effect. The electron distribution makes electrons easy to delocalize and creates vacancies. However, dopants are often needed to increase hole mobility, especially for non-planar TPA which could have longer intermolecular distance.

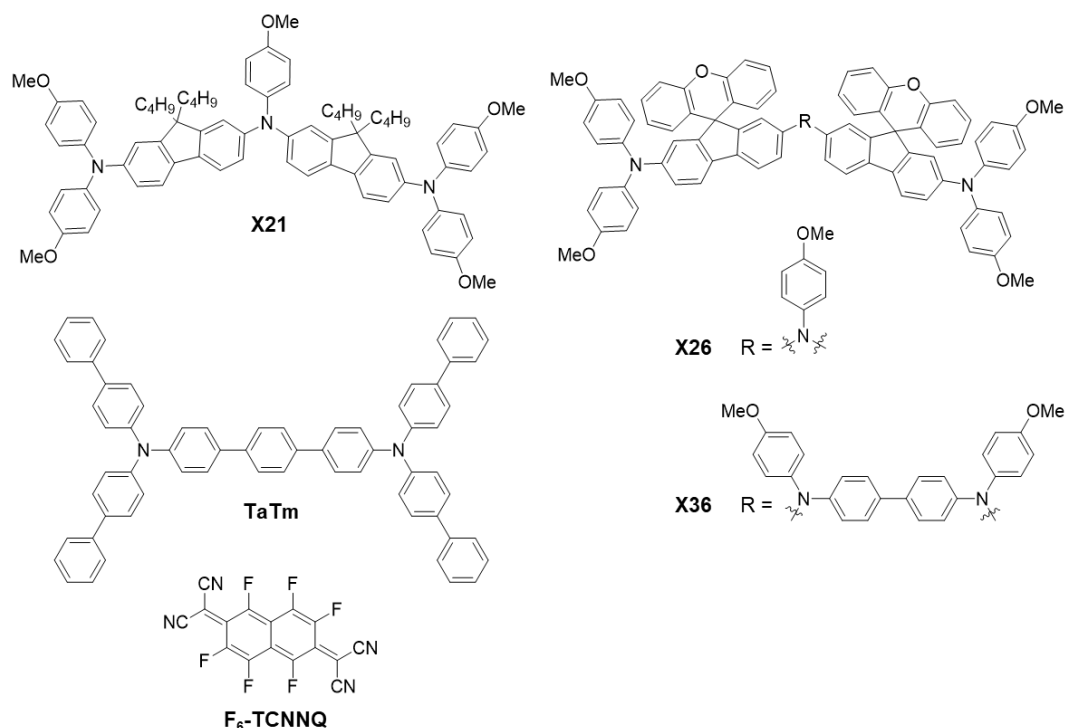


Figure 17. Chemical structures of TPA-based HTMs.

The strategy developed by Bolink *et al.* consisted in successively depositing a thin layer of pristine HTM and another of doped HTM. Similar layer arrangement can be applied for the ETM. In this way, layer thickness was well controlled and full coverage of the substrate was obtained. This method was found to be beneficial for OPVs. In PSCs, it is suggested to limit diffusion of dopants to the perovskite or undesirable reactions at the interface that could alter perovskite stability. Thereby, by combining pristine **TaTm** and **F₆-TCNNQ-doped TaTm** layers, they obtained 16.5 % in p-i-n PSCs and 20.3 % in n-i-p planar configuration (Figure 17).⁹⁵

Recently, Johansson *et al.* reported the influence of pendant groups on fluorene units of TPA-based HTMs (Figure 17). It was suggested that larger size substituents led on one hand to longer conjugation and thus, higher conductivity, and on the other hand to lower solubility of the material. Thereby, best PCEs of 17.3, 19.2 % and 18.2 % were respectively obtained for **X21**, **X26** and **X36**.⁹⁶

4.1.3.4 Aza-based HTMs

Among aza-based HTMs, triazatruxene and azulene-core HTMs demonstrated good PV performances in PSCs. Triazatruxene are made of three indole units linked by a benzene ring and constitute an extended delocalized π -system.

Nazeeruddin *et al.* optimized structure of triazatruxene-based HTMs. Among the reported materials, **KR131** exhibited most promising PV performances (Figure 18). KR131 has a symmetrical planar star-

shape comprising electron-rich methoxy arms. PSCs based on this material achieved up to 18.3 % efficiency.⁹⁷ Through reduction of the length of the alkyl chain and introduction of a poly(9-vinylcarbazole) (PVK) interlayer at the perovskite/HTM interface, Su *et al.* promoted the PCE to 18.8 % employing **SP-12** as HTM (Figure 18). PVK was suggested to improve stability of the device by creating a protective layer for the perovskite preventing degradation from the HTM or the atmosphere. It was also found that PVK reduced charge recombinations at the interface.⁹⁸ Besides, replacing triazatruxene by truxene core, Chen *et al.* reported **Trux-OMeTAD** in inverted PSCs (Figure 18). 2D conjugated structure results in high hole mobility appropriate surface properties for the formation of perovskite layer. Without dopant, remarkable PCE as high as 18.6 % was obtained in PSCs.⁹⁹

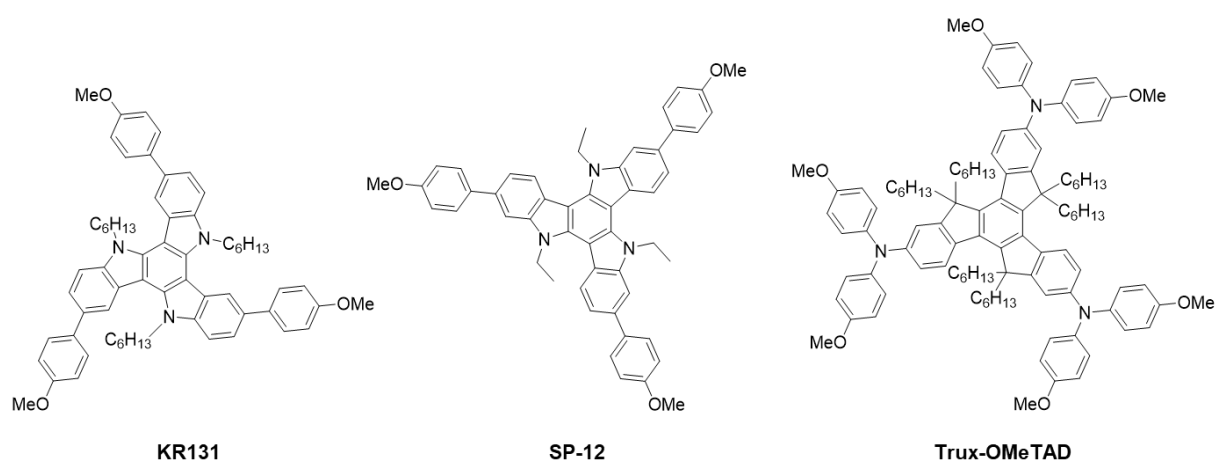


Figure 18. Chemical structure of aza-based HTMs.

4.1.3.5 Carbazole-based HTMs

Carbazole and its derivatives also present great interest for hole transport in PSCs. They have been widely employed in organic electronics owing to their good charge transport properties and excellent thermal and chemical stability.¹⁰⁰ Moreover, opto-electronic properties of carbazole-based materials are easily tuned through functionalization.

To the best of our knowledge, best performance of carbazole-core-based molecule was achieved by with **CZ-TA**, which consists of tetra-dimethoxy-phenyl substituted carbazole (Figure 19). PSCs exhibited similar PCE of 18.3 % as spiro-OMeTAD.¹⁰¹

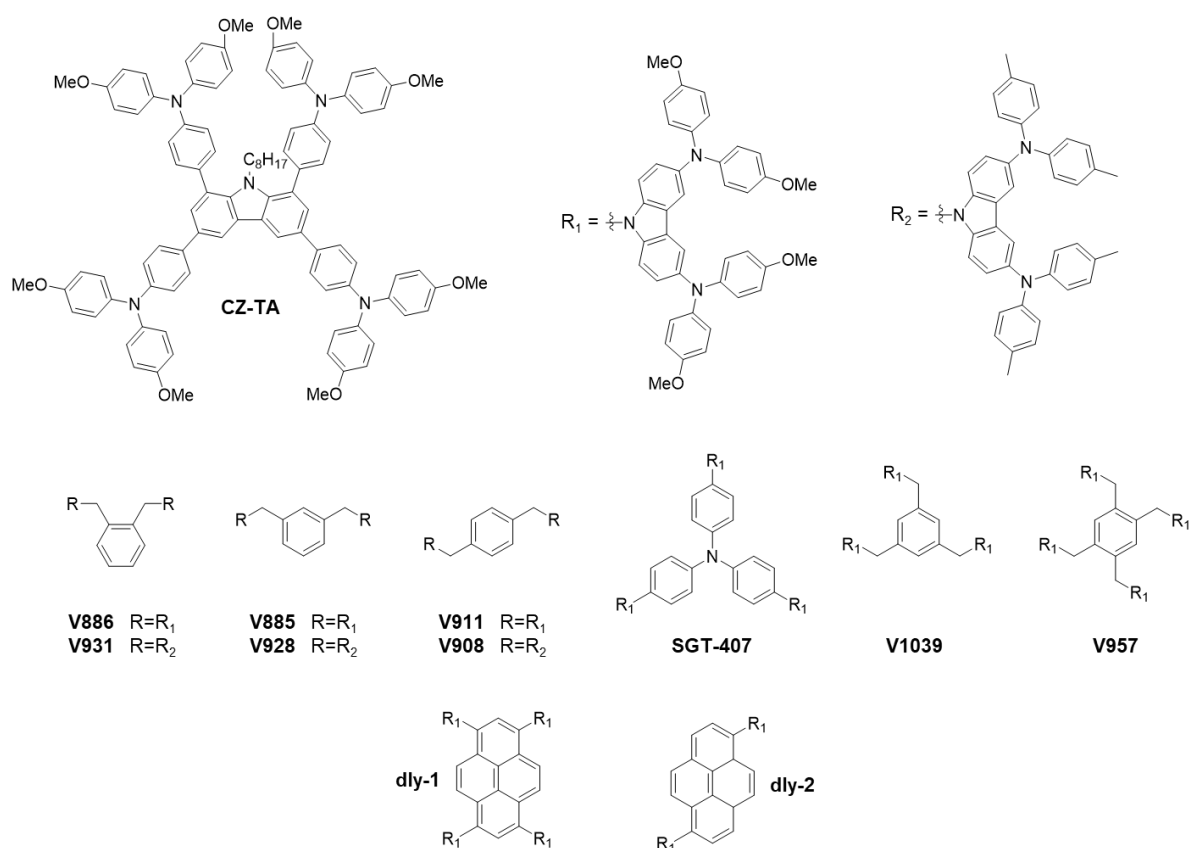


Figure 19. Chemical structure of carbazole-based HTMs.

Recently, Getautis *et al.* studied the effect of different phenyl cores di-substituted with carbazole dimethoxyphenylamine moieties (Figure 19). Few device performance differences were recorded according to the meta, para or ortho substitution position of the moieties around the phenyl. All **V911**, **V885** and **V886** reached PCE as high as 18.5 %. Removing methoxy ending groups (**V908**, **V928**, **V931**), PCE further dropped to 16.5 %.¹⁰² Earlier, Sung *et al.* reported tri-substituted phenyl in **SGT-407**, where 13.9 % were achieved.¹⁰³ Inserting a methyl between the core and the moieties (**V1039**), Getautis *et al.* achieved 17.4 % efficiency. Finally they reported a tetra-substituted HTM, **V957**, which exhibited 17.1 % PCE.¹⁰² Meng *et al.* reported tetra- and di-substituted pyrenes, called **dly-1** and **dly-2**, respectively. Similarly to the phenyl-core molecules, the di-substituted pyrene reached higher PCE, *i.e.* 18.2 % for dly-2 vs. 17.2 % for dly-1.¹⁰⁴

4.1.4 Polymer HTMs

Semiconducting polymers integration to photovoltaic devices is motivated by their lower cost, higher stability and, better film-forming and charge transport properties compared to small molecules. Some polymers such as **PEDOT:PSS**, **PC₆₀BM** or **P3HT**, come from OPVs while novel materials were specifically designed for PSCs.

4.1.4.1 Thiophene-based polymer HTMs

Insertion of thiophene units have been shown to importantly enhance charge transport properties in organic molecules. Thiophene-based polymers have the additional interest of extending conjugation.

PEDOT:PSS is a commercial semiconducting polymer which has been widely employed in organic electronic devices owing to its high conductivity, facile and smooth film-forming, and good transparency (Figure 20). First inverted PSCs were based on this material.³⁶ Although pristine **PEDOT** possesses honourable conductivity $> 10^{-1} \text{ S.cm}^{-1}$, PSS is necessary to reduce recombination rate and so improve PCE.¹⁰⁵ Benefiting from optimizations of the full inverted device, record efficiency overpassing 20.1 % was obtained employing PEDOT:PSS polymer as HTM.⁶³ It is noteworthy to say that PEDOT:PSS is solubilized in water and consequently cannot be employed in n-i-p PSCs. Alternatives to PSS dopant were investigated to extend lifetime of PSCs. Song *et al.* got as far doping PEDOT by graphene oxide (**PEDOT:GO**), and achieved PCE up to 18.1 %.¹⁰⁶

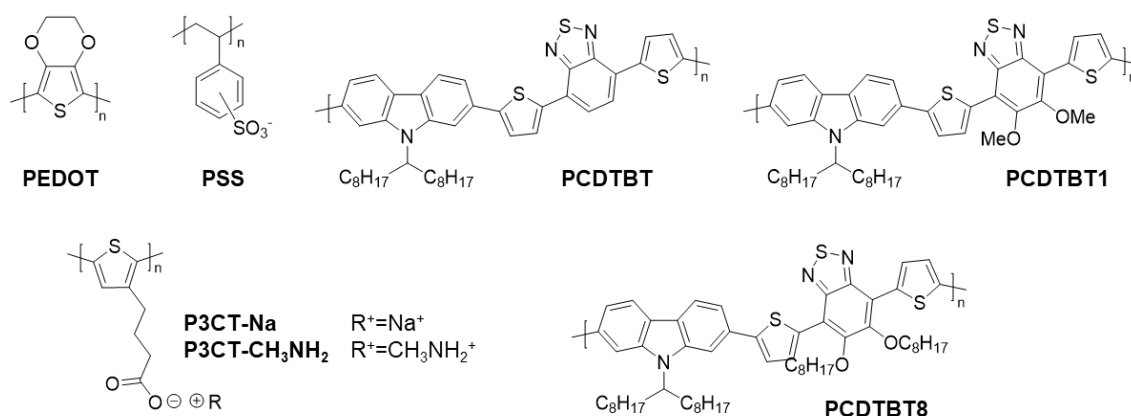


Figure 20. Chemical structures of thiophene-based polymer HTMs.

More original structures were developed by introducing ionic groups. **P3CT-Na** was introduced in inverted PSCs by Fang *et al.* (Figure 20). The impressive PCE of 16.6 % was ascribed to a better energy level alignment as compared to PEDOT:PSS. Furthermore, high PCE were achievable with very thin layers.¹⁰⁷ More recently, same group further enhanced device efficiency by replacing the sodium cation by methyl ammonium to form **P3CT-CH₃NH₂**. Employing this novel polyelectrolyte as HTM, remarkable PCE as high as 19.6 % was recorded.¹⁰⁸

Wang *et al.* studied dopant-free polymers composed of carbazole and thiophene units: **PCDTBT**, **PCDTBT1** and **PCDTBT8** (Figure 20). PCDTBT1 achieved higher efficiency of 19.1 % thanks to its more effective suppression of charge recombinations, vs. 16.4 % with PCDTBT and 14.8 % with PCDTBT8.¹⁰⁹

4.1.4.2 Triphenylamine-based polymer HTMs

TPA-based polymer HTMs have been investigated as for regular structures for the replacement of spiro-OMeTAD as for inverted structures. Such conjugated materials have the advantage to exhibit better film-forming and superior charge transport properties than small molecules.

Seok *et al.* reported **PTAA** as the first polymer introduced in PSCs replacing spiro-OMeTAD.³⁰ At this time, PCE was only 12 % (Figure 21). Through optimization of mesoporous device, Seok *et al.* demonstrated a record PCE of 22.6 % in small cells and 19.7 % in 1 cm² cells, which is the highest efficiency ever reported in PSCs.⁵

A similar **poly-TPD** HTM as PTAA was demonstrated to be a good candidate in inverted PSCs with a maximum PCE of 15.3 % (Figure 21).¹¹⁰ On the other hand, **PTAA** was also found to be an excellent HTM for inverted structures. Huang *et al.* reported a certified PCE of 20.6 % with enhanced stability after defect passivation. This result overpassed performances of PEDOT:PSS-based PSCs.¹¹¹

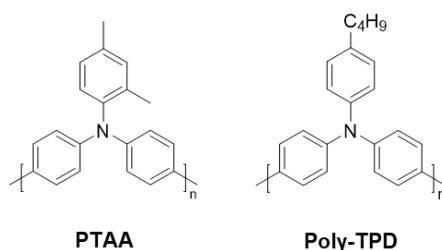


Figure 21. Chemical structures of TPA-based polymer HTMs.

Hole mobility, HOMO level, PV performances, and solar cell details of HTMs reaching PCE higher than 18 % in PSCs are summarized in Table 1.

Table 1. Details of HTMs reaching PCE higher 18 % in PSCs.

HTM ^a	Dopants	μ^b cm ² .V ⁻¹ .s ⁻¹	HOMO eV	V _{oc} V	J _{sc} mA.cm ⁻²	FF	PCE %	Perovskite	Ref
Spiro-OMeTAD	LiTFSI, tBP, FK209	10 ⁻⁴ – 10 ⁻⁵	-5.20	1.16	23.2	0.79	21.3	(FAPbI ₃) _{0.85} (MAPbBr ₃) _{0.15}	72
NiO:N-RGO	none			1.09	22.9	0.76	18.8	MAPbI _{3-x} Cl _x	78
CuSCN:rGO	none	1.20 × 10 ⁻³		1.11	23.2	0.78	20.4	Cs(FAPbI ₃) _{0.85} (MAPbBr ₃) _{0.15}	80
H11	LiTFSI, tBP, FK209	1.58 × 10 ⁻⁴	-5.00	1.12	23.3	0.72	18.9	(FAPbI ₃) _{0.85} (MAPbBr ₃) _{0.15}	85
V859	LiTFSI, tBP, FK209	2.30 × 10 ⁻⁵	-4.98	1.12	23.3	0.75	19.5	(FAPbI ₃) _{0.85} (MAPbBr ₃) _{0.15}	86
V862	LiTFSI, tBP, FK209	8.00 × 10 ⁻⁵	-5.00	1.14	22.5	0.77	20.0	(FAPbI ₃) _{0.85} (MAPbBr ₃) _{0.15}	86
HT2	LiTFSI, tBP, FK209	1.01 × 10 ⁻⁴		1.11	22.3	0.73	18.0	(FAPbI ₃) _{0.85} (MAPbBr ₃) _{0.15}	87
FDT	LiTFSI, tBP, FK209		-5.16	1.15	22.7	0.76	20.2	(FAPbI ₃) _{0.85} (MAPbBr ₃) _{0.15}	88
X59	LiTFSI, tBP, FK209	5.50 × 10 ⁻⁵	-5.15	1.13	23.4	0.73	19.8	(FAPbI ₃) _{0.85} (MAPbBr ₃) _{0.15}	89
X60	LiTFSI, tBP, FK209	1.90 × 10 ⁻⁴	-5.15	1.14	24.4	0.71	19.8	(FAPbI ₃) _{0.85} (MAPbBr ₃) _{0.15}	89
X55	LiTFSI, tBP, FK209	6.81 × 10 ⁻⁴	-5.23	1.15	23.4	0.77	20.8	(FAPbI ₃) _{0.85} (MAPbBr ₃) _{0.15}	90
Z26	LiTFSI, tBP, FK209	1.34 × 10 ⁻⁴	-5.16	1.13	23.6	0.75	20.1	(FAPbI ₃) _{0.85} (MAPbBr ₃) _{0.15}	91
ATT-OMe	LiTFSI, tBP, FK209		-5.32	1.07	21.8	0.78	18.1	(FAPbI ₃) _{0.85} (MAPbBr ₃) _{0.15}	92
BTT-3	LiTFSI, tBP, FK209		-5.40	1.07	21.9	0.77	18.2	MAPbI ₃	93
Z30	LiTFSI, tBP	6.70 × 10 ⁻⁵	-5.27	1.11	23.5	0.73	19.2	(FAPbI ₃) _{0.85} (MAPbBr ₃) _{0.15}	94
TaTm	F ₆ -TCNNQ	4.00 × 10 ⁻³	-5.40	1.14	22.1	0.81	20.3	MAPbI ₃	95
X26	LiTFSI, tBP, FK209	2.79 × 10 ⁻⁴	-5.08	1.11	24.3	0.75	19.2	(FAPbI ₃) _{0.85} (MAPbBr ₃) _{0.15}	96
X36	LiTFSI, tBP, FK209	5.05 × 10 ⁻⁴	-5.12	1.06	23.7	0.76	18.2	(FAPbI ₃) _{0.85} (MAPbBr ₃) _{0.15}	96
KR131	LiTFSI, tBP, FK209	2.80 × 10 ⁻⁵	-5.22	1.15	20.7	0.77	18.3	(FAPbI ₃) _{0.85} (MAPbBr ₃) _{0.15}	97
SP-12	LiTFSI, tBP, FK209	2.41 × 10 ⁻⁴	-5.41	1.08	22.8	0.77	18.8	MAPbI _{3-x} Cl _x	98
Trux-OMeTAD	none	2.30 × 10 ⁻³	-5.28	1.02	23.2	0.79	18.6	MAPbI ₃	99
CZ-TA	LiTFSI, tBP	1.65 × 10 ⁻⁴	-5.11	1.04	21.7	0.81	18.3	MA _{0.7} FA _{0.3} PbI ₃	101
V911	LiTFSI, tBP, FK209	4.00 × 10 ⁻⁴	-5.07	1.10	22.4	0.76	18.9	(FAPbI ₃) _{0.85} (MAPbBr ₃) _{0.15}	102
V885	LiTFSI, tBP, FK209	1.00 × 10 ⁻⁴	-5.06	1.10	22.4	0.76	18.9	(FAPbI ₃) _{0.85} (MAPbBr ₃) _{0.15}	102
V886	LiTFSI, tBP, FK209	2.00 × 10 ⁻⁵	-5.04	1.11	22.3	0.76	18.5	(FAPbI ₃) _{0.85} (MAPbBr ₃) _{0.15}	102
dly-2	LiTFSI, tBP	1.42 × 10 ⁻³	-4.88	1.04	23.2	0.76	18.2	(FAPbI ₃) _{0.85} (MAPbBr ₃) _{0.15}	104
PEDOT:PSS	PSS	≈ 10 ⁻²	-5.20	1.03	23.5	0.83	20.1	MAPbI ₃	63
PEDOT:GO	GO		-5.42	1.02	21.6	0.82	18.1	MA _{0.7} FA _{0.3} PbI ₃	106
P3CT-CH₃NH₂	none	1.08 × 10 ⁻⁵	-5.25	1.09	22.2	0.81	19.6	MAPbI ₃	108
PCDTBT1	none		-5.38	1.10	22.2	0.78	19.1	(FAPbI ₃) _{0.85} (MAPbBr ₃) _{0.15}	109
PTAA	LiTFSI, tBP	10 ⁻² – 10 ⁻³	-5.25	1.11	25.0	0.82	22.6	(FAPbI ₃) _{0.85} (MAPbBr ₃) _{0.15}	5
PTAA	none	10 ⁻² – 10 ⁻³	-5.25	1.14	23.7	0.78	21.0	(FAPbI ₃) _{0.85} (MAPbBr ₃) _{0.15}	111

^a HTM employed in mesoscopic structure (dark blue), n-i-p planar structure (light blue) or p-i-n inverted structure (green). ^b Hole mobility.

4.2 Dopant-free HTMs

The route towards low-cost and sustainable PSCs went through the design of dopant-free HTMs. Among the materials previously reported, NiO, CuSCN, Trux-OMeTAD and PTAA showed that additive-free HTM could go with high efficiency. In the following examples, it is shown that high PCE

can also be achieved with dopant-free HTMs through structural modifications, extension of conjugation in the material or addition of interfacial layers in the device.

Among metallo-organic compounds, pristine **CuPc** exhibits high hole mobility, low price and is compatible with flexible devices. In n-i-p structures combined with a cheap carbon electrode, PCE reached up to 16.1 %, while comparable PCE of 15.4 % was obtained in inverted PSCs.¹¹² In both cases, stability of the devices was reported to be improved.

For organic compounds, incorporation of thiophene groups has been shown to increase intramolecular force through CH/ π bonds and π - π interactions and thus, is an interesting strategy to improve conductivity of materials.¹¹³ Two dopant-free benzo[1,2b:4,5b']-dithiophene- (BDT-) based HTMs introduced by Yang *et al.* are presented. By extending the conjugation of BDT by inserting thiophene units, **DOR3T-TBDT** achieved promising PCE of 14.9 % with improved stability without any additive.¹¹⁴ In **DERDTS-TBDT**, thiophene units were replaced by electron-donating dithienosilole units resulting in a deeper HOMO level and an increased PCE of 16.2 % without any dopant.¹¹⁵ **P3HT** is a common thiophene-based polymer which has been first studied for OPVs. Snaith et al. developed a composite HTL made of P3HT-functionalized single-walled carbon nanotubes (**P3HT-SWNTs**) embedded in a PMMA matrix, which enhanced PCE of regular PSCs to 15.3 %.¹¹⁶ P3HT has also the advantage to have good stability and to be compatible with flexible devices. Besides, inserted in mesoscopic devices as an interlayer between the perovskite and spiro-OMeTAD, PCE was promoted to 19 %. P3HT was found to reduce charge recombination at the perovskite/HTM interface and to greatly enhance device stability.¹¹⁷ Other polymers based on thiophene derivatives, **pBBTa-BDT1** and **pBBTa-BDT2**, were synthesized by Marks *et al.* The additional phenyl on the dipthiophene unit of pBBTa-BDT1 resulted in lower hole mobility, and thus, lower PCE than pBBTa-BDT2. Owing to the highly ordering π -face-down on perovskite surface of pBBTa-BDT2, chemical dopants were unnecessary, and maximum PCE of 14.4 % was reached. Moreover, thermal stability and resistivity to moisture of devices was enhanced. At this time, it was the highest PV performance reported in PSCs based on an undoped HTM.¹¹⁸

Multiple TPA structures have been successfully synthesized to perform efficiently without the need of chemical dopants. **ST1**, containing 3 phenylamine ending groups achieved PCE up to 15.4 %.¹¹⁹ Zhang *et al.* fabricated a (D)- π -D- π -D conjugated molecule. **Z33** exhibited similar PCE of 15.4 %. Replacing methyl by methoxy ending groups, FF was improved resulting in 16.1 % PCE.¹²⁰ They further developed “butterfly-shaped” **Z1011**.¹²¹ Similar PV performance as doped spiro-OMeTAD (16.3 % for pristine Z1011 vs. 16.5 %) were achieved owing to the higher thermal stability and higher hole mobility of Z1011. However, synthetic route towards this material is complicated. Guo *et al.*

introduced a TPA derivative molecule as dopant-free HTM for inverted p-i-n PSCs. PCE was promoted from 13.8 % to 17.7 % replacing PEDOT:PSS by **m-MTDATA**, and modifying the PbI_2 ratio of the perovskite precursor solution.¹²²

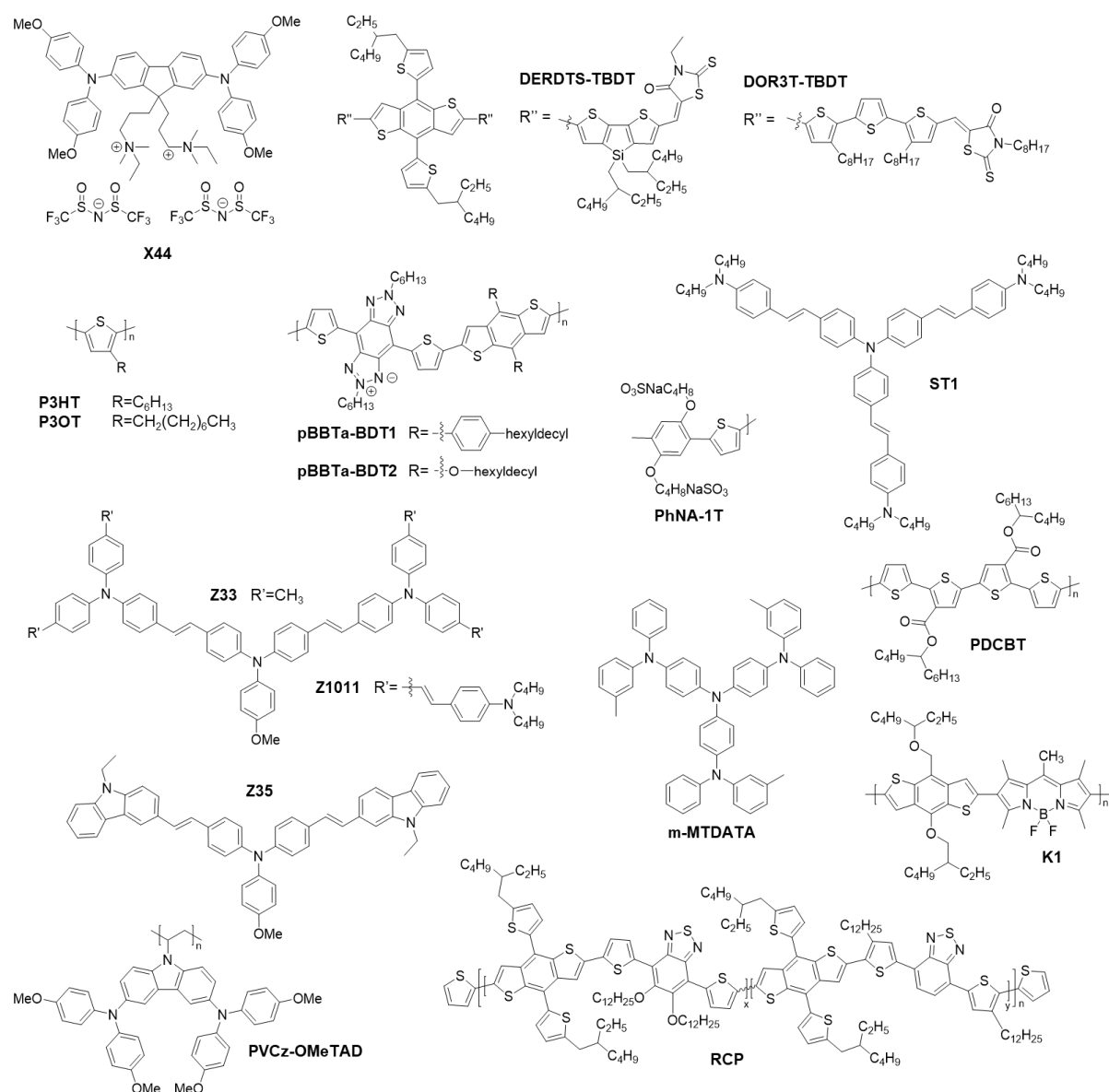


Figure 22. Efficient dopant-free HTMs.

Zhang *et al.* developed cost-effective dopant-free conjugated molecules. Carbazole moieties made **Z35** the most performing exhibiting PCE up to 16.1 %. Insertion of double bonds between TPA units increased conjugation effect and conductivity of the material.¹²⁰ Besides, PVK was suggested to improve stability of the device by creating a protective layer for the perovskite preventing degradation from the HTM or the atmosphere.¹⁰⁹ **PVCz-OMeTAD** was introduced as effective dopant-free HTM exhibiting up to 16.1 % PCE.¹²³

Combining chemical groups with different properties was another strategy to improve properties of HTMs. Hong *et al.* introduced **K1** as HTM in inverted PSCs. Combination of BDT and 4,4-difluoro-4-bora-3a,4a-diaza-s-indacene (BODIPY) units afforded well aligned HOMO level to the perovskite VB and high LUMO level, leading to 16.0 % PCE.¹²⁴ Besides, Park *et al.* synthesized a block copolymer **RCP** which is the combination of P-OR (x block) and P-R (y block). The high mobility of P-OR and the low HOMO level of P-R resulted in efficient RCP HTM, exhibiting up to 17.3 % without additives.¹²⁵

Incorporation of ionic groups also demonstrated to enhance charge transport properties of P3CT. Sun *et al.* inserted positively charge **X44** with TFSI⁻ as counter ion. In this way, conductivity of the material was increased. Without any dopant, PCE of 16.2 % was reached.¹²⁶ Besides, Son *et al.* proposed **PhNa-1T** HTM which achieved maximum PCE of 14.7 % with improved stability. At this time, it was the highest efficiency reported for flexible inverted PSCs.¹²⁷

Finally, performances of dopant-free HTMs were boosted by device engineering. Hydrophobic conjugated polymers are desirable HTMs to protect the perovskite layer from moisture. However, perovskite can be difficult to process on top of them in inverted devices. To improve perovskite formation, oxygen plasma was applied on the polymer layer to make the surface more hydrophilic and enhance contact between the polymer and the perovskite. Thereby, Neher *et al.* fabricated inverted PSCs using undoped polymers as HTMs treated with oxygen plasma. PCE as high as 16.1, 16.5, 17.4 % were obtained employing **P3HT**, **poly-TPD** and **P3OT**, respectively. The formation of an oxygen rich surface, is suggested to increase conductivity of polymers and improve charge extraction.¹²⁸ Through introduction of a thin interlayer of cost-effective tantalum-doped tungsten oxide (Ta-WOx), Snaith *et al.* achieved remarkable PCE of 21.2 % employing undoped polymer **PDCBT** as HTM in n-i-p planar PSCs.¹²⁹

Hole mobility, HOMO level, PV performances and solar cell details of HTMs cited above are summarized in Table 2.

Table 2. Details of dopant-free HTMs reaching PCE higher 14.5 % in PSCs.

HTM ^a	μ^b cm ² .V ⁻¹ .s ⁻¹	HOMO eV	V _{oc} V	J _{sc} mA.cm ⁻²	FF	PCE %	Perovskite	Ref
CuPc	10 ⁻² – 10 ⁻³	-5.20	1.05	20.8	0.74	16.1	MAPbI ₃	112
DOR3T-TBDT	2.60 x 10 ⁻¹	-5.50	1.04	20.7	0.74	14.9	MAPbI _{3-x} Cl _x	114
DERDTS-TBDT	1.00 x 10 ⁻⁴	-5.20	1.05	21.2	0.72	16.2	MAPbI _{3-x} Cl _x	115
P3HT-SWNTs			1.02	22.7	0.66	15.3	MAPbI _{3-x} Cl _x	116
pBBTa-BDT2	1.2 x 10 ⁻³	-5.21	0.95	20.3	0.75	14.5	MAPbI _{3-x} Cl _x	118
ST1	4.57 x 10 ⁻⁴	-5.24	1.06	21.1	0.66	15.4	MAPbI ₃	119
Z33		-5.34	1.09	20.4	0.66	15.4	MAPbI ₃	120
Z1011	8.49 x 10 ⁻⁴	-5.21	1.10	20.5	0.70	16.3	MAPbI ₃	121
m-MTDATA		-5.10	1.03	21.6	0.80	17.7	MAPbI ₃	122
Z35	6.15 x 10 ⁻⁴	-5.42	1.06	21.2	0.70	16.1	MAPbI ₃	120
PVCz-OMeDAD	3.44 x 10 ⁻⁴	-5.24	1.09	22.0	0.68	16.1	(FAPbI ₃) _{0.85} (MAPbBr ₃) _{0.15}	123
K1	2.96 x 10 ⁻⁵	-5.29	1.06	19.2	0.78	16.0	MAPbI ₃	124
RCP	3.90 x 10 ⁻³	-5.41	1.08	21.9	0.75	17.3	MAPbI ₃	125
X44	9.03 x 10 ⁻⁴	-5.06	1.09	21.7	0.69	16.2	(FAPbI ₃) _{0.85} (MAPbBr ₃) _{0.15}	126
PhNa-1T		-5.20	1.03	18.4	0.77	14.7	MAPbI ₃	127
P3HT		-5.20	1.00	20.1	0.80	16.1	MAPbI ₃	128
P3OT		-5.00	1.06	21.7	0.75	17.4	MAPbI ₃	128
Poly-TPD		-5.40	1.03	21.4	0.75	16.5	MAPbI ₃	128
PDCBT		-5.30	1.17	22.7	0.80	21.2	(FAPbI ₃) _{0.83} (MAPbBr ₃) _{0.17}	129

^a HTM employed in mesoscopic structure (dark blue), n-i-p planar structure (light blue) or p-i-n inverted structure (green). ^b Hole mobility.

Conclusion

Emergence of PSCs has renewed the success of the PV field. The efforts for understanding properties of perovskite material has been beneficial to rapidly enhance device efficiency and furthermore, has opened new applications for this material such as hybrid light emitting diodes, photodetectors, x-ray imaging... The race towards high efficiency was also accompanied by the development of semiconducting materials specifically designed for this application.

On the HTM side, small molecules boosted by dopants demonstrated high PV performances particularly for mesoscopic devices. In the panel of the novel synthesized molecules, the compromise between high efficiency, long lifetime and cost-effective fabrication is not easy to find.

On the other hand, polymers could present enhanced conjugation, increased π - π interactions, and easy film-forming through solution process, and thus, rely less on doping. Additional to high PV performances reported as doped as well as undoped HTMs, they have been shown to improve the PSC stability, in particular in n-i-p devices by forming a barrier layer against oxygen and moisture. They have also been applied at the interface of the perovskite and the HTM to avoid the diffusion of the HTM dopants into the perovskite. Several strategies are still under investigations, like the combinations of specific properties through block-copolymers, or the insertion of ionic species to form polyelectrolytes that could improve charge transport properties of the materials.

References

1. NREL Best Research-Cell Efficiencies. <https://www.nrel.gov/pv/assets/pdfs/pv-efficiencies-07-17-2018.pdf> (accessed September 2018).
2. Green, M. A.; Hishikawa, Y.; Dunlop, E. D.; Levi, D. H.; Hohl-Ebinger, J.; Ho-Baillie, A. W. Y., Solar cell efficiency tables (version 52). *Progress in Photovoltaics: Research and Applications* **2018**, 26 (7), 427-436.
3. Enerdata Global Energy Statistical Yearbook 2018. <https://yearbook.enerdata.net/total-energy/world-consumption-statistics.html> (accessed September 2018).
4. Lee, T. D.; Ebong, A. U., A review of thin film solar cell technologies and challenges. *Renewable and Sustainable Energy Reviews* **2017**, 70, 1286-1297.
5. Yang, W. S.; Park, B.-W.; Jung, E. H.; Jeon, N. J.; Kim, Y. C.; Lee, D. U.; Shin, S. S.; Seo, J.; Kim, E. K.; Noh, J. H.; Seok, S. I., Iodide management in formamidinium-lead-halide-based perovskite layers for efficient solar cells. *Science* **2017**, 356 (6345), 1376.
6. Zhou, X.; Jankowska, J.; Dong, H.; Prezhdov, O. V., Recent theoretical progress in the development of perovskite photovoltaic materials. *Journal of Energy Chemistry* **2018**, 27 (3), 637-649.
7. Zhang, Q.; Ting, H.; Wei, S.; Huang, D.; Wu, C.; Sun, W.; Qu, B.; Wang, S.; Chen, Z.; Xiao, L., Recent progress in lead-free perovskite (-like) solar cells. *Materials Today Energy* **2018**, 8, 157-165.
8. Eames, C.; Frost, J. M.; Barnes, P. R. F.; O'Regan, B. C.; Walsh, A.; Islam, M. S., Ionic transport in hybrid lead iodide perovskite solar cells. *Nature Communications* **2015**, 6, 7497.
9. Chen, Q.; De Marco, N.; Yang, Y.; Song, T.-B.; Chen, C.-C.; Zhao, H.; Hong, Z.; Zhou, H.; Yang, Y., Under the spotlight: The organic-inorganic hybrid halide perovskite for optoelectronic applications. *Nano Today* **2015**, 10 (3), 355-396.
10. Chao, L.; Wang, Z.; Xia, Y.; Chen, Y.; Huang, W., Recent progress on low dimensional perovskite solar cells. *Journal of Energy Chemistry* **2018**, 27 (4), 1091-1100.
11. Miyata, A.; Mitoglu, A.; Plochocka, P.; Portugall, O.; Wang, J. T.-W.; Stranks, S. D.; Snaith, H. J.; Nicholas, R. J., Direct measurement of the exciton binding energy and effective masses for charge carriers in organic-inorganic tri-halide perovskites. *Nature Physics* **2015**, 11, 582.
12. Herz, L. M., Charge-Carrier Mobilities in Metal Halide Perovskites: Fundamental Mechanisms and Limits. *ACS Energy Letters* **2017**, 2 (7), 1539-1548.
13. Stoumpos, C. C.; Malliakas, C. D.; Kanatzidis, M. G., Semiconducting Tin and Lead Iodide Perovskites with Organic Cations: Phase Transitions, High Mobilities, and Near-Infrared Photoluminescent Properties. *Inorganic Chemistry* **2013**, 52 (15), 9019-9038.
14. Hao, F.; Stoumpos, C. C.; Chang, R. P. H.; Kanatzidis, M. G., Anomalous Band Gap Behavior in Mixed Sn and Pb Perovskites Enables Broadening of Absorption Spectrum in Solar Cells. *Journal of the American Chemical Society* **2014**, 136 (22), 8094-8099.
15. Noh, J. H.; Im, S. H.; Heo, J. H.; Mandal, T. N.; Seok, S. I., Chemical Management for Colorful, Efficient, and Stable Inorganic-Organic Hybrid Nanostructured Solar Cells. *Nano Letters* **2013**, 13 (4), 1764-1769.
16. Unger, E. L.; Bowring, A. R.; Tassone, C. J.; Pool, V. L.; Gold-Parker, A.; Cheacharoen, R.; Stone, K. H.; Hoke, E. T.; Toney, M. F.; McGehee, M. D., Chloride in Lead Chloride-Derived Organo-Metal Halides for Perovskite-Absorber Solar Cells. *Chemistry of Materials* **2014**, 26 (24), 7158-7165.

17. Dar, M. I.; Arora, N.; Gao, P.; Ahmad, S.; Grätzel, M.; Nazeeruddin, M. K., Investigation Regarding the Role of Chloride in Organic–Inorganic Halide Perovskites Obtained from Chloride Containing Precursors. *Nano Letters* **2014**, *14* (12), 6991-6996.
18. Tang, Z.; Uchida, S.; Bessho, T.; Kinoshita, T.; Wang, H.; Awai, F.; Jono, R.; Maitani, M. M.; Nakazaki, J.; Kubo, T.; Segawa, H., Modulations of various alkali metal cations on organometal halide perovskites and their influence on photovoltaic performance. *Nano Energy* **2018**, *45*, 184-192.
19. Jeon, N. J.; Noh, J. H.; Kim, Y. C.; Yang, W. S.; Ryu, S.; Seok, S. I., Solvent engineering for high-performance inorganic–organic hybrid perovskite solar cells. *Nature Materials* **2014**, *13*, 897.
20. Liu, M.; Johnston, M. B.; Snaith, H. J., Efficient planar heterojunction perovskite solar cells by vapour deposition. *Nature* **2013**, *501*, 395.
21. Xiao, M.; Huang, F.; Huang, W.; Dkhissi, Y.; Zhu, Y.; Etheridge, J.; Gray-Weale, A.; Bach, U.; Cheng, Y.-B.; Spiccia, L., A Fast Deposition-Crystallization Procedure for Highly Efficient Lead Iodide Perovskite Thin-Film Solar Cells. *Angewandte Chemie International Edition* **2014**, *53* (37), 9898-9903.
22. Yoon, W.; Boercker, J. E.; Lumb, M. P.; Tischler, J. G.; Jenkins, P. P.; Walters, R. J. In *Vapor deposition of organic-inorganic hybrid perovskite thin-films for photovoltaic applications*, 2014 IEEE 40th Photovoltaic Specialist Conference (PVSC), 8-13 June 2014; 2014; pp 1577-1580.
23. Tong, G.; Li, H.; Li, G.; Zhang, T.; Li, C.; Yu, L.; Xu, J.; Jiang, Y.; Shi, Y.; Chen, K., Mixed cation perovskite solar cells by stack-sequence chemical vapor deposition with self-passivation and gradient absorption layer. *Nano Energy* **2018**, *48*, 536-542.
24. Kojima, A.; Teshima, K.; Shirai, Y.; Miyasaka, T., Organometal Halide Perovskites as Visible-Light Sensitizers for Photovoltaic Cells. *Journal of the American Chemical Society* **2009**, *131* (17), 6050-6051.
25. Kim, H.-S.; Lee, C.-R.; Im, J.-H.; Lee, K.-B.; Moehl, T.; Marchioro, A.; Moon, S.-J.; Humphry-Baker, R.; Yum, J.-H.; Moser, J. E.; Grätzel, M.; Park, N.-G., Lead Iodide Perovskite Sensitized All-Solid-State Submicron Thin Film Mesoscopic Solar Cell with Efficiency Exceeding 9%. *Scientific Reports* **2012**, *2*, 591.
26. Etgar, L.; Gao, P.; Xue, Z.; Peng, Q.; Chandiran, A. K.; Liu, B.; Nazeeruddin, M. K.; Grätzel, M., Mesoscopic CH₃NH₃PbI₃/TiO₂ Heterojunction Solar Cells. *Journal of the American Chemical Society* **2012**, *134* (42), 17396-17399.
27. Lee, M. M.; Teuscher, J.; Miyasaka, T.; Murakami, T. N.; Snaith, H. J., Efficient Hybrid Solar Cells Based on Meso-Superstructured Organometal Halide Perovskites. *Science* **2012**, *338* (6107), 643.
28. Ball, J. M.; Lee, M. M.; Hey, A.; Snaith, H. J., Low-temperature processed meso-superstructured to thin-film perovskite solar cells. *Energy & Environmental Science* **2013**, *6* (6), 1739-1743.
29. Leijtens, T.; Eperon, G. E.; Pathak, S.; Abate, A.; Lee, M. M.; Snaith, H. J., Overcoming ultraviolet light instability of sensitized TiO₂ with meso-superstructured organometal tri-halide perovskite solar cells. *Nature Communications* **2013**, *4*, 2885.
30. Heo, J. H.; Im, S. H.; Noh, J. H.; Mandal, T. N.; Lim, C.-S.; Chang, J. A.; Lee, Y. H.; Kim, H.-j.; Sarkar, A.; Nazeeruddin, M. K.; Grätzel, M.; Seok, S. I., Efficient inorganic–organic hybrid heterojunction solar cells containing perovskite compound and polymeric hole conductors. *Nature Photonics* **2013**, *7*, 486.

31. Yella, A.; Lee, H.-W.; Tsao, H. N.; Yi, C.; Chandiran, A. K.; Nazeeruddin, M. K.; Diau, E. W.-G.; Yeh, C.-Y.; Zakeeruddin, S. M.; Grätzel, M., Porphyrin-Sensitized Solar Cells with Cobalt (II/III)–Based Redox Electrolyte Exceed 12 Percent Efficiency. *Science* **2011**, *334* (6056), 629.
32. Abrusci, A.; Stranks, S. D.; Docampo, P.; Yip, H.-L.; Jen, A. K. Y.; Snaith, H. J., High-Performance Perovskite-Polymer Hybrid Solar Cells via Electronic Coupling with Fullerene Monolayers. *Nano Letters* **2013**, *13* (7), 3124-3128.
33. Burschka, J.; Pellet, N.; Moon, S.-J.; Humphry-Baker, R.; Gao, P.; Nazeeruddin, M. K.; Grätzel, M., Sequential deposition as a route to high-performance perovskite-sensitized solar cells. *Nature* **2013**, *499*, 316.
34. Liang, K.; Mitzi, D. B.; Prikas, M. T., Synthesis and Characterization of Organic–Inorganic Perovskite Thin Films Prepared Using a Versatile Two-Step Dipping Technique. *Chemistry of Materials* **1998**, *10* (1), 403-411.
35. Shi, Y.; Xing, Y.; Li, Y.; Dong, Q.; Wang, K.; Du, Y.; Bai, X.; Wang, S.; Chen, Z.; Ma, T., CH₃NH₃PbI₃ and CH₃NH₃PbI₃–xCl_x in Planar or Mesoporous Perovskite Solar Cells: Comprehensive Insight into the Dependence of Performance on Architecture. *The Journal of Physical Chemistry C* **2015**, *119* (28), 15868-15873.
36. Jeng, J.-Y.; Chiang, Y.-F.; Lee, M.-H.; Peng, S.-R.; Guo, T.-F.; Chen, P.; Wen, T.-C., CH₃NH₃PbI₃ Perovskite/Fullerene Planar-Heterojunction Hybrid Solar Cells. *Advanced Materials* **2013**, *25* (27), 3727-3732.
37. Malinkiewicz, O.; Yella, A.; Lee, Y. H.; Espallargas, G. M.; Graetzel, M.; Nazeeruddin, M. K.; Bolink, H. J., Perovskite solar cells employing organic charge-transport layers. *Nature Photonics* **2013**, *8*, 128.
38. Kumar, M. H.; Yantara, N.; Dharani, S.; Graetzel, M.; Mhaisalkar, S.; Boix, P. P.; Mathews, N., Flexible, low-temperature, solution processed ZnO-based perovskite solid state solar cells. *Chemical Communications* **2013**, *49* (94), 11089-11091.
39. Matteocci, F.; Razza, S.; Di Giacomo, F.; Casaluci, S.; Mincuzzi, G.; Brown, T. M.; D'Epifanio, A.; Licoccia, S.; Di Carlo, A., Solid-state solar modules based on mesoscopic organometal halide perovskite: a route towards the up-scaling process. *Physical Chemistry Chemical Physics* **2014**, *16* (9), 3918-3923.
40. Koh, T. M.; Fu, K.; Fang, Y.; Chen, S.; Sum, T. C.; Mathews, N.; Mhaisalkar, S. G.; Boix, P. P.; Baikie, T., Formamidinium-Containing Metal-Halide: An Alternative Material for Near-IR Absorption Perovskite Solar Cells. *The Journal of Physical Chemistry C* **2014**, *118* (30), 16458-16462.
41. Pellet, N.; Gao, P.; Gregori, G.; Yang, T.-Y.; Nazeeruddin, M. K.; Maier, J.; Grätzel, M., Mixed-Organic-Cation Perovskite Photovoltaics for Enhanced Solar-Light Harvesting. *Angewandte Chemie International Edition* **2014**, *53* (12), 3151-3157.
42. Jeon, N. J.; Noh, J. H.; Yang, W. S.; Kim, Y. C.; Ryu, S.; Seo, J.; Seok, S. I., Compositional engineering of perovskite materials for high-performance solar cells. *Nature* **2015**, *517*, 476.
43. Liu, C.; Wang, K.; Du, P.; Yi, C.; Meng, T.; Gong, X., Efficient Solution-Processed Bulk Heterojunction Perovskite Hybrid Solar Cells. *Advanced Energy Materials* **2015**, *5* (12), 1402024.
44. Yang, W. S.; Noh, J. H.; Jeon, N. J.; Kim, Y. C.; Ryu, S.; Seo, J.; Seok, S. I., High-performance photovoltaic perovskite layers fabricated through intramolecular exchange. *Science* **2015**, *348* (6240), 1234.

45. Roldán-Carmona, C.; Gratiá, P.; Zimmermann, I.; Grancini, G.; Gao, P.; Graetzel, M.; Nazeeruddin, M. K., High efficiency methylammonium lead triiodide perovskite solar cells: the relevance of non-stoichiometric precursors. *Energy & Environmental Science* **2015**, *8* (12), 3550-3556.
46. Son, D.-Y.; Lee, J.-W.; Choi, Y. J.; Jang, I.-H.; Lee, S.; Yoo, P. J.; Shin, H.; Ahn, N.; Choi, M.; Kim, D.; Park, N.-G., Self-formed grain boundary healing layer for highly efficient CH₃NH₃PbI₃ perovskite solar cells. *Nature Energy* **2016**, *1*, 16081.
47. (a) Kim, Y. C.; Jeon, N. J.; Noh, J. H.; Yang, W. S.; Seo, J.; Yun, J. S.; Ho-Baillie, A.; Huang, S.; Green, M. A.; Seidel, J.; Ahn, T. K.; Seok, S. I., Beneficial Effects of PbI₂ Incorporated in Organo-Lead Halide Perovskite Solar Cells. *Advanced Energy Materials* **2015**, *6* (4), 1502104; (b) Bi, D.; Tress, W.; Dar, M. I.; Gao, P.; Luo, J.; Renevier, C.; Schenk, K.; Abate, A.; Giordano, F.; Correa Baena, J.-P.; Decoppet, J.-D.; Zakeeruddin, S. M.; Nazeeruddin, M. K.; Grätzel, M.; Hagfeldt, A., Efficient luminescent solar cells based on tailored mixed-cation perovskites. *Science Advances* **2016**, *2* (1).
48. Saliba, M.; Matsui, T.; Seo, J.-Y.; Domanski, K.; Correa-Baena, J.-P.; Nazeeruddin, M. K.; Zakeeruddin, S. M.; Tress, W.; Abate, A.; Hagfeldt, A.; Grätzel, M., Cesium-containing triple cation perovskite solar cells: improved stability, reproducibility and high efficiency. *Energy & Environmental Science* **2016**, *9* (6), 1989-1997.
49. Saliba, M.; Matsui, T.; Domanski, K.; Seo, J.-Y.; Ummadisingu, A.; Zakeeruddin, S. M.; Correa-Baena, J.-P.; Tress, W. R.; Abate, A.; Hagfeldt, A.; Grätzel, M., Incorporation of rubidium cations into perovskite solar cells improves photovoltaic performance. *Science* **2016**, *354* (6309), 206.
50. Tang, Z.; Bessho, T.; Awai, F.; Kinoshita, T.; Maitani, M. M.; Jono, R.; Murakami, T. N.; Wang, H.; Kubo, T.; Uchida, S.; Segawa, H., Hysteresis-free perovskite solar cells made of potassium-doped organometal halide perovskite. *Scientific Reports* **2017**, *7* (1), 12183.
51. Bi, D.; Yi, C.; Luo, J.; Decoppet, J.-D.; Zhang, F.; Zakeeruddin, Shaik M.; Li, X.; Hagfeldt, A.; Grätzel, M., Polymer-templated nucleation and crystal growth of perovskite films for solar cells with efficiency greater than 21%. *Nature Energy* **2016**, *1*, 16142.
52. (a) Yi, C.; Li, X.; Luo, J.; Zakeeruddin, S. M.; Grätzel, M., Perovskite Photovoltaics with Outstanding Performance Produced by Chemical Conversion of Bilayer Mesostructured Lead Halide/TiO₂ Films. *Advanced Materials* **2016**, *28* (15), 2964-2970; (b) Li, X.; Bi, D.; Yi, C.; Decoppet, J.-D.; Luo, J.; Zakeeruddin, S. M.; Hagfeldt, A.; Grätzel, M., A vacuum flash-assisted solution process for high-efficiency large-area perovskite solar cells. *Science* **2016**, *353* (6294), 58.
53. Berhe, T. A.; Su, W.-N.; Chen, C.-H.; Pan, C.-J.; Cheng, J.-H.; Chen, H.-M.; Tsai, M.-C.; Chen, L.-Y.; Dubale, A. A.; Hwang, B.-J., Organometal halide perovskite solar cells: degradation and stability. *Energy & Environmental Science* **2016**, *9* (2), 323-356.
54. (a) Zhao, X.; Wang, M., Organic hole-transporting materials for efficient perovskite solar cells. *Materials Today Energy* **2018**, *7*, 208-220; (b) Yang, X.; Wang, H.; Cai, B.; Yu, Z.; Sun, L., Progress in hole-transporting materials for perovskite solar cells. *Journal of Energy Chemistry* **2018**, *27* (3), 650-672.
55. Heo, J. H.; Im, S. H., Highly reproducible, efficient hysteresis-less CH₃NH₃PbI₃-xCl_x planar hybrid solar cells without requiring heat-treatment. *Nanoscale* **2016**, *8* (5), 2554-2560.
56. Ke, W.; Xiao, C.; Wang, C.; Saparov, B.; Duan, H.-S.; Zhao, D.; Xiao, Z.; Schulz, P.; Harvey, S. P.; Liao, W.; Meng, W.; Yu, Y.; Cimaroli, A. J.; Jiang, C.-S.; Zhu, K.; Al-Jassim, M.; Fang, G.; Mitzi, D. B.; Yan, Y., Employing Lead Thiocyanate Additive to Reduce the Hysteresis and Boost the Fill Factor of Planar Perovskite Solar Cells. *Advanced Materials* **2016**, *28* (26), 5214-5221.

57. Jeong, I.; Jung, H.; Park, M.; Park, J. S.; Son, H. J.; Joo, J.; Lee, J.; Ko, M. J., A tailored TiO₂ electron selective layer for high-performance flexible perovskite solar cells via low temperature UV process. *Nano Energy* **2016**, *28*, 380-389.
58. Anaraki, E. H.; Kermanpur, A.; Steier, L.; Domanski, K.; Matsui, T.; Tress, W.; Saliba, M.; Abate, A.; Grätzel, M.; Hagfeldt, A.; Correa-Baena, J.-P., Highly efficient and stable planar perovskite solar cells by solution-processed tin oxide. *Energy & Environmental Science* **2016**, *9* (10), 3128-3134.
59. Ahn, N.; Kwak, K.; Jang, M. S.; Yoon, H.; Lee, B. Y.; Lee, J.-K.; Pikhitsa, P. V.; Byun, J.; Choi, M., Trapped charge-driven degradation of perovskite solar cells. *Nature Communications* **2016**, *7*, 13422.
60. Yang, D.; Zhou, X.; Yang, R.; Yang, Z.; Yu, W.; Wang, X.; Li, C.; Liu, S.; Chang, R. P. H., Surface optimization to eliminate hysteresis for record efficiency planar perovskite solar cells. *Energy & Environmental Science* **2016**, *9* (10), 3071-3078.
61. Sung, H.; Ahn, N.; Jang, M. S.; Lee, J.-K.; Yoon, H.; Park, N.-G.; Choi, M., Transparent Conductive Oxide-Free Graphene-Based Perovskite Solar Cells with over 17% Efficiency. *Advanced Energy Materials* **2015**, *6* (3), 1501873.
62. Bi, C.; Wang, Q.; Shao, Y.; Yuan, Y.; Xiao, Z.; Huang, J., Non-wetting surface-driven high-aspect-ratio crystalline grain growth for efficient hybrid perovskite solar cells. *Nature Communications* **2015**, *6*, 7747.
63. Wang, Q.; Dong, Q.; Li, T.; Gruverman, A.; Huang, J., Thin Insulating Tunneling Contacts for Efficient and Water-Resistant Perovskite Solar Cells. *Advanced Materials* **2016**, *28* (31), 6734-6739.
64. Wei, J.; Zhao, Y.; Li, H.; Li, G.; Pan, J.; Xu, D.; Zhao, Q.; Yu, D., Hysteresis Analysis Based on the Ferroelectric Effect in Hybrid Perovskite Solar Cells. *The Journal of Physical Chemistry Letters* **2014**, *5* (21), 3937-3945.
65. Zhang, Y.; Liu, M.; Eperon, G. E.; Leijtens, T. C.; McMeekin, D.; Saliba, M.; Zhang, W.; de Bastiani, M.; Petrozza, A.; Herz, L. M.; Johnston, M. B.; Lin, H.; Snaith, H. J., Charge selective contacts, mobile ions and anomalous hysteresis in organic-inorganic perovskite solar cells. *Materials Horizons* **2015**, *2* (3), 315-322.
66. Bergmann, V. W.; Weber, S. A. L.; Javier Ramos, F.; Nazeeruddin, M. K.; Grätzel, M.; Li, D.; Domanski, A. L.; Lieberwirth, I.; Ahmad, S.; Berger, R., Real-space observation of unbalanced charge distribution inside a perovskite-sensitized solar cell. *Nature Communications* **2014**, *5*, 5001.
67. Grätzel, M., The light and shade of perovskite solar cells. *Nature Materials* **2014**, *13*, 838.
68. Cai, M.; Wu, Y.; Chen, H.; Yang, X.; Qiang, Y.; Han, L., Cost-Performance Analysis of Perovskite Solar Modules. *Advanced Science* **2016**, *4* (1), 1600269.
69. Commission, E. E. Restriction of Hazardous Substances. <https://eur-lex.europa.eu/legal-content/EN/TXT/?uri=CELEX:32015L0863> (accessed October 2018).
70. Bach, U.; Lupo, D.; Comte, P.; Moser, J. E.; Weissörtel, F.; Salbeck, J.; Spreitzer, H.; Grätzel, M., Solid-state dye-sensitized mesoporous TiO₂ solar cells with high photon-to-electron conversion efficiencies. *Nature* **1998**, *395*, 583.
71. Krüger, J.; Plass, R.; Cevey, L.; Piccirelli, M.; Grätzel, M.; Bach, U., High efficiency solid-state photovoltaic device due to inhibition of interface charge recombination. *Applied Physics Letters* **2001**, *79* (13), 2085-2087.
72. Cho, K. T.; Paek, S.; Grancini, G.; Roldán-Carmona, C.; Gao, P.; Lee, Y.; Nazeeruddin, M. K., Highly efficient perovskite solar cells with a compositionally engineered perovskite/hole transporting material interface. *Energy & Environmental Science* **2017**, *10* (2), 621-627.

73. Sun, W.; Ye, S.; Rao, H.; Li, Y.; Liu, Z.; Xiao, L.; Chen, Z.; Bian, Z.; Huang, C., Room-temperature and solution-processed copper iodide as the hole transport layer for inverted planar perovskite solar cells. *Nanoscale* **2016**, *8* (35), 15954-15960.
74. Hu, L.; Peng, J.; Wang, W.; Xia, Z.; Yuan, J.; Lu, J.; Huang, X.; Ma, W.; Song, H.; Chen, W.; Cheng, Y.-B.; Tang, J., Sequential Deposition of CH₃NH₃PbI₃ on Planar NiO Film for Efficient Planar Perovskite Solar Cells. *ACS Photonics* **2014**, *1* (7), 547-553.
75. Jung, J. W.; Chueh, C.-C.; Jen, A. K. Y., A Low-Temperature, Solution-Processable, Cu-Doped Nickel Oxide Hole-Transporting Layer via the Combustion Method for High-Performance Thin-Film Perovskite Solar Cells. *Advanced Materials* **2015**, *27* (47), 7874-7880.
76. Chen, W.; Wu, Y.; Yue, Y.; Liu, J.; Zhang, W.; Yang, X.; Chen, H.; Bi, E.; Ashraful, I.; Grätzel, M.; Han, L., Efficient and stable large-area perovskite solar cells with inorganic charge extraction layers. *Science* **2015**, *350* (6263), 944.
77. Park, J. H.; Seo, J.; Park, S.; Shin, S. S.; Kim, Y. C.; Jeon, N. J.; Shin, H.-W.; Ahn, T. K.; Noh, J. H.; Yoon, S. C.; Hwang, C. S.; Seok, S. I., Efficient CH₃NH₃PbI₃ Perovskite Solar Cells Employing Nanostructured p-Type NiO Electrode Formed by a Pulsed Laser Deposition. *Advanced Materials* **2015**, *27* (27), 4013-4019.
78. Zhang, F.; Mezgeb, M. M.; Guo, W.; Xu, H.; Liu, X.-y., An efficient and simple dual effect by under-layer abduction design for highly flexible NiOx-based perovskite solar cells. *Journal of Power Sources* **2018**, *399*, 246-253.
79. Chavhan, S.; Miguel, O.; Grande, H.-J.; Gonzalez-Pedro, V.; Sánchez, R. S.; Barea, E. M.; Mora-Seró, I.; Tena-Zaera, R., Organo-metal halide perovskite-based solar cells with CuSCN as the inorganic hole selective contact. *Journal of Materials Chemistry A* **2014**, *2* (32), 12754-12760.
80. Arora, N.; Dar, M. I.; Hinderhofer, A.; Pellet, N.; Schreiber, F.; Zakeeruddin, S. M.; Grätzel, M., Perovskite solar cells with CuSCN hole extraction layers yield stabilized efficiencies greater than 20%. *Science* **2017**, *358* (6364), 768.
81. Ye, S.; Sun, W.; Li, Y.; Yan, W.; Peng, H.; Bian, Z.; Liu, Z.; Huang, C., CuSCN-Based Inverted Planar Perovskite Solar Cell with an Average PCE of 15.6%. *Nano Letters* **2015**, *15* (6), 3723-3728.
82. (a) Wang, Y.; Liu, X.; Shan, H.; Chen, Q.; Liu, T.; Sun, X.; Ma, D.; Zhang, Z.; Xu, J.; Xu, Z.-X., Tetra-alkyl-substituted copper (II) phthalocyanines as dopant-free hole-transport layers for planar perovskite solar cells with enhanced open circuit voltage and stability. *Dyes and Pigments* **2017**, *139*, 619-626; (b) Yang, G.; Wang, Y.-L.; Xu, J.-J.; Lei, H.-W.; Chen, C.; Shan, H.-Q.; Liu, X.-Y.; Xu, Z.-X.; Fang, G.-J., A facile molecularly engineered copper (II) phthalocyanine as hole transport material for planar perovskite solar cells with enhanced performance and stability. *Nano Energy* **2017**, *31*, 322-330; (c) Kumar, C. V.; Sfyri, G.; Raptis, D.; Stathatos, E.; Lianos, P., Perovskite solar cell with low cost Cu-phthalocyanine as hole transporting material. *RSC Advances* **2015**, *5* (5), 3786-3791.
83. Wang, J.-M.; Wang, Z.-K.; Li, M.; Zhang, C.-C.; Jiang, L.-L.; Hu, K.-H.; Ye, Q.-Q.; Liao, L.-S., Doped Copper Phthalocyanine via an Aqueous Solution Process for Normal and Inverted Perovskite Solar Cells. *Advanced Energy Materials* **2017**, *8* (2), 1701688.
84. Haider, M.; Zhen, C.; Wu, T.; Liu, G.; Cheng, H.-M., Boosting efficiency and stability of perovskite solar cells with nickel phthalocyanine as a low-cost hole transporting layer material. *Journal of Materials Science & Technology* **2018**, *34* (9), 1474-1480.
85. Zhang, J.; Hua, Y.; Xu, B.; Yang, L.; Liu, P.; Johansson, M. B.; Vlachopoulos, N.; Kloo, L.; Boschloo, G.; Johansson, E. M. J.; Sun, L.; Hagfeldt, A., The Role of 3D Molecular Structural Control in

New Hole Transport Materials Outperforming Spiro-OMeTAD in Perovskite Solar Cells. *Advanced Energy Materials* **2016**, 6 (19), 1601062.

86. Malinauskas, T.; Saliba, M.; Matsui, T.; Daskeviciene, M.; Urnikaite, S.; Gratia, P.; Send, R.; Wonneberger, H.; Bruder, I.; Graetzel, M.; Getautis, V.; Nazeeruddin, M. K., Branched methoxydiphenylamine-substituted fluorene derivatives as hole transporting materials for high-performance perovskite solar cells. *Energy & Environmental Science* **2016**, 9 (5), 1681-1686.

87. Hua, Y.; Zhang, J.; Xu, B.; Liu, P.; Cheng, M.; Kloo, L.; Johansson, E. M. J.; Sveinbjörnsson, K.; Aitola, K.; Boschloo, G.; Sun, L., Facile synthesis of fluorene-based hole transport materials for highly efficient perovskite solar cells and solid-state dye-sensitized solar cells. *Nano Energy* **2016**, 26, 108-113.

88. Saliba, M.; Orlandi, S.; Matsui, T.; Aghazada, S.; Cavazzini, M.; Correa-Baena, J.-P.; Gao, P.; Scopelliti, R.; Mosconi, E.; Dahmen, K.-H.; De Angelis, F.; Abate, A.; Hagfeldt, A.; Pozzi, G.; Graetzel, M.; Nazeeruddin, M. K., A molecularly engineered hole-transporting material for efficient perovskite solar cells. *Nature Energy* **2016**, 1, 15017.

89. (a) Bi, D.; Xu, B.; Gao, P.; Sun, L.; Grätzel, M.; Hagfeldt, A., Facile synthesized organic hole transporting material for perovskite solar cell with efficiency of 19.8%. *Nano Energy* **2016**, 23, 138-144; (b) Xu, B.; Bi, D.; Hua, Y.; Liu, P.; Cheng, M.; Grätzel, M.; Kloo, L.; Hagfeldt, A.; Sun, L., A low-cost spiro[fluorene-9,9'-xanthene]-based hole transport material for highly efficient solid-state dye-sensitized solar cells and perovskite solar cells. *Energy & Environmental Science* **2016**, 9 (3), 873-877.

90. Xu, B.; Zhang, J.; Hua, Y.; Liu, P.; Wang, L.; Ruan, C.; Li, Y.; Boschloo, G.; Johansson, E. M. J.; Kloo, L.; Hagfeldt, A.; Jen, A. K. Y.; Sun, L., Tailor-Making Low-Cost Spiro[fluorene-9,9'-xanthene]-Based 3D Oligomers for Perovskite Solar Cells. *Chem* **2017**, 2 (5), 676-687.

91. Zhang, F.; Wang, Z.; Zhu, H.; Pellet, N.; Luo, J.; Yi, C.; Liu, X.; Liu, H.; Wang, S.; Li, X.; Xiao, Y.; Zakeeruddin, S. M.; Bi, D.; Grätzel, M., Over 20% PCE perovskite solar cells with superior stability achieved by novel and low-cost hole-transporting materials. *Nano Energy* **2017**, 41, 469-475.

92. Zimmermann, I.; Urieta-Mora, J.; Gratia, P.; Aragón, J.; Grancini, G.; Molina-Ontoria, A.; Ortí, E.; Martín, N.; Nazeeruddin, M. K., High-Efficiency Perovskite Solar Cells Using Molecularly Engineered, Thiophene-Rich, Hole-Transporting Materials: Influence of Alkyl Chain Length on Power Conversion Efficiency. *Advanced Energy Materials* **2016**, 7 (6), 1601674.

93. Molina-Ontoria, A.; Zimmermann, I.; Garcia-Benito, I.; Gratia, P.; Roldán-Carmona, C.; Aghazada, S.; Graetzel, M.; Nazeeruddin, M. K.; Martín, N., Benzotrithiophene-Based Hole-Transporting Materials for 18.2 % Perovskite Solar Cells. *Angewandte Chemie International Edition* **2016**, 55 (21), 6270-6274.

94. Zhang, F.; Wang, S.; Zhu, H.; Liu, X.; Liu, H.; Li, X.; Xiao, Y.; Zakeeruddin, S. M.; Grätzel, M., Impact of Peripheral Groups on Phenothiazine-Based Hole-Transporting Materials for Perovskite Solar Cells. *ACS Energy Letters* **2018**, 3 (5), 1145-1152.

95. Momblona, C.; Gil-Escrig, L.; Bandiello, E.; Hutter, E. M.; Sessolo, M.; Lederer, K.; Blochwitz-Nimoth, J.; Bolink, H. J., Efficient vacuum deposited p-i-n and n-i-p perovskite solar cells employing doped charge transport layers. *Energy & Environmental Science* **2016**, 9 (11), 3456-3463.

96. (a) Zhang, J.; Xu, B.; Johansson, E. M. J.; Hadadian, M.; Correa Baena, J. P.; Liu, P.; Hua, Y.; Vlachopoulos, N.; Johansson, E. M. J.; Boschloo, G.; Sun, L.; Hagfeldt, A., Constructive Effects of Alkyl Chains: A Strategy to Design Simple and Non-Spiro Hole Transporting Materials for High-Efficiency Mixed-Ion Perovskite Solar Cells. *Advanced Energy Materials* **2016**, 6 (13), 1502536; (b) Zhang, J.; Xu, B.; Yang, L.; Ruan, C.; Wang, L.; Liu, P.; Zhang, W.; Vlachopoulos, N.; Kloo, L.; Boschloo, G.; Sun, L.; Hagfeldt, A.; Johansson, E. M. J., The Importance of Pendant Groups on Triphenylamine-Based Hole

Transport Materials for Obtaining Perovskite Solar Cells with over 20% Efficiency. *Advanced Energy Materials* **2017**, 8 (2), 1701209.

97. Rakstys, K.; Abate, A.; Dar, M. I.; Gao, P.; Jankauskas, V.; Jacopin, G.; Kamarauskas, E.; Kazim, S.; Ahmad, S.; Grätzel, M.; Nazeeruddin, M. K., Triazatruxene-Based Hole Transporting Materials for Highly Efficient Perovskite Solar Cells. *Journal of the American Chemical Society* **2015**, 137 (51), 16172-16178.

98. Su, P.-Y.; Huang, L.-B.; Liu, J.-M.; Chen, Y.-F.; Xiao, L.-M.; Kuang, D.-B.; Mayor, M.; Su, C.-Y., A multifunctional poly-N-vinylcarbazole interlayer in perovskite solar cells for high stability and efficiency: a test with new triazatruxene-based hole transporting materials. *Journal of Materials Chemistry A* **2017**, 5 (5), 1913-1918.

99. Huang, C.; Fu, W.; Li, C.-Z.; Zhang, Z.; Qiu, W.; Shi, M.; Heremans, P.; Jen, A. K. Y.; Chen, H., Dopant-Free Hole-Transporting Material with a C3h Symmetrical Truxene Core for Highly Efficient Perovskite Solar Cells. *Journal of the American Chemical Society* **2016**, 138 (8), 2528-2531.

100. (a) Kim, H.-S.; Kim, C.-H.; Ha, C.-S.; Lee, J.-K., Organic solar cell devices based on PVK/porphyrin system. *Synthetic Metals* **2001**, 117 (1), 289-291; (b) Deschler, F.; Riedel, D.; Ecker, B.; von Hauff, E.; Da Como, E.; MacKenzie, R. C. I., Increasing organic solar cell efficiency with polymer interlayers. *Physical Chemistry Chemical Physics* **2013**, 15 (3), 764-769.

101. Yin, X.; Guan, L.; Yu, J.; Zhao, D.; Wang, C.; Shrestha, N.; Han, Y.; An, Q.; Zhou, J.; Zhou, B.; Yu, Y.; Grice, C. R.; Awni, R. A.; Zhang, F.; Wang, J.; Ellingson, R. J.; Yan, Y.; Tang, W., One-step facile synthesis of a simple carbazole-cored hole transport material for high-performance perovskite solar cells. *Nano Energy* **2017**, 40, 163-169.

102. Magomedov, A.; Paek, S.; Gratia, P.; Kasparavicius, E.; Daskeviciene, M.; Kamarauskas, E.; Gruodis, A.; Jankauskas, V.; Kantminiene, K.; Cho, K. T.; Rakstys, K.; Malinauskas, T.; Getautis, V.; Nazeeruddin, M. K., Diphenylamine-Substituted Carbazole-Based Hole Transporting Materials for Perovskite Solar Cells: Influence of Isomeric Derivatives. *Advanced Functional Materials* **2018**, 28 (9), 1704351.

103. Sung, S. D.; Kang, M. S.; Choi, I. T.; Kim, H. M.; Kim, H.; Hong, M.; Kim, H. K.; Lee, W. I., 14.8% perovskite solar cells employing carbazole derivatives as hole transporting materials. *Chemical Communications* **2014**, 50 (91), 14161-14163.

104. Li, D.; Shao, J.-Y.; Li, Y.; Li, Y.; Deng, L.-Y.; Zhong, Y.-W.; Meng, Q., New hole transporting materials for planar perovskite solar cells. *Chemical Communications* **2018**, 54 (13), 1651-1654.

105. Liu, J.; Pathak, S.; Stergiopoulos, T.; Leijtens, T.; Wojciechowski, K.; Schumann, S.; Kausch-Busies, N.; Snaith, H. J., Employing PEDOT as the p-Type Charge Collection Layer in Regular Organic-Inorganic Perovskite Solar Cells. *The Journal of Physical Chemistry Letters* **2015**, 6 (9), 1666-1673.

106. Yu, J. C.; Hong, J. A.; Jung, E. D.; Kim, D. B.; Baek, S.-M.; Lee, S.; Cho, S.; Park, S. S.; Choi, K. J.; Song, M. H., Highly efficient and stable inverted perovskite solar cell employing PEDOT:GO composite layer as a hole transport layer. *Scientific Reports* **2018**, 8 (1), 1070.

107. Li, X.; Liu, X.; Wang, X.; Zhao, L.; Jiu, T.; Fang, J., Polyelectrolyte based hole-transporting materials for high performance solution processed planar perovskite solar cells. *Journal of Materials Chemistry A* **2015**, 3 (29), 15024-15029.

108. Li, X.; Wang, Y.-C.; Zhu, L.; Zhang, W.; Wang, H.-Q.; Fang, J., Improving Efficiency and Reproducibility of Perovskite Solar Cells through Aggregation Control in Polyelectrolytes Hole Transport Layer. *ACS applied materials & interfaces* **2017**, 9 (37), 31357-31361.

109. Cai, F.; Cai, J.; Yang, L.; Li, W.; Gurney, R. S.; Yi, H.; Iraqi, A.; Liu, D.; Wang, T., Molecular engineering of conjugated polymers for efficient hole transport and defect passivation in perovskite solar cells. *Nano Energy* **2018**, *45*, 28-36.
110. Zhao, D.; Sexton, M.; Park, H.-Y.; Baure, G.; Nino, J. C.; So, F., High-Efficiency Solution-Processed Planar Perovskite Solar Cells with a Polymer Hole Transport Layer. *Advanced Energy Materials* **2014**, *5* (6), 1401855.
111. Zheng, X.; Chen, B.; Dai, J.; Fang, Y.; Bai, Y.; Lin, Y.; Wei, H.; Zeng, Xiao C.; Huang, J., Defect passivation in hybrid perovskite solar cells using quaternary ammonium halide anions and cations. *Nature Energy* **2017**, *2*, 17102.
112. (a) Zhang, F.; Yang, X.; Cheng, M.; Wang, W.; Sun, L., Boosting the efficiency and the stability of low cost perovskite solar cells by using CuPc nanorods as hole transport material and carbon as counter electrode. *Nano Energy* **2016**, *20*, 108-116; (b) Han, J.; Tu, Y.; Liu, Z.; Liu, X.; Ye, H.; Tang, Z.; Shi, T.; Liao, G., Efficient and stable inverted planar perovskite solar cells using dopant-free CuPc as hole transport layer. *Electrochimica Acta* **2018**, *273*, 273-281.
113. Franckevičius, M.; Mishra, A.; Kreuzer, F.; Luo, J.; Zakeeruddin, S. M.; Grätzel, M., A dopant-free spirobi[cyclopenta[2,1-b:3,4-b']dithiophene] based hole-transport material for efficient perovskite solar cells. *Materials Horizons* **2015**, *2* (6), 613-618.
114. Liu, Y.; Chen, Q.; Duan, H.-S.; Zhou, H.; Yang, Y.; Chen, H.; Luo, S.; Song, T.-B.; Dou, L.; Hong, Z.; Yang, Y., A dopant-free organic hole transport material for efficient planar heterojunction perovskite solar cells. *Journal of Materials Chemistry A* **2015**, *3* (22), 11940-11947.
115. Liu, Y.; Hong, Z.; Chen, Q.; Chen, H.; Chang, W.-H.; Yang, Y.; Song, T.-B.; Yang, Y., Perovskite Solar Cells Employing Dopant-Free Organic Hole Transport Materials with Tunable Energy Levels. *Advanced Materials* **2015**, *28* (3), 440-446.
116. Habisreutinger, S. N.; Leijtens, T.; Eperon, G. E.; Stranks, S. D.; Nicholas, R. J.; Snaith, H. J., Carbon Nanotube/Polymer Composites as a Highly Stable Hole Collection Layer in Perovskite Solar Cells. *Nano Letters* **2014**, *14* (10), 5561-5568.
117. Huang, L.-B.; Su, P.-Y.; Liu, J.-M.; Huang, J.-F.; Chen, Y.-F.; Qin, S.; Guo, J.; Xu, Y.-W.; Su, C.-Y., Interface engineering of perovskite solar cells with multifunctional polymer interlayer toward improved performance and stability. *Journal of Power Sources* **2018**, *378*, 483-490.
118. Liao, H.-C.; Tam, T. L. D.; Guo, P.; Wu, Y.; Manley, E. F.; Huang, W.; Zhou, N.; Soe, C. M. M.; Wang, B.; Wasielewski, M. R.; Chen, L. X.; Kanatzidis, M. G.; Facchetti, A.; Chang, R. P. H.; Marks, T. J., Dopant-Free Hole Transporting Polymers for High Efficiency, Environmentally Stable Perovskite Solar Cells. *Advanced Energy Materials* **2016**, *6* (16), 1600502.
119. Zhao, X.; Zhang, F.; Yi, C.; Bi, D.; Bi, X.; Wei, P.; Luo, J.; Liu, X.; Wang, S.; Li, X.; Zakeeruddin, S. M.; Grätzel, M., A novel one-step synthesized and dopant-free hole transport material for efficient and stable perovskite solar cells. *Journal of Materials Chemistry A* **2016**, *4* (42), 16330-16334.
120. Zhang, F.; Liu, X.; Yi, C.; Bi, D.; Luo, J.; Wang, S.; Li, X.; Xiao, Y.; Zakeeruddin, S. M.; Grätzel, M., Dopant-Free Donor (D)- π -D- π -D Conjugated Hole-Transport Materials for Efficient and Stable Perovskite Solar Cells. *ChemSusChem* **2016**, *9* (18), 2578-2585.
121. Zhang, F.; Yi, C.; Wei, P.; Bi, X.; Luo, J.; Jacopin, G.; Wang, S.; Li, X.; Xiao, Y.; Zakeeruddin, S. M.; Grätzel, M., A Novel Dopant-Free Triphenylamine Based Molecular "Butterfly" Hole-Transport Material for Highly Efficient and Stable Perovskite Solar Cells. *Advanced Energy Materials* **2016**, *6* (14), 1600401.

122. Liu, C.; Zhang, D.; Li, Z.; Zhang, X.; Shen, L.; Guo, W., Efficient 4,4',4''-tris(3-methylphenylphenylamino)triphenylamine (m-MTDATA) Hole Transport Layer in Perovskite Solar Cells Enabled by Using the Nonstoichiometric Precursors. *Advanced Functional Materials* **2018**, *28* (36), 1803126.
123. Xu, Y.; Bu, T.; Li, M.; Qin, T.; Yin, C.; Wang, N.; Li, R.; Zhong, J.; Li, H.; Peng, Y.; Wang, J.; Xie, L.; Huang, W., Non-Conjugated Polymer as an Efficient Dopant-Free Hole-Transporting Material for Perovskite Solar Cells. *ChemSusChem* **2017**, *10* (12), 2578-2584.
124. Kyeong, M.; Lee, J.; Lee, K.; Hong, S., BODIPY-Based Conjugated Polymers for Use as Dopant-Free Hole Transporting Materials for Durable Perovskite Solar Cells: Selective Tuning of HOMO/LUMO Levels. *ACS applied materials & interfaces* **2018**, *10* (27), 23254-23262.
125. Kim, G.-W.; Kang, G.; Kim, J.; Lee, G.-Y.; Kim, H. I.; Pyeon, L.; Lee, J.; Park, T., Dopant-free polymeric hole transport materials for highly efficient and stable perovskite solar cells. *Energy & Environmental Science* **2016**, *9* (7), 2326-2333.
126. Zhang, J.; Xu, B.; Yang, L.; Mingorance, A.; Ruan, C.; Hua, Y.; Wang, L.; Vlachopoulos, N.; Lira-Cantú, M.; Boschloo, G.; Hagfeldt, A.; Sun, L.; Johansson, E. M. J., Incorporation of Counter Ions in Organic Molecules: New Strategy in Developing Dopant-Free Hole Transport Materials for Efficient Mixed-Ion Perovskite Solar Cells. *Advanced Energy Materials* **2017**, *7* (14), 1602736.
127. Jo, J. W.; Seo, M.-S.; Park, M.; Kim, J.-Y.; Park, J. S.; Han, I. K.; Ahn, H.; Jung, J. W.; Sohn, B.-H.; Ko, M. J.; Son, H. J., Improving Performance and Stability of Flexible Planar-Heterojunction Perovskite Solar Cells Using Polymeric Hole-Transport Material. *Advanced Functional Materials* **2016**, *26* (25), 4464-4471.
128. Zhang, S.; Stolterfoht, M.; Armin, A.; Lin, Q.; Zu, F.; Sobus, J.; Jin, H.; Koch, N.; Meredith, P.; Burn, P. L.; Neher, D., Interface Engineering of Solution-Processed Hybrid Organohalide Perovskite Solar Cells. *ACS applied materials & interfaces* **2018**, *10* (25), 21681-21687.

Chapter 2

Perovskite Solar Cell Fabrication

In this chapter are described the fabrication steps and the optimizations to elaborate mesoscopic, n-i-p planar and p-i-n inverted perovskite solar cells. These three architectures are used as reference cells in the following chapters.

1 Introduction

Three architectures are considered in this manuscript: n-i-p mesoscopic, n-i-p planar and p-i-n planar inverted PSCs. These devices were made of materials commonly employed in PSCs, and inspired from best performing devices at the time they were elaborated. The objective was to make reference devices to further incorporate our polymers. Reference devices require to exhibit reliable efficiency, high enough to be able to understand mechanisms when modifying the devices and to add value to the novel materials we introduce. The hysteresis was evaluated by a hysteresis index defined as $HI = (PCE_{reverse} - PCE_{forward}) / PCE_{reverse}$. All of the experiments are detailed at the end of the manuscript.

2 n-i-p Planar perovskite solar cells

2.1 Fabrication steps of planar perovskite solar cells

n-i-p planar PSCs are fabricated on a transparent conductive oxide. FTO substrates are preferentially used due to their much better thermal stability compared to ITO. These substrates are then coated with a TiO_2 blocking layer (bl- TiO_2) from solution and calcined to insure a good electron transport. Planar devices employed $MAPbI_{3-x}Cl_x$ perovskite, since it has been demonstrated to be particularly efficient owing to the long diffusion length of charge carriers.¹ Then, a hole transporting material (HTM) made of spiro-OMeTAD doped with LiTFSI and tBP is deposited onto the perovskite film. The perovskite and the HTM deposition were performed in N_2 glove box and aged overnight in 15% RH (relative humidity) atmosphere, before the thermal evaporation of the gold electrodes. The energy diagram and the fabrication steps of n-i-p planar PSCs are depicted in Figure 22 and Figure 23.

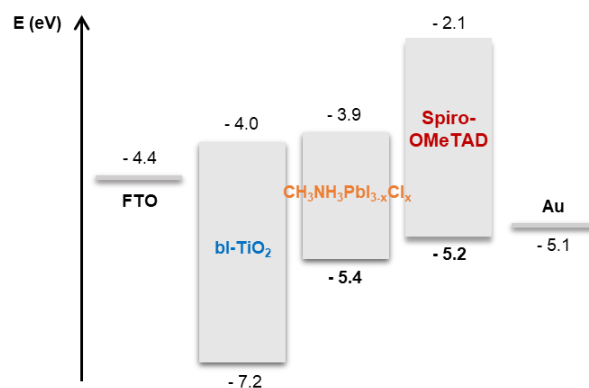


Figure 23. Energy diagram of n-i-p planar PSCs.

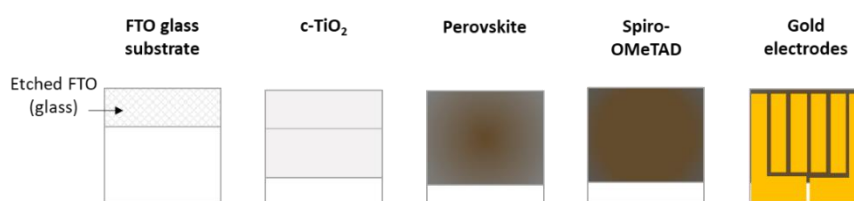


Figure 24. Fabrication steps of regular planar PSCs.

2.2 Optimizations of the process

2.2.1 TiO₂ blocking layer

In the first devices, the bl-TiO_2 was deposited by spray-pyrolysis. This method allows the deposition of a thin and smooth layer of TiO_2 . However, many parameters such as the deposition speed and the distance from the samples, rely on the experimenter and can lead to heterogeneities between devices. In order to improve the reproducibility, spin-coating and atomic layer deposition (ALD) methods were compared. Spin-coating deposition was realized by using the same precursor solution as for spray-coating. ALD consists in successively depositing monolayers of titanium from TiCl_4 , which are grafted to oxygen in replacement of hydrogen on the surface, and OH from water which bond to titanium, replacing chloride (Figure 25). This method allows the formation of a compact layer of TiO_2 with a well control of the thickness.

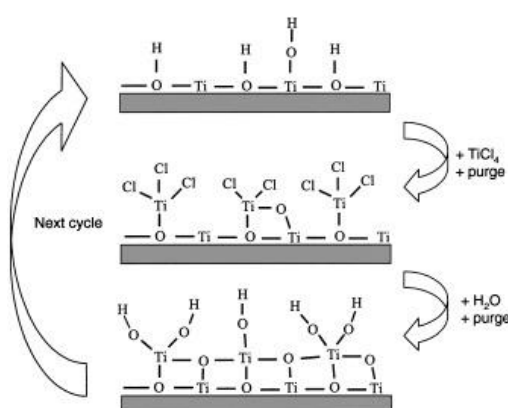


Figure 25. Schematic ALD process of TiO_2 layer from TiCl_4 and H_2O .

For each deposition method, thickness of TiO_2 was optimized in solar cells (Figure 26). Best performances are given in Table 3. For the spin-coating deposition, thickness was varied with the precursor solution concentration and the speed and acceleration of the rotation, from few nanometers to around 100 nm. ALD thickness was varied with the number of cycles. Spray coating

thickness was varied with the volume and the concentration of the precursor solution, from few nanometers to about 230 nm. Maximum PCE of 15.5 % was obtained for the spin-coated device. However, hysteresis was found to be the largest. The unreliability of the spray-coating method is confirmed with non-linear evolution of PCE with the thickness. Devices from ALD gave poor PV performances. This could be due to the crystallinity of the TiO_2 . As it was not possible to control the phase by XRD due to the too thin TiO_2 thickness, a calcination step at 500°C was performed after the ALD to insure the prevalence of the anatase phase instead of the amorphous phase. However, similar PV performances were obtained. Another reason could be the formation of HCl byproduct when using TiCl_4 , which can etch the film during the deposition.²

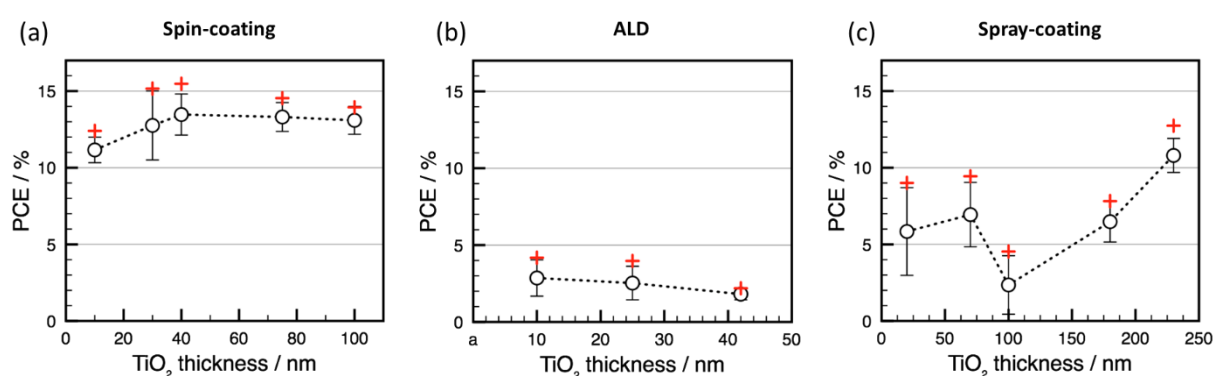


Figure 26. PCE (reverse scan) as a function of the TiO_2 thickness for (a) spin coating method, (b) ALD, and (c) spray-coating deposition. Red crosses represent maximum PCE while rounds are average PCE on 8 cells and their standard deviation.

As the interface between TiO_2 and the perovskite is important for electron extraction and performances of planar PSCs, TiO_2 surface was modified by grafting 3-aminopropyltriethoxysilane (APTES) (Figure 27). Surface hydroxyl groups of the TiO_2 blocking layer can substitute the ethoxy group on the silicon atom to give $-\text{Ti}-\text{O}-\text{Si}-(\text{CH}_2)_3-\text{NH}_2$ linkages, the amino group being expected to form specific interactions with the perovskite. Thus, amino-silanes have been previously used to improve wettability and quality of perovskite thin films.³ They can enhance adhesion between the TiO_2 and the perovskite, reduce trap states and even reduce hysteresis. The modification process was operated on spin-coated TiO_2 substrates. In PSCs, these modified layers finally exhibited lower performances than pristine TiO_2 . V_{oc} and J_{sc} were significantly reduced and hysteresis is still huge (Table 3). It may be due to an over functionalization of the surface. APTES may unfavourably modify the TiO_2 CB level for the electron extraction and/or the surface properties for the formation of the perovskite crystal. Therefore, this method has not been further optimized.

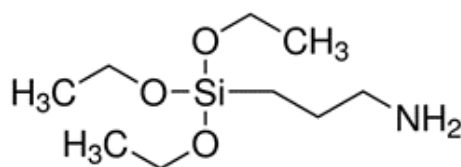


Figure 27. Chemical structure of APTES.

Table 3. Best and average (8 cells) PV performances and hysteresis index of PSCs based on different TiO₂ processes.

	Reverse scan				Forward scan				HI
	J _{sc}	V _{oc}	FF	PCE	J _{sc}	V _{oc}	FF	PCE	
	<i>mA.cm⁻²</i>	<i>V</i>		%	<i>mA.cm⁻²</i>	<i>V</i>		%	
Spin	22.55 ^a	1.00	0.69	15.48	22.65	0.77	0.31	5.43	0.65
coating	21.34 ^b	0.95	0.66	13.47	21.28	0.69	0.30	4.47	0.67
	± 1.07 ^c	± 0.04	± 0.02	± 1.34	± 1.11	± 0.06	± 0.02	± 0.69	± 0.02
ALD	15.62	0.78	0.34	4.18	17.87	0.61	0.15	1.68	0.60
	11.31	0.83	0.30	2.86	12.05	0.73	0.15	1.20	0.56
	± 3.85	± 0.05	± 0.04	± 1.18	± 5.78	± 0.12	± 0.04	± 0.39	± 0.07
Spray	21.23	0.91	0.66	12.74	21.50	0.85	0.61	11.11	0.13
coating (ref)	20.68	0.87	0.59	10.20	20.83	0.78	0.51	8.29	0.23
	± 0.86	± 0.04	± 0.13	± 1.71	± 0.95	± 0.05	± 0.14	± 2.16	± 0.06
Silane on	16.48	0.79	0.65	8.48	16.50	0.61	0.37	3.72	0.56
spin coating	15.90	0.73	0.50	6.06	15.88	0.58	0.34	3.10	0.42
	± 0.46	± 0.12	± 0.16	± 2.63	± 0.50	± 0.14	± 0.02	± 0.68	± 0.23

^a Best cell; ^b average on 8 cells; ^c standard deviation of the average.

Optimized thicknesses were measured by observing the cross section of the films by scanning electron microscopy (SEM), while surface roughness was measured by atomic force microscopy (AFM) (Table 4). Optimal spin-coating thickness was around 40 nm, which is in agreement with the literature. APTES functionalization didn't modify the thickness. Surprisingly, optimal thickness of spray-coating devices was about 230 nm, which corresponds more to the thickness of mesoporous TiO₂ layer in mesoscopic devices. Roughness was found to be reduced to 20 nm for spin-coating devices, while ALD TiO₂ roughness follows the one of the FTO substrate (40 nm).

Table 4. Thickness and roughness of TiO₂ films deposited on FTO-glass substrates.

Deposition method	Optimal thickness <i>nm</i>	Roughness <i>nm</i>
Spin coating	≈ 40	21
ALD	≈ 10	39
Spray coating	≈ 230	25
Silane on spin coating	≈ 40	19

Finally, we observed the quality of the perovskite layer coated on top of these TiO₂ layers by SEM. In all devices, perovskite formed islands of different size, shape and texturing (Figure 28). Perovskite edges seems to better adhere the TiO₂ surface modified with APTES. This indicates that surface state of TiO₂ varies from deposition technics and influences perovskite film forming. In the next experiments, TiO₂ spray pyrolysis process is replaced by spin-coating process which gives higher efficiencies in PSCs.

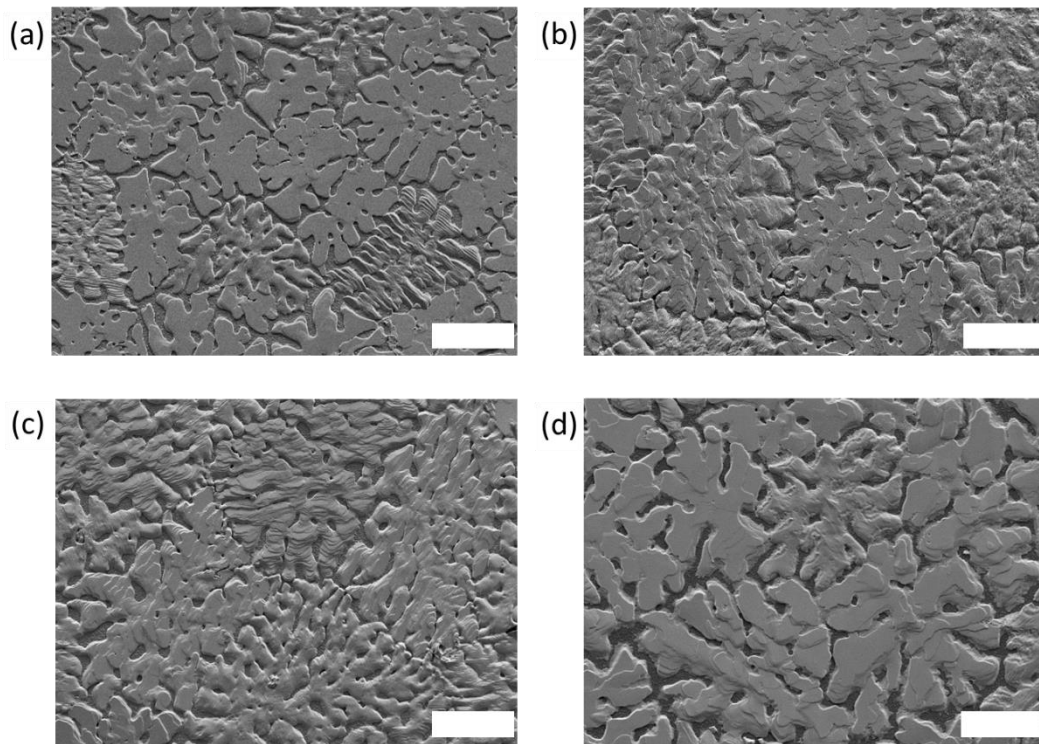


Figure 28. SEM surface images of perovskite films coated on top of (a) spin-coated, (b) ALD, (c) spray-coated TiO₂, and (d) silane-modified TiO₂. Scale bar = 20 μm.

2.2.2 TiO₂ post treatments

Several TiO₂ post treatments were tested in order to improve the film-forming of the perovskite. TiCl₄ treatment has been previously employed in DSCs to densify the bl-TiO₂ layer and improve photocurrent due to a small downward shift of the CB of TiO₂ and a reduction of recombinations at the interface.⁴ On the other hand, SnCl₄ is often used to prepare SnO₂ layers and replace TiO₂.⁵ SnO₂ has the advantages to be processable at low temperatures, to be more stable and more conductive than TiO₂, and is often reported to passivate the interface with the perovskite especially in planar devices.⁶ Therefore, TiCl₄ treatment was compared to SnCl₄ treatment. These treatments consist in immersing spin-coated TiO₂ substrates into TiCl₄ or SnCl₄ solutions at 70°C for 1h and finally drying the layers at 500°C and 180°C for TiCl₄ and SnCl₄, respectively. In this way, small amount of TiO₂ or SnO₂ was deposited.

AFM surface of treated TiO₂ and their respective roughness are given in Figure 29, as well as SEM surface images of corresponding perovskites. Roughness was slightly increased upon treatments as well as surface covering of the perovskite, especially for SnCl₄.

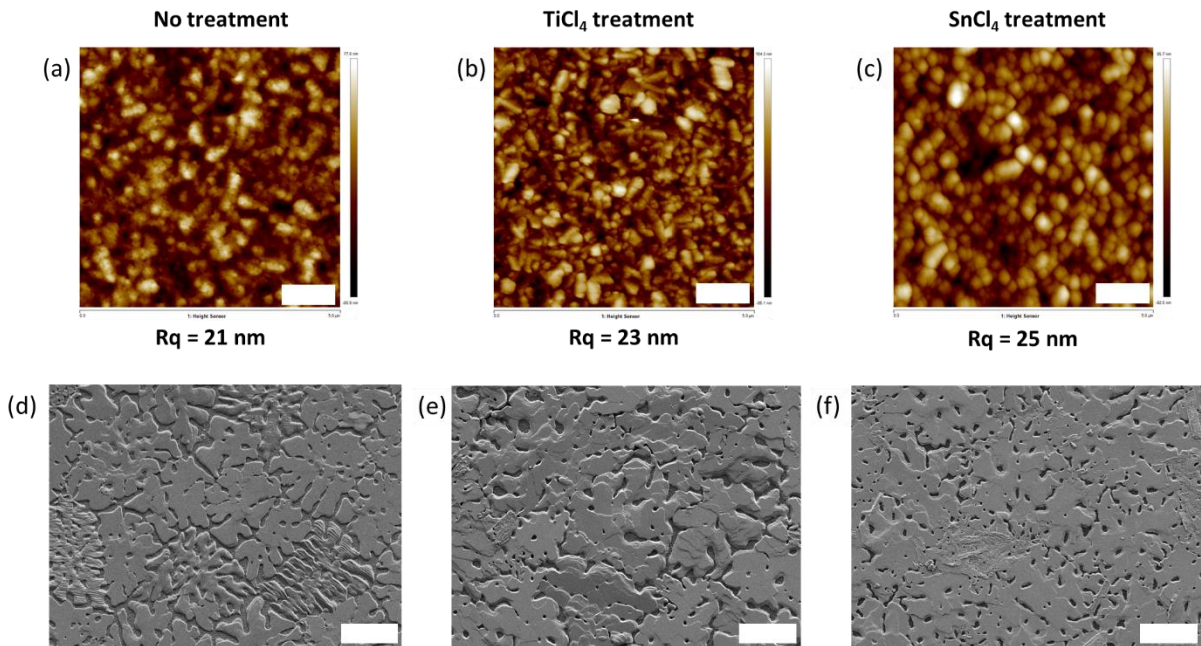


Figure 29. (a), (b), (c) AFM topographic views of TiO₂ (scale bar = 1 μ m) and (d), (e), (f), corresponding SEM surface images of perovskite films (scale bar = 20 μ m) for (a), (d) untreated, (b), (e) TiCl₄ and (c), (f) SnCl₄ treated TiO₂.

Despite better covering of the perovskite on the SnCl₄ treated surface, the SnO₂ resulting layer considerably reduced the photocurrent and the voltage in devices (Table 5). In this case, the

combination of TiO_2 and SnO_2 did not improve electron collection in devices. On the other hand, despite slightly reduced J_{sc} , TiCl_4 treated devices exhibited improved V_{oc} up to 1.08 V and a higher FF which resulted in a maximum PCE of 16 %. Hysteresis was reduced but is still largely present in the devices. In the following experiments, TiCl_4 treatment step was systematically implemented in the PSC process.

Table 5. Best and average PV performances and hysteresis index of PSCs involving TiCl_4 or SnCl_4 treatments.

	Reverse scan				Forward scan				HI
	J_{sc}	V_{oc}	FF	PCE	J_{sc}	V_{oc}	FF	PCE	
	mA.cm^{-2}	V		%	mA.cm^{-2}	V		%	
Without (ref)	22.55 ^a	1.00	0.69	15.48	22.65	0.77	0.31	5.43	0.65
	21.34 ^b	0.95	0.66	13.47	21.28	0.69	0.30	4.47	0.67
	$\pm 1.07^c$	± 0.04	± 0.02	± 1.34	± 1.11	± 0.06	± 0.02	± 0.69	± 0.02
TiCl_4	20.61	1.08	0.72	15.99	20.74	0.96	0.50	10.00	0.37
	20.72	1.00	0.68	14.11	21.11	0.86	0.35	6.42	0.57
	± 0.44	± 0.05	± 0.05	± 1.36	± 0.97	± 0.10	± 0.13	± 2.75	± 0.18
SnCl_4	7.50	0.82	0.52	3.20	3.99	0.51	0.11	0.21	0.93
	4.63	0.82	0.70	2.32	2.52	0.56	0.09	0.13	0.94
	± 2.12	± 0.03	± 0.34	± 0.77	± 1.66	± 0.04	± 0.02	± 0.09	± 0.21

^a Best cell; ^b average on 8 cells; ^c standard deviation of the average.

TiO_2 surface was treated with UV-ozone in order to make the surface more hydrophilic by forming surface hydroxyl groups and eliminating adventitious carbon species. To investigate the effect of increasing hydrophobicity of the surface by removing the UV-ozone treatment step was replaced by a surface treatment involving CF_4 plasma. CF_4 plasma is expected to make the surface more hydrophobic owing to the introduction of fluorine on the surface. Perovskite surface SEM images revealed that the more hydrophobic the substrate the better the perovskite covering (Figure 30).

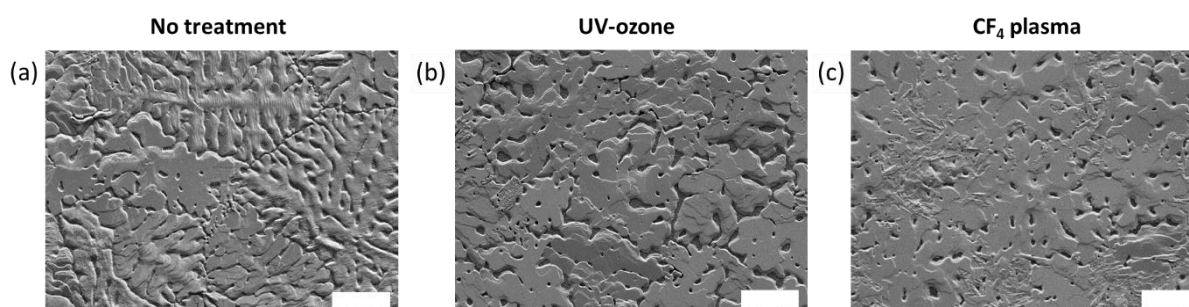


Figure 30. SEM surface images of perovskite film according to TiO_2 treatments. Scale bar = 20 μm .

However, once again, larger perovskite covering doesn't necessary imply higher PV performances (Table 6). PSCs involving the CF₄ plasma step exhibited lower V_{oc}, and thus lower PCE with larger hysteresis. Absence of treatment decreased all PV parameters. Best performances are finally obtained for the reference device involving UV-ozone treatment.

Table 6. Best and average PV performances and hysteresis index of PSCs involving different TiO₂ surface treatments.

	Reverse scan				Forward scan				HI
	J _{sc}	V _{oc}	FF	PCE	J _{sc}	V _{oc}	FF	PCE	
	<i>mA.cm⁻²</i>	<i>V</i>		%	<i>mA.cm⁻²</i>	<i>V</i>		%	
UV-ozone	20.61 ^a	1.08	0.72	15.99	20.74	0.96	0.50	10.00	0.37
(ref)	20.72 ^b	1.00	0.68	14.11	21.11	0.86	0.35	6.42	0.57
	± 0.44 ^c	± 0.05	± 0.05	± 1.36	± 0.97	± 0.10	± 0.13	± 2.75	± 0.18
No	18.38	0.97	0.70	12.50	18.03	0.50	0.36	3.27	0.74
treatment	18.15	0.85	0.62	9.73	17.90	0.51	0.38	3.65	0.63
	± 0.83	± 0.12	± 0.09	± 2.74	± 0.94	± 0.09	± 0.10	± 1.70	± 0.10
CF₄	21.15	0.92	0.73	14.26	20.38	0.75	0.29	4.43	0.69
plasma	20.59	0.87	0.65	11.64	21.35	0.62	0.31	4.08	0.65
	± 0.99	± 0.04	± 0.08	± 1.98	± 0.83	± 0.10	± 0.05	± 1.09	± 0.07

^a Best cell; ^b average on 8 cells; ^c standard deviation of the average.

It is worth mentioning that contact angle of perovskite precursor solution has also been measured on all TiO₂ surfaces tested, but were all under 15°, which is considered as completely wet surface. Therefore, wettability of surfaces has not been further discussed.

2.2.3 Perovskite process

The objective was to improve the perovskite covering playing on perovskite process and perovskite precursor solution formulation. A larger perovskite surface would lead to improved absorption and photocurrent while reducing recombinations by avoiding contacts between the HTM and the ETM through perovskite-free areas.

First, the influence of the perovskite drying temperature was studied in the 100 to 140°C temperature range. The drying time was adapted according to the darkness of the film. Once final dark colour reached, perovskite was dried 5 more minutes before being removed from the hotplate. Gradual drying process was also introduced, from 65 to 100°C by increasing temperature by 10°C every 10 minutes and then keeping the perovskite at 100°C for 1h. SEM surface images of the corresponding perovskites are depicted in Figure 31. The reference device was dried for 45 min at 120°C. Original and significantly different perovskite morphologies were obtained. Perovskite films

with some pinholes were obtained when dried below 110°C while perovskite islands were formed above 120°C. High temperature drying led to a dewetting of the perovskite and on the other hand, flatten the grains making the film smoother.

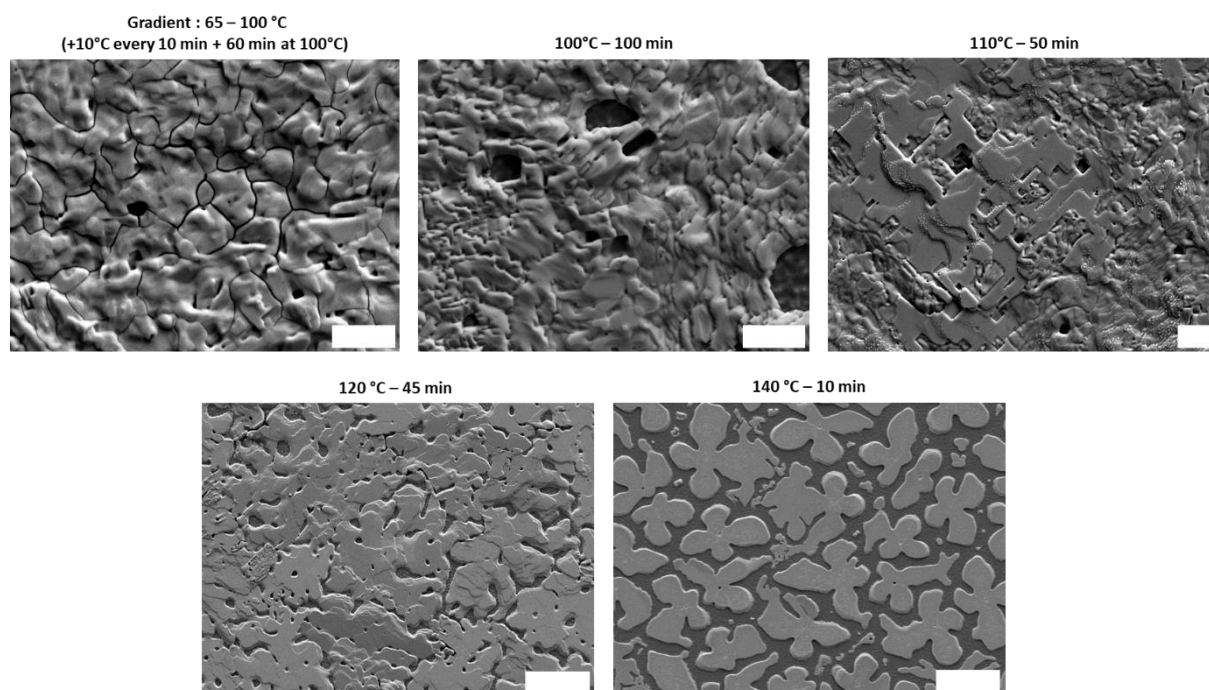


Figure 31. SEM surface images of perovskite dried under different conditions. Scale bar = 20 μm .

Regarding the absorption spectra of the films, all the perovskite had the typical MAPbI_3 absorption shape, with a first increase in absorption at around 760 nm and a second one around 560 nm (Figure 32). The most absorbing film was the one gradually dried from 65 to 100 °C, followed by the reference device dried at 120°C. The less absorbing perovskite was dried at 140°C, which also corresponds to the less covered substrate.

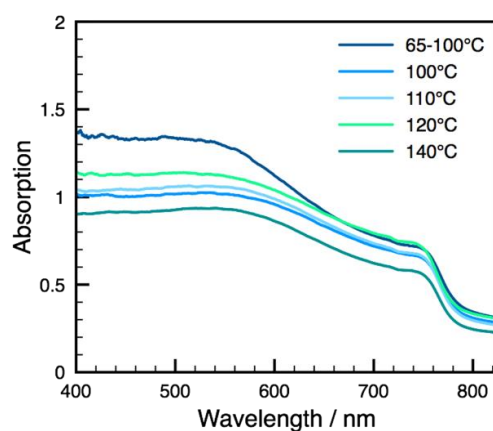


Figure 32. Absorption spectra of perovskite dried under different conditions.

The best performing perovskite into PSCs remained the reference one (Table 7). Despite poor covering, the perovskite dried at 140°C exhibited higher PCE than the gradually dried one. The absence of grain boundaries in the case of perovskite islands may avoid charge recombinations. As well, the flat grains may induce a better contact with the charge extracting layers.

Table 7. Best and average PV performances and hysteresis index of PSCs dried in different conditions.

	Reverse scan				Forward scan				HI
	J _{sc}	V _{oc}	FF	PCE	J _{sc}	V _{oc}	FF	PCE	
	<i>mA.cm⁻²</i>	<i>V</i>		%	<i>mA.cm⁻²</i>	<i>V</i>		%	
Gradient	19.21 ^a	0.90	0.71	12.27	19.28	0.67	0.31	4.05	0.67
	17.71 ^b	0.86	0.60	9.22	18.06	0.69	0.31	3.87	0.57
	± 2.07 ^c	± 0.05	± 0.08	± 2.42	± 1.99	± 0.09	± 0.03	± 1.05	± 0.10
100°C	12.23	0.86	0.36	4.06	9.87	0.87	0.18	1.54	0.62
100 min	9.82	0.86	0.35	2.84	8.49	0.81	0.17	1.18	0.58
	± 3.29	± 0.07	± 0.08	± 0.97	± 2.36	± 0.06	± 0.02	± 0.41	± 0.07
110°C	10.69	0.73	0.47	3.68	10.26	0.57	0.15	0.90	0.76
50 min	9.93	0.65	0.36	2.37	9.16	0.55	0.18	0.89	0.56
	± 0.86	± 0.08	± 0.12	± 1.16	± 1.10	± 0.09	± 0.02	± 0.15	± 0.23
120°C	20.61	1.08	0.72	15.99	20.74	0.96	0.50	10.00	0.37
45 min	20.72	1.00	0.68	14.11	21.11	0.86	0.35	6.42	0.57
	± 0.44	± 0.05	± 0.05	± 1.36	± 0.97	± 0.10	± 0.13	± 2.75	± 0.18
(ref)									
140°C	19.56	0.99	0.66	12.81	19.52	0.68	0.35	4.65	0.64
10 min	19.58	0.90	0.59	10.50	18.12	0.56	0.26	2.76	0.74
	± 0.07	± 0.07	± 0.05	± 1.54	± 3.33	± 0.07	± 0.08	± 1.32	± 0.11

^a Best cell; ^b average on 8 cells; ^c standard deviation of the average.

To improve the perovskite layer quality, another strategy consists in incorporating additives or solvents to the perovskite precursor solution. Inorganic acids such as HI and HCl were reported to improve coverage of perovskite film due to the better solubility of the materials, and the possible reaction of the acid with PbI₂ or PbCl₂ to form an intermediate that adjusts the crystallization kinetics.⁷ Besides, the Lewis acid-base adduct approach consists in adding polar aprotic solvent such as pyridine or DMSO, into the perovskite precursor solution. It could interact with the PbI₂ or PbCl₂ and form an adduct, which results in a better control of the perovskite crystallization.⁸ Water additive has also been shown to improve the perovskite quality particularly when processed in atmosphere.⁹ Finally, a range of alkyl halide additives were incorporated to the perovskite precursor solution to enhance perovskite covering and efficiency of PSCs. This effect was attributed to the

participation of the halogens to the perovskite growth *via* chelation with Pb^{2+} which is modulated by the steric effect of the alkyl chain length.¹⁰ Therefore, the effect of several additives, including HCl, H_2O , pyridine (PYR), DMSO, 1,8-diiodooctane (DIO), 1-bromooctane (1BO) and 1-bromobutane (1BB), on the perovskite coverage and PV performances has been investigated.

The perovskite morphologies were observed by SEM (Figure 33). For H_2O , PYR, DMSO, DIO, and especially HCl, perovskite island size was enlarged and seemed closer to each other, meaning that surface coverage is improved. For 1BO, a dense network of grain-like perovskite was formed, while for 1BB, perovskite looked porous and did not cover completely the TiO_2 layer. Therefore, absorption of the perovskite was improved by the addition of HCl or 1BO (Figure 34).

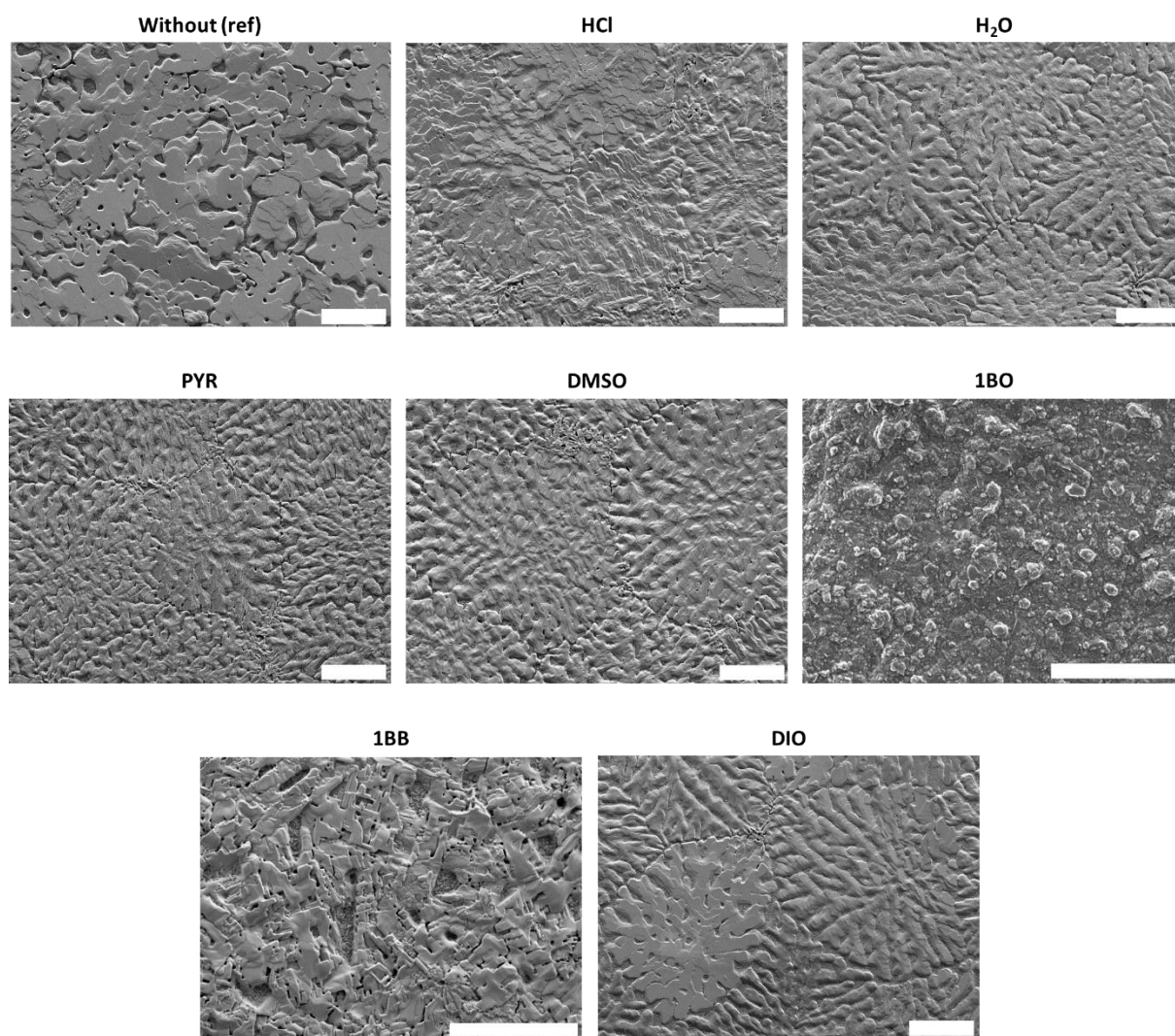


Figure 33. SEM surface images of FTO/ TiO_2 /perovskite from perovskite solutions containing 1 wt.% of additive.

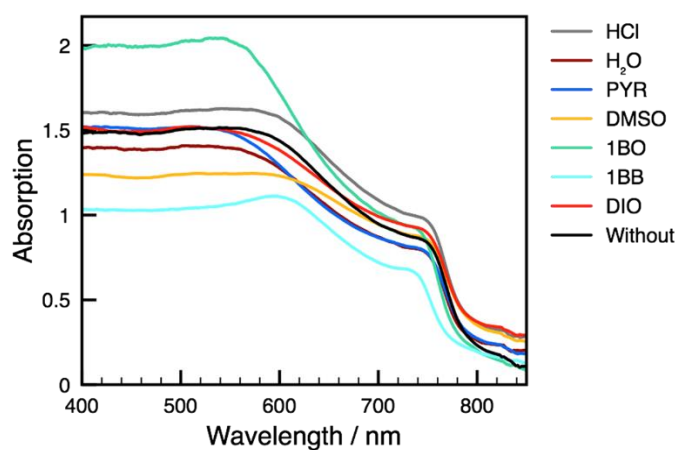


Figure 34. Effect of additives on the perovskite absorption.

However, none of the additive enhanced PV performances (Table 8). HCl, 1BB and pyridine devices showed a current excess for their reverse scan that could lead to an overestimation of the FF (Figure 35). Thereby, a best PCE about 14 % was obtained when pyridine was used as additive.

Table 8. Best PV performances and hysteresis index of PSCs containing additives.

Additive	Reverse scan				Forward scan				HI
	J_{sc}	V_{oc}	FF	PCE	J_{sc}	V_{oc}	FF	PCE	
	$mA.cm^{-2}$	V		%	$mA.cm^{-2}$	V		%	
HCl	14.81	0.91	0.91	12.27	13.56	0.69	0.21	1.95	0.84
H ₂ O	19.24	0.76	0.54	7.90	17.40	0.50	0.23	1.98	0.75
PYR	20.62	0.92	0.74	14.04	19.94	0.75	0.31	4.62	0.67
DMSO	16.80	0.81	0.54	7.31	15.65	0.63	0.22	2.11	0.71
1BO	20.74	0.85	0.64	11.28	19.04	0.53	0.20	2.02	0.82
1BB	13.25	0.89	0.94	10.98	11.97	0.62	0.20	1.50	0.86
DIO	19.02	0.74	0.62	8.76	12.80	0.52	0.14	0.94	0.89

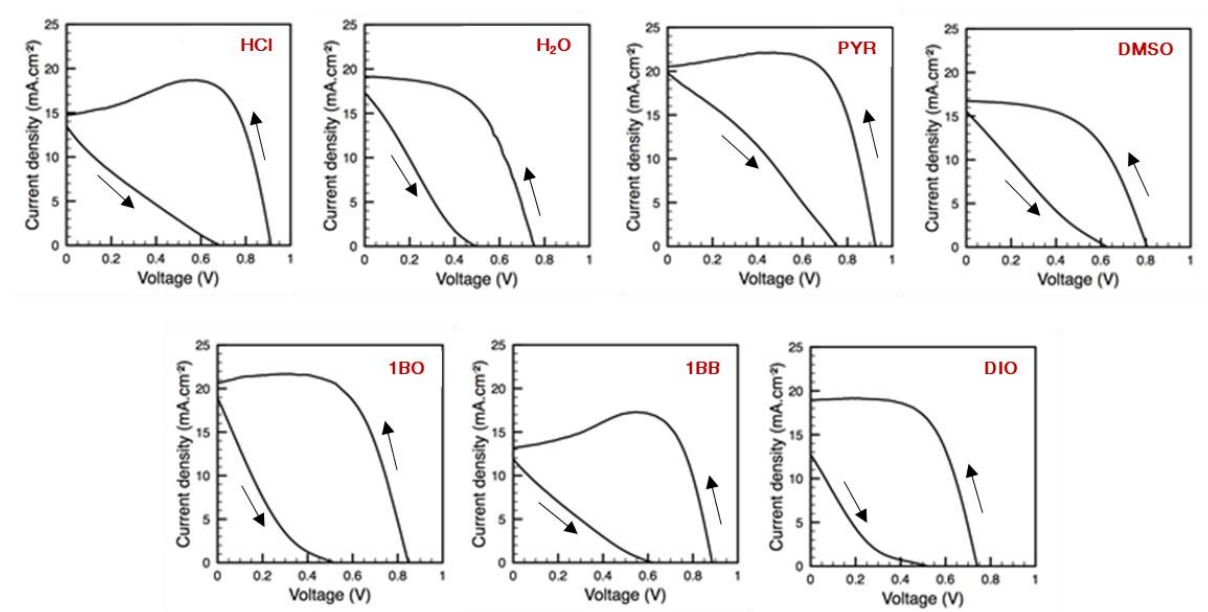


Figure 35. Best I-V curves of PSCs including additives in their preparation.

XRD measurement was performed on the best performing perovskite, *i.e.* without additives. The position of the peaks attributed to the perovskite and the absence of reflection peaks around 24° and 30° reveal a cubic phase.¹¹ No peak associated to PbI_2 at around 11° was found, indicating the full conversion of PbI_2 into perovskite. Peaks at around 25° and 36° were attributed to anatase TiO_2 polymorph.

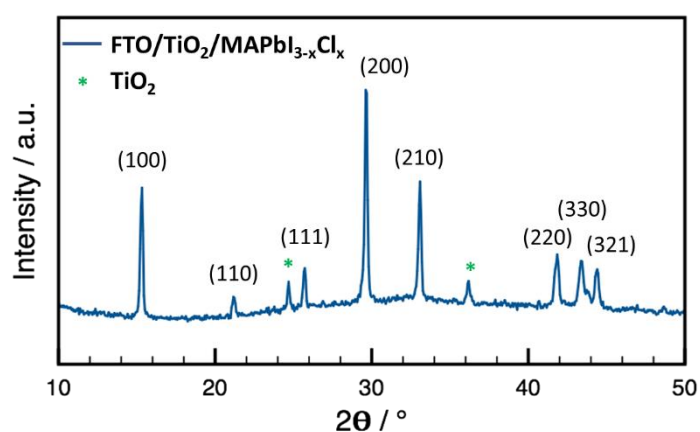


Figure 36. XRD pattern of $\text{MAPbI}_{3-x}\text{Cl}_x$ coated on FTO/TiO_2 .

2.3 Reference PV performances of planar perovskite solar cells

In summary, the main preparation steps leading to the reference n-i-p planar PSCs involve: i) UV-ozone treatment of the FTO substrates; ii) deposition of the bI-TiO_2 layer by spin-coating of a TiAcAc solution followed by calcination in air; iii) post-treatment with TiCl_4 ; iv) formation of the $\text{MAPbI}_{3-x}\text{Cl}_x$ layer by spin-coating of a MAI/PbCl_2 solution followed by annealing at 120°C ; iv) deposition of the HTM layer by spin-coating from a spiro-OMeTAD solution doped with LiTFSI and tBP; v) evaporation of gold contacts. The as-prepared n-i-p planar PSC exhibited a maximum PCE of 16.0 % and an average PCE of 14.1 % (Table 9). Hysteresis is still quite large for the device while reproducibility is acceptable (Figure 37).

Table 9. Best and average PV performances and hysteresis index of the reference n-i-p planar PSCs.

HTM	Reverse scan				Forward scan				HI
	J_{sc}	V_{oc}	FF	PCE	J_{sc}	V_{oc}	FF	PCE	
	mA.cm^{-2}	V		%	mA.cm^{-2}	V		%	
Spiro-OMeTAD	20.61 ^a	1.08	0.72	15.99	20.74	0.96	0.50	10.00	0.37
	20.72 ^b	1.00	0.68	14.11	21.11	0.86	0.35	6.42	0.57
	$\pm 0.44^c$	± 0.05	± 0.05	± 1.36	± 0.97	± 0.10	± 0.13	± 2.75	± 0.18

^a Best cell; ^b average on 8 cells; ^c standard deviation of the average.

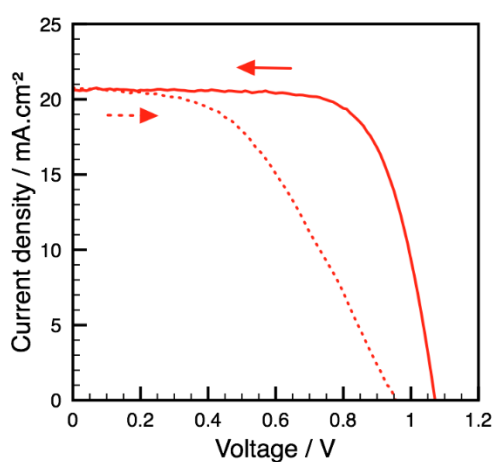


Figure 37. I-V curves of the best performing n-i-p planar device.

3 Mesoscopic perovskite solar cells

3.1 Fabrication of mesoscopic perovskite solar cells

More elaborated mesoscopic PSCs were fabricated, benefiting from device optimizations in the perovskite community. Thereby, TiO_2 blocking (bl- TiO_2) layer has been optimized by introducing lithium, from LiTFSI, and magnesium, from $\text{Mg}(\text{TFSI})_2$. Magnesium has been demonstrated to shift the fermi level of TiO_2 in favourable configuration to decrease resistivity and enhance electron collection,¹² while lithium reduced electronic trap states and accelerated electron transport.¹³ Consequently, combination of these two metals should improve PCE and decrease hysteresis. As well, mesoporous TiO_2 (mp- TiO_2) layer was treated with LiTFSI salt to improve electron extraction.¹⁴ Mixed cation and mixed halide lead-based perovskite material was chosen as active material. $\text{MA}_{0.15}\text{FA}_{0.85}\text{PbBr}_{0.45}\text{I}_{2.55}$ is now largely employed in highly efficient PSCs owing to a compromise between a broad absorption range relying on Br^- , and an improved stability brought by FA^+ . Performances were further enhanced by the introduction of potassium, from KI, which was found to better align the conduction band of the perovskite with the one the TiO_2 and to reduce defects into the perovskite layer.¹⁵ The perovskite layer was deposited by the anti-solvent spin-coating method. Formulation of spiro-OMeTAD still contained LiTFSI and tBP dopants. From the mp- TiO_2 deposition step, the fabrication was realized in dry conditions. The fabrication steps and the energy diagram of mesoscopic PSCs are depicted in Figure 38 and Figure 39.

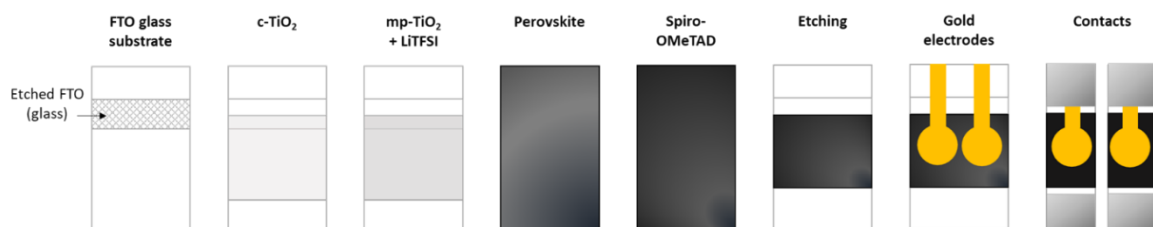


Figure 38. Fabrication steps of mesoscopic PSCs.

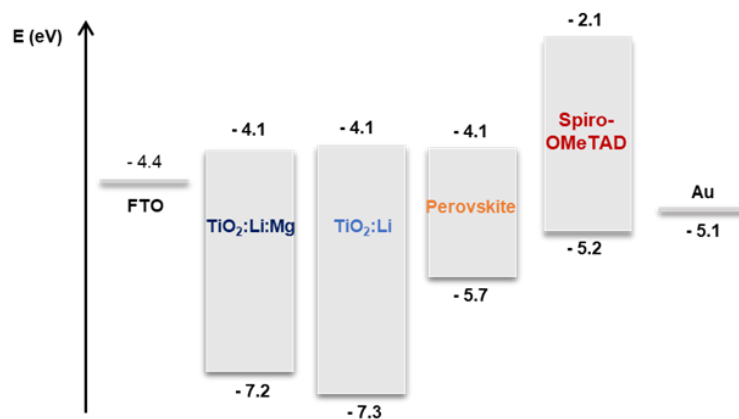


Figure 39. Energy diagram of the mesoscopic PSCs.

3.2 Reference PV performances of mesoscopic perovskite solar cells

High efficiencies, over 18 % without ageing, with relatively good reproducibility were obtained with this process (Table 10). Since this was the range of efficiencies typically reached with this recipe, no further optimization of the process was performed. Hysteresis was considerably reduced compared to regular planar PSCs. Potassium-free PSCs were fabricated and compared to doped ones to evidence the crucial role of potassium in the device hysteresis (Table 10, Figure 40). The larger hysteresis of the undoped PSCs is characterized by a lower V_{oc} (1.05 vs. 1.10 V) and especially a lower FF (0.44 vs. 0.53) for the forward scan. According to Tang et. al., hysteresis can be minimized through the addition of KI by limiting defects and extending carrier lifetime into the perovskite crystal.¹⁵

Table 10. Best and average PV performances of doped and undoped PSCs with K^+ .

	Reverse scan				Forward scan				HI
	J_{sc}	V_{oc}	FF	PCE	J_{sc}	V_{oc}	FF	PCE	
	$mA.cm^{-2}$	V		%	$mA.cm^{-2}$	V		%	
w/o K^+	22.76	1.10	0.74	18.33	22.94	1.06	0.53	12.93	0.295
	22.72	1.09	0.71	17.48	22.82	1.05	0.44	10.63	0.397
	$\pm 0.08^*$	± 0.01	± 0.03	± 0.93	± 0.10	± 0.02	± 0.10	± 2.63	± 0.122
with K^+	22.45	1.10	0.73	18.44	22.71	1.10	0.71	17.71	0.039
	22.31	1.11	0.73	18.12	22.65	1.10	0.70	17.46	0.037
	$\pm 0.25^*$	± 0.01	± 0.02	± 0.55	± 0.23	± 0.01	± 0.03	± 0.71	± 0.013

*Average of 10 PSCs.

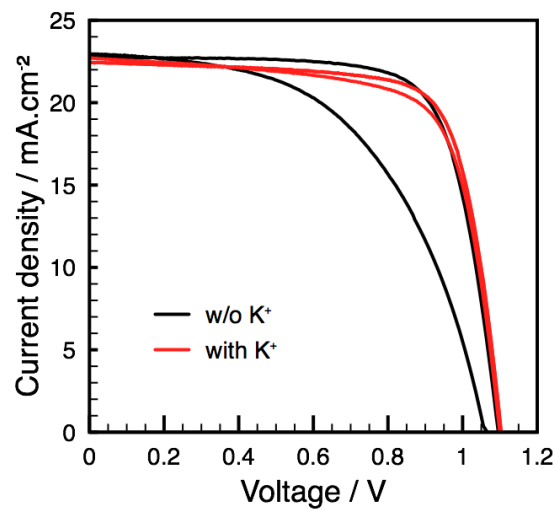


Figure 40. Best I-V curves of doped and undoped PSCs with K^+ .

4 Inverted Perovskite Solar Cells

4.1 Fabrication steps

p-i-n Inverted PSCs were elaborated on ITO substrates since the fabrication steps did not imply high temperature processes. PEDOT:PSS and PC₆₀BM were chosen for the hole and the electron collection respectively. Perovskite was made from PbI₂ and MAI, and deposited by the anti-solvent spin-coating method. The whole device was processed in N₂ glovebox. Processes were also optimized in order to make semi-transparent PSCs. The fabrication process and the energy diagram of inverted PSCs are described in Figure 41 and Figure 42.

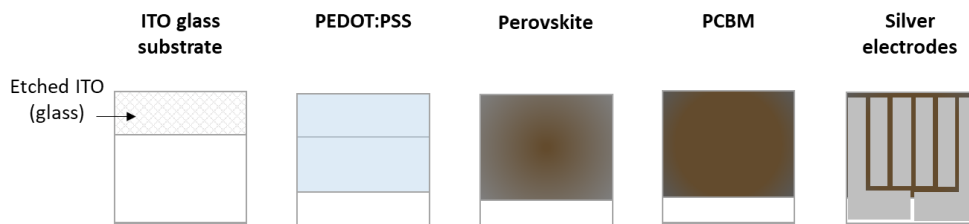


Figure 41. Fabrication steps of inverted PSCs.

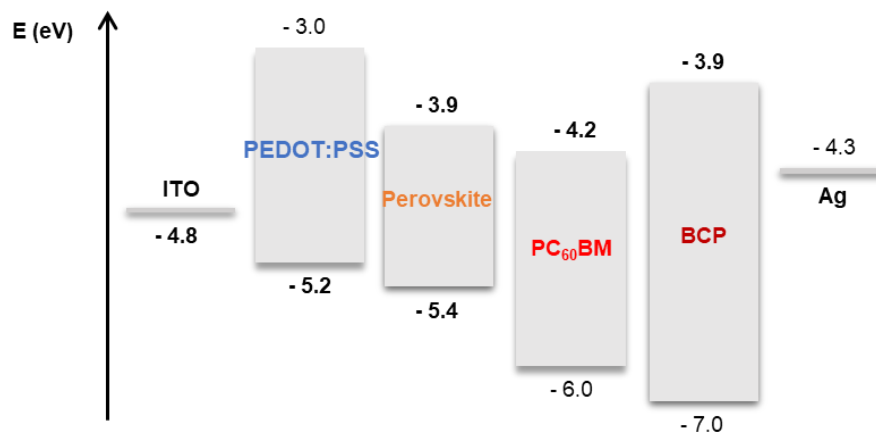


Figure 42. Energy diagram of inverted PSCs.

4.2 Optimizations of the process

Before making PSCs, several perovskite precursor solutions have been tested to obtain a dense perovskite layer on PEDOT:PSS. Three formulations, detailed in Table 12, have been studied. Formulation A consisted in simply dissolving PbI₂ and MAI in DMF as reported in many papers. Besides, the Lewis acid-base adduct approach was developed to improve the perovskite quality. Moreover, DMF was found to possibly alter the PEDOT:PSS layer. Therefore, two other formulations

have been tested: B containing γ -butyrolactone (GBL), DMSO, and N-methyl-2-pyrrolidone (NMP), and C a mixture of DMF and DMSO.

Table 11. Perovskite formulations.

Formulation	Perovskite material	Solvent/Additive	Anti-solvent
A	PbI ₂ :MAI (1:1)	DMF (54 wt.%)	Chlorobenzene
B	PbI ₂ :MAI (1:1)	GBL:DMSO (7:3 vol.) + 5 vol.% NMP (35 wt.%)	Chlorobenzene
C	PbI ₂ :MAI (1:1)	DMF:DMSO (9:1 vol.)	Chlorobenzene

The morphologies of the films formed on top of PEDOT:PSS were revealed by AFM and depicted in Figure 43. Formulation A and B formed needle-like perovskites while homogeneous grains were formed with formulation C. The shape and the size of the grains obtained in formulation C were further revealed by the amplitude AFM image in Figure 43d. The needle-like structure could be due to the different crystallization kinetics between PbI₂ and MAI. The formation of the MAI-PbI₂-DMSO adduct in the formulation C allows the compounds to crystallize at the same time and to form smooth perovskite grains.

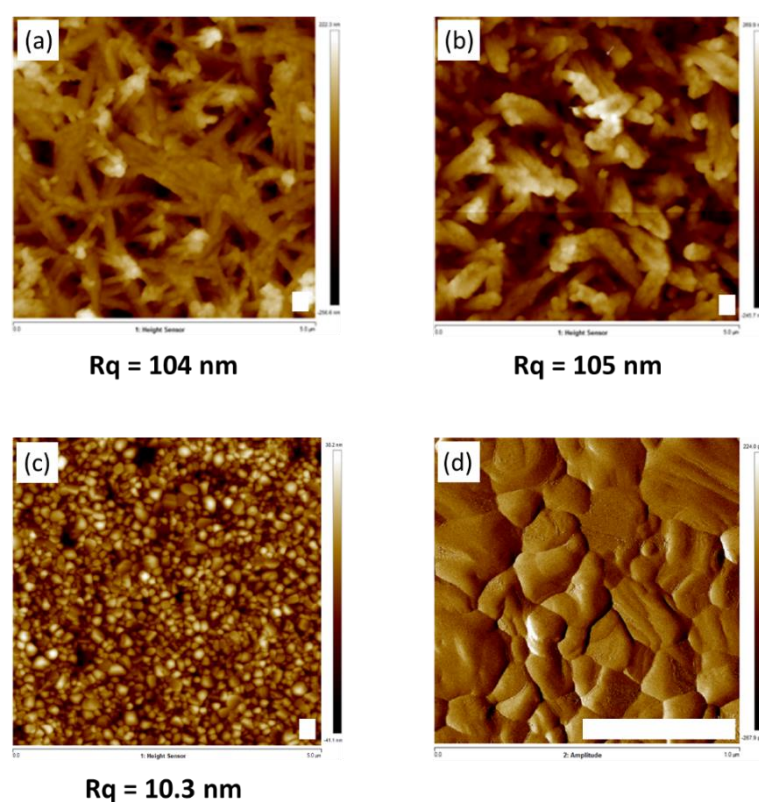


Figure 43. AFM images and corresponding roughness of perovskite films from (a) solution A, (b) solution B, and (c, d) solution C. Scale bar = 500 nm.

The final perovskite from formulation C was characterized by XRD. All of the observable peaks are associated to the perovskite cubic phase.¹¹ No peak at around 11° that could be attributed to PbI_2 was found, meaning that the conversion of PbI_2 into hybrid perovskite is complete.

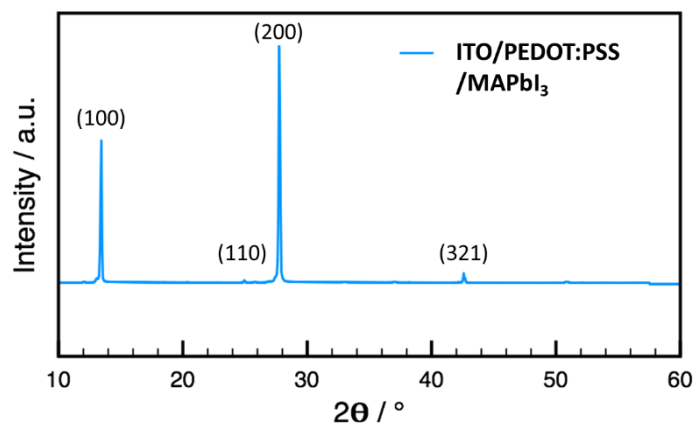


Figure 44. XRD pattern of the best performing perovskite coated on ITO/PEDOT:PSS.

Secondly, layer thicknesses were optimized into PSCs (Figure 45). If not mentioned, I-V curves and PV performances refer to forward scans, which gave higher efficiencies than reverse scans. PEDOT:PSS and PC_{60}BM thicknesses were varied with the spin coating speed. The perovskite thickness was changed with the concentration of the precursor solution. Thicknesses were determined with a profilometer. Optimal thicknesses for inverted PSCs were 50 nm for the PEDOT:PSS, about 400 nm for the perovskite and about 30 nm for the PC_{60}BM .

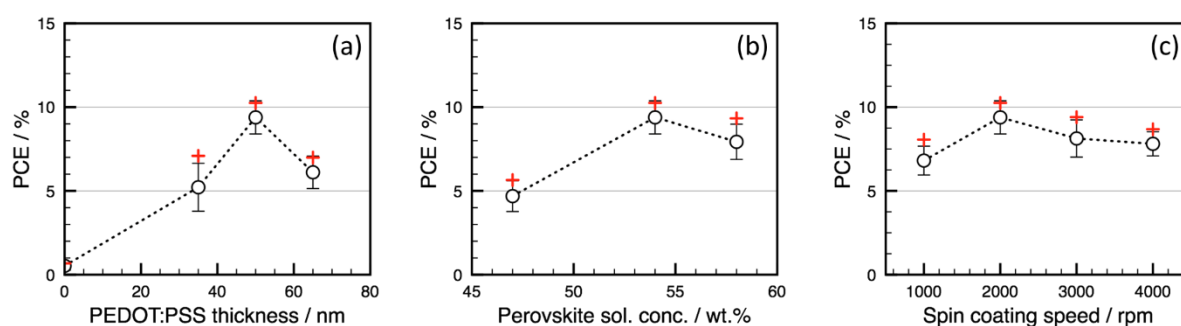


Figure 45. PCE of inverted solar cells according to (a) PEDOT:PSS thickness, (b) perovskite solution concentration, and (c) PC_{60}BM spin coating conditions. Red cross = maximum PCE; black circles = average PCE (8 cells).

PEDOT:PSS was formulated with 5 % of DMSO and 0.04 % of zonyl to improve the conductivity and the homogeneity of the film.¹⁶ Compared to pristine PEDOT:PSS, formulated PEDOT:PSS gave in PSCs significantly higher V_{oc} and led to reduced the hysteresis (Table 12).

Table 12. Best and average PV performances of inverted PSCs based on pristine and formulated PEDOT:PSS.

PEDOT:PSS	Reverse scan				Forward scan				HI
	J_{sc}	V_{oc}	FF	PCE	J_{sc}	V_{oc}	FF	PCE	
	$mA.cm^{-2}$	V		%	$mA.cm^{-2}$	V		%	
Pristine	19.81	0.67	0.49	6.64	20.50	0.82	0.59	10.25	-0.54
	20.36	0.78	0.47	7.65	20.59	0.83	0.54	9.39	-0.26
	± 0.90	± 0.11	± 0.05	± 1.88	± 0.98	± 0.03	± 0.06	± 0.99	± 0.24
Formulated	20.59	0.92	0.45	8.98	20.97	0.92	0.53	10.53	-0.17
	20.51	0.91	0.44	8.36	20.17	0.92	0.53	10.01	-0.20
	± 0.60	± 0.02	± 0.03	± 0.61	± 0.83	± 0.02	± 0.03	± 0.61	± 0.08

Bathocuproine (BCP) is currently used as buffer layer between the ETL and the top electrode to help extraction of electrons in inverted PSCs.¹⁷ BCP can be deposited either by spin-coating or by evaporation. These two methods were compared in our devices (Figure 46a). According to the reported process, BCP spin coated layer should be around 10 nm.¹⁸ The BCP thickness was easier to control by evaporation and remained uncertain by spin-coating. Thus, when comparing the two processes, the possible thickness difference has to be considered too. Best PCE was obtained by spin-coating the BCP layer. Average PCE without and with spin-coated BCP were similar. The optimal BCP thickness was obtained by varying the spin-coater speed (Figure 46b). The PCE decreased together with the BCP thickness, meaning that BCP is actually deposited despite the low concentration high spin-coater speed. On the other hand, evaporation of BCP was macroscopically not homogeneous. This could explain lower PCEs (Figure 47).

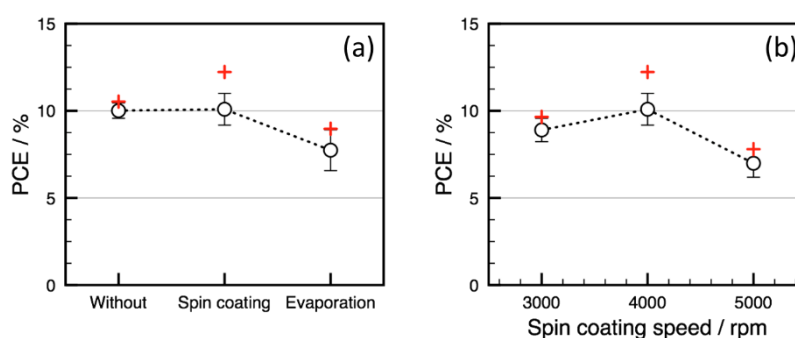


Figure 46. PCE of inverted PSCs according to (a) the deposition method of BCP, and (b) the spin coating parameters of BCP. Red cross = maximum PCE; black circles = average PCE (8 cells).

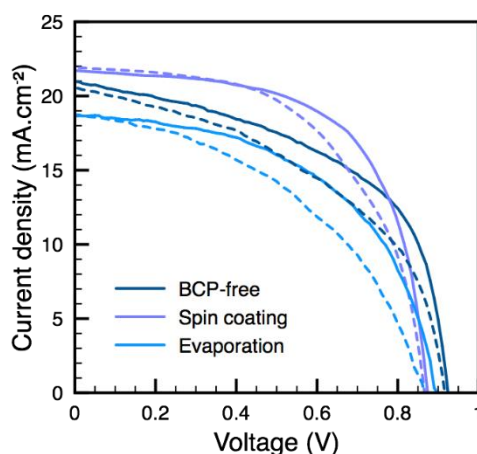


Figure 47. Best I-V curves of BCP free, spin-coated BCP and evaporated BCP PSCs. Full line = forward scan; dotted line = reverse scan.

4.3 Reference PV performances of planar perovskite solar cells

Finally, the best PSC exhibited an efficiency of 12.23 %. Best and average (20 cells) PV performances of our reference inverted PSCs are reported in Table 13. Compared to the state-of-the-art inverted PSCs, V_{oc} and FF are quite low. Hysteresis is still present and characterized by lower J_{sc} and FF for the reverse scan.

Table 13. PV characteristics of reference inverted PSCs.

HTM	Reverse scan				Forward scan				HI
	J_{sc}	V_{oc}	FF	PCE	J_{sc}	V_{oc}	FF	PCE	
	$mA.cm^{-2}$	V		%	$mA.cm^{-2}$	V		%	
PEDOT:PSS	21.95	0.87	0.56	10.86	21.68	0.88	0.63	12.23	-0.13
	18.23	0.83	0.50	7.72	19.36	0.87	0.59	10.09	-0.35
	± 2.69	± 0.05	± 0.07	± 1.77	± 1.88	± 0.03	± 0.04	± 0.91	± 0.20

EQE of the best device was also recorded (Figure 48). The peak at around 350 nm could be attributed to the PbI_2 resulting from the degradation of perovskite. The extracted J_{sc} , i.e. $13.30 mA.cm^{-2}$, was lower than that expected, i. e. over $21 mA.cm^{-2}$ (Table 13). This could be explained by the EQE lamp that illuminated only a part of the cell without using a mask. The non-illuminated part may act as a shunting load, resulting in lower photocurrent.¹⁹

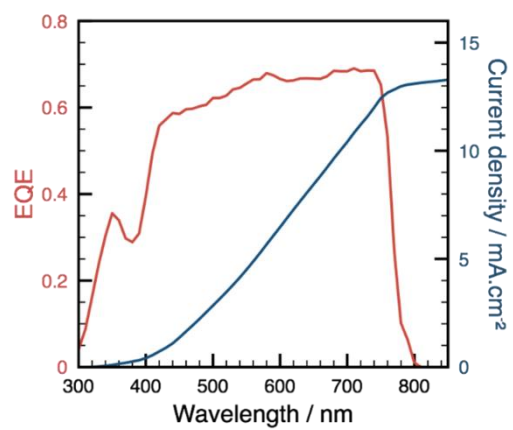


Figure 48. EQE and extracted J_{sc} of the reference inverted PSC.

Conclusion

This chapter described the fabrication steps and optimizations brought to the three types of PSCs considered.

The first architecture optimized was the n-i-p planar. The main challenge was to find the best conditions to minimize the hysteresis and maximize the efficiency through optimizations of the TiO_2 layer and of the perovskite layer. Compromise between perovskite coverage and perovskite crystal quality was necessary. In optimal conditions, a best power conversion efficiency (PCE) of 15.99 % was reached. This solar cells will be used in Chapter 3 to introduce new functionalized polyvinylcarbazole.

Secondly, n-i-p mesoscopic PSCs were fabricated. The maximum PCE achieved was 18.44 % with a significantly reduced hysteresis. The better performances compared to n-i-p planar devices are attributed to the mesoscopic TiO_2 layer that helps for the electron extraction, to the mixed $\text{MA}_{0.15}\text{FA}_{0.85}\text{PbI}_{2.55}\text{Br}_{0.45}$ perovskite properties and to the doping of the materials. Doping TiO_2 with LiTFSI and $\text{Mg}(\text{TFSI})_2$, and the perovskite with K^+ tune the energetic properties of the materials in a favourable way for the solar cell operation. These devices will be used in Chapter 3 to introduce the most promising polyvinylcarbazole derivative studied in planar configuration, and in Chapter 4 to incorporate novel polyelectrolytes as HTMs or as dopant.

Through process optimization, the best PCE reached in inverted PSCs was 12.2 % with a reasonable hysteresis. These performances are quite far from the actual state-of-the-art (> 20 %) and could be further optimized via materials and device engineering. These devices will be used in Chapter 5 to investigate the possibility to be used as semi-transparent devices.

References

1. Unger, E. L.; Bowring, A. R.; Tassone, C. J.; Pool, V. L.; Gold-Parker, A.; Cheacharoen, R.; Stone, K. H.; Hoke, E. T.; Toney, M. F.; McGehee, M. D., Chloride in Lead Chloride-Derived Organo-Metal Halides for Perovskite-Absorber Solar Cells. *Chemistry of Materials* **2014**, 26 (24), 7158-7165.
2. Leem, J.; Park, I.; Li, Y., ; Zhou, W.; Jin, Z.; Shin, S.; Min, Y.-S., Role of HCl in Atomic Layer Deposition of TiO₂ Thin Films from Titanium Tetrachloride and Water. *Korean Chem. Soc.* **2014**, 35 (4), 1195.
3. Wang, Y.-Q.; Xu, S.-B.; Deng, J.-G.; Gao, L.-Z., Enhancing the efficiency of planar heterojunction perovskite solar cells via interfacial engineering with 3-aminopropyl trimethoxy silane hydrolysate. *Royal Society open science* **2017**, 4 (12), 170980-170980.
4. O'Regan, B. C.; Durrant, J. R.; Sommeling, P. M.; Bakker, N. J., Influence of the TiCl₄ Treatment on Nanocrystalline TiO₂ Films in Dye-Sensitized Solar Cells. 2. Charge Density, Band Edge Shifts, and Quantification of Recombination Losses at Short Circuit. *The Journal of Physical Chemistry C* **2007**, 111 (37), 14001-14010.
5. Jiang, Q.; Zhang, X.; You, J., SnO₂: A Wonderful Electron Transport Layer for Perovskite Solar Cells. *Small* **2018**, 14 (31), 1801154.
6. Duan, J.; Xiong, Q.; Feng, B.; Xu, Y.; Zhang, J.; Wang, H., Low-temperature processed SnO₂ compact layer for efficient mesostructure perovskite solar cells. *Applied Surface Science* **2017**, 391, 677-683.
7. Li, Y.; Ji, L.; Liu, R.; Zhang, C.; Mak, C. H.; Zou, X.; Shen, H.-H.; Leu, S.-Y.; Hsu, H.-Y., A review on morphology engineering for highly efficient and stable hybrid perovskite solar cells. *Journal of Materials Chemistry A* **2018**, 6 (27), 12842-12875.
8. Lee, J.-W.; Kim, H.-S.; Park, N.-G., Lewis Acid–Base Adduct Approach for High Efficiency Perovskite Solar Cells. *Accounts of Chemical Research* **2016**, 49 (2), 311-319.
9. He, T.; Liu, Z.; Zhou, Y.; Ma, H., The stable perovskite solar cell prepared by rapidly annealing perovskite film with water additive in ambient air. *Solar Energy Materials and Solar Cells* **2018**, 176, 280-287.
10. Chueh, C.-C.; Liao, C.-Y.; Zuo, F.; Williams, S. T.; Liang, P.-W.; Jen, A. K. Y., The roles of alkyl halide additives in enhancing perovskite solar cell performance. *Journal of Materials Chemistry A* **2015**, 3 (17), 9058-9062.
11. Luo, S.; Daoud, W. A., Crystal Structure Formation of CH₃NH₃PbI(3-x)Cl(x) Perovskite. *Materials (Basel, Switzerland)* **2016**, 9 (3), 123.
12. Zhang, H.; Shi, J.; Xu, X.; Zhu, L.; Luo, Y.; Li, D.; Meng, Q., Mg-doped TiO₂ boosts the efficiency of planar perovskite solar cells to exceed 19%. *Journal of Materials Chemistry A* **2016**, 4 (40), 15383-15389.
13. Liu, D.; Li, S.; Zhang, P.; Wang, Y.; Zhang, R.; Sarvari, H.; Wang, F.; Wu, J.; Wang, Z.; Chen, Z. D., Efficient planar heterojunction perovskite solar cells with Li-doped compact TiO₂ layer. *Nano Energy* **2017**, 31, 462-468.
14. Giordano, F.; Abate, A.; Correa Baena, J. P.; Saliba, M.; Matsui, T.; Im, S. H.; Zakeeruddin, S. M.; Nazeeruddin, M. K.; Hagfeldt, A.; Graetzel, M., Enhanced electronic properties in mesoporous

TiO₂ via lithium doping for high-efficiency perovskite solar cells. *Nature Communications* **2016**, 7, 10379.

15. Tang, Z.; Bessho, T.; Awai, F.; Kinoshita, T.; Maitani, M. M.; Jono, R.; Murakami, T. N.; Wang, H.; Kubo, T.; Uchida, S.; Segawa, H., Hysteresis-free perovskite solar cells made of potassium-doped organometal halide perovskite. *Scientific Reports* **2017**, 7 (1), 12183.

16. Hofmann, A., Aqueous dispersions of conducting polymers for opto-electronic applications. . *PhD Thesis, Université de Bordeaux* **2016**.

17. Yoshida, H., Electron Transport in Bathocuproine Interlayer in Organic Semiconductor Devices. *The Journal of Physical Chemistry C* **2015**, 119 (43), 24459-24464.

18. Chen, C.; Zhang, S.; Wu, S.; Zhang, W.; Zhu, H.; Xiong, Z.; Zhang, Y.; Chen, W., Effect of BCP buffer layer on eliminating charge accumulation for high performance of inverted perovskite solar cells. *RSC Advances* **2017**, 7 (57), 35819-35826.

19. Scheer, R.; Schock, H.-W., *Chalcogenide Photovoltaics: Physics, Technologies, and Thin Film Devices*. Wiley ed.; 2011; p 384.

Chapter 3

Functionalized-Polyvinylcarbazoles as Hole Transporting Materials

Modified poly(9-vinylcarbazole)s were investigated as hole transporting materials for n-i-p planar and mesoscopic hybrid perovskite solar cells. Opto-electronic and charge transport properties of the polymers were studied prior to be incorporated into solar cells. PV performances of the corresponding devices were compared to the standard PSCs using spiro-OMeTAD as hole transporter.

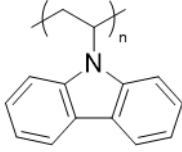
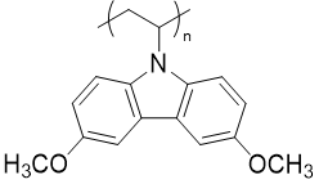
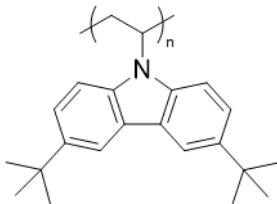
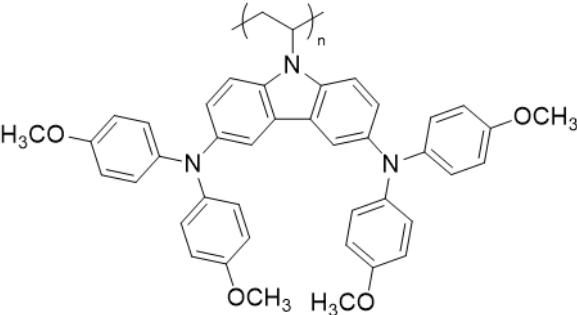
1 Introduction

As presented in the first Chapter, the HTM is a key material ruling both performance and stability of PSCs. Essential for efficient extraction of holes, it also prevents perovskite from degradation induced by ambient air and humidity. One of the most studied and effective HTM reported is the spiro-OMeTAD. However, due to burdensome synthesis and purification methods, this material is relatively expensive. Moreover, its limited stability makes it unsuitable for industrial scale production.¹ Therefore, new HTMs, either organic or inorganic, have been investigated to replace spiro-OMeTAD.²

Some of them include small carbazole-based molecules, like X51 (9,9'-([1,1'-biphenyl]-4,4'-diyl)bis(N3,N3,N6,N6-tetrakis(4-methoxy-phenyl)-9H-carbazole-3,6-diamine) and star-shape derivatives, which have been incorporated into PSCs.³ These materials showed similar properties to spiro-OMeTAD but their synthesis and purification remain complicated limiting, the quantities produced. Furthermore, the solar cells involving these HTMs still suffer from stability issues. On the other hand, poly(9-vinylcarbazole) (PVK) is a p-type semiconducting polymer, commercially available and easily produced in large quantities through controlled radical polymerization.⁴ Due to its stability arising from its polymeric backbone, hydrophobicity, large hole mobility and solution processability, PVK has been widely used in organic electronic devices, as light emitting diodes and organic solar cells.⁵ Recently, despite a relatively low HOMO level (-5.8 eV), PVK and PVK-based polymers were successfully introduced in PSCs. Replacing PEDOT:PSS by a thin layer of PVK led to a 15.8 % PCE in inverted structure.⁶ PVK has also been used as an interlayer between the perovskite and a triazatruxene-based HTM in order to enhance hole extraction and insulate the perovskite layer from ambient moisture, thus leading to 18.8 % PCE.⁷ Additionally, it was recently shown that hyper-branched PVKs outperform P3HT in ITO/TiO₂/perovskite/HTM/Ag structure.⁸

Thereby, three novel PVK derivatives were synthesized and studied as HTM (Table 14). Properties of PVK were tuned through functionalization. PVK-(OCH₃)₂, has methoxy substituents which have been shown to enhance the conductivity of HTMs.⁹ PVK-(tBu)₂, was functionalized with *tert*-butyl groups. Alkyl chains were expected to improve solubility and film-forming of the material.¹⁰ PVK-[N(PhOCH₃)₂]₂, which mimics spiro-OMeTAD substituents, contains triphenylamine groups that are used to bring stability and good charge transport properties in HTMs.¹¹ The properties and PV performances of the devices including these polymers as HTM were compared with those of systems using standard spiro-OMeTAD in PSCs.

Table 14. PVK derivatives studied in the following and the corresponding experimental M_n .

PVK Poly(9-vinylcarbazole)	PVK-(OCH₃)₂ Poly[(3,6-dimethoxy)-9-vinylcarbazole]
 $M_n = 2\,990 \text{ g/mol}$ $\bar{D} = 1.3$	 $M_n = 8\,500 \text{ g/mol}$ $\bar{D} = 1.2$
PVK-(tBu)₂ Poly[(3,6-di- <i>tert</i> -butyl)-9-vinylcarbazole]	PVK-[N(PhOCH₃)₂]₂ Poly[N3,N3,N6,N6-tetrakis(4-methoxyphenyl)-9-vinylcarbazole-3,6-diamine]
 $M_n = 8\,600 \text{ g/mol}$ $\bar{D} = 1.6$	 $M_n = 8\,030 \text{ g/mol}$ $M_n = 11\,730 \text{ g/mol}$ $\bar{D} = 1.3$ $\bar{D} = 1.4$

The synthesis of PVK-[N(PhOCH₃)₂]₂ has required only three steps as depicted in Scheme 1. First a well-defined polymer of controlled molecular weight was obtained through controlled radical polymerization via Reversible Addition Fragmentation Transfer (RAFT). To check the influence of the molecular weight on the properties of the functionalized polymers as well as on the performance of the solar cells, two PVK homopolymers were synthesized (PVK of 3.0 kg.mol⁻¹ or 7.0 kg.mol⁻¹). Further bromination using N-bromosuccinimide yielded the 3,6-bromo-functionalized PVKs. Finally, 4,4'-dimethoxydiphenylamine substituents were introduced via a Pd-catalyzed Buchwald-Hartwig reaction to give the target polymers PVK-[N(PhOCH₃)₂]₂ (PVK-[N(PhOCH₃)₂]₂) of 8.0 kg.mol⁻¹ and 11.7 kg.mol⁻¹). On the other hand, PVK-(tBu)₂ was synthesized from PVK (7.0 kg.mol⁻¹) by Friedel-Crafts alkylation, whereas PVK-(OCH₃)₂ was prepared from PVK-Br₂ (from PVK of 7.0 kg.mol⁻¹) by direct displacement of bromine (Figure 49).

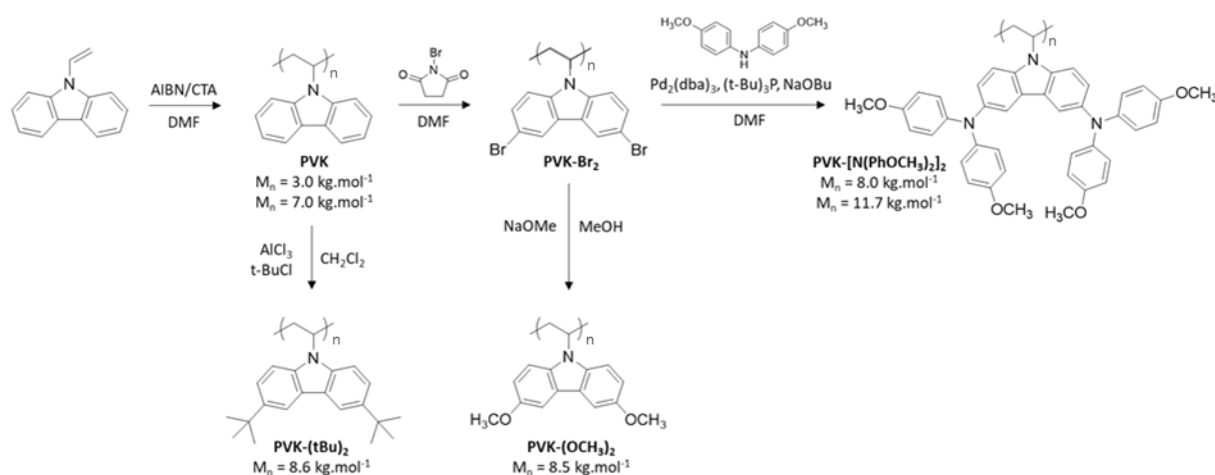


Figure 49. Synthetic routes towards PVK-(tBu)₂, PVK-(OCH₃)₂ and PVK-[N(PhOCH₃)₂]₂.

¹H NMR and FTIR analyses of all samples show a complete and successful functionalization with the typical spectroscopic features of the different moieties. The functionalization processes were also evidenced by the evolution of the molecular weight and the dispersity determined by Size Exclusion Chromatography (SEC) and the macromolecular characteristics of the products. All of the characterizations are provided in Experimental Details. Moreover, it is worth underlining the simple purification procedure used through Soxhlet extraction for PVK-[N(PhOCH₃)₂]₂, which facilitates the material production. Due to the polymeric backbone and the nature of the material, it is very easy to get rid of impurities and obtain a pure functionalized polymer.

2 Properties of the PVK derivatives

2.1 Thermal analyses

Thermal analyses, i.e. determination of the glass transition temperature (T_g) and of the degradation temperatures, were performed in order to evaluate the thermal stability of the polymers (Table 15). Thermogravimetric analyses (TGA) indicate that the polymers are rather stable, with a mass loss lower than 10 % up to 365°C (Figure 50). Differential scanning calorimetry evidences a lower glass transition temperature of PVK (203°C) as compared to PVK-[N(PhOCH₃)₂]₂ (222°C) and PVK-(OCH₃)₂ (219°C) (Figure 51). It is worth mentioning that no glass transition was observed for PVK-(tBu)₂, and neither crystallization nor melting processes occurred for all materials between 0 and 250°C.

Table 15. T_g and degradation temperature of the PVK derivatives.

Polymer	T_g °C	Degradation temperature ^a °C
PVK	203	402
PVK-(OCH ₃) ₂	219	366
PVK-(tBu) ₂	- ^b	416
PVK-[N(PhOCH ₃) ₂] ₂ (8.0 kg.mol ⁻¹)	222	419

^a 10 % mass loss; ^b No T_g between 0 and 250°C.

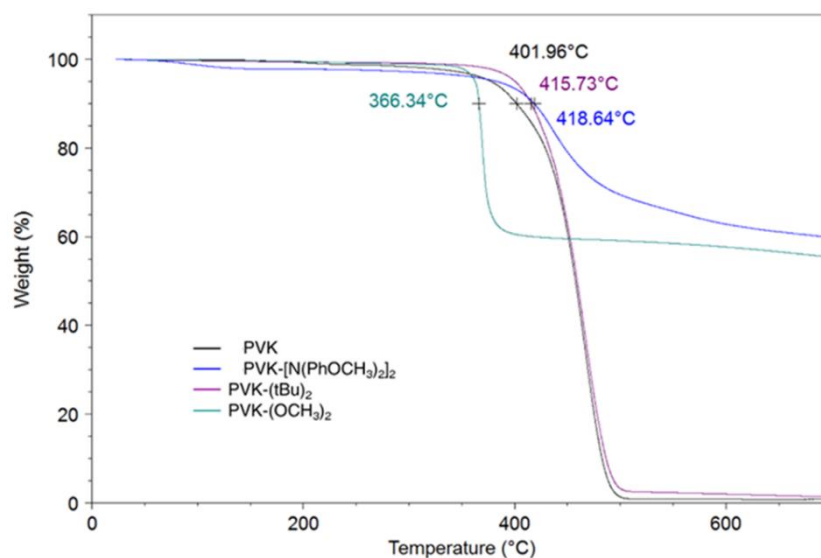


Figure 50. TGA analysis of the PVK and PVK-(tBu)₂ in ambient atmosphere and, PVK-(OCH₃)₂ and PVK-[N(PhOCH₃)₂]₂ in inert atmosphere.

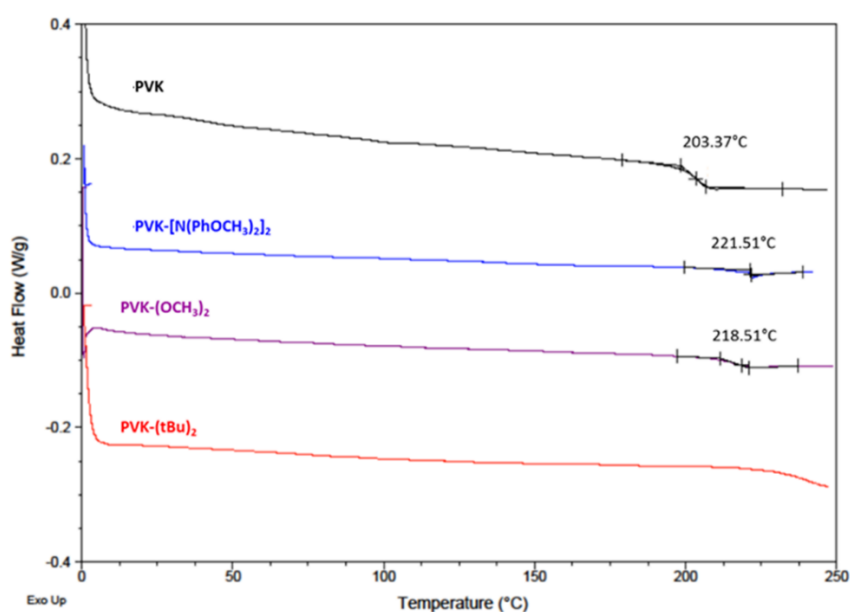


Figure 51. DSC scans of the PVK derivatives.

2.2 Solubility

Polymer solubility was tested in polar and non-polar solvents at a concentration of 50 mg/mL (Table 16). Non-polar solvents such as chlorobenzene, toluene or diethyl ether are suitable for the depositions of HTM since they cannot dissolve the perovskite. On the contrary, perovskite layer can be altered by polar solvents like acetonitrile, acetone or alcohols. All polymers were soluble in chlorobenzene, and thus can be deposited on top of the perovskite. We notice that the dimethoxyphenylamine moieties of PVK-[N(PhOCH₃)₂]₂ improve the solubility of PVK in several polar solvents.

Table 16. Solubility of the polymers in different solvents.

Solvent		PVK	PVK-(OCH ₃) ₂	PVK-(tBu) ₂	PVK-[N(PhOCH ₃) ₂] ₂ (8.0 kg.mol ⁻¹)
Non-polar	Toluene	+	+	+	+
	Chlorobenzene	+	+	+	+
	Chloroform	+	+	+	+
	Dichloromethane		+	+	+
Polar	Acetone	-	+	-	-
	DMF		-	-	+
	DMSO		-	-	+
	Acetonitrile	-	-	-	+
	Ethanol	-	-	-	-
	Methanol	-	-	-	-

2.3 Opto-electronic properties

Absorption and emission spectra of polymer solutions of 0.01 % in THF were recorded (Figure 52). Excitation wavelengths of emission spectra were determined by the position of the maximum absorption peak. The optical energy bandgap (E_g) was determined by the intersection of the absorption and the emission curves, which were found to be 381, 412 and 355 nm for PVK-(OCH₃)₂, PVK-(tBu)₂ and PVK-[N(PhOCH₃)₂]₂, respectively.

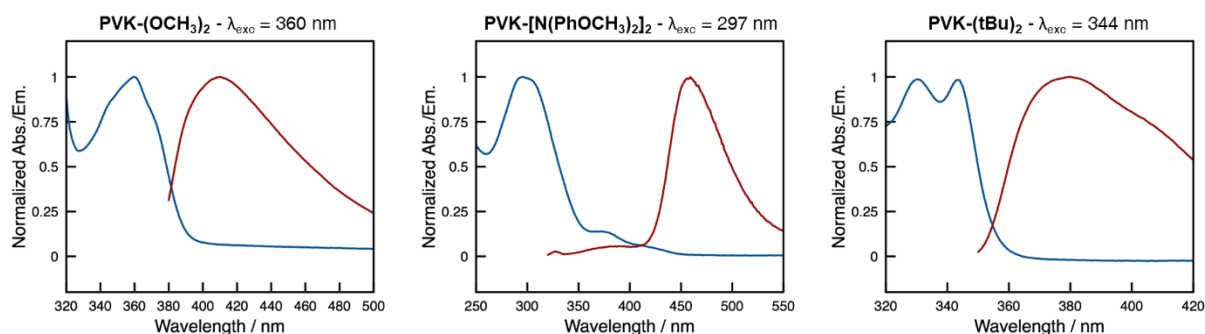


Figure 52. Absorption and emission spectra of PVK derivatives diluted in THF (0.01 %).

HOMO level of the polymers should ideally be close to - 5.4 eV, which is about the reported energy position of the perovskite maximum VB, to efficiently collect holes.¹² To evaluate the HOMO level, photoelectron spectroscopy in air (PESA) was performed on polymer thin films deposited on glass (Figure 53). HOMO levels were deduced by extrapolation of the two trend curves corresponding to the emission region and the base line. The error was estimated to be ± 0.05 eV.

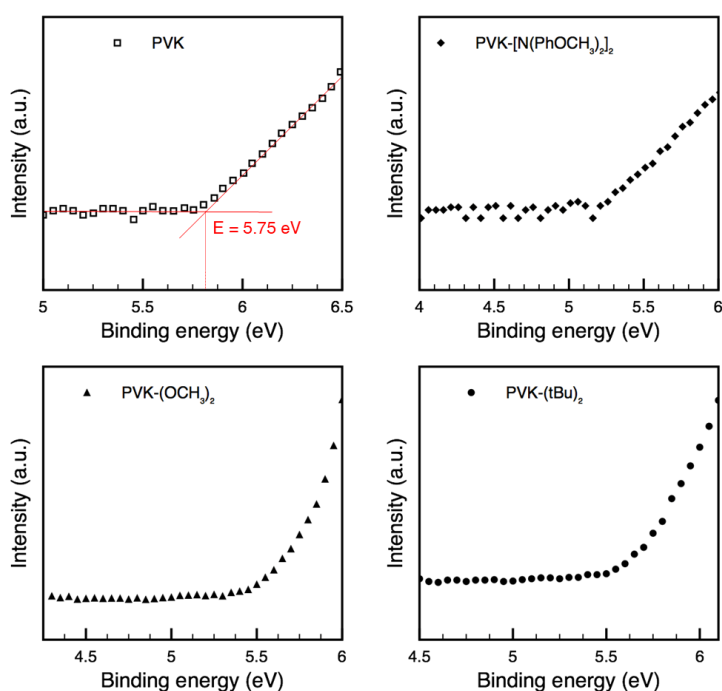


Figure 53. UP spectra in atmosphere of PVK and its derivatives.

Energy levels of the polymers are summarized in Table 17. It is noteworthy that functionalization of PVK increased the HOMO level without dramatically affecting the LUMO level. Among the different polymers, PVK-[N(PhOCH₃)₂]₂ has the most suitable HOMO level of the polymers because it is slightly

higher than the maximum VB of the perovskite. Functionalization with methoxy and *tert*-butyl moieties did not increase the HOMO level enough to make PVK-(tBu)₂ and PVK-(OCH₃)₂ in favourable energy configuration for PSC application.

Table 17. Energy levels of the PVK derivatives.

Polymer	E _g ^a eV	E _{HOMO} eV	E _{LUMO} ^b eV
PVK-(OCH ₃) ₂	3.25	- 5.52	- 2.27
PVK-(tBu) ₂	3.50	- 5.64	- 2.14
PVK-[N(PhOCH ₃) ₂] ₂ (8.0 kg.mol ⁻¹)	3.00	- 5.23	- 2.23

^a From absorption and emission spectra. ^b E_{LUMO} = E_{HOMO} + E_g.

2.4 Charge transport properties

Hole mobility represents the ability of holes to move through a material. Hole mobility was measured for the polymers by the space-charge-limited current (SCLC) method. This method allows to measure the hole mobility perpendicular to the film through a simple device architecture. The mono-polar device, *i.e.* hole-only, is composed of a thin semiconductor layer (200 nm – 2 μm) sandwiched between an injection contact and a blocking contact. Charge carrier mobility is determined by applying a voltage to the device while measuring the driven electric current. At low current, ohmic I-V characteristic is observed. When increasing the current, additional charges are injected resulting in an increase in the charge carrier density and in the current density beyond the ohmic behaviour. This creates a space-charge density distribution decreasing in the direction of the current. Assuming that charge carrier mobility is uniform and independent of electric field and charge carrier density, the Mott-Gurney law (Equation 1) is applicable to extract the charge carrier mobility.¹³

$$J = \frac{9}{8} \mu \epsilon \epsilon_0 \frac{V^2}{d^3} \quad (1)$$

where ϵ_0 is the vacuum permittivity, ϵ the permittivity and d the thickness of the semiconductor. The permittivity of organic semiconductors is roughly around 3-4. The permittivity of our materials being unknown, it was fixed at 3.5.

Hole mobility of functionalized-PVK was compared to spiro-OMeTAD. Effect of LiTFSI and tBP dopants on the hole mobility of the materials was also investigated. Dopants were incorporated in the same proportions as employed in the case of spiro-OMeTAD, *i.e.* a LiTFSI molar ratio of 0.28 and a tBP molar ratio of 3.3. The hole-only device structure was ITO/PEDOT:PSS (50 nm)/HTM (300-400 nm)/Au (80 nm). PEDOT:PSS and the HTM were deposited by spin-coating, whereas gold electrode was

thermally evaporated. I-V measurements were performed in the dark, in air, at 25°C, following a reported protocol explained in Experimental Details.^{13a} Hole mobilities are reported in Table 18.

Table 18. Hole mobility of pristine HTMs calculated from the Mott-Gurney law. The data reported are the average of 8 measurements.

HTM	Hole mobility <i>cm²/V.s</i>	
	Pure	Doped
Spiro-OMeTAD	9.52 ± 1.23 E-07	1.42 ± 0.61 E-04
PVK	1.37 ± 0.37 E-06	
PVK-(OCH₃)₂	1.52 ± 0.56 E-07	7.79 ± 0.87 E-07
PVK-(tBu)₂	5.65 ± 0.78 E-07	3.69 ± 0.52 E-07
PVK-[N(PhOCH₃)₂]₂ (8.0 kg.mol⁻¹)	1.43 ± 0.68 E-05	1.67 ± 0.32 E-03

Spiro-OMeTAD and PVK hole mobilities were found to be around 10⁻⁶ cm².V⁻¹.s⁻¹, which is in the range of the values reported in the literature for these materials.¹⁴ Methoxy and *tert*-butyl substitution resulted in a little decrease in hole mobility, while the dimethoxyphenylamine substituted PVK was found to have an enhanced hole mobility, an order of magnitude higher compared to PVK and spiro-OMeTAD. On the other hand, only the hole mobility of PVK-[N(PhOCH₃)₂]₂ was improved upon the addition of dopants. LiTFSI and tBP were found to similarly dope dimethoxyphenylamine moieties of the polymer and spiro-OMeTAD. Therefore, doped PVK-[N(PhOCH₃)₂]₂ exhibited hole mobility of 1.7 x 10⁻³ cm².V⁻¹.s⁻¹ which is one order of magnitude higher than that found for doped spiro-OMeTAD.

As organic semiconductors assume a field dependence of mobility, spiro-OMeTAD and PVK-[N(PhOCH₃)₂]₂ results were compared to another model. For materials displaying electric field dependence of mobility, the mobility is given by the Equation 2:

$$\mu = \mu_0 \exp(\gamma \sqrt{F}) \quad (2)$$

where μ_0 is the mobility at zero field, γ the field dependence of mobility and F the electric field. This field dependence effect can be related to traps or disorder. The SCLC current density is approximated by the Murgatroyd expression in Equation 3:

$$J = \frac{9}{8} \mu_0 \epsilon \epsilon_0 \frac{V^2}{d^3} \exp \left(0.891 \gamma \sqrt{\frac{V}{d}} \right) \quad (3)$$

Figure 54 represents experimental and fitted J-V² curves of pure and doped materials, and Table 19 summarized fixed and calculated parameters. Values of the mobility μ and the mobility at zero

electric field μ_0 are comparable, revealing a low field dependence of mobility. This also confirms hole mobility values calculated from the Mott-Gurney law in Table 18.

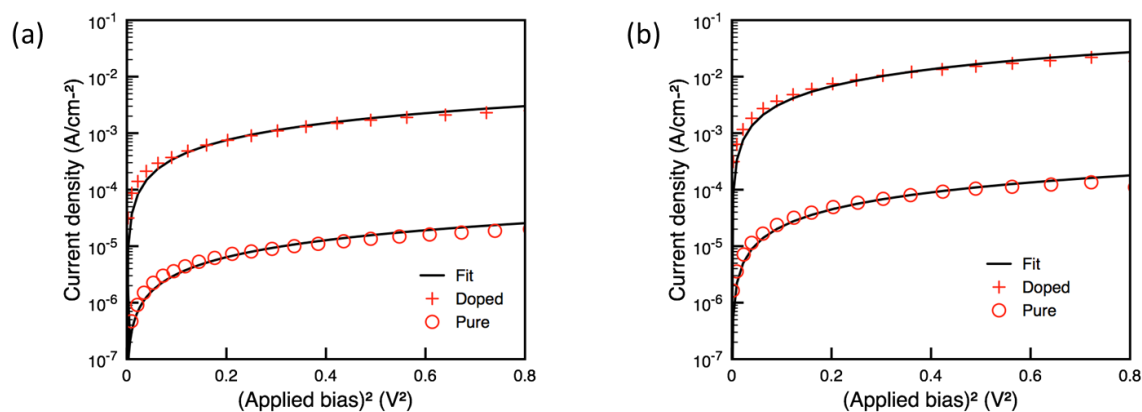


Figure 54. J - V^2 curves of pure and doped (a) spiro-OMeTAD and (b) PVK-[N(PhOCH₃)₂]₂ fitted with the Murgatroyd expression.

Table 19. Hole mobility of pure and doped spiro-OMeTAD and PVK-[N(PhOCH₃)₂]₂ calculated from the Murgatroyd model.

HTM		μ_0	γ	F	μ
		$\text{cm}^2/\text{V.s}$	$\text{cm}^{1/2}/\text{V}^{1/2}$	V/cm	$\text{cm}^2/\text{V.s}$
Spiro-OMeTAD	Pure	1.66 E-06	1.15 E-06	1.62 E05	1.66 E-06
	Doped	2.03 E-04	1.14 E-03	5.94 E04	2.68 E-04
PVK-	Pure	1.54 E-05	1.15 E-03	1.08 E05	2.25 E-05
[N(PhOCH ₃) ₂] ₂	Doped	1.05 E-03	1.01 E-03	2.28 E04	1.22 E-03
(8.0 kg.mol ⁻¹)					

μ_0 : mobility at zero field; γ : field dependence of the mobility; F: electric field; μ : hole mobility.

All of the functionalized PVK present good thermal stability and good solubility in chlorobenzene. The most suitable energy levels to be incorporated as HTM in PSCs were measured for PVK-[N(PhOCH₃)₂]₂. Moreover, it was found to exhibit higher hole mobility than spiro-OMeTAD which can be further enhanced by chemical doping.

3 PVK derivatives as HTM in planar perovskite solar cells

3.1 Preliminary results

Functionalized PVK were tested as HTM and compared to spiro-OMeTAD in planar FTO/c-TiO₂/CH₃NH₃PbI_{3-x}Cl_x/HTM/Au PSCs. The HTM process was exactly the same as for spiro-OMeTAD solution. Solution concentration was 4.3 wt.%. Materials were first studied without dopants. Due to different solution properties, HTM thickness layers varied from 80 to 180 nm (Table 20).

Table 20. Thickness of HTMs in PSCs.

HTM	Spiro-OMeTAD	PVK	PVK-(OCH ₃) ₂	PVK-(tBu) ₂	PVK-[N(PhOCH ₃) ₂] ₂ (8.0 kg.mol ⁻¹)
Thickness nm	180	80	120	110	130

I-V curves were measured under AM1.5 illumination with an incident power of 100 mW/cm². Best I-V curves and PCEs are given in Figure 55. Not surprisingly, undoped spiro-OMeTAD exhibited very poor PV performance due to low hole mobility. PVK-(OCH₃)₂ and PVK-(tBu)₂ did not perform better possibly due to the mismatching energy levels and their low charge transport properties. In this preliminary study, PVK-[N(PhOCH₃)₂]₂ achieved the worst PCEs while PVK exhibited the best PCE of 2.46 %.

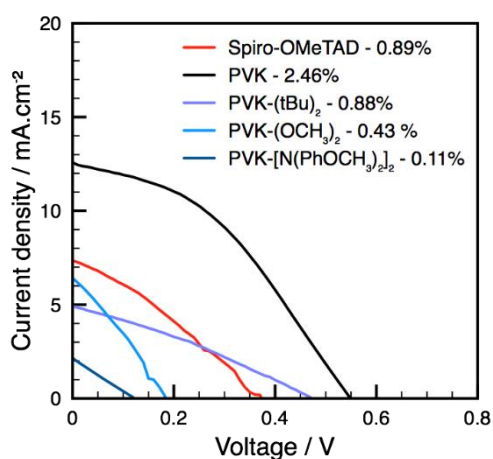


Figure 55. I-V curves (reverse scan) of PSCs containing undoped HTMs and their corresponding PCE.

The experiment was repeated by doping the materials with LiTFSI and tBP in the same proportions as for spiro-OMeTAD. The concentrations are noted as x:y:z, where x corresponds to one spiro-OMeTAD or one polymer unit, y to the molar ratio of LiTFSI and z to the tBP molar ratio. Thus, the doping concentration was 1:0.28:3.3. Dopants are especially expected to improve PV performances of PVK-

$[N(\text{PhOCH}_3)_2]_2$ since they considerably improved its hole mobility. Best and average PV parameters and hysteresis indexes (HIs), based on 8 cells are given in Table 21 and depicted in Figure 56. Hysteresis index was defined as $\text{HI} = (\text{PCE}_{\text{reverse}} - \text{PCE}_{\text{forward}}) / \text{PCE}_{\text{reverse}}$. PCE of devices incorporating PVK as HTM were not improved by dopants. PVK-(tBu) $_2$ and PVK-(OCH $_3$) $_2$ still exhibited low PV performances with efficiencies not exceeding 3.4 % with a large hysteresis. In contrast, more encouraging results were obtained with PVK-[N(PhOCH $_3$) $_2$] $_2$. Similar J_{sc} as spiro-OMeTAD, over 20 mA.cm^{-2} , were achieved with this polymer. The V_{oc} is suggested to decrease because of the higher HOMO level of the polymer compared to spiro-OMeTAD. Therefore, next experiments are dedicated to the optimization of the PVK-[N(PhOCH $_3$) $_2$] $_2$ -based PSCs in order to improve the V_{oc} , the FF and performances of the forward scan of the PSCs.

Table 21. Best and average PV parameters and hysteresis index of PSCs using different HTMs.

HTM	Reverse scan				Forward scan				HI
	J_{sc}	V_{oc}	FF	PCE	J_{sc}	V_{oc}	FF	PCE	
	mA.cm^{-2}	V		%	mA.cm^{-2}	V		%	
Spiro-OMeTAD	20.61 ^a	1.08	0.72	15.99	20.74	0.96	0.50	10.00	0.37
	20.72 ^b	1.00	0.68	14.11	21.11	0.86	0.35	6.42	0.57
	$\pm 0.44^c$	± 0.05	± 0.05	± 1.36	± 0.97	± 0.10	± 0.13	± 2.75	± 0.18
PVK	10.59	0.56	0.42	2.48	9.73	0.55	0.28	1.47	0.41
	9.23	0.52	0.38	1.85	8.95	0.55	0.29	1.40	0.23
	± 1.52	± 0.03	± 0.02	± 0.46	± 1.59	± 0.04	± 0.09	± 0.27	± 0.14
PVK-(OCH$_3$)$_2$	13.79	0.74	0.33	3.37	14.50	0.38	0.23	0.97	0.62
	8.48	0.70	0.41	2.15	8.77	0.37	0.20	0.71	0.71
	± 5.19	± 0.03	± 0.11	± 0.95	± 5.18	± 0.04	± 0.03	± 0.08	± 0.08
PVK-(tBu)$_2$	12.65	0.38	0.34	1.66	10.50	0.44	0.211	0.97	0.41
	12.87	0.34	0.33	1.46	10.86	0.41	0.210	0.95	0.35
	± 0.41	± 0.04	± 0.01	± 0.22	± 1.15	± 0.04	± 0.002	± 0.18	± 0.06
PVK-	20.25	0.94	0.66	12.51	20.91	0.79	0.35	5.79	0.54
[N(PhOCH$_3$)$_2$]$_2$	20.02	0.94	0.64	12.03	20.00	0.81	0.34	5.48	0.54
(8.0 kg.mol$^{-1}$)	± 0.18	± 0.01	± 0.02	± 0.44	± 1.16	± 0.012	± 0.02	± 0.58	± 0.06

^a Best cell; ^b average on 8 cells; ^c standard deviation of the average.

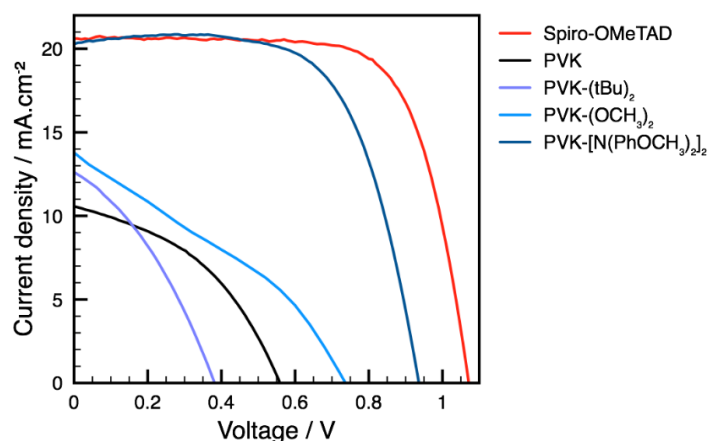


Figure 56. Best I-V curves (reverse scan) of PSCs containing LiTFSI and tBP doped HTMs.

3.2 Case of PVK-[N(PhOCH₃)₂]₂

3.2.1 Photovoltaic performances

To study the effect of the molecular weight of the PVK-[N(PhOCH₃)₂]₂ on PV performances, another batch of PVK-[N(PhOCH₃)₂]₂ was synthesized with a molecular weight (M_n) of 11730 g/mol. In the following, PVK-[N(PhOCH₃)₂]₂ with molecular weights (M_n) of 8030 and 11730 g/mol are named low M_n and high M_n PVK-[N(PhOCH₃)₂]₂, respectively. The HOMO level as well as the hole mobility were found to be similar to the lower M_n polymer, *i.e.* about -5.22 eV for the HOMO level and 2.2×10^{-5} and $1.2 \times 10^{-3} \text{ cm}^2 \cdot \text{V}^{-1} \cdot \text{s}^{-1}$ for the hole mobility of the pristine and the doped polymer, respectively.

The thickness of the polymer layer was optimized by varying the concentration of the HTM precursor solution. The initial concentration was 4.3 wt.%. The optimal solution concentrations were found to be 5.1 wt.% and 4.3 wt.% for the lower and the higher M_n polymers, respectively (Figure 58a and b). The associated thicknesses were estimated through the SEM cross-section images of the PSCs, and were about 150 nm for both polymers (Figure 57). This similar thickness obtained from two different concentrations can be explained by the viscosity difference of the two HTM precursor solutions. We can also notice that both polymers formed homogeneous and smooth films on top of the perovskite.

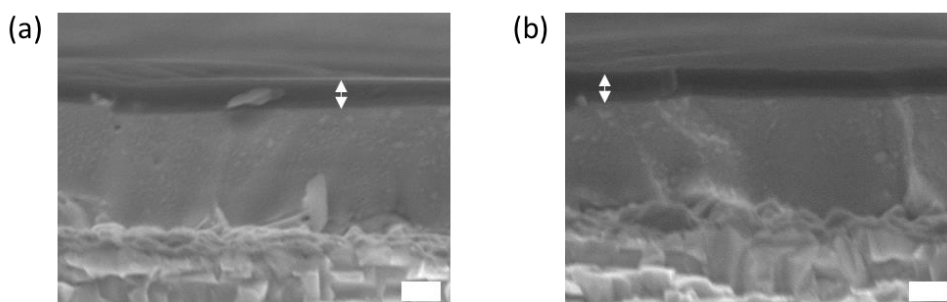


Figure 57. SEM cross-sections of (a) low M_n and (b) high M_n polymer-based PSCs. Scale bar = 200 nm.

Comparable PCE of up to 12.68 and 12.82 % were respectively achieved with the low and the high M_n PVK- $[N(\text{PhOCH}_3)_2]_2$ (Figure 58c and Table 22). Hysteresis was reduced but still present in the high M_n PVK- $[N(\text{PhOCH}_3)_2]_2$ -based PSCs. It is also noteworthy that in the case of the high M_n PVK- $[N(\text{PhOCH}_3)_2]_2$, series resistance R_s , corresponding to the inverse of the slope at $V=V_{oc}$, was reduced, suggesting better conductivity of the layer.

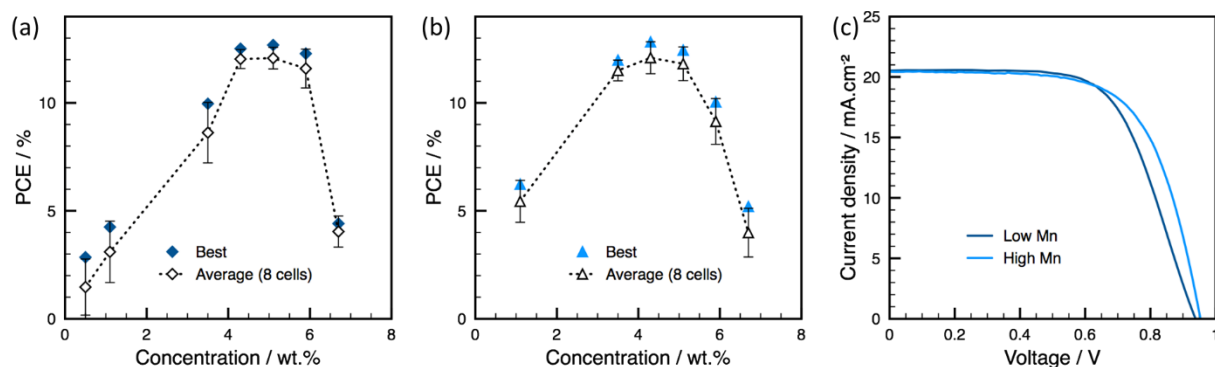


Figure 58. Best and average PCE (reverse scan) of PSCs according to the solution concentration of the (a) low M_n and (b) high M_n PVK- $[N(\text{PhOCH}_3)_2]_2$ HTM. (c) Best I-V curves (reverse scan) of the low and high M_n PVK- $[N(\text{PhOCH}_3)_2]_2$ -based PSCs.

Table 22. Best and average PV parameters and hysteresis index of low or high M_n PVK- $[N(\text{PhOCH}_3)_2]_2$ -based PSCs.

PVK- $[N(\text{PhOCH}_3)_2]_2$	Reverse scan				Forward scan				HI
	J_{sc}	V_{oc}	FF	PCE	J_{sc}	V_{oc}	FF	PCE	
	mA.cm^{-2}	V		%	mA.cm^{-2}	V		%	
Low M_n	20.54 ^a	0.94	0.66	12.68	21.78	0.71	0.35	5.28	0.55
5.1 wt.%	20.09 ^b	0.941	0.64	12.07	20.22	0.79	0.33	5.36	0.55
	$\pm 0.31^c$	± 0.005	± 0.02	± 0.50	± 1.43	± 0.06	± 0.02	± 0.55	± 0.06
High M_n	20.43	0.95	0.66	12.82	21.47	0.85	0.52	9.55	0.25
4.3 wt.%	20.90	0.91	0.64	12.09	20.70	0.78	0.38	6.22	0.49
	± 1.12	± 0.04	± 0.03	± 0.74	± 0.64	± 0.05	± 0.11	± 2.40	± 0.17

^a Best cell; ^b average on 8 cells; ^c standard deviation of the average.

The dopant concentrations were then optimized employing the highest M_n PVK- $[N(\text{PhOCH}_3)_2]_2$. The reference dopant concentration was 1:0.28:3.3. LiTFSI concentration was first optimized by fixing the tBP ratio at 3.3. PCE was improved to over 14 % by doubling the amount of LiTFSI (Figure 59). It especially increased J_{sc} and slightly reduced the hysteresis (Table 23). This may be attributed to the

small increase in hole mobility from 1.2×10^{-3} to $3.1 \times 10^{-3} \text{ cm}^2 \cdot \text{V}^{-1} \cdot \text{s}^{-1}$. tBP was then optimized by fixing the LiTFSI ratio at 0.56. PCE was not further improved by varying the tBP ratio.

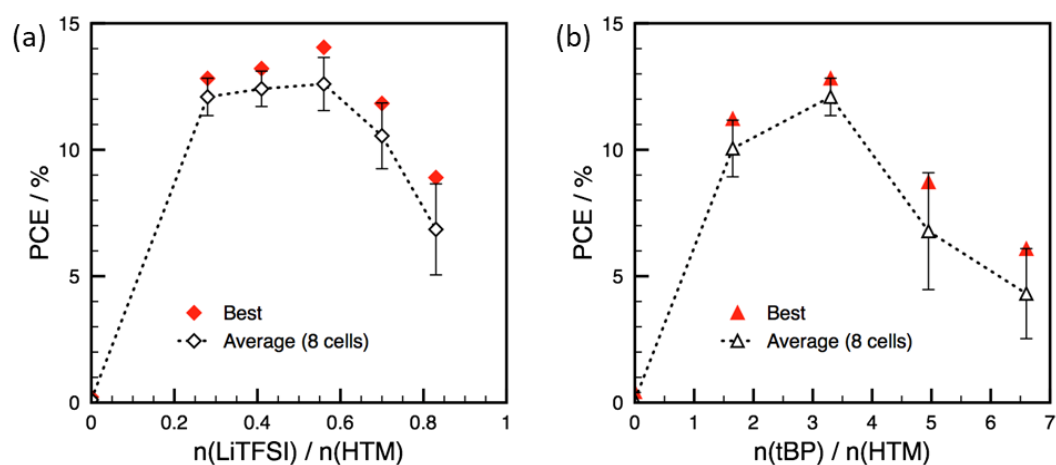


Figure 59. Optimization of the PCE according to (a) the LiTFSI (with a tBP ratio of 3.3) and (b) the tBP (with a LiTFSI ratio of 0.56) molar ratios.

The optimized 1:0.56:3.3 dopant concentration was then tested in the low M_n PVK- $[\text{N}(\text{PhOCH}_3)_2]_2$ -based PSCs. As well, J_{sc} was enhanced and hysteresis was slightly reduced, improving the PCE to 13.86 % (Table 23). Compared to spiro-OMeTAD average performances, polymer-based PSCs exhibit comparable J_{sc} for both scans and enhanced FF in the case of the forward scan, inducing lower HI. In Table 23, it is noteworthy that R_s of both forward and reverse scans are lower using the high M_n PVK- $[\text{N}(\text{PhOCH}_3)_2]_2$ as HTM.

Table 23. Best and average PV performances and hysteresis index of spiro-OMeTAD and PVK- $[\text{N}(\text{PhOCH}_3)_2]_2$ -based PSCs after optimization.

HTM	Reverse scan				Forward scan				HI
	J_{sc}	V_{oc}	FF	PCE	J_{sc}	V_{oc}	FF	PCE	
	$\text{mA} \cdot \text{cm}^{-2}$	V		%	$\text{mA} \cdot \text{cm}^{-2}$	V		%	
Spiro-OMeTAD	20.61 ^a	1.08	0.72	15.99	20.74	0.96	0.50	10.00	0.37
	20.72 ^b	1.00	0.68	14.11	21.11	0.86	0.35	6.42	0.57
	$\pm 0.44^c$	± 0.05	± 0.05	± 1.36	± 0.97	± 0.10	± 0.13	± 2.75	± 0.18
PVK-	22.17	0.92	0.68	13.86	22.17	0.82	0.53	9.55	0.31
$[\text{N}(\text{PhOCH}_3)_2]_2$	20.53	0.91	0.65	12.10	21.01	0.75	0.42	6.62	0.46
Low M_n	± 1.29	± 0.03	± 0.03	± 1.38	± 1.14	± 0.06	± 0.06	± 1.58	± 0.10
PVK-	22.07	0.95	0.67	14.05	22.09	0.89	0.50	9.90	0.30
$[\text{N}(\text{PhOCH}_3)_2]_2$	20.82	0.94	0.64	12.50	20.85	0.85	0.42	7.42	0.41
High M_n	± 0.97	± 0.01	± 0.03	± 1.05	± 1.26	± 0.04	± 0.08	± 2.10	± 0.14

^a Best cell; ^b average on 8 cells; ^c standard deviation of the average.

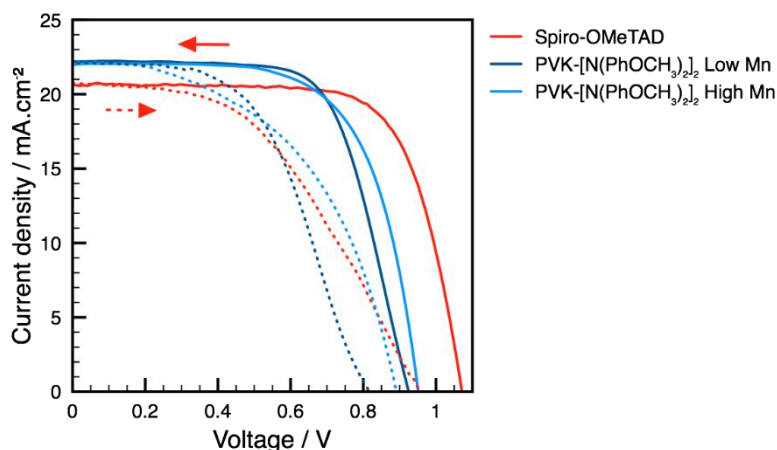


Figure 60. Best I-V curves of PSCs using spiro-OMeTAD or PVK-[N(PhOCH₃)₂]₂ as HTM.

The IPCE of the best devices was measured between 300 and 800 nm, and the associated current density was integrated (Figure 61). The peaks between 350 and 400 nm are often associated to the presence of PbI₂ resulting from the non-conversion into perovskite or to the degradation of the perovskite. Highest EQE was obtained with the high M_n PVK-[N(PhOCH₃)₂]₂ and the lowest with spiro-OMeTAD. The J_{sc} extracted from IPCE were 9.11, 10.45 and 11.47 mA.cm⁻² for spiro-OMeTAD, low M_n PVK-[N(PhOCH₃)₂]₂ and high M_n PVK-[N(PhOCH₃)₂]₂ respectively. This is about half of the values obtained from I-V curves. At least, same J_{sc} trend as I-V curves was observed. Reasons for J_{sc} difference between IPCE and I-V curves have been discussed in the literature. In our setup, only a part of the active area of the cell was illuminated by the EQE lamp. It has been explained that the non-illuminated part could act as a shunting load decreasing the shunt resistance in the device, resulting in lower photocurrent.¹⁵

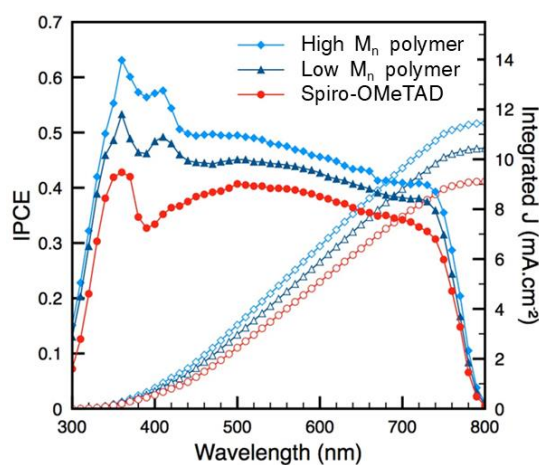


Figure 61. IPCE and integrated current density of the best devices.

Finally, the reproducibility of the solar cells was further studied by comparing the reverse efficiency of 30 cells for each HTM (Figure 62). Even if the best PCEs were still obtained with spiro-OMeTAD, average PCE are comparable: 11.66 ± 3.13 % for spiro-OMeTAD, 11.30 ± 1.95 % for the high M_n and 11.11 ± 1.98 % for the low M_n PVK-[N(PhOCH₃)₂]₂.

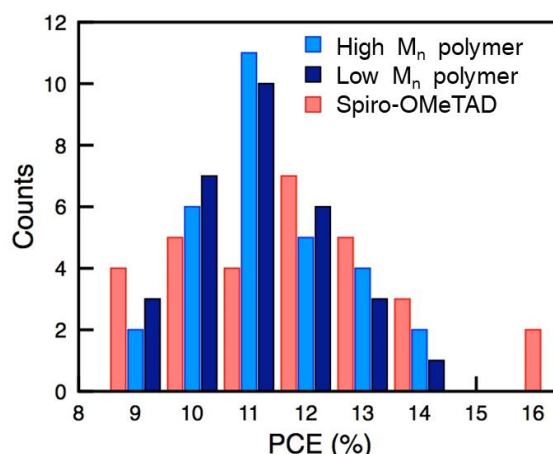


Figure 62. PCE (reverse scan) histogram of spiro-OMeTAD and PVK-[N(PhOCH₃)₂]₂ based PSCs.

3.2.2 Interfacial energetics

UP spectra were performed in order to compare the electronic properties of pristine and doped spiro-OMeTAD and PVK-[N(PhOCH₃)₂]₂ deposited on perovskite, by recording the corresponding work function (Φ) and valence band maximum (VBM). Characterization details are given in the Experimental Details section. The thickness of the spiro-OMeTAD and of the PVK-[N(PhOCH₃)₂]₂ layers were about 100 nm, respectively. The thinner PVK-[N(PhOCH₃)₂]₂ layer was estimated under 30 nm by SEM. The HOMO and the secondary electron cut-off regions of the UP spectra are presented in Figure 63 and the extracted values are reported in Table 24. The work function was determined as $\Phi = E_{\text{excitation}}$ (21.22 eV) - binding energy. The perovskite work function was found at 1.77 eV, suggesting a strong n-doping of the perovskite. The band diagram of perovskite-HTM interface is depicted in Figure 64.

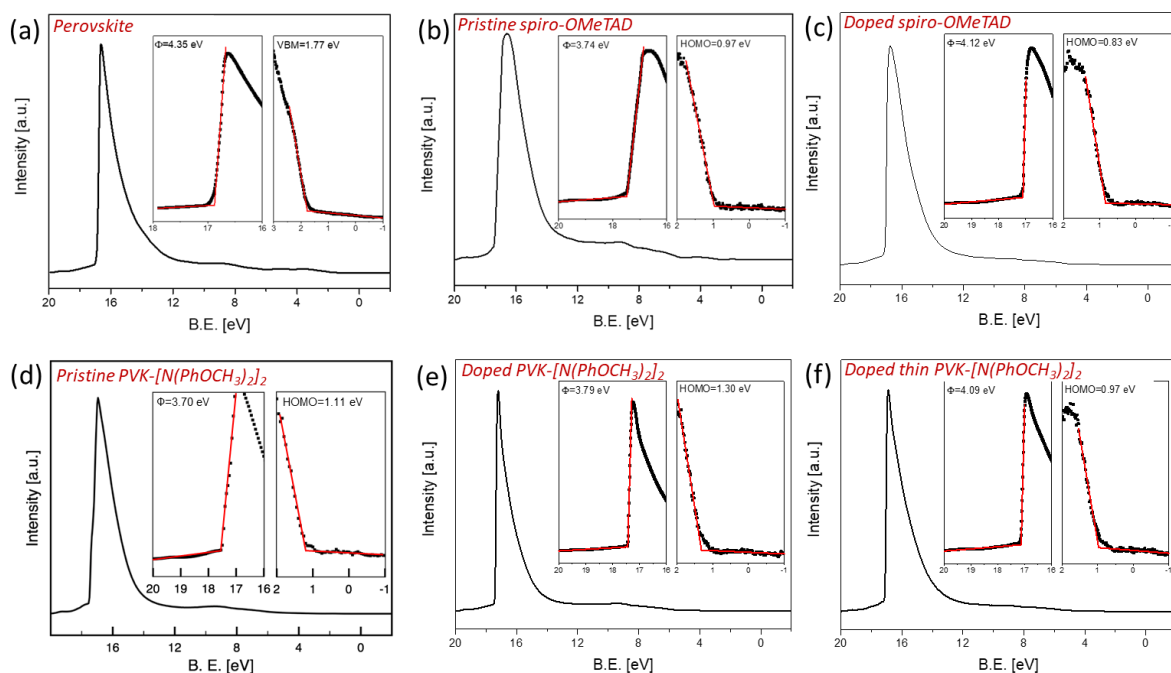


Figure 63. UP spectra of (a) the perovskite, (b) pristine spiro-OMeTAD, (c) doped spiro-OMeTAD, (d) pristine PVK-[N(PhOCH₃)₂]₂, (e) doped PVK-[N(PhOCH₃)₂]₂ and, (f) thin layer of doped PVK-[N(PhOCH₃)₂]₂.

Table 24. VBM and work function of the HTMs determined by UPS (± 0.05 eV), HOMO levels from UPS and PESA.

HTM		VBM	Φ	HOMO ^a	HOMO ^b
		eV	eV	eV	eV
Spiro-OMeTAD	Pristine	-0.97	3.74	-4.77	-5.25
	Doped	-0.83	4.12	-4.95	-5.35
PVK-[N(PhOCH ₃) ₂] ₂	Pristine	-1.11	3.70	-4.81	-5.22
	Doped	-1.30	3.79	-5.09	-5.25
(11.7 kg.mol ⁻¹)	Doped - thinner	-0.97	4.09	-5.06	- ^c

^a HOMO = Φ - VBM, from UPS; ^b HOMO from PESA; ^c not measured.

For spiro-OMeTAD, introduction of dopants brings the HOMO from 0.97 to 0.83 eV to the fermi level, confirming the p-doping of the material. On the other hand, the HOMO of the PVK-[N(PhOCH₃)₂]₂ is moved from 1.11 to 1.30 eV to the fermi level upon the addition of dopants. However, when decreasing the layer thickness of the doped PVK-[N(PhOCH₃)₂]₂, the HOMO was found to be closer (0.97 eV) to the fermi level than the undoped PVK-[N(PhOCH₃)₂]₂. Additionally, the shift between the VBM of the perovskite and the HOMO edge of the doped HTMs was about 0.9 eV for the doped spiro-OMeTAD and, 0.8 and 0.5 eV for the thin and the thick doped PVK-[N(PhOCH₃)₂]₂, respectively.

The influence of the thickness on the position of the band energy cannot be clearly explained. The experiment should be repeated for a better understanding. Bringing all the data together, the HOMO level of the PVK-[N(PhOCH₃)₂]₂, tend to be closer to the perovskite VBM. In one hand, it could be beneficial for the V_{oc} of the device which is theoretically related to energy difference between the HOMO of the HTM and the CB or LUMO of the ETM. On the other hand, closer perovskite VBM and HTM HOMO may increase recombination rates at the interface and reduce the V_{oc}.

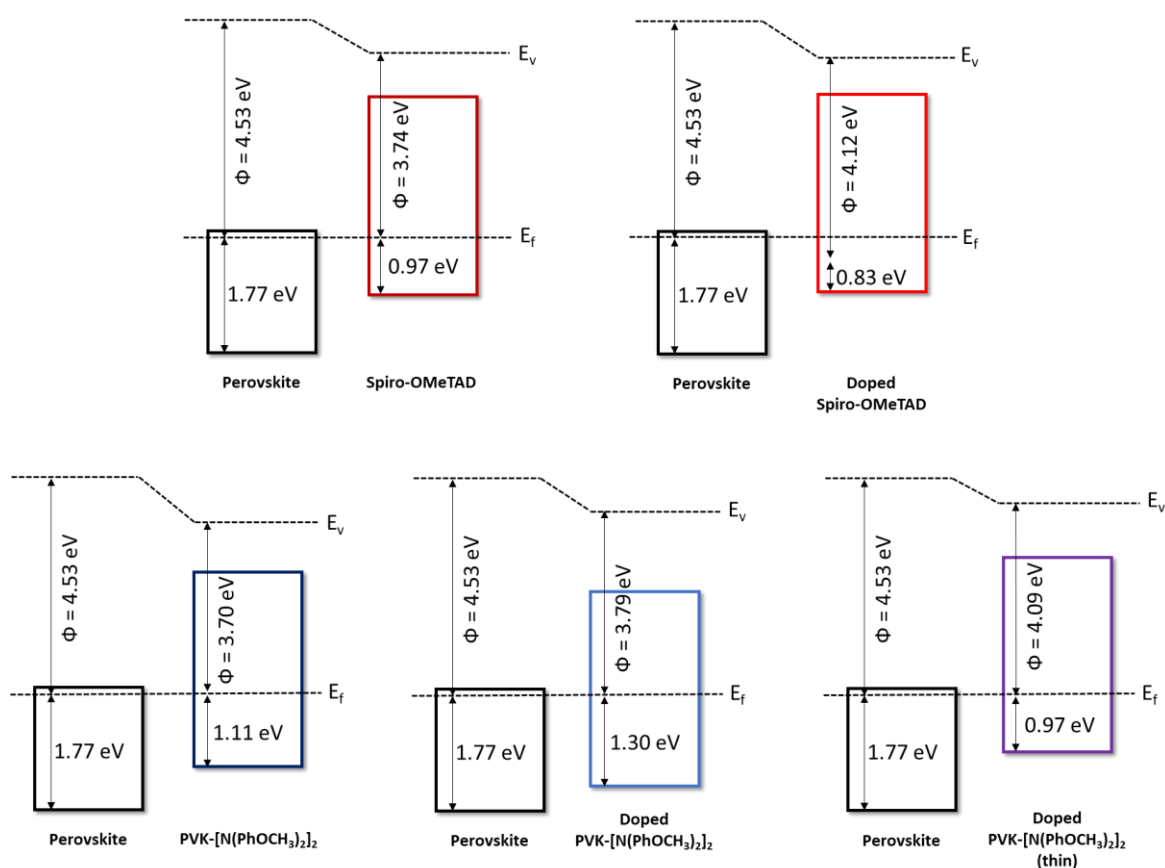


Figure 64. Energy diagram of HTMs from UPS data.

HOMO levels from PESA and from UPS are compared in Table 24. The different values between the two technics can be explained by the organic contaminants at the surface of the HTMs exposed to atmosphere. In PESA, doping decreased the HOMO level of PVK-[N(PhOCH₃)₂]₂ of 0.03 eV while in UPS, it was decreased of 0.30 eV. For spiro-OMeTAD, the addition of dopants decreased the HOMO level of 0.10 eV according to PESA, and to 0.20 eV according to UPS. Despite significantly different HOMO levels measured, both technics tend to show that addition of dopant in spiro-OMeTAD or PVK-[N(PhOCH₃)₂]₂ decreased the HOMO level.

3.2.3 Stability

The stability of the most efficient devices was evaluated by regularly measuring I-V curves of spiro-OMeTAD and PVK-[N(PhOCH₃)₂]₂-based PSCs stored in different conditions: in inert atmosphere (N₂ glovebox), in dry atmosphere, and in atmosphere with a relative humidity (RH) about 10 % (Figure 65). PSCs were kept in ambient light and ambient temperature without encapsulation. In all cases, PVK-[N(PhOCH₃)₂]₂-based PSCs performed well and longer than spiro-OMeTAD-based devices. Under nitrogen, PVK-[N(PhOCH₃)₂]₂-based PSC kept its initial efficiency after 2 months while spiro-OMeTAD-based PSC exhibited around 65 % of its initial efficiency (Figure 65a). In dry atmosphere, efficiency of spiro-OMeTAD devices drastically decreased from the day after its processing. The increase in efficiency for the high M_n PVK-[N(PhOCH₃)₂]₂ could be attributed to the end of the evaporation of the remaining chlorobenzene used for the HTM deposition and/or to the slow doping of the HTM through oxygen exposure.¹⁶ After a 10-day experiment PCE was stable and slightly decreased after 2 weeks. Meanwhile, the lower M_n PVK-[N(PhOCH₃)₂]₂ still exhibited about 65 % of its initial PCE (Figure 65b). Finally, in more humid atmosphere, although spiro-OMeTAD PSC was slightly more stable than in dry atmosphere, it achieved only around 30 % of its initial efficiency after 10 days, while the PVK-[N(PhOCH₃)₂]₂-based device was around 65 %. This comparative study indicates the superior stability of the PSCs using PVK-[N(PhOCH₃)₂]₂ as HTM.

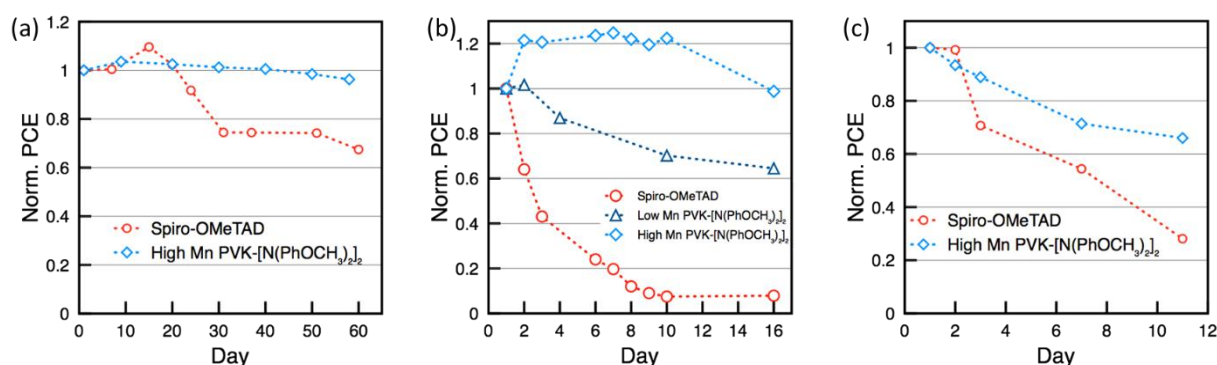


Figure 65. Normalized PCE of PSCs employing spiro-OMeTAD or PVK-[N(PhOCH₃)₂]₂ as HTM stored in (a) glove box, (b) dry atmosphere and, (c) atmosphere with 20% RH.

Since dopants have been shown to be responsible for the poor stability of spiro-OMeTAD as well as bubbles formed during the spin-coating deposition, morphologies of pure and doped HTMs were controlled by AFM (Figure 66a-d).¹⁷ Homogeneous layers were formed with pure materials. Upon the addition of dopants, no change in morphology was observed for the polymer, whereas holes ($\varnothing \approx 50$ nm) were formed on top of the spiro-OMeTAD layer. Same defects were observed in SEM cross-

section images of freshly made spiro-OMeTAD devices while in contrast, polymer layer remains homogeneous in 4-week aged devices (Figure 66e and f).

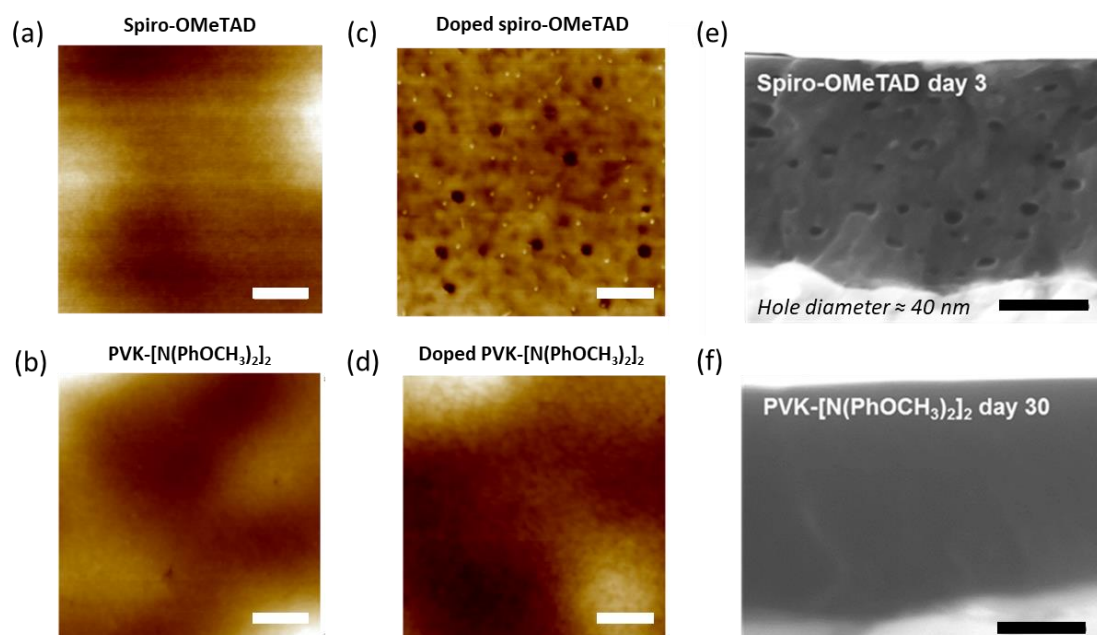


Figure 66. AFM topographic views of HTM thin films on top of FTO/TiO₂/perovskite. (a) spiro-OMeTAD ($R_q = 3.3$ nm), (b) PVK-[N(PhOCH₃)₂]₂ ($R_q = 2.6$ nm), (c) doped spiro-OMeTAD ($R_q = 4.3$ nm), and (d) doped PVK-[N(PhOCH₃)₂]₂ ($R_q = 3.2$ nm). SEM cross sections of PSCs using as HTM (e) spiro-OMeTAD after a 3-day ageing in dry room or (f) PVK-[N(PhOCH₃)₂]₂ after a 30-day ageing in dry room. Scale bars = 200 nm.

In addition, contact angle measurements of a water drop in contact with spiro-OMeTAD and the high M_n PVK-[N(PhOCH₃)₂]₂ films clearly showed the higher hydrophobicity of the polymer (Figure 67). Therefore, we postulate that the higher stability of the PVK-[N(PhOCH₃)₂]₂-based devices may result from their better film-forming and covering of the perovskite layer, which are further improved with a higher M_n . The polymer is thought to act as a protective layer, insulating the hybrid perovskite from the atmosphere and preventing the device from degradation.

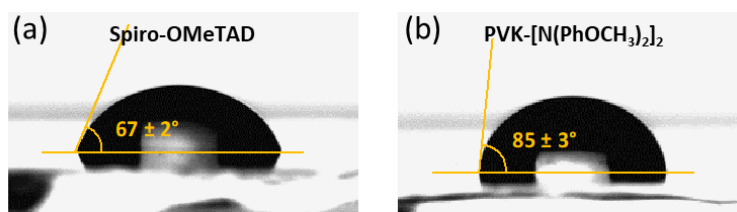


Figure 67. Contact angle measurement of a water drop on (a) spiro-OMeTAD and on (b) PVK-[N(PhOCH₃)₂]₂ thin films.

4 PVK-[N(PhOCH₃)₂]₂ as HTM in mesoscopic perovskite solar cells

In this part, PVK-[N(PhOCH₃)₂]₂ is compared to spiro-OMeTAD in more efficient, stable, and reproducible PSCs: FTO/bl-TiO₂/mp-TiO₂/K⁺ doped MA_{0.15}FA_{0.85}PbI_{2.55}Br_{0.45}/HTM/Au mesoscopic PSCs. The objective was to confirm the results obtained in planar PSCs. The high M_n PVK-[N(PhOCH₃)₂]₂ (11.7 kg.mol⁻¹) was employed since it achieved the best performances.

In order to find the best formulation for this device, 3 different recipes were tested: the one optimized in planar PSCs (F1), the spiro-OMeTAD one optimized for mesoscopic PSCs (F2) and an optimized polymer recipe used by Seok *et al.* for PTAA (F3).¹⁸ The various formulations are summarized in Table 25.

Table 25. PVK-[N(PhOCH₃)₂]₂ formulation details.

	F1	F2	F3
Expected thickness nm	≈ 150	≈ 200	≈ 10
Solvent	chlorobenzene	chlorobenzene	toluene
Concentration wt. %	7.2	6.2	1.14
[LiTFSI]* mg/ml	625	520	170
n_{LiTFSI} / n_{HTM}	0.56	0.5	0.1
n_{tBP} / n_{HTM}	3	3.3	0.6

*Concentration of the LiTFSI solution in acetonitrile, used to dope HTMs.

PV performances are reported in Table 26 and best I-V curves are displayed in Figure 68. Optimized devices with spiro-OMeTAD reached over 18 % PCE. Formulation giving the highest efficiencies for the PVK-[N(PhOCH₃)₂]₂ was F2. The best PCE recorded was 10.67 % with reduced hysteresis compared to spiro-OMeTAD and good reproducibility. F1 gave similar PCE with lower J_{sc}, higher FF and larger hysteresis. The thinner less doped PVK-[N(PhOCH₃)₂]₂ layer obtained with F3 further decreased J_{sc}, increased FF and enlarged hysteresis. As mentioned before, lower V_{oc} could be expected with PVK-[N(PhOCH₃)₂]₂ due to the higher HOMO level. However, in this case V_{oc} difference between spiro-OMeTAD and the polymer is even larger, about 0.2 V.

Table 26. Best and average PV parameters and hysteresis index of PSCs using different formulations for the HTM.

HTM	Reverse scan				Forward scan				HI
	J_{sc}	V_{oc}	FF	PCE	J_{sc}	V_{oc}	FF	PCE	
	$mA.cm^{-2}$	V		%	$mA.cm^{-2}$	V		%	
Spiro-	22.45 ^a	1.10	0.73	18.44	22.71	1.10	0.71	17.71	0.04
OMeTAD	22.31 ^b	1.11	0.73	18.12	22.65	1.10	0.70	17.46	0.04
F2	$\pm 0.25^c$	± 0.01	± 0.02	± 0.55	± 0.23	± 0.01	± 0.03	± 0.01	± 0.01
PVK-	17.80	0.91	0.65	10.54	18.56	0.93	0.58	10.00	0.05
[N(PhOCH₃)₂]₂	17.18	0.88	0.67	10.03	18.02	0.90	0.58	9.44	0.06
F1	± 0.56	± 0.04	± 0.01	± 0.51	± 0.51	± 0.04	± 0.01	± 0.54	± 0.01
PVK-	18.25	0.90	0.65	10.67	19.04	0.92	0.59	10.44	0.02
[N(PhOCH₃)₂]₂	18.20	0.89	0.62	9.99	18.96	0.92	0.58	10.02	-0.01
F2	± 0.38	± 0.01	± 0.03	± 0.71	± 0.37	± 0.01	± 0.02	± 0.32	± 0.04
PVK-	15.10	0.88	0.69	9.10	15.49	0.91	0.60	8.40	0.08
[N(PhOCH₃)₂]₂	15.03	0.86	0.59	7.69	15.43	0.90	0.58	8.12	-0.18
F3	± 0.24	± 0.02	± 0.17	± 2.42	± 0.29	± 0.01	± 0.01	± 0.20	± 0.52

^a Best cell; ^b average on 4 cells; ^c standard deviation of the average.

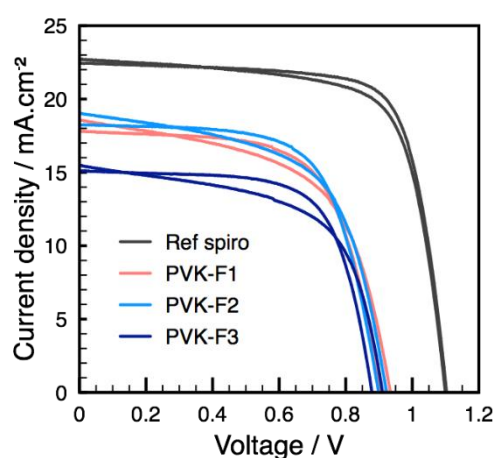


Figure 68. Best I-V curves (forward and reverse scans) of PSCs with different HTM formulations.

Dopant concentrations have been optimized by simultaneously varying LiTFSI and tBP ratios. The reference doping ratio corresponds to 1:0.5:3.3. When increasing dopant concentration, V_{oc} was reduced and J_{sc} and FF increased up to a maximum reached for the 1:1.25:8.25 dopant concentration. Thereby, PCE was improved from 11.93 to 14.49 %. This suggests that dopants improved charge transport properties of the polymer inducing a reduction of R_s and an increase of R_{sh} . For the next

experiments, dopant formulation was fixed at 1:1.25:8.25. The hole mobility of the doped polymer calculated with the Mott Gurney law was $2.8 \times 10^{-3} \text{ cm}^2 \cdot \text{V}^{-1} \cdot \text{s}^{-1}$.

Table 27. Best and average PV parameters and hysteresis index of PSCs using different PVK-[N(PhOCH₃)₂]₂ dopant concentrations.

	Reverse scan				Forward scan				HI
	J _{sc}	V _{oc}	FF	PCE	J _{sc}	V _{oc}	FF	PCE	
	<i>mA.cm⁻²</i>	<i>V</i>		%	<i>mA.cm⁻²</i>	<i>V</i>		%	
1:0.25:1.65	18.40 ^a	0.952	0.54	9.49	19.62	0.994	0.51	10.04	-0.06
	17.78 ^b	0.955	0.55	9.36	18.95	0.991	0.48	9.03	0.03
	± 0.62 ^c	± 0.031	± 0.01	± 0.68	± 0.78	± 0.015	± 0.03	± 0.76	± 0.07
1:0.5:3.3 (Ref)	19.10	0.952	0.66	11.93	19.55	0.985	0.59	11.27	0.06
	18.45	0.950	0.64	11.29	18.64	0.979	0.59	10.76	0.05
	± 0.53	± 0.004	± 0.01	± 0.50	± 0.81	± 0.005	± 0.01	± 0.65	± 0.04
1:0.75:4.95	19.49	0.891	0.75	12.94	19.88	0.905	0.71	12.69	0.02
	18.35	0.880	0.75	12.15	18.43	0.894	0.70	11.59	0.05
	± 1.71	± 0.014	± 0.01	± 1.15	± 2.04	± 0.013	± 0.02	± 1.55	± 0.04
1:1:6.6	21.19	0.857	0.78	14.08	21.31	0.863	0.73	13.44	0.05
	21.29	0.869	0.76	14.02	21.46	0.876	0.72	13.52	0.04
	± 0.10	± 0.011	± 0.02	± 0.20	± 0.16	± 0.011	± 0.02	± 0.24	± 0.01
1:1.25:8.25	21.80	0.870	0.76	14.49	22.00	0.873	0.72	13.87	0.04
	21.38	0.868	0.76	14.18	21.40	0.871	0.73	13.60	0.04
	± 0.31	± 0.002	± 0.01	± 0.34	± 0.56	± 0.004	± 0.01	± 0.44	± 0.01
1:1.5:9.9	21.43	0.847	0.76	13.85	21.65	0.857	0.72	13.32	0.04
	20.60	0.846	0.77	13.42	20.91	0.853	0.70	12.56	0.06
	± 0.76	± 0.001	± 0.02	± 0.33	± 0.73	± 0.004	± 0.01	± 0.72	± 0.04

^a Best cell; ^b average on 4 cells; ^c standard deviation of the average.

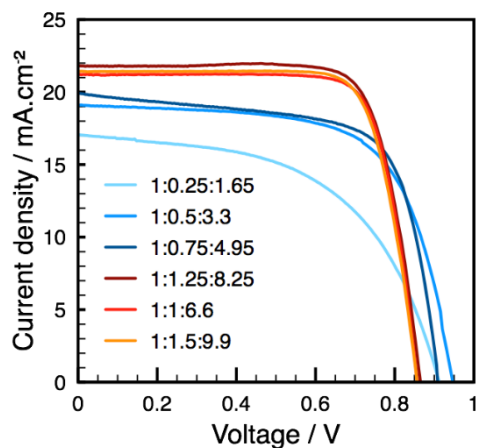


Figure 69. Best I-V curves (reverse scan) of PSCs depending on the HTM dopant concentration.

Finally, the thickness of PVK-[N(PhOCH₃)₂]₂ was optimized by varying the spin-coating parameters. Thickness layers were determined from the SEM cross-section images of the devices (Figure 70). These images show the homogeneity of the PVK-[N(PhOCH₃)₂]₂ layers, well covering the perovskite without pinholes. Optimal PCE of 14.69 % was obtained for the 90-nm thick PVK-[N(PhOCH₃)₂]₂ (Table 28).

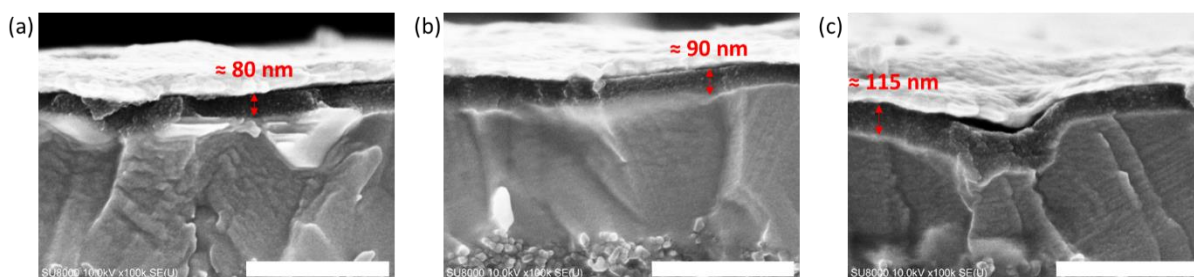


Figure 70. SEM cross-section images (10 kV) of polymer-based PSCs with different HTM thickness.

Table 28. Best and average PV parameters and hysteresis index of PSCs according to the PVK-[N(PhOCH₃)₂]₂ thickness.

	Reverse scan				Forward scan				HI
	J _{sc}	V _{oc}	FF	PCE	J _{sc}	V _{oc}	FF	PCE	
	<i>mA.cm⁻²</i>	<i>V</i>		%	<i>mA.cm⁻²</i>	<i>V</i>		%	
80 nm	21.33 ^a	0.89	0.75	14.25	21.56	0.90	0.72	13.99	0.018
(6000 rpm 1s)^d	21.22 ^b	0.885	0.75	14.10	21.40	0.898	0.720	13.84	0.019
	± 0.30 ^c	± 0.002	± 0.01	± 0.17	± 0.30	± 0.003	± 0.003	± 0.22	± 0.004
90 nm	21.78	0.890	0.75	14.69	21.87	0.90	0.73	14.40	0.02
(4000 rpm 1s) (Ref)	21.89	0.886	0.75	14.54	21.94	0.901	0.73	14.45	0.006
	± 0.26	± 0.002	± 0.01	± 0.05	± 0.28	± 0.001	± 0.01	± 0.08	± 0.005
115 nm	21.85	0.887	0.75	14.53	22.24	0.894	0.73	14.46	0.005
(4000 rpm 2s)	21.84	0.885	0.73	14.25	22.77	0.898	0.71	14.22	0.002
	± 0.37	± 0.004	± 0.02	± 0.21	± 0.32	± 0.005	± 0.01	± 0.19	± 0.005

^a Best cell; ^b average on 4 cells; ^c standard deviation of the average; ^d spin-coater speed and acceleration time.

Despite optimizations of the layer, V_{oc} is still relatively low. In planar PSCs discussed above, V_{oc} of PSCs made of spiro-OMeTAD and the polymer was quite close. One of the difference between the two architectures is the perovskite composition. In mesoscopic PSCs, the perovskite additionally contains formamidinium, bromide and potassium, and an excess of lead. This composition may locally modify the energy levels of the perovskite or the interactions between the polymer and the perovskite at the interface. Thereby, the next experiments are dedicated to the modification of the perovskite interface and its effect on PV performances of PVK-[N(PhOCH₃)₂]₂-based PSCs.

A reported study showed that the potassium of the perovskite is mainly located at the perovskite grain surface and thus, might be present at the perovskite/HTM interface.¹⁹ Therefore, potassium-free PSCs were fabricated. As previously discussed, potassium-free PSCs exhibit larger hysteresis but improved J_{sc} (Table 29, Figure 71). However, V_{oc} was slightly reduced.

Table 29. Best and average PV parameters and hysteresis index of K⁺-free PSCs using PVK-[N(PhOCH₃)₂]₂ as HTM.

	Reverse scan				Forward scan				HI
	J _{sc}	V _{oc}	FF	PCE	J _{sc}	V _{oc}	FF	PCE	
	<i>mA.cm⁻²</i>	<i>V</i>		%	<i>mA.cm⁻²</i>	<i>V</i>		%	
Without KI	22.49 ^a	0.87	0.73	14.16	22.59	0.844	0.44	8.44	0.40
	22.64 ^b	0.86	0.72	14.06	22.67	0.840	0.42	8.03	0.43
	± 0.14 ^c	± 0.01	± 0.02	± 0.12	± 0.24	± 0.003	± 0.02	± 0.31	± 0.02

^a Best cell; ^b average on 4 cells; ^c standard deviation of the average.

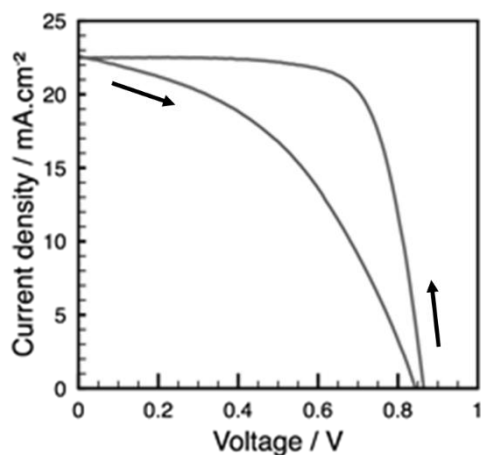


Figure 71. Best I-V curve of K^+ -free PSC using PVK- $[N(PhOCH_3)_2]_2$ as HTM.

The $MA_{0.15}FA_{0.85}PbI_{2.55}Br_{0.45}$ perovskite we use contains an excess of lead. To make the perovskite/HTM interface less lead rich, solutions of either MAI, FAI, MABr or FAI:MABr (0.85:0.15) were deposited on top of the perovskite layer. Solutions were prepared in IPA (10 mg/mL). 200 μ L of solution were dropped 5 times during the spinning of the substrate. Then, the substrates were rinsed with IPA to remove the excess of salt and were dried at 80°C for 20 min. The PV performances of the resulting PSCs are given in Table 30 and Figure 72. All of the solutions had the effect to improve the V_{oc} , up to 1.07 V with MABr, and the PCE. This may be due to a reduction of recombination at the interface. J_{sc} was enhanced in the case of MABr:FAI. Despite a best PCE of 17.17 %, MAI modified PSCs exhibited poor reproducibility. In addition, FF was slightly decreased. Optimizations of the process would be needed to further improve both performances and reproducibility of the PVK- $[N(PhOCH_3)_2]_2$ -based PSCs.

Table 30. Best and average PV parameters and hysteresis index of PSCs with modified perovskite/PVK- $[N(PhOCH_3)_2]_2$ interface.

	Reverse scan				Forward scan				HI
	J_{sc}	V_{oc}	FF	PCE	J_{sc}	V_{oc}	FF	PCE	
	$mA.cm^{-2}$	V		%	$mA.cm^{-2}$	V		%	
Without (Ref)	21.78 ^a	0.89	0.75	14.69	21.87	0.90	0.73	14.40	0.018
	21.29 ^b	0.89	0.75	14.28	21.74	0.90	0.71	13.06	0.04
	$\pm 0.21^c$	± 0.01	± 0.03	± 0.41	± 0.24	± 0.01	± 0.04	± 0.92	± 0.04
MAI	22.58	1.00	0.75	17.03	23.10	1.00	0.74	17.17	-0.01
	21.27	0.96	0.70	14.25	21.74	0.96	0.68	14.40	-0.02
	± 1.34	± 0.04	± 0.06	± 2.12	± 1.62	± 0.04	± 0.04	± 2.15	± 0.14
FAI	22.86	0.93	0.73	15.50	23.26	0.94	0.71	15.45	0.003
	21.61	0.95	0.70	14.95	22.26	0.96	0.70	14.86	0.006
	± 0.99	± 0.01	± 0.06	± 0.47	± 0.76	± 0.01	± 0.01	± 0.42	± 0.01
MABr	20.64	1.066	0.69	15.13	20.98	1.055	0.64	14.27	0.06
	20.76	1.068	0.68	14.70	20.41	1.054	0.64	13.85	0.056
	± 0.46	± 0.003	± 0.02	± 0.31	± 0.40	± 0.002	± 0.01	± 0.31	± 0.003
MABr:FAI (0.15:0.85)	22.29	1.02	0.73	16.71	22.62	1.03	0.68	15.90	0.05
	22.10	0.98	0.66	14.33	22.68	0.99	0.68	15.25	0.01
	± 0.45	± 0.03	± 0.10	± 2.50	± 0.36	± 0.02	± 0.03	± 1.11	± 0.03

^a Best cell; ^b average on 4 cells; ^c standard deviation of the average.

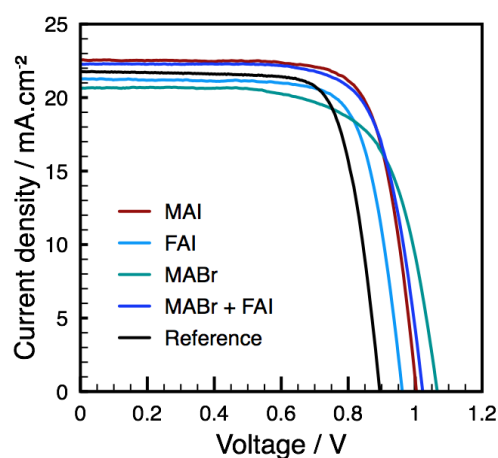


Figure 72. Best I-V curves (reverse scan) of PSCs with modified perovskite/PVK- $[N(PhOCH_3)_2]_2$ interface.

5 Dopant-free PVK-[N(PhOCH₃)₂]₂ HTM in planar PSCs

Recently, Huang *et al.* have reported PVCz-OMeDAD which has the same structure as PVK-[N(PhOCH₃)₂]₂.²⁰ The polymer was obtained through a different synthetic route, *i.e.* by the free-radical polymerization of the vinyl monomers, leading to average molecular weight of 14 kg.mol⁻¹ and a dispersity of 1.6. Without dopants, the HOMO level was determined at -5.24 eV by cyclic voltammetry and the hole mobility was found to be 3.4×10^{-4} cm².V⁻¹.s⁻¹ by the SCLC method. They achieved 16.1 % PCE in FTO/bl-TiO₂/mp-TiO₂/MA_{0.15}FA_{0.85}PbI_{2.55}Br_{0.45}/HTM/Au PSCs with an optimal thickness layer about 30 nm without the use of dopants, that they attributed to good charge transport properties and to the hole extraction capability of the material. However, no chemical characterizations of the polymer were given, neither comments on the hysteresis and the stability of the devices.

Since poor PV performances were obtained in thin and dopant-less polymer-based mesoscopic PSCs, the potential of PVK-[N(PhOCH₃)₂]₂ (11.7 kg.mol⁻¹) as dopant-free HTM was investigated in n-i-p planar PSCs. To do so, the device architecture was optimized. The polymer thickness layer was decreased to reduce the hole-transportation pathway to the top electrode and to compensate the loss in conduction properties of the polymer layer when undoped. Moreover, a thin layer, about 10 nm, of molybdenum oxide (MoOx) was thermally evaporated between the HTM and the gold electrode. The deeper CB of the MoOx is expected to further attract holes and thus, facilitate charge extraction. The device materials and architecture are represented in the energy diagram in Figure 73.

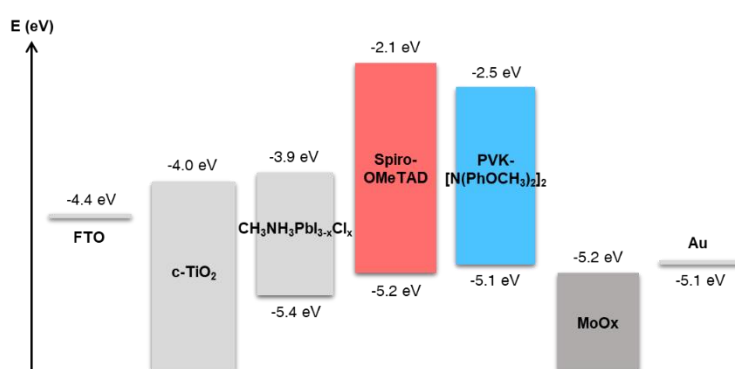


Figure 73. Energy diagram of the planar n-i-p dopant-free PSCs.

PVK-[N(PhOCH₃)₂]₂ thickness was reduced from 124 to 38 nm (\pm 5 nm) by decreasing the HTM precursor solution concentration and by increasing the speed and the acceleration of the spin-coater. Best and average PCE from both reverse and forward scans are represented in Figure 74. Best PCE of 10.63 % was obtained for an optimal polymer thickness of 85 nm. V_{oc} , J_{sc} and FF followed the same

trend, with a maximum at 85 nm. It is also noticeable that the hysteresis tends to be reduced with thicker layers.

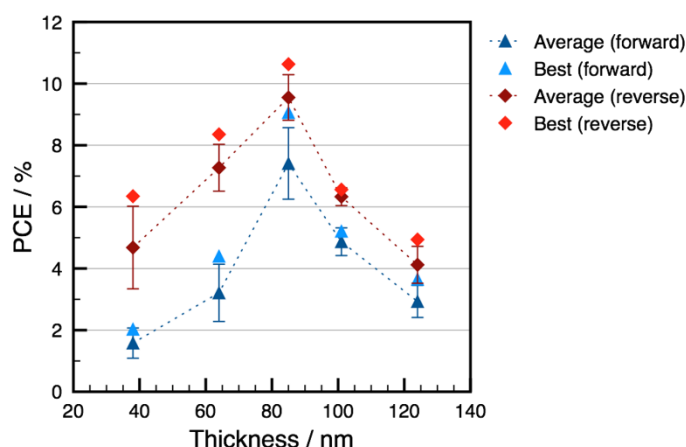


Figure 74. Best and average PCE of 8 cells from reverse and forward I-V scans as a function of the PVK-[N(PhOCH₃)₂]₂ thickness.

Spiro-OMeTAD was then introduced in similar devices and compared to PVK-[N(PhOCH₃)₂]₂. Spiro-OMeTAD thickness was reduced to around 75 nm. Higher J_{sc} and V_{oc} were obtained with the polymer than with spiro-OMeTAD, resulting in a slightly higher best PCE of 10.63 % vs. 10.23 % (Table 31 and Figure 75a). The higher performances of the pristine PVK-[N(PhOCH₃)₂]₂ could also be explained by the higher hole mobility compared to pristine spiro-OMeTAD ($\approx 10^{-5}$ vs. $\approx 10^{-6}$ cm².V⁻¹.s⁻¹). As for previous architectures, hysteresis was larger in spiro-OMeTAD-based PSCs. Interestingly, addition of dopants into the HTMs considerably reduced efficiency of PSCs. J_{sc} and V_{oc} were considerably decreased polymer-based devices. Unbalance charge extraction could explain the lower J_{sc} and larger hysteresis.

Table 31. Best and average PV parameters of undoped spiro-OMeTAD and PVK-[N(PhOCH₃)₂]₂-based PSCs.

		Reverse scan				Forward scan				HI
		J _{sc}	V _{oc}	FF	PCE	J _{sc}	V _{oc}	FF	PCE	
		<i>mA.cm⁻²</i>	<i>V</i>		%	<i>mA.cm⁻²</i>	<i>V</i>		%	
Spiro-OMeTAD	Pure	18.04 ^a	0.87	0.65	10.23	17.30	0.79	0.43	5.93	0.42
		18.04 ^b	0.85	0.65	9.85	17.71	0.79	0.45	6.36	0.35
		± 0.51 ^c	± 0.02	± 0.01	± 0.35	± 0.70	± 0.01	± 0.03	± 0.66	± 0.06
	Doped	17.18	0.75	0.34	4.44	16.67	0.66	0.28	3.06	0.31
PVK-[N(PhOCH₃)₂]₂	Pure	19.68	0.95	0.57	10.63	19.95	0.90	0.50	9.06	0.15
		19.15	0.93	0.54	9.55	19.36	0.87	0.44	7.74	0.23
		± 2.08	± 0.02	± 0.06	± 0.74	± 2.01	± 0.03	± 0.06	± 0.95	± 0.07
	Doped	11.76	0.68	0.78	6.29	8.97	0.62	0.21	1.17	0.81

^a Best cell; ^b average on 8 cells; ^c standard deviation of the average.

The evolution of the PCE of the best undoped devices was followed during one month (Figure 75b). Samples were stored in inert atmosphere at 25°C in ambient light. After 4 weeks of experiment, both PSCs exhibited above 60 % of their initial efficiency, suggesting a faster degradation than the doped-HTM and MoOx-free PSCs. Degradation may be induced by the MoOx layer through instabilities at the HTM/MoOx interface or by the thinner layer of the HTM.

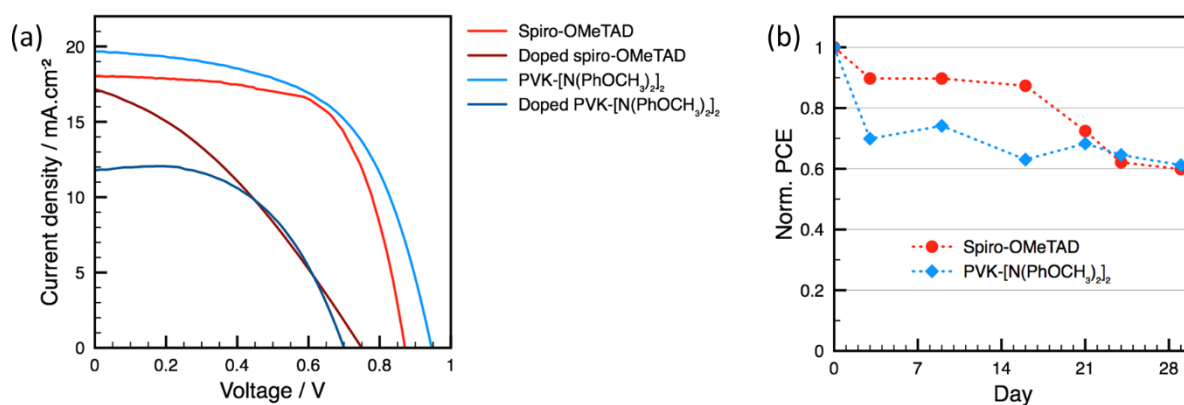


Figure 75. (a) Best I-V curves (reverse scans) of MoOx-based PSCs with doped and undoped HTMs. (b) Stability of the best performing PSCs based on undoped spiro-OMeTAD and PVK-[N(PhOCH₃)₂]₂.

Conclusion

To summarize, new functionalized poly(9-vinylcarbazole)s were introduced in PSCs. Their electronic and charge transport properties were determined, before being incorporated as hole transporting materials in PSCs. The suitable energy alignment and the high hole mobility of the PVK-[N(PhOCH₃)₂]₂ led to average photovoltaic performances close to those of spiro-OMeTAD with a best PCE achievement over 14.0 % in n-i-p planar devices. Importantly, the higher quality HTL provides a hydrophobic barrier preventing the perovskite from degradation induced by moisture present in atmosphere, resulting in an enhanced stability of the devices. These first results highlight the potential of the fine tuning of PVK properties through post-functionalization.

Incorporated into state-of-the-art mesoscopic PSCs, PVK-[N(PhOCH₃)₂]₂ exhibited up to 14.7 % PCE, due to a relatively low V_{oc} . It was found that the lead-rich perovskite employed in the mesoscopic PSCs affect the perovskite/HTM interface. By modifying the perovskite surface by depositing MAI, FAI or MABr salts, the V_{oc} was significantly improved yielding enhanced performances of the PSCs. Further investigations dealing with the composition of the perovskite surface and the interactions with PVK-[N(PhOCH₃)₂]₂ would be needed to explain this effect.

Finally, into modified planar devices, dopant-free PVK-[N(PhOCH₃)₂]₂ exhibited slightly higher PCE of 10.6 % than dopant-free spiro-OMeTAD PSCs.

Here it was demonstrated that doping of the polymer remains essential to improve its charge transport properties, and that behind the properties of the material itself, the choice of the device architecture and the reference material are of importance for the promotion of a novel HTM.

References

1. Jena, A. K.; Numata, Y.; Ikegami, M.; Miyasaka, T., Role of spiro-OMeTAD in performance deterioration of perovskite solar cells at high temperature and reuse of the perovskite films to avoid Pb-waste. *Journal of Materials Chemistry A* **2018**, 6 (5), 2219-2230.
2. (a) Zhao, X.; Wang, M., Organic hole-transporting materials for efficient perovskite solar cells. *Materials Today Energy* **2018**, 7, 208-220; (b) Yang, X.; Wang, H.; Cai, B.; Yu, Z.; Sun, L., Progress in hole-transporting materials for perovskite solar cells. *Journal of Energy Chemistry* **2018**, 27 (3), 650-672.
3. (a) Xu, B.; Sheibani, E.; Liu, P.; Zhang, J.; Tian, H.; Vlachopoulos, N.; Boschloo, G.; Kloo, L.; Hagfeldt, A.; Sun, L., Carbazole-Based Hole-Transport Materials for Efficient Solid-State Dye-Sensitized Solar Cells and Perovskite Solar Cells. *Advanced Materials* **2014**, 26 (38), 6629-6634; (b) Sung, S. D.; Kang, M. S.; Choi, I. T.; Kim, H. M.; Kim, H.; Hong, M.; Kim, H. K.; Lee, W. I., 14.8% perovskite solar cells employing carbazole derivatives as hole transporting materials. *Chemical Communications* **2014**, 50 (91), 14161-14163.
4. Limburg, W. W.; Williams, D. J., Variation in Inter-Ring Interactions in a Series of Carbazyl Group Containing Polymers. *Macromolecules* **1973**, 6 (5), 787-788.
5. Kim, H.-S.; Kim, C.-H.; Ha, C.-S.; Lee, J.-K., Organic solar cell devices based on PVK/porphyrin system. *Synthetic Metals* **2001**, 117 (1), 289-291.
6. Yang, L.; Yan, Y.; Cai, F.; Li, J.; Wang, T., Poly(9-vinylcarbazole) as a hole transport material for efficient and stable inverted planar heterojunction perovskite solar cells. *Solar Energy Materials and Solar Cells* **2017**, 163, 210-217.
7. Su, P.-Y.; Huang, L.-B.; Liu, J.-M.; Chen, Y.-F.; Xiao, L.-M.; Kuang, D.-B.; Mayor, M.; Su, C.-Y., A multifunctional poly-N-vinylcarbazole interlayer in perovskite solar cells for high stability and efficiency: a test with new triazatruxene-based hole transporting materials. *Journal of Materials Chemistry A* **2017**, 5 (5), 1913-1918.
8. Zhou, Z.; Zhao, Y.; Zhang, C.; Zou, D.; Chen, Y.; Lin, Z.; Zhen, H.; Ling, Q., A facile one-pot synthesis of hyper-branched carbazole-based polymer as a hole-transporting material for perovskite solar cells. *Journal of Materials Chemistry A* **2017**, 5 (14), 6613-6621.
9. Magomedov, A.; Paek, S.; Gratia, P.; Kasparavicius, E.; Daskeviciene, M.; Kamarauskas, E.; Gruodis, A.; Jankauskas, V.; Kantminiene, K.; Cho, K. T.; Rakstys, K.; Malinauskas, T.; Getautis, V.; Nazeeruddin, M. K., Diphenylamine-Substituted Carbazole-Based Hole Transporting Materials for Perovskite Solar Cells: Influence of Isomeric Derivatives. *Advanced Functional Materials* **2018**, 28 (9), 1704351.
10. Zimmermann, I.; Urieta-Mora, J.; Gratia, P.; Aragón, J.; Grancini, G.; Molina-Ontoria, A.; Ortí, E.; Martín, N.; Nazeeruddin, M. K., High-Efficiency Perovskite Solar Cells Using Molecularly Engineered, Thiophene-Rich, Hole-Transporting Materials: Influence of Alkyl Chain Length on Power Conversion Efficiency. *Advanced Energy Materials* **2016**, 7 (6), 1601674.
11. Zhang, F.; Wang, S.; Zhu, H.; Liu, X.; Liu, H.; Li, X.; Xiao, Y.; Zakeeruddin, S. M.; Grätzel, M., Impact of Peripheral Groups on Phenothiazine-Based Hole-Transporting Materials for Perovskite Solar Cells. *ACS Energy Letters* **2018**, 3 (5), 1145-1152.
12. Jung, H. S.; Park, N.-G., Perovskite Solar Cells: From Materials to Devices. *Small* **2014**, 11 (1), 10-25.
13. (a) Blakesley, J. C.; Castro, F. A.; Kylberg, W.; Dibb, G. F. A. *Protocol for extracting a space-charge limited mobility benchmark from a single hole-only or electron-only current-voltage curve*; National Physical Laboratory: 2014; (b) Blakesley, J. C.; Castro, F. A.; Kylberg, W.; Dibb, G. F. A.;

- Arantes, C.; Valaski, R.; Cremona, M.; Kim, J. S.; Kim, J.-S., Towards reliable charge-mobility benchmark measurements for organic semiconductors. *Organic Electronics* **2014**, *15* (6), 1263-1272.
14. (a) Ambrozevich, S.; van der Auweraer, M.; Dirin, D.; Parshin, M.; Vasil'ev, R.; Vitukhnovsky, A., Hole mobility and trapping in PVK films doped with CdSe/CdS and CdSe quantum dots. *Journal of Russian Laser Research* **2008**, *29* (6), 526-537; (b) Snaith, H. J.; Grätzel, M., Enhanced charge mobility in a molecular hole transporter via addition of redox inactive ionic dopant: Implication to dye-sensitized solar cells. *Applied Physics Letters* **2006**, *89* (26), 262114.
15. Scheer, R.; Schock, H.-W., *Chalcogenide Photovoltaics: Physics, Technologies, and Thin Film Devices*. Wiley ed.; 2011; p 384.
16. Juarez-Perez, E. J.; Leyden, M. R.; Wang, S.; Ono, L. K.; Hawash, Z.; Qi, Y., Role of the Dopants on the Morphological and Transport Properties of Spiro-MeOTAD Hole Transport Layer. *Chemistry of Materials* **2016**, *28* (16), 5702-5709.
17. Hawash, Z.; Ono, L. K.; Raga, S. R.; Lee, M. V.; Qi, Y., Air-Exposure Induced Dopant Redistribution and Energy Level Shifts in Spin-Coated Spiro-MeOTAD Films. *Chemistry of Materials* **2015**, *27* (2), 562-569.
18. Yang, W. S.; Park, B.-W.; Jung, E. H.; Jeon, N. J.; Kim, Y. C.; Lee, D. U.; Shin, S. S.; Seo, J.; Kim, E. K.; Noh, J. H.; Seok, S. I., Iodide management in formamidinium-lead-halide-based perovskite layers for efficient solar cells. *Science* **2017**, *356* (6345), 1376.
19. Stranks, S. D.; Eperon, G. E.; Grancini, G.; Menelaou, C.; Alcocer, M. J. P.; Leijtens, T.; Herz, L. M.; Petrozza, A.; Snaith, H. J., Electron-Hole Diffusion Lengths Exceeding 1 Micrometer in an Organometal Trihalide Perovskite Absorber. *Science* **2013**, *342* (6156), 341.
20. Xu, Y.; Bu, T.; Li, M.; Qin, T.; Yin, C.; Wang, N.; Li, R.; Zhong, J.; Li, H.; Peng, Y.; Wang, J.; Xie, L.; Huang, W., Non-Conjugated Polymer as an Efficient Dopant-Free Hole-Transporting Material for Perovskite Solar Cells. *ChemSusChem* **2017**, *10* (12), 2578-2584.

Chapter 4

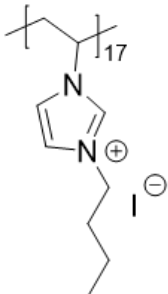
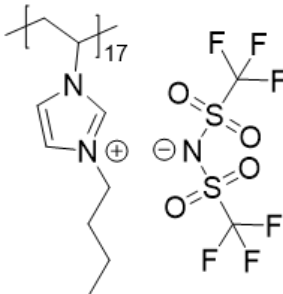
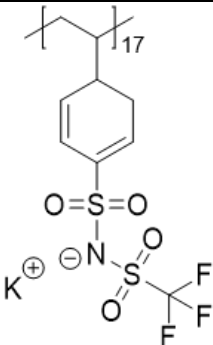
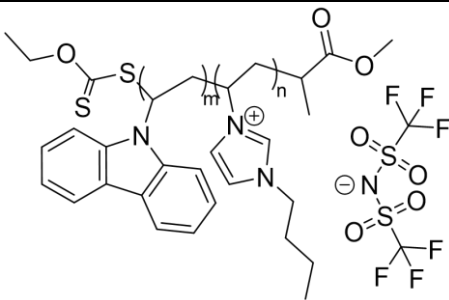
Polyelectrolytes in Perovskite Solar Cells

In this part, four polyelectrolytes are incorporated into perovskite solar cells. The properties of the polyelectrolytes for a potential application as HTM, dopant for HTMs, or dopant for the perovskite are studied. Thin film properties and photovoltaic performances of doped spiro-OMeTAD and doped perovskite are investigated. A new method to efficiently dope spiro-OMeTAD is presented.

1 Introduction

Polyelectrolytes are ionic polymers comprising ionic and/or ionisable groups in their units. Polycations contain positive charges, polyanions negative charges, and polyampholytes both positive and negative charges. They are stabilized by a counter ion. Poly(ionic liquid)s (PILS) are polyelectrolytes made from monomers containing ionic liquid specie. Due to specific electrochemical interactions, they are widely used to modify properties of aqueous solutions. Polyelectrolytes exhibit also high ionic conductivities that make them suitable for various applications in devices such as membranes for fuel cells, electrolytes for DSSCs, batteries or electrochemical supercapacitors.¹

Table 32. Polyelectrolytes studied in this part.

PVBI-I Poly(1-butyl-3-vinylimidazolium iodide)	PVBI-TFSI Poly(1-butyl-3-vinylimidazolium bis(trifluoromethylsulfonyl)imide)
 $M_n = 2140 \text{ g.mol}^{-1}$	 $M_n = 7350 \text{ g.mol}^{-1}$
PSTFSI-K Poly(4-styrenesulfonyl(trifluoromethylsulfonyl)imide) potassium	PILS(TFSI)-b-PVK Poly(1-butyl-3-vinylimidazolium bis(trifluoromethylsulfonyl)imide)-b-poly(9-vinylcarbazole)
 $M_n = 6000 \text{ g.mol}^{-1}$	 $m:n = 30:70$ $M_n = 10720 \text{ g.mol}^{-1}$

Herein, we propose to integrate polyelectrolytes into PSCs. The studied polyelectrolytes are two imidazolium based PILS (PVBI-I and PVBI-TFSI), a polyanion (PSTFSI-K) and a block copolymer made of

PVK and imidazolium-based PILS blocks (PILS(TFSI)-*b*-PVK) (Table 32). In the following, we investigate their potential use as HTM, dopant for spiro-OMeTAD, or additive for the organic-inorganic hybrid perovskite. Synthesis details and characterizations (NMR and SEC/GPC) of the polyelectrolytes are provided in the Experimental Details section.

1.1 Potential use as hole transport material

As mentioned in Chapter 1, conjugated and non-conjugated polymers have been successfully used as hole transport materials in PSCs. The most popular conjugated polyelectrolyte employed in the field of organic electronics is PEDOT:PSS. It was introduced for the first time in planar inverted PSCs in 2015 by Jeng *et. al.*, the corresponding devices showing PCEs below 4 %.² Further optimization of the active layer materials pushed PCEs above 20 %.³ To circumvent issues related to the acidity of PEDOT:PSS, other polyelectrolytes were developed as HTM in planar inverted PSCs. Thus, CPE-K polyelectrolyte (Figure 76) achieved over 12 % efficiency as the first alternative to PEDOT:PSS in 2015.⁴ More recently P3CT-Na (Figure 76) reported improved PCE of 16.6 % versus PEDOT:PSS which was attributed to a well match of energy levels in the device.⁵ No examples of the use of poly(ionic liquid)s or block copolymers as HTM in PSCs have been described in the literature. However, the good electronic conductivity of ionic liquids and poly(9-vinylcarbazole) (PVK) could make PVBI-I, PVBI-TFSI and PILS(TFSI)-*b*-PVK good candidates as HTMs.

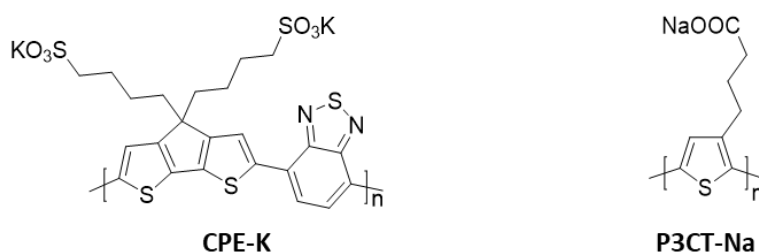


Figure 76. CPE-K and P3CT-Na structures.

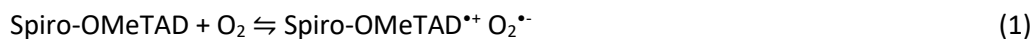
1.2 Potential use as dopant for spiro-OMeTAD

Organic semiconductors suffer from low conductivity and require p-type doping to perform similarly to traditional inorganic semiconductors. In the case of spiro-OMeTAD, doping via oxidation reaction can be slowly achieved by oxygen and either light or thermal excitation.⁶ To accelerate this process, lithium bis(trifluoromethanesulfonyl)imide salt (LiTFSI) and *tert*-butylpyridine (tBP) are usually added to the HTM precursor solution. Unlike chemical dopants, LiTFSI is a redox inactive couple which doesn't directly react with spiro-OMeTAD but catalyses the oxidation reaction.⁷ On the other hand,

tBP helps to solubilize all species and improve the wetting of the HTM solution on the perovskite film by increasing its polarity. In DSSCs, it has also been reported to adsorb to the TiO₂ surface, resulting in a downshifting of the TiO₂ conduction band, and to fill trap states of the TiO₂.⁸

However, this oxygen and light exposure dependency makes the doping process difficult to control and to reproduce. Moreover, oxygen rich atmosphere, that may also contain certain amount of moisture, and the use of hygroscopic salts could compromise the stability of the final device as it is well known that humidity could be detrimental for perovskite performance.⁹ In addition, it has been reported that Li⁺ cations can diffuse either through the perovskite to the TiO₂ interface,¹⁰ or through the HTM to the gold top electrode. In any case, pinholes and channels are created into the layer, accelerating the degradation of the devices. Damage of the perovskite layer can also be induced by tBP which, after ageing, forms PbI₂ complex,¹² or iodopyridinate complex.¹³ Finally, tBP can easily evaporate during the process or the storage of solar cells due to its relatively low boiling point.¹⁴

In order to find valuable alternatives to the LiTFSI-tBP cocktail, doping mechanisms of spiro-OMeTAD were investigated.^{7, 15} p-Type chemical doping consists in introducing chemical impurities into the organic semiconductor, able to transfer positive charge to the molecule, increasing the hole density in the layer. Deepest trap states should be filled by these created holes, and thus increase hole mobility. Spiro-OMeTAD oxidation process by oxygen is described by the Reaction (1). Reaction (2) occurs in presence of metal-TFSI salt. Kinetics of the reaction will depend on the nature of the alkali metal. Although LiTFSI accelerate oxidation reaction, it was not the case for NaTFSI. However, in conjunction with an acid like H₃PO₄, spiro-OMeTAD oxidation reaction can occur. In the same study, it was demonstrated that a moderate acid like H₃PO₄ cannot oxidize spiro-OMeTAD itself. This drives us to the reaction (3), where it is suggested that the acid function accelerate the oxidation reaction with the metal-TFSI salt.¹⁵



Due to their strong Coulomb field, ionic species affect in two ways the charge transport. The Coulomb wells can overlap resulting in a reduction of the barrier height for hopping process, but can also induce additional trap states. Nonetheless, in the case where the trap sites are close enough, hopping process can occur between them. On the other hand, in the presence of a Brønsted acid,

hydrogen bonding between spiro-OMeTAD and the acidic proton was evidenced. It is expected to induce partial positive charge and reduce columbic trapping in spiro-OMeTAD.¹⁵

Doping of spiro-OMeTAD can also be realized by direct one electron oxidation. Introduction of cobalt (FK102, FK209, FK269),¹⁶ or molybdenum complexes ($\text{Mo}(\text{tfd-COCF}_3)_3$, $\text{Mo}(\text{tfd-CO}_2\text{Me})_3$) (Figure 77) to spiro-OMeTAD leads to an equilibrium reaction where an electron is transferred from the spiro-OMeTAD to the complex.¹⁷ In the case of copper salts (CuSCN , CuI), charge transfer results in the formation of composite with spiro-OMeTAD.¹⁸ Another strategy consists of the direct introduction of spiro-OMeTAD oxidized forms, $\text{spiro}^{2+}(\text{TFSI})_2^-$ or $\text{spiro}^{2+}(\text{PF}_6)_2^-$. In presence of excess of neutral spiro-OMeTAD, doubly oxidized spiro-OMeTAD forms twice the amount of singly oxidized spiro-OMeTAD.¹⁹ Strong electron accepting compounds such as tin(IV) chloride (SnCl_4),²⁰ perfluoro-tetracyanoquinodimethane (F_4TCNQ),²¹ tris(pentafluorophenyl)borane,²² or benzoyl peroxide,²³ can also be employed as dopants for spiro-OMeTAD.

Though the addition of these materials to spiro-OMeTAD was found to improve the conductivity, for most of these materials, obtaining the best device performances still require the use of LiTFSI and tBP. The benefit of these additives is that spiro-OMeTAD oxidation can be achieved in inert atmosphere, without involving oxygen. The whole device process can be realized without the need to be exposed to atmosphere, avoiding device degradation. The FK209 cobalt complex is today the best additive to the spiro-OMeTAD-LiTFSI-tBP system that can achieve higher stability and in some processes higher efficiencies.

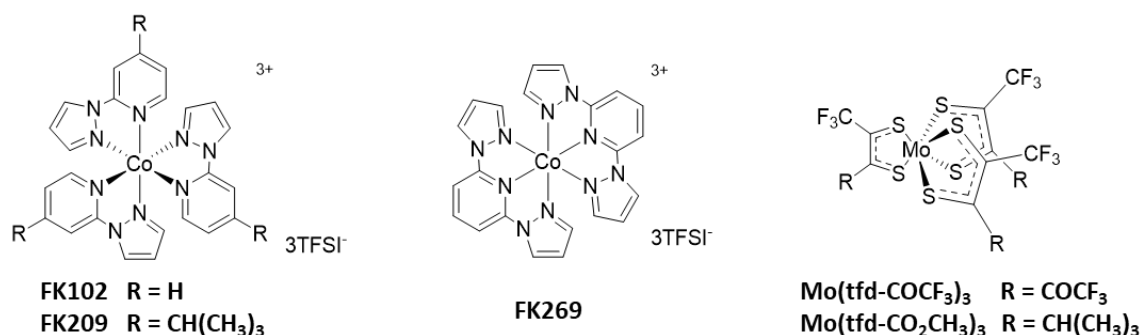


Figure 77. Structure of cobalt and molybdenum-based dopants.

Few examples of efficient alternative dopants are reported. $\text{Mo}(\text{tfd-COCF}_3)_3$ complex achieved efficiencies of up to 17.8 %, and improved stability without employing LiTFSI or tBP.¹⁷ Tris(pentafluorophenyl) borane doped PTAA, through the formation of an adduct, exhibited a PCE as high as 19 % with good stability.²⁴ It was the first time that a novel dopant showed an efficiency higher than a device based on the classical LiTFSI-tBP dopants.

A last alternative to LiTFSI and tBP are *N*-heterocyclic ionic liquids (Figure 78). Ionic liquids have the advantage to be non-volatile, to have high ionic conductivity, an excellent stability in air and a good ability to solvate chemicals. In the range of ionic liquids, protic and aprotic ionic liquids can be distinguished. Protic ionic liquids, able to transfer protons, can be assimilated to Brønsted acid-base couples. First, Abate *et. al.* demonstrated the ability of an imidazole-based ionic liquid (Himi-TFSI) to chemically oxidize spiro-OMeTAD in DSSCs.²⁵ The mechanism proposed relies on the Brønsted acid-base property of the ionic liquid, generating a hydrogen bonding with the spiro-OMeTAD amine. Based on this study, Zhang *et. al.* used BuPylm-TFSI with a pyridyl ending group which was supposed to fulfil the role of tBP, i.e. suppress charge recombination at the TiO₂/perovskite interface in PSCs.²⁶ In both cases, conductivity of spiro-OMeTAD was efficiently increased without using LiTFSI nor tBP. More recently, a pyridinium based ionic liquid was successfully introduced in spiro-OMeTAD achieving efficiency of 14 % with improved stability.²⁷ The doping mechanism proposed was similar to LiTFSI, where BMPy-TFSI accelerated the oxidation reaction of spiro-OMeTAD with oxygen.

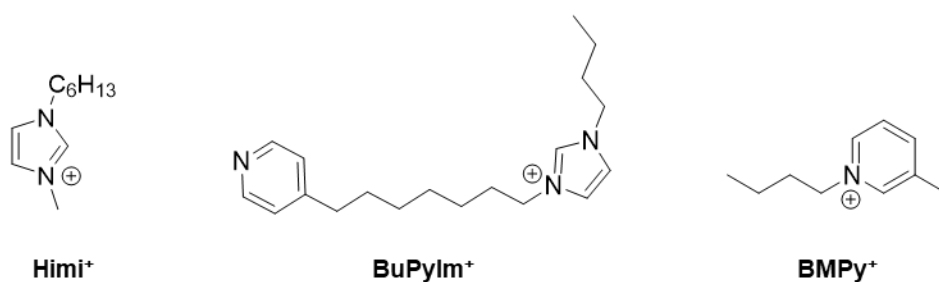


Figure 78. Chemical structures of *N*-heterocyclic ionic liquid dopants.

As a consequence, the polyelectrolytes shown in Table 1 should have the ability to dope spiro-OMeTAD. Poly(ionic liquid)s are expected to efficiently dope spiro-OMeTAD following the mechanisms previously described with imidazolium-based ionic liquids. PSTFSI-K is also supposed to dope spiro-OMeTAD. The doping mechanism is speculated to be the same as using LiTFSI. The larger size of the polymer should be less prone to diffusing through the HTM or the perovskite layer. Thus, this could improve film homogeneity, moisture and oxygen resistance, and device stability. Incorporating PILS(TFSI)-*b*-PVK, the poly(ionic liquid) block is expected to dope spiro-OMeTAD while the PVK block enhances hole conductivity in the layer.

1.3 Potential use as dopant for the perovskite

The motivation for doping the hybrid perovskite mainly comes from the difficulties to form perovskite thin films of high quality, and its instability towards humidity but also heat and UV light.

Various examples of ionic liquids as solvent or dopant for the perovskite can be found in the literature: tetraphenylphosphonium iodide and chloride,²⁸ 1-hexyl-3-methylimidazolium chloride,²⁹ 1-ethylpyridinium chloride,³⁰ methyl ammonium formate,³¹ 1,1,1-trifluoro-ethyl-ammonium iodide,³² and 1-methyl-3-(1H,1H,2H,2H-nonafluorohexyl)-imidazolium iodide.³³ Generally, ionic liquids are reported to enlarge crystal size, minimize trap sites, enhance stability of PSCs, but do not necessarily lead to higher PV performances. The most performing system employed 2 mol.% of 1-allyl-3-methylimidazolium iodide in the MAPbI₃ perovskite precursor solution to reach over 19 % efficiency with improved stability.³⁴ In the case of imidazolium-based ionic liquids, the extended lifetime of the devices is attributed to the hydrophobic nature of the imidazolium salt, and to the improved quality of the perovskite film. Moreover, it was demonstrated that it had negligible effect on the perovskite crystal structure.³³

Polymers and polyelectrolytes have also been introduced as additives to the perovskite precursor solution in order to improve the morphology and the stability of the films. First attempt employing MEH-PPV improved the crystallinity of the formed perovskite-polymer nanocomposite, but led to efficiencies of only 3%.³⁵ It paved the way to polymers such as PVP,³⁶ PEG,³⁷ and PMMA,³⁸ and polyelectrolytes like PDAA-Cl,³⁹ and PVAm-HI.⁴⁰ The improved film forming and stability of the devices were attributed to a crosslink effect through hydrogen bonding between the polymers and the ammonium cation. In the case of PVAm-HI, the ammoniums of the polyvinylammonium are considered as nucleation sites, connecting the crystals together and suppressing grain boundaries. A best efficiency of 16.3 % was achieved with this system. Best PV performances were obtained using PMMA as a template and stabilizer for the crystal growth which led to efficiencies exceeding 21 %.³⁸

Finally, bulk heterojunctions were found to be structures of interest to enhance PV performances. The addition of a fullerene derivative into the perovskite blend allows to increase the interface between the perovskite and the n-type material to enhance charge separation and transport. It was first introduced by Sargent *et. al.* who reported a significant reduction of the hysteresis and an increase of efficiency from 12.0 % to 14.4 %.⁴¹ Further research was focused on processes or modifications of the fullerene to improve its solubility in chlorobenzene.⁴²

Poly(ionic liquid)s may also have same benefits as ionic liquids on the perovskite morphology. The iodide counter anion of PVBI⁺ could be integrated to the perovskite crystal. Through hydrogen bonding, polymers may help the perovskite crystal growth. Polymer-perovskite bulk heterojunction could also minimize grain boundaries defects and improve hole extraction. Moreover, K⁺ alkali cation of PSTFSI-K could dope the perovskite as KI salt. However, polyelectrolytes have good ionic conductivity. Into the perovskite layer, it could encourage ionic diffusion and enlarge the hysteresis.

2 Properties of the polyelectrolytes

2.1 Solubility

First of all, solubility of the polyelectrolytes was tested in different common solvents with different polarities in a concentration of 50 mg/mL (Table 33). As mentioned before, non-polar solvents are suitable for the deposition of HTM on top of the perovskite, while polar solvents can alter the perovskite layer. All of the polyelectrolytes showed good solubilities in DMF and DMSO but were poorly soluble in chlorobenzene. Although it is compromising for an application as HTM, they should be easily used as dopants in the perovskite. PVBI-TFSI was partially soluble in toluene, and PILS(TFSI)-*b*-PVK in chloroform and dichloromethane. The poly(ionic liquid)s, PVBI-I and PVBI-TFSI were well soluble in acetonitrile, which is usually employed to dissolve the LiTFSI salt. PSTFSI-K and PILS(TFSI)-*b*-PVK were partially soluble in this last solvent.

Table 33. Solubility of the polymers in different solvents.

Solvent	ϵ^a	bp ^b °C	PSTFSI-K	PILS(TFSI)- <i>b</i> - PVK	PVBI-I	PVBI-TFSI
Toluene	2.38	111	-	-	-	+/-
Chlorobenzene	5.62	132	-	-	-	-
Chloroform	4.81	61	-	+/-		
Dichloromethane	8.93	40	-	+/-		
Diethyl ether	4.33	35	-			
Ethyl acetate	6.02	77	+/-		+	+
Acetone	20.7	56	+/-	-	+	+
DMF	36.7	152	+	+	+	+
DMSO	46.7	189	+	+	+	+
Acetonitrile	37.5	82	+/-	+/-	+	+
Ethanol	24.5	78	-	-		
Methanol	32.7	65	+ (T > 70°C)	+ (T > 70°C)		
Water	80.1	100	+	-	-	-

^a ϵ : dielectric constant; ^b bp: boiling point.

2.2 Opto-electronic properties

Absorption spectra of polymers were recorded in solution (0.01 %), in quartz cells, between 800 and 200 nm (Figure 79a). PSTFSI-K was dissolved in water, while PVBI-I and PVBI-TFSI in acetonitrile. The absorption of the copolymer was recorded until 300 nm due to the short cut of the DMF. The polyelectrolytes did not absorb in the visible range, and thus would not affect the absorption of the

perovskite. PVBI-TFSI showed an absorption peak at 221 nm with a small bump around 280 nm, PVBI-I at 245 nm, PSTFSI-K at 230 nm with a small bump at 260 nm, and finally, PILS(TFSI)-*b*-PVK showed two peaks at 330 and 343 nm.

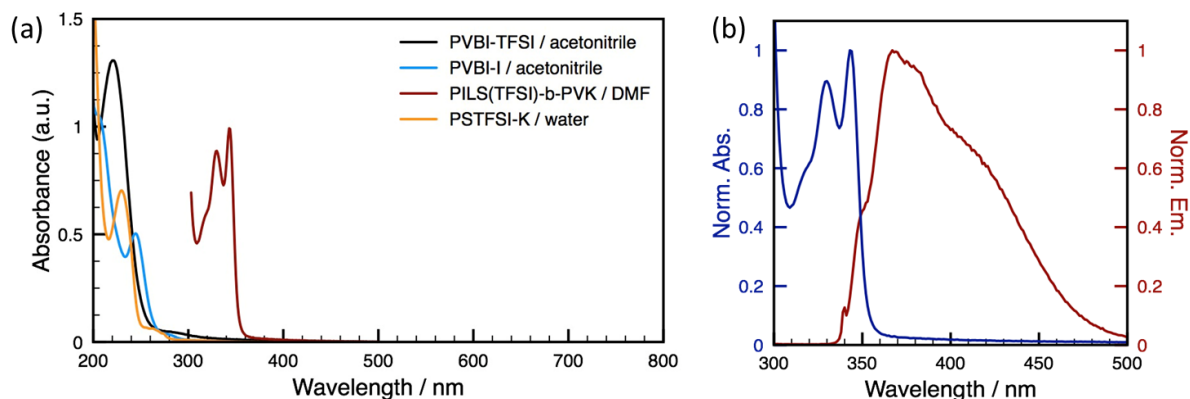


Figure 79. (a) Absorption spectra of PVBI-TFSI, PVBI-I, PILS(TFSI)-*b*-PVK and PSTFSI-K. (b) Emission and absorption spectra of PILS(TFSI)-*b*-PVK.

Emission spectra were recorded by exciting the solution at the wavelength of the first absorption peak. However, our apparatus does not allow excitation wavelength below 300 nm. Thus, only the emission of the copolymer, was performed at an excitation wavelength of 340 nm (Figure 79b). The bandgap of the material, defined by the intersection of the absorption and emission spectra, was measured at 349 nm, i.e. 3.57 eV. Since PSTFSI-K, PVBI-TFSI and PVBI-I absorbed at shorter wavelength, their bandgap was even larger. Basically, a semiconductor is defined with a bandgap around 1 eV and an insulator with a bandgap > 5 eV. Our polymers are somewhere in between, PILS(TFSI)-*b*-PVK being the most “semiconducting” one.

For an application as HTM, HOMO level of the polyelectrolyte should be close to the - 5.7 eV valence band maximum of the perovskite. To evaluate the HOMO level, photoelectron spectroscopy was performed on PSTFSI-K and PILS(TFSI)-*b*-PVK films deposited on glass, from DMSO and DMF respectively. However, no ionization potential was found between 4 and 7 eV. HOMO levels of PVBI-TFSI and PVBI-I were not measured due to the poor quality of the films coated, even dissolved in good solvents.

Finally, regarding the poor solubility of the materials in non-polar solvents, the difficulties to coat homogeneous films, and discrepancy between HOMO levels and the perovskite valence band, none was found suitable for an application as HTM in n-i-p PSCs. Therefore, further experiments are dedicated to the potential use of the polyelectrolytes as dopants for spiro-OMeTAD and the perovskite.

3 Polyelectrolytes as alternative dopants to LiTFSI for spiro-OMeTAD

3.1 Preliminary results

The standard HTM precursor solution is composed of spiro-OMeTAD, LiTFSI previously dissolved in acetonitrile, and tBP. Herein, the objective was to replace LiTFSI by one of our polyelectrolytes PSTFSI-K, PILS(TFSI)-*b*-PVK, PVBI-I or PVBI-TFSI, in order to enhance photovoltaic performances and/or stability of the devices. Therefore, a preliminary study of solubility, and the effect of the dopants on the HOMO level of the HTMs were investigated, before making perovskite solar cells.

3.1.1 Solubility

The first step was to properly dissolve the polymers with the spiro-OMeTAD. The concentrations are expressed in molar equivalence as $x:y:z$, where x corresponds to spiro-OMeTAD, y to LiTFSI or to the polyelectrolytes (moles of monomer), and z to tBP. To properly dissolve LiTFSI to the solution of spiro-OMeTAD in chlorobenzene, LiTFSI is previously dissolved in high concentration in acetonitrile (520 mg/mL). However, this pre-dissolution of the dopants was not possible with our materials due to the few quantities available. Thus, our first attempt was to directly dissolve the dopants and spiro-OMeTAD in chlorobenzene. Same amount of acetonitrile used in LiTFSI-spiro was added. PVBI-I and PVBI-TFSI were successfully incorporated to the spiro-OMeTAD solution, probably due to their good solubility in acetonitrile. However, PSTFSI-K and PILS(TFSI)-*b*-PVK were not soluble even after hours of sonication, stirring up to 100°C, or replacing acetonitrile by DMF. The second approach consisted in solubilizing HTMs and PSTFSI-K or PILS(TFSI)-*b*-PVK in DMF, letting evaporate the DMF overnight on a hot plate at 200°C, and resolubilizing species in chlorobenzene. In the end, the solutions were milky-brown, probably due to the degradation of spiro-OMeTAD, meaning that the solubility of the materials was not improved, and one or both materials were degraded. So, the first process was chosen to make the solutions whatever the polyelectrolytes introduced in spiro-OMeTAD.

3.1.2 HOMO level

Doping allows to control the fermi level position of the semiconductor to facilitate charge carrier injection. HOMO levels of spiro-OMeTAD were measured by PESA in Figure 80 and are reported in Table 34. HOMO levels are deduced by extrapolation of the two trend curves as depicted for pristine Spiro-OMeTAD in Figure 80. Uncertainty of 0.05 eV is assumed using this method. Films were deposited by spin coating on glass substrates and dried at 70°C for 10 min. Excess of particles were removed from the solutions containing PSTFSI-K and PILS(TFSI)-*b*-PVK with a PTFE filter of 1 μm to improve the quality of the films. Effective doping should deep spiro-OMeTAD HOMO level. PVBI-TFSI, PSTFSI-K and PILS(TFSI)-*b*-PVK were able to reduce the HOMO level of spiro-OMeTAD, especially

PSTFSI-K and PILS(TFSI)-*b*-PVK who reached similar HOMO value as LiTFSI. PVBI-I was the only additive that increased the HOMO level of spiro-OMeTAD.

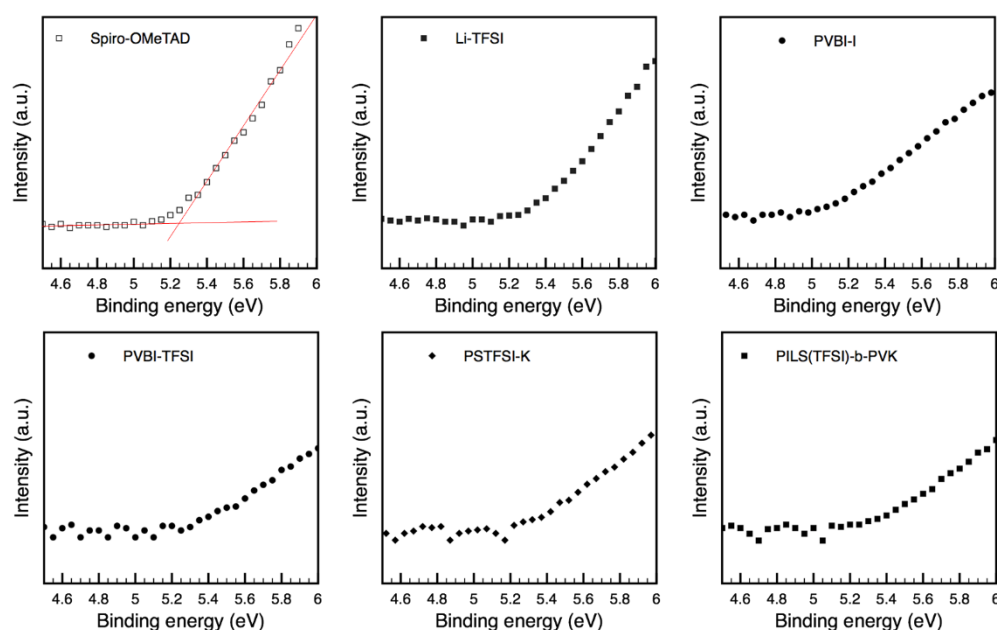


Figure 80. UPS spectra of pristine spiro-OMeTAD and doped spiro-OMeTAD films with LiTFSI, PVBI-I, PVBI-TFSI, PSTFSI-K, and PILS(TFSI)-*b*-PVK.

Table 34. HOMO level of spiro-OMeTAD doped with one of the dopant and tBP. Molar equivalence was 1:0.5:3.3.

Dopant	HOMO level eV
None	- 5.25
LiTFSI	- 5.35
PVBI-I	- 5.10
PVBI-TFSI	- 5.30
PSTFSI-K	- 5.34
PILS(TFSI)- <i>b</i> -PVK	- 5.35

3.1.3 Perovskite solar cells

Finally, the performances of the same mixtures were tested in mesoporous PSCs, where the architecture was described in Chapter 2. The process was exactly the same for polymer dopants than for LiTFSI. The molar equivalence was 1:0.5:3.3. Solutions were spin-coated at 4000 rpm for 30 s and dried at 70°C for 10 min. I-V curves were measured under AM1.5 illumination with an incident power

of 100 mW/cm². Best and average PV parameters and hysteresis indexes, *i.e.* HIs, based on 4 cells are given in Table 21. Hysteresis index was defined as $HI = (PCE_{reverse} - PCE_{forward}) / PCE_{reverse}$.

Table 35. Best and average PV parameters and hysteresis index of PSCs using different dopant in spiro-OMeTAD.

HTM dopant	Reverse scan				Forward scan				HI
	J _{sc}	V _{oc}	FF	PCE	J _{sc}	V _{oc}	FF	PCE	
	mA.cm ⁻²	V		%	mA.cm ⁻²	V		%	
LiTFSI	22.45 ^a	1.10	0.73	18.44	22.71	1.10	0.71	17.71	0.039
	22.31 ^b	1.107	0.73	18.12	22.65	1.104	0.70	17.46	0.037
	± 0.25 ^c	± 0.005	± 0.02	± 0.55	± 0.23	± 0.006	± 0.03	± 0.013	± 0.013
PVBI-TFSI	23.07	1.139	0.73	19.14	23.34	1.13	0.683	18.07	0.056
	22.81	1.137	0.72	18.69	23.08	1.13	0.682	17.81	0.047
	± 0.21	± 0.003	± 0.01	± 0.45	± 0.20	± 0.01	± 0.003	± 0.23	± 0.012
PVBI-I	16.03	1.02	0.22	3.57	14.61	1.00	0.22	3.18	0.109
	11.99	0.96	0.19	2.32	10.13	0.93	0.20	2.00	0.154
	± 3.94	± 0.06	± 0.03	± 1.16	± 4.13	± 0.07	± 0.02	± 1.08	± 0.043
PSTFSI-K	21.12	1.09	0.58	13.30	21.70	1.09	0.50	11.78	0.114
	20.88	1.09	0.55	12.47	21.33	1.09	0.49	11.29	0.093
	± 0.42	± 0.01	± 0.04	± 1.17	± 0.62	± 0.01	± 0.02	± 0.73	± 0.029
PILS(TFSI)- b-PVK	19.95	1.08	0.56	12.04	20.42	1.09	0.49	10.82	0.101
	19.73	1.07	0.54	11.43	20.23	1.08	0.46	10.08	0.118
	± 0.32	± 0.01	± 0.01	± 0.48	± 0.31	± 0.01	± 0.03	± 0.88	± 0.052

^a Best cell; ^b average on 4 cells; ^c standard deviation of the average.

PVBI-I doped spiro-OMeTAD PSCs exhibited the worst PV performances with a particularly low FF (< 0.2) resulting in PCEs about 2%. Undesirable interactions with the perovskite led after ageing to the formation of holes in the perovskite layer. On the other hand, acceptable J_{sc}, around 20 mA.cm⁻², and V_{oc}, between 1.05 and 1.14 V, were measured with PVBI-TFSI, PSTFSI-K and PILS(TFSI)-b-PVK. However, low FFs were obtained for PSTFSI-K and PILS(TFSI)-b-PVK, limiting the PCEs to 12%. Low FFs might be associated to the heterogeneous morphology of the HTLs due to the limited solubility of the polymer dopants. It is noteworthy that high PCEs, 19.14 % for the best device, were obtained with PVBI-TFSI (Figure 81). This performance was even higher than the best device doped with LiTFSI without ageing. This increase in efficiency was the result of an increase in V_{oc}, 1.14 vs. 1.10 V, in fill factor, 0.73 vs. 0.71, and in J_{sc}, 23.07 vs. 22.45 mA.cm⁻².

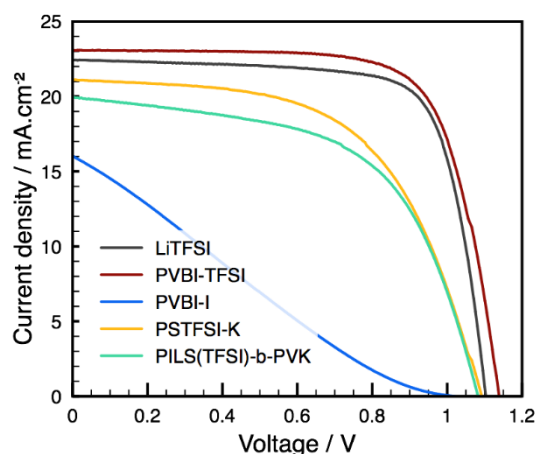


Figure 81. Best I-V curves of PSCs using different dopants in spiro-OMeTAD.

Regarding the high performances obtained with PVBI-TFSI in spiro-OMeTAD, the effect of PVBI-TFSI was also studied employing PVK-[N(PhOCH₃)₂]₂ as HTM. The optimal formulation for LiTFSI in mesoporous solar cells, 1:2.5:8.25, was used to compare both dopants. HOMO level of pristine PVK-[N(PhOCH₃)₂]₂ was -5.23 eV. It was significantly reduced to -5.39 with LiTFSI and to -5.43 eV with PVBI-TFSI (Figure 82).

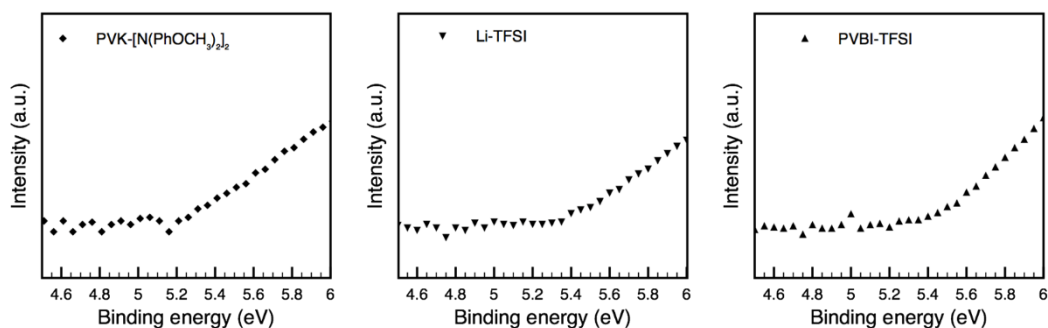


Figure 82. UPS spectra of pristine PVK-[N(PhOCH₃)₂]₂ and PVK-[N(PhOCH₃)₂]₂ doped with LiTFSI and PVBI-TFSI.

However, lower PV performances were obtained with PVBI-TFSI, with a maximum efficiency of 12.2 % against 14.7 % with LiTFSI (Figure 83, Table 36). Hysteresis was also larger, with higher efficiencies for the forward scan. The different effect of PVBI-TFSI on the HTMs may be related to their different size. Spiro-OMeTAD molecule is more likely to interact and to be doped by PVBI-TFSI than the PVK-[N(PhOCH₃)₂]₂ polymer.

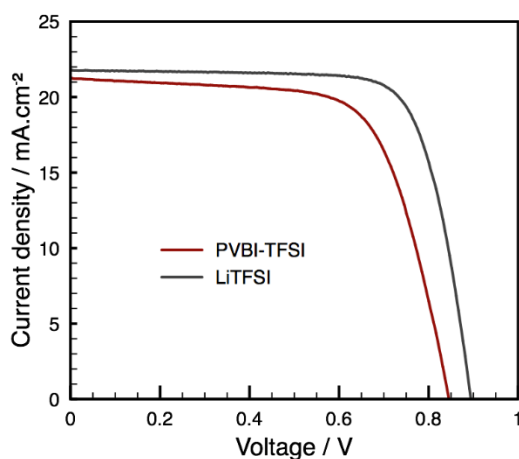


Figure 83. Best I-V curves of PSCs using different dopants in PVK-[N(PhOCH₃)₂]₂.

Table 36. Best and average PV performances and hysteresis index of PVK-[N(PhOCH₃)₂]₂-based PCSs doped with LiTFSI or PVBI-TFSI.

HTM	Reverse scan				Forward scan				HI
dopant	J _{sc}	V _{oc}	FF	PCE	J _{sc}	V _{oc}	FF	PCE	
	mA.cm ⁻²	V		%	mA.cm ⁻²	V		%	
LiTFSI	21.78 ^a	0.894	0.754	14.69	21.87	0.901	0.730	14.40	0.020
	21.59 ^b	0.886	0.7474	14.28	21.74	0.895	0.708	13.78	0.036
	± 0.21 ^c	± 0.011	± 0.026	± 0.41	± 0.24	± 0.005	± 0.042	± 0.92	± 0.039
PVBI-TFSI	17.06	0.830	0.618	8.74	21.25	0.845	0.677	12.16	-0.391
	14.29	0.795	0.586	6.82	21.23	0.841	0.670	11.97	-0.990
	± 3.74	± 0.042	± 0.040	± 2.37	± 0.11	± 0.005	± 0.015	± 0.31	± 0.919

^a Best cell; ^b average on 4 cells; ^c standard deviation of the average.

In summary, these preliminary results clearly indicate that the spiro-OMeTAD-PVBI-TFSI-tBP system is the most promising one to reach high efficiencies with low hysteresis. Therefore, the study was pursued through the optimization of the devices containing PVBI-TFSI and tBP doped spiro-OMeTAD. In the following parts, Li-spiro and PVBI-spiro refer respectively to LiTFSI and tBP doped spiro-OMeTAD and to PVBI-TFSI and tBP doped spiro-OMeTAD.

3.2 PVBI-TFSI and tBP doped spiro-OMeTAD

3.2.1 Photovoltaic performances

PVBI-TFSI concentration, tBP concentration, annealing conditions, and amount of acetonitrile were optimized. For each parameter, the best and the average PV performance and hysteresis index of 4 cells were compared.

First, the PVBI-TFSI and tBP concentrations were simultaneously varied in the layer, from 0.25 to 2 molar equivalent of PVBI-TFSI vs. spiro-OMeTAD, and from 0.83 to 13.2 of tBP vs. spiro-OMeTAD (Table 37, Figure 84).

Table 37. PV parameters and hysteresis index of PSCs using different concentrations of PVBI-TFSI and tBP in spiro-OMeTAD.

HTM dopant	Reverse scan				Forward scan				HI
	J _{sc}	V _{oc}	FF	PCE	J _{sc}	V _{oc}	FF	PCE	
	<i>mA.cm⁻²</i>	<i>V</i>		%	<i>mA.cm⁻²</i>	<i>V</i>		%	
1:0.25:1.7	22.84 ^a	1.12	0.71	18.25	23.14	1.11	0.67	17.13	0.062
	22.68 ^b	1.12	0.71	17.94	22.96	1.11	0.67	16.96	0.055
	± 0.12 ^c	± 0.01	± 0.01	± 0.47	± 0.13	± 0.01	± 0.01	± 0.39	± 0.006
1:0.5:3.3 (Ref)	22.69	1.133	0.714	18.35	23.01	1.124	0.679	17.55	0.044
	22.60	1.134	0.710	18.19	22.90	1.125	0.680	17.52	0.037
	± 0.07	± 0.001	± 0.004	± 0.15	± 0.09	± 0.002	± 0.004	± 0.13	± 0.006
1:1:6.6	22.75	1.15	0.77	20.29	22.99	1.16	0.76	20.33	-0.002
	22.72	1.14	0.76	19.80	22.94	1.15	0.75	19.86	-0.003
	± 0.21	± 0.01	± 0.01	± 0.54	± 0.17	± 0.01	± 0.01	± 0.64	± 0.007
1:1.5:9.9	22.88	1.13	0.76	19.74	23.11	1.13	0.76	19.88	-0.007
	22.81	1.12	0.764	19.56	23.04	1.12	0.763	19.73	-0.009
	± 0.06	± 0.01	± 0.001	± 0.15	± 0.06	± 0.01	± 0.001	± 0.12	± 0.003
1:2:13.2	22.60	1.139	0.73	18.85	22.98	1.135	0.73	19.02	-0.009
	22.30	1.134	0.73	18.45	22.62	1.129	0.73	18.76	-0.017
	± 0.36	± 0.003	± 0.01	± 0.41	± 0.40	± 0.004	± 0.01	± 0.27	± 0.023

^a Best cell; ^b average on 4 cells; ^c standard deviation of the average.

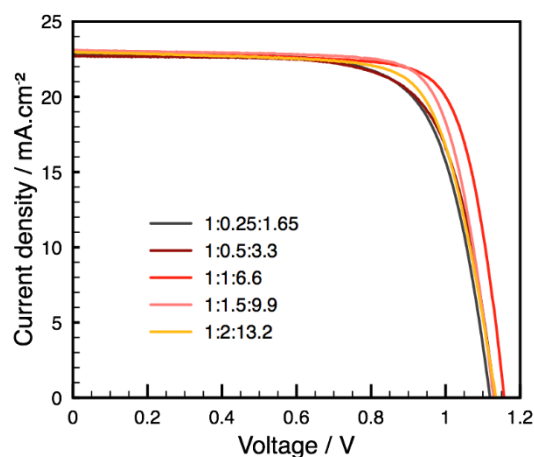


Figure 84. Best I-V curves of PSCs using different concentrations of PVBI-TFSI and tBP vs. spiro-OMeTAD.

Optimal V_{oc} , FF, and PCE were obtained by doubling the PVBI-TFSI and tBP concentrations (1:1:6.6) compared to the standard Li-spiro. A best PCE of 20.33 % was recorded, thanks to improved V_{oc} , as high as 1.16 V, and FF of 0.76. Moreover, hysteresis was reduced to a HI of -0.003, corresponding to a difference in efficiency of 0.06 % between the forward scan and the reverse scan. Interestingly, the hysteresis behaviour can be tuned by the concentration of PVBI-TFSI and tBP. When increasing the dopants concentration, the positive HI decreased and became negative, meaning that the efficiency of the forward scan exceeds the one of the reverse scan.

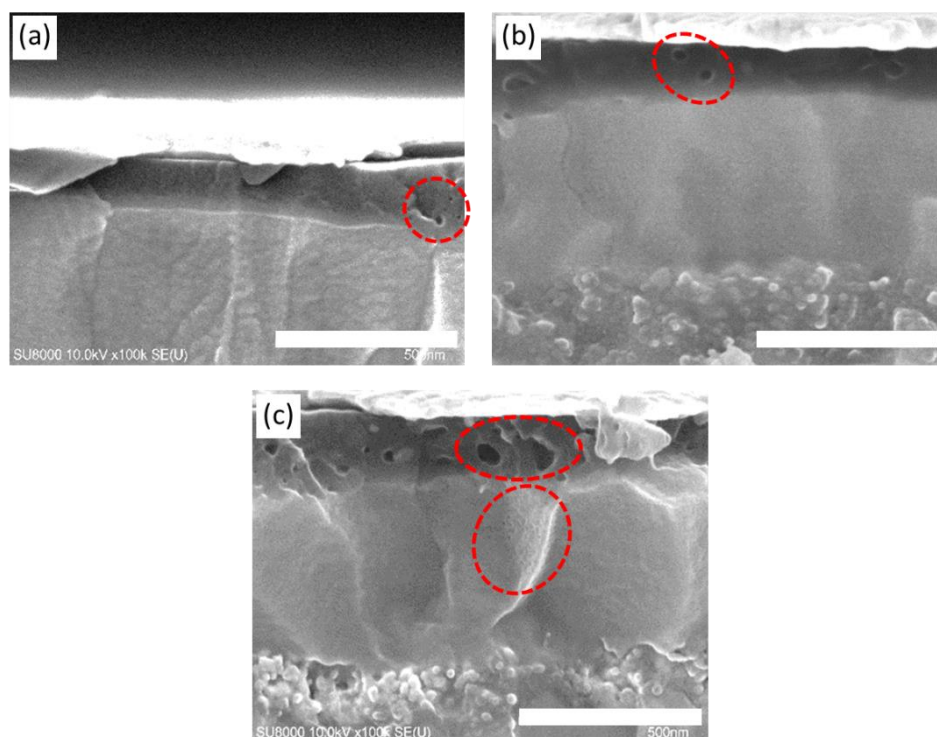


Figure 85. SEM cross sections of PSCs containing (a) Li-spiro, (b) 1:1:6.6 PVBI-spiro, and (c) 1:1.5:9.9 PVBI-spiro. Some holes are circled in red. Scale bar = 500 nm.

The morphology of the layers was controlled by looking at the cross section of devices by SEM (Figure 85). In the Li-spiro layer, typical holes with a diameter about 15 nm can be distinguished. In the PVBI-spiro, less but larger holes, about 40 nm, were revealed. Additional to bigger and more numerous holes when increasing the doping, small holes were formed in the perovskite near the perovskite/HTM interface, explaining the decrease in PV performances. Holes in the perovskite may result from the ability of tBP to dissolve the perovskite.

Three annealing conditions were then tested for the 1:1:6.6 concentration: the classical annealing at 70°C for 10 min, a flash annealing at 160°C for 20 s and no annealing. The flash annealing may degrade the HTL resulting in significantly reduced V_{oc} , FF and PCE (Table 38, Figure 86). On the other hand, no annealing step led to slightly higher PV performances, improved reproducibility, but larger hysteresis. The process without annealing was selected in the hope of reaching higher efficiencies in the next experiments.

Table 38. PV parameters and hysteresis index of PSCs with PVBI-spiro annealed in different conditions.

Annealing conditions	Reverse scan				Forward scan				HI
	J_{sc}	V_{oc}	FF	PCE	J_{sc}	V_{oc}	FF	PCE	
	$mA.cm^{-2}$	V		%	$mA.cm^{-2}$	V		%	
No annealing	22.80 ^a	1.153	0.768	20.21	23.04	1.156	0.764	20.35	-0.007
	20.81 ^b	1.155	0.765	20.16	23.06	1.156	0.760	20.27	-0.005
	$\pm 0.03^c$	± 0.003	± 0.003	± 0.04	± 0.03	± 0.002	± 0.004	± 0.07	± 0.003
Annealing at 70°C (Ref)	22.75	1.15	0.77	20.29	22.99	1.16	0.76	20.33	-0.002
	22.72	1.14	0.76	19.80	22.94	1.15	0.75	19.86	-0.003
	± 0.21	± 0.01	± 0.01	± 0.54	± 0.17	± 0.01	± 0.01	± 0.64	± 0.007
Flash annealing at 160°C	22.45	1.10	0.69	17.12	22.81	1.11	0.67	16.90	0.013
	22.05	1.07	0.68	16.19	22.52	1.08	0.65	15.94	0.015
	± 0.76	± 0.06	± 0.01	± 1.38	± 0.50	± 0.05	± 0.01	± 1.34	± 0.003

^a Best cell; ^b average on 4 cells; ^c standard deviation of the average.

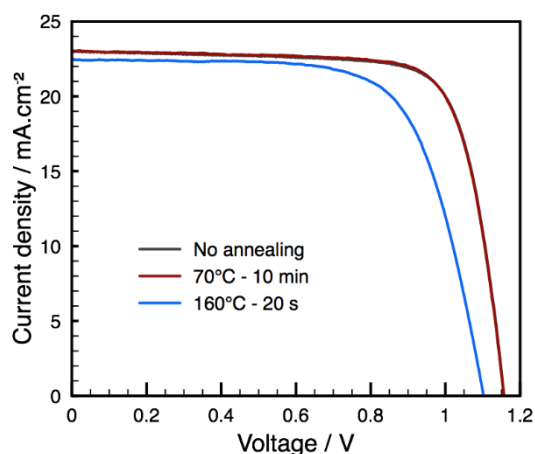


Figure 86. Best I-V curves of PSCs with PVBI-spiro annealed in different conditions.

The effect of the tBP on the PV performances was then investigated (Table 39, Figure 87). Optimal efficiency and hysteresis index were obtained for the reference concentration. When increasing tBP concentration, keeping PVBI-TFSI concentration constant, hysteresis index decreases, similarly to the increase in both PVBI-TFSI and tBP concentrations. SEM images revealed better HTM morphology but more holes in the perovskite layer when tBP concentration was increased (Figure 88). So finally, defects in the HTM were mainly the result of the PVBI-TFSI, whereas holes in the perovskite crystal were the result of the tBP.

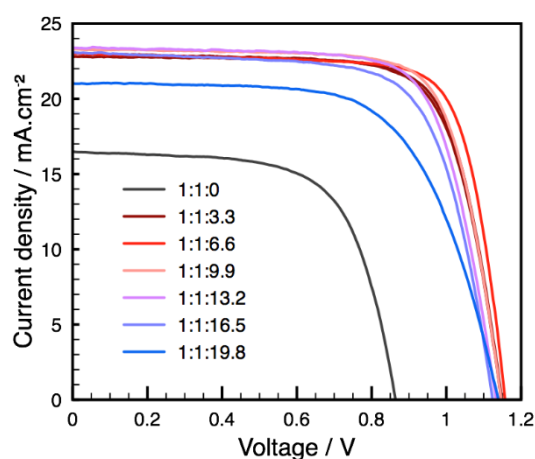


Figure 87. Best I-V curves of PSCs employing different concentrations of tBP in 1:1:x PVBI-spiro.

Table 39. PV parameters and hysteresis index of PSCs employing different concentrations of tBP in 1:1:z PVBI-spiro.

HTM dopant	Reverse scan				Forward scan				HI
	J _{sc}	V _{oc}	FF	PCE	J _{sc}	V _{oc}	FF	PCE	
	<i>mA.cm⁻²</i>	<i>V</i>		%	<i>mA.cm⁻²</i>	<i>V</i>		%	
1:1:0	16.48 ^a	0.86	0.66	9.37	16.98	0.87	0.61	8.99	0.041
	14.16 ^b	0.86	0.64	7.83	14.45	0.86	0.59	7.36	0.064
	± 2.92 ^c	± 0.01	± 0.02	± 1.78	± 3.04	± 0.01	± 0.02	± 1.82	± 0.021
1:1:3.3	22.81	1.147	0.738	19.29	23.01	1.148	0.740	19.55	-0.013
	22.66	1.143	0.737	19.08	22.92	1.143	0.735	19.25	-0.009
	± 0.16	± 0.003	± 0.002	± 0.16	± 0.11	± 0.004	± 0.007	± 0.24	± 0.006
1:1:6.6	22.80	1.153	0.768	20.21	23.04	1.156	0.764	20.35	-0.007
(Ref)	20.81	1.155	0.765	20.16	23.06	1.156	0.760	20.27	-0.005
	± 0.03	± 0.003	± 0.003	± 0.04	± 0.03	± 0.002	± 0.004	± 0.07	± 0.003
1:1:9.9	23.00	1.146	0.747	19.68	23.32	1.147	0.745	19.92	-0.012
	23.01	1.137	0.744	19.46	23.27	1.138	0.745	19.73	-0.014
	± 0.07	± 0.007	± 0.019	± 0.42	± 0.13	± 0.007	± 0.013	± 0.23	± 0.011
1:1:13.2	21.71	1.13	0.71	17.37	23.39	1.13	0.73	19.31	-0.112
	20.12	1.11	0.68	15.33	22.72	1.12	0.71	17.96	-0.195
	± 2.21	± 0.01	± 0.06	± 2.97	± 0.94	± 0.01	± 0.02	± 1.26	± 0.166
1:1:16.5	20.19	1.11	0.67	14.89	23.08	1.12	0.70	18.22	-0.224
	18.16	1.10	0.61	12.30	22.33	1.12	0.66	16.66	-0.366
	± 1.80	± 0.01	± 0.04	± 1.98	± 0.75	± 0.01	± 0.02	± 1.53	± 0.109
1:1:19.8	17.85	1.13	0.57	11.46	21.01	1.14	0.65	15.46	-0.349
	17.26	1.12	0.60	11.47	21.27	1.13	0.58	13.85	-0.205
	± 1.07	± 0.018	± 0.04	± 1.21	± 0.62	± 0.02	± 0.09	± 2.06	± 0.104

^a Best cell; ^b average on 4 cells; ^c standard deviation of the average.

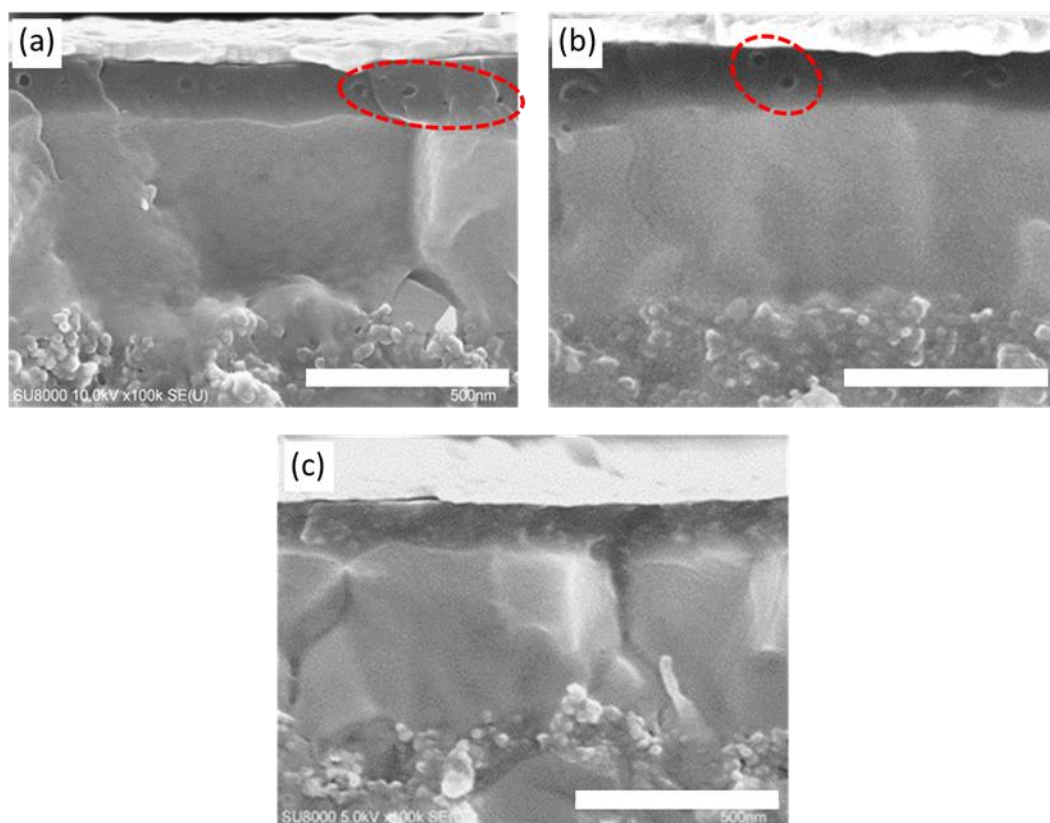


Figure 88. SEM cross sections of PSCs containing (a) 1:1:3.3, (b) 1:1:6.6, and (c) 1:1:16.5 PVBI-spiro. Some holes are circled in red. Scale bar = 500 nm.

Despite the benefits for the materials' solubility, acetonitrile is able to dissolve the perovskite. So the concentration of LiTFSI in acetonitrile had to be carefully optimized to ensure the spiro-OMeTAD doping without altering the perovskite crystals. The standard PVBI-spiro recipe was compared to devices made without acetonitrile and to devices containing twice amount of acetonitrile, *i.e.* 3.4 vol.% (Table 40). Although holes in the HTL were suppressed along with acetonitrile, PV performances were not improved (Figure 89, Figure 90). Actually acetonitrile did not dramatically affect PV performances. Nonetheless, some trends may be put forward. When increasing acetonitrile concentration, slightly lower J_{sc} , higher V_{oc} , and narrower hysteresis were measured. The optimal concentration was the initial concentration of 1.7 vol.%.

Table 40. Best and average (4 cells) PV parameters of PSCs with different concentration of acetonitrile in PVBI-spiro.

Acetonitrile (vol.%)	Reverse scan				Forward scan				HI
	J_{sc}	V_{oc}	FF	PCE	J_{sc}	V_{oc}	FF	PCE	
	$mA.cm^{-2}$	V		%	$mA.cm^{-2}$	V		%	
0	23.06 ^a	1.129	0.750	19.54	23.27	1.135	0.751	19.85	-0.016
	22.81 ^b	1.125	0.754	19.35	23.02	1.133	0.755	19.64	-0.015
	$\pm 0.30^c$	± 0.003	± 0.003	± 0.21	± 0.31	± 0.003	± 0.003	± 0.25	± 0.003
1.7 (Ref)	22.80	1.153	0.768	20.21	23.04	1.156	0.764	20.35	-0.007
	22.81	1.155	0.765	20.16	23.06	1.156	0.760	20.27	-0.005
	± 0.03	± 0.003	± 0.003	± 0.04	± 0.03	± 0.002	± 0.004	± 0.07	± 0.003
3.4	23.10	1.141	0.759	20.00	22.99	1.142	0.764	20.06	-0.003
	22.78	1.145	0.755	19.70	22.89	1.147	0.754	19.78	-0.004
	± 0.296	± 0.005	± 0.002	± 0.23	± 0.16	± 0.005	± 0.008	± 0.237	± 0.001

^a Best cell; ^b average on 4 cells; ^c standard deviation of the average.

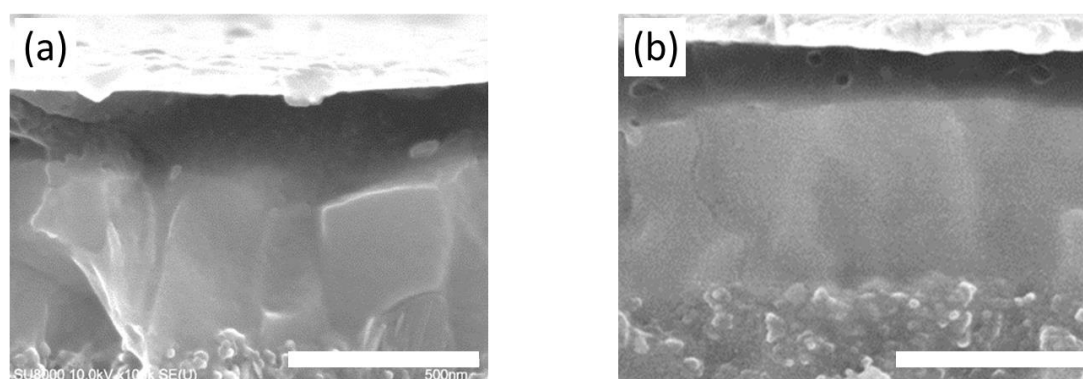


Figure 89. SEM cross sections of PSCs (a) without, and (b) with 1.7 vol.% of acetonitrile in PVBI-spiro. Scale bar = 500 nm.

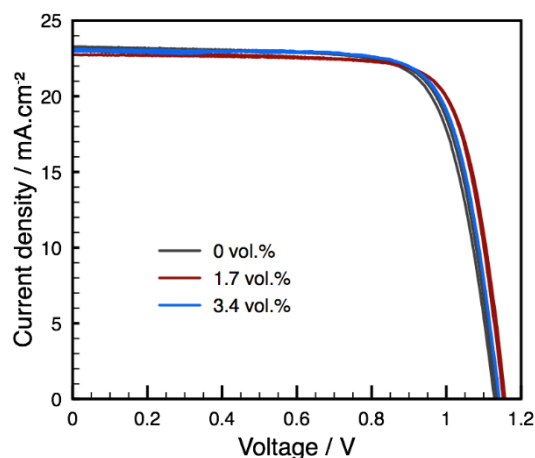


Figure 90. Best I-V curves of PSCs with different concentrations of acetonitrile in PVBI-spiro.

The best PSCs were obtained for PVBI-TFSI and tBP doped spiro-OMeTAD, in 1:1:6.6 concentration, containing 1.7 vol.% of acetonitrile, processed without annealing. The best IV curves for PVBI-spiro and Li-spiro are displayed on Figure 91a. A best PCE of 20.35 % was recorded, over 10 % higher than the 18.44 % of the standard Li-spiro PSCs. This improved efficiency is attributed mainly to the increased V_{oc} , from 1.10 to 1.16 V, as well as the enhancement of the FF, from 0.74 to 0.76, and in J_{sc} , from 22.45 to 23.04 $\text{mA}\cdot\text{cm}^{-2}$. IPCE measurements were also performed on the best performing devices, resulting in an integrated current density of 22.36 and 20.94 $\text{mA}\cdot\text{cm}^{-2}$ for PVBI-spiro and the Li-spiro devices respectively. J_{sc} calculated from IPCE measurements is in good agreement with J_{sc} from I-V curves (Figure 91b).

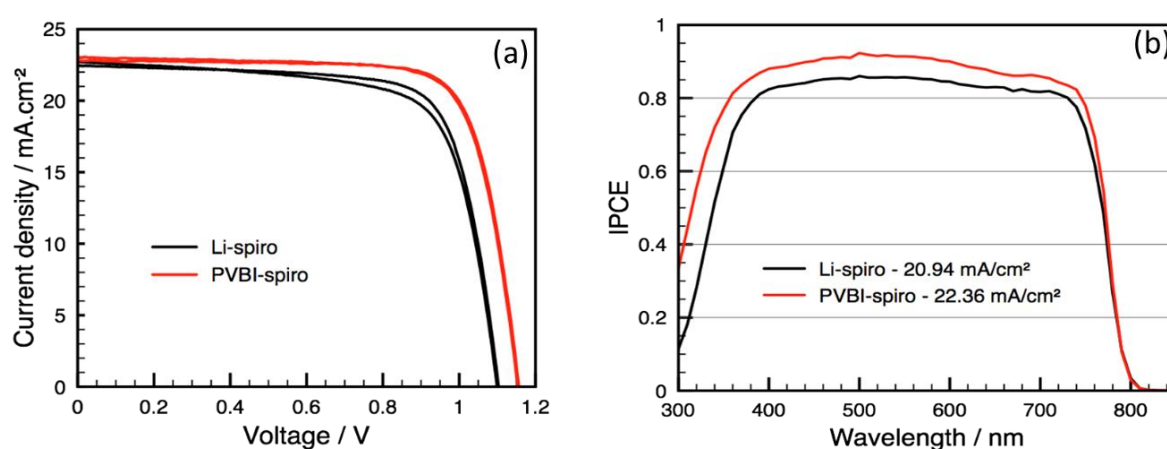


Figure 91. (a) Best I-V curves of Li-spiro and PVBI-spiro-based PSCs, and (b) their associated IPCE

To confirm the higher performances of PVBI-TFSI compared to LiTFSI, 20 PVBI-spiro-based devices were fabricated and compared to 20 Li-spiro devices (Table 41). As previously, higher J_{sc} , V_{oc} , FF and reduced hysteresis were obtained when employing PVBI-spiro. In both cases, standard deviation was very low (Figure 92).

Table 41. Average (20 cells) PV parameters and hysteresis index of Li-spiro and PVBI-spiro devices.

	Reverse scan				Forward scan				HI
	J_{sc} $\text{mA}\cdot\text{cm}^{-2}$	V_{oc} V	FF	PCE %	J_{sc} $\text{mA}\cdot\text{cm}^{-2}$	V_{oc} V	FF	PCE %	
PVBI-TFSI	22.92 ^a	1.150	0.745	19.64	23.14	1.151	0.742	19.75	-0.006
	$\pm 0.21^b$	± 0.009	± 0.023	± 0.59	± 0.21	± 0.010	± 0.021	± 0.57	± 0.004
LiTFSI	22.18	1.102	0.712	17.59	22.51	1.099	0.673	16.65	0.054
	± 0.36	± 0.012	± 0.012	± 0.54	± 0.31	± 0.014	± 0.021	± 0.73	± 0.019

^a Average on 20 cells; ^b standard deviation of the average.

In this part, PVBI-spiro-based devices have been successfully optimized to reach efficiencies over 20 %, suggesting an efficient doping of spiro-OMeTAD by PVBI-TFSI. The hysteresis was considerably reduced and was found to be particularly influenced by PVBI-TFSI and tBP concentrations. The following discussion is dedicated to the understanding of the doping mechanism of spiro-OMeTAD by PVBI-TFSI, to the origin of the reduced hysteresis and to the stability of the devices.

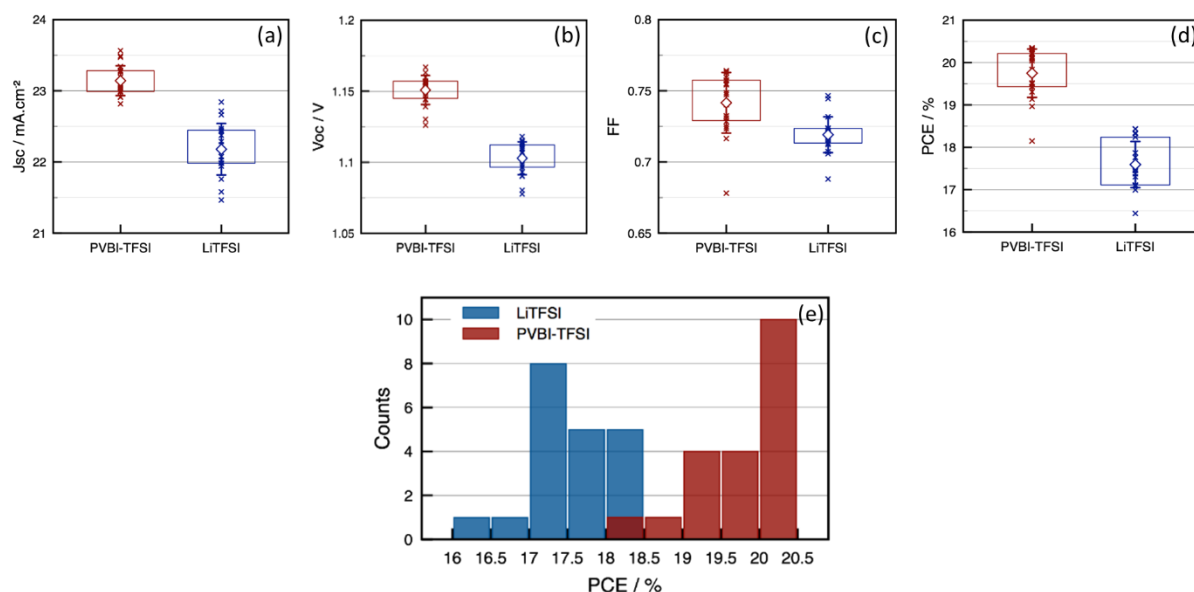


Figure 92. Statistical representations of (a) J_{sc} , (b) V_{oc} , (c) FF, and (d) PCE of PSCs containing either Li-spiro or PVBI-spiro, and (e) the histogram of all device efficiency.

3.2.2 Understanding of the doping mechanism

Spiro-OMeTAD oxidation can be simply observed by a colour change in the precursor solution (Figure 93). Without any dopant, spiro-OMeTAD solution is transparent/light yellow-green. No colour change was observed when LiTFSI solution and tBP were successively added. On the other hand, when PVBI-TFSI was incorporated to the spiro-OMeTAD, the solution immediately turned red. This colour change was suppressed when tBP was further added. After exposure to ambient light for few minutes, the solution turned red again. This final reaction was temporarily reversible with light. Light exposure kept the solution reddish.

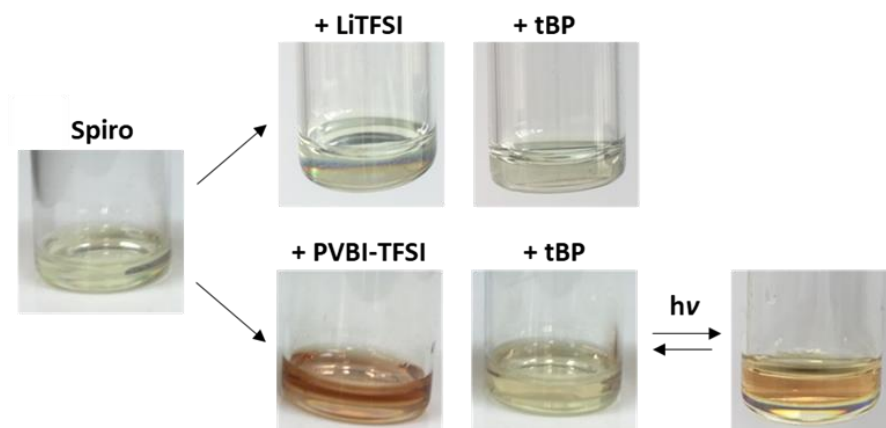


Figure 93. Colour changes during the Li-spiro and PVBI-spiro treatments.

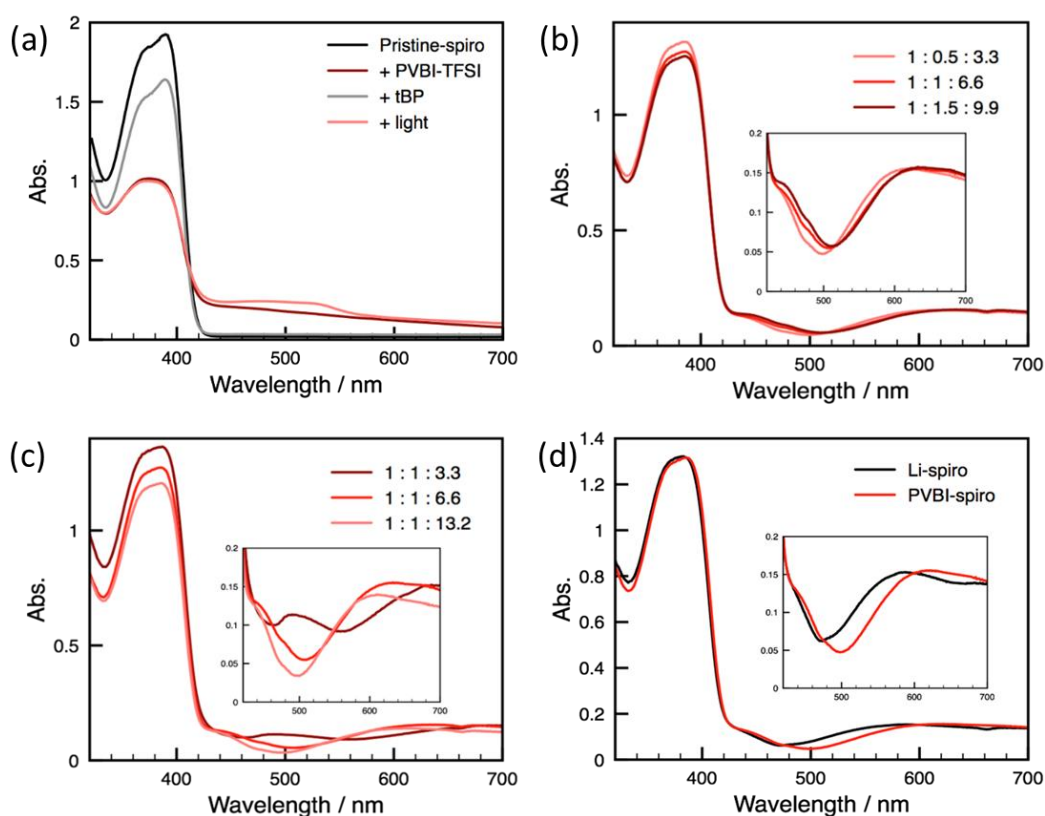


Figure 94. Absorption spectra in solution of (a) the PVBI-spiro solution process. Absorption spectra in thin films varying (b) PVBI-TFSI together with tBP, (c) only tBP concentrations. (d) Thin film absorption of PVBI-spiro and Li-spiro (1:0.5:3.3).

To understand the mechanisms governing the spiro-OMeTAD oxidation process and their dependency to tBP and irradiance, absorption spectra were recorded in solution for each step and are shown in Figure 94a. Pristine spiro-OMeTAD showed an absorption at 390 nm which remarkably decreased with the addition of PVBI-TFSI. This phenomenon was associated with the concomitant appearance of a feature at around 510 nm which can be attributed to oxidized spiro-OMeTAD

species. After the addition of tBP only the pristine spiro-OMeTAD peak at 390 nm remained. The intensity of this last peak was significantly reduced, suggesting that part of spiro-OMeTAD has reacted to form a species not detectable in the visible range. To clearly determine the influence of light, the solution was exposed to the solar simulator light for 30 min ($P = 100 \text{ mW.cm}^{-2}$). It is noteworthy that the exposure step to simulated sunlight induced an increase in temperature of the solution. After irradiation, the oxidized spiro-OMeTAD species were formed while the intensity of the pristine spiro-OMeTAD peak was further reduced. This experiment proved that spiro-OMeTAD oxidation occurs in presence of PVBI-TFSI.

These results in solution were compared to the absorption spectra of thin films processed under ambient light, in identical conditions to those used in complete devices (Figure 94b). Small variations were observed due to different kinetics. The same feature at 390 nm as for pristine spiro-OMeTAD was found. Alongside, two distinct peaks around 450 nm and 600 nm showed up. Based on computed absorption spectra of different spiro-OMeTAD forms published by Abate and coworkers, peaks at 450 nm and 580 nm can be assigned to spiro-OMeTAD-NH \cdot while peaks at 500 nm and 690 nm are assigned to oxidized spiro-OMeTAD \cdot^+ .²⁵ With a simultaneous increase of PVBI-TFSI and tBP or a decrease of tBP concentration, pristine-spiro-OMeTAD peak at 390 nm decreased while peaks associated to spiro-OMeTAD-NH \cdot tend to be red shifted, up to the spiro-OMeTAD \cdot^+ form in the case of 1:1:3.3 concentration (Figure 94b, c). These results confirm that PVBI-TFSI is able to oxidize spiro-OMeTAD more readily when less amount of tBP is present. Importantly, using Li-spiro in the same concentration, the peaks attributed to the oxidized spiro-OMeTAD were blue-shifted. This suggests that Li-spiro has a weaker tendency to oxidize spiro-OMeTAD compared to that of PVBI-TFSI (Figure 94d).

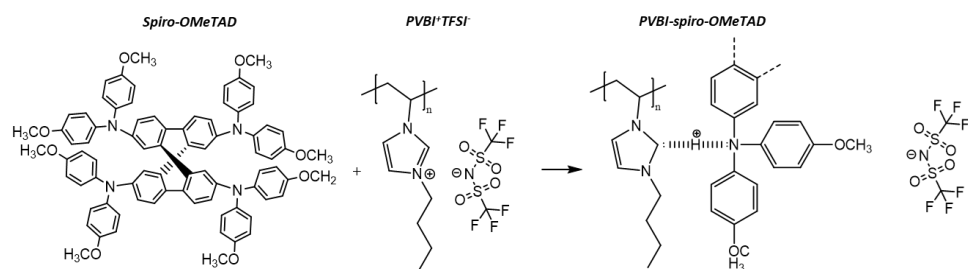
At first glance, the oxidation of spiro-OMeTAD by PVBI-TFSI is not obvious. Previous study showed that the strong acid H-TFSI can protonate spiro-OMeTAD due to its high dissociation constant.²⁵ Meanwhile, a moderate acid like H₃PO₄ cannot oxidize spiro-OMeTAD itself. However in the presence of alkali metal salts, it was demonstrated that the acidic proton can interact with the amine functions of spiro-OMeTAD molecules, resulting in higher conductivity.¹⁵ Regarding the 18.6 pKa of the imidazole, our poly(ionic liquid) cannot be considered as a strong acid. Moreover, *N*-heterocyclic carbenes (NHCs) are usually formed by deprotonation of azolium salts with a strong base in dry and air-free conditions.⁴³

On the other hand, the oxidation of spiro-OMeTAD by *N*-heterocyclic ionic liquids has already been described in the literature.²⁵⁻²⁶ The proposed mechanism considered the *N*-heterocyclic ionic liquid as a weak Brønsted acid, able to protonate spiro-OMeTAD. An interaction between the most acidic

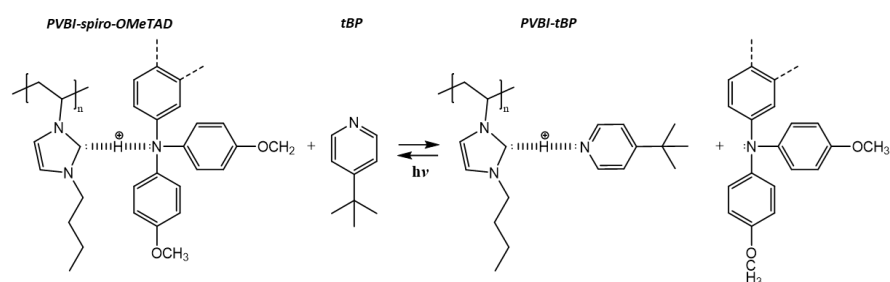
proton of the ionic liquid and the tertiary amine functions of the spiro-OMeTAD was justified by proton NMR, by a shift of the concerned proton and a quench of the aromatic protons of the spiro-OMeTAD. However, paramagnetic species were evidenced by EPR (Electron Paramagnetic Resonance) when the strong acid H-TFSI was employed, and no evidence of carbenes was given.

Based on these observations and studies reported earlier,²⁵⁻²⁶ we propose that the most acidic proton on PVBI⁺ can be shared or even transferred to the basic nitrogen of the spiro-OMeTAD. In presence of tBP, PVBI⁺ may preferentially interact with the nitrogen of tBP, breaking PVBI-spiro-OMeTAD interaction. Meanwhile, under light exposure, interactions with the most photo-reactive materials, *i.e.* spiro-OMeTAD may be favoured at the expense of tBP. With further intense and longer light exposure, the PVBI⁺ proton may be transferred to spiro-OMeTAD to form PVBI carbene and spiro-OMeTAD-NH⁺. Finally, the spiro-OMeTAD proton may combine to form spiro-OMeTAD^{•+} and H₂. Carbenes may stay free or combine each other forming a double bond. This mechanism is illustrated in Figure 95.

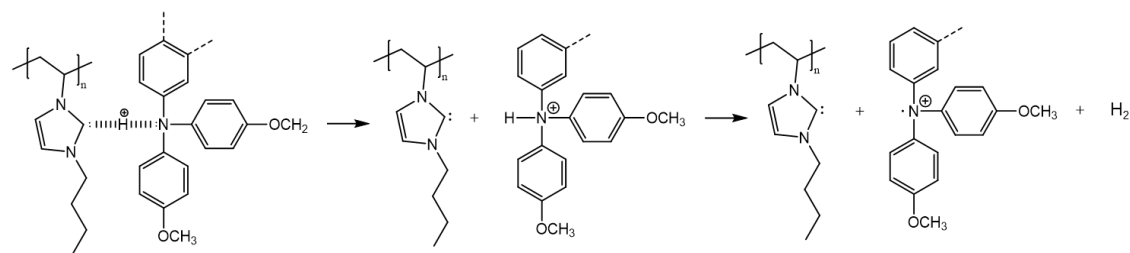
Reaction 1: Interactions between PVBI⁺ and spiro-OMeTAD.



Reaction 2: Reversible interactions with light between PVBI⁺ and either spiro-OMeTAD or tBP.



Reaction 3: Protonation of the spiro-OMeTAD by PVBI⁺ and proton transfer from spiro-OMeTAD to tBP.



Reaction 4: Combination of carbenes.

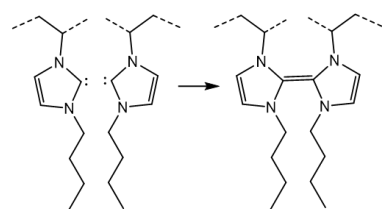


Figure 95. Proposed mechanism of spiro-OMeTAD oxidation by PVBI-TFSI in presence of tBP.

To verify the mechanism and shed light on the possible interactions between spiro-OMeTAD and PVBI-TFSI, ¹H NMR was performed. Usually, oxidation is evidenced by a broadening and/or a shifting of the associated protons and/or a decrease in signal intensity. The structure and the purity of the materials were previously controlled by ¹H NMR (see the Experimental Details section).

Mixing spiro-OMeTAD and PVBI-TFSI (1:1) in THF led to a signal broadening of the aromatic protons of the spiro-OMeTAD without shifting, at 7.37, 6.85, 6.77 and 6.48 ppm, and a slight decrease in intensity (vs. the methoxy protons peak at 3.72 ppm) (Figure 96). This peak broadening can stem from the formation of specific interactions between spiro-OMeTAD and PVBI-TFSI, increasing the relaxation time of spiro-OMeTAD in solution, and/or to the formation of the spiro-OMeTAD^{•+} radical cation. However, as the presence of the polymer can increase the viscosity of the medium and, as a result, increase the relaxation time of spiro-OMeTAD, the effects on spiro-OMeTAD were studied in detail using the monomer VBI-TFSI as a model reaction.

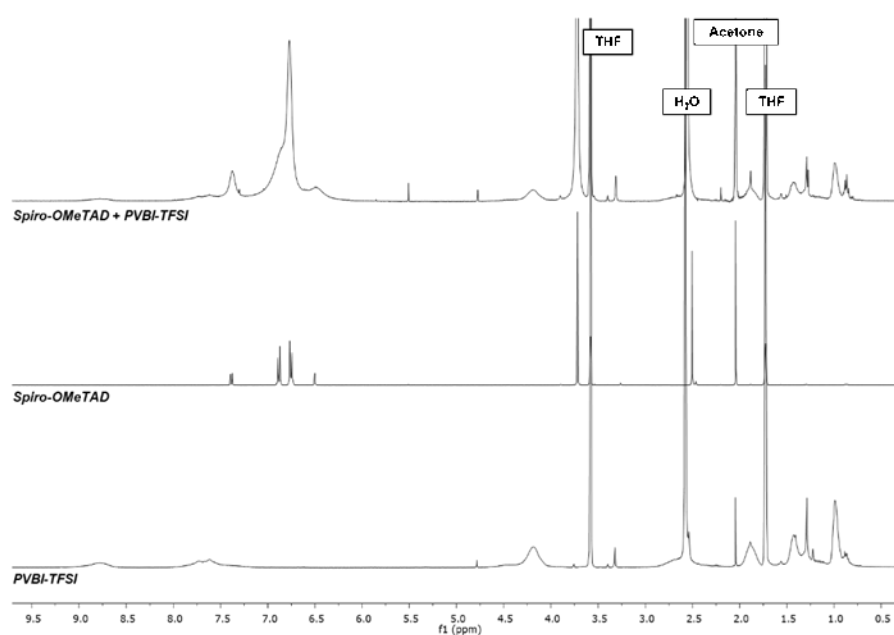


Figure 96. ¹H 400 MHz NMR spectra of spiro-OMeTAD, PVBI-TFSI, and a mixture (1:1) in d₈-THF.

Solutions of spiro-OMeTAD containing 50, 25 and 13 mol.% of VBI-TFSI were compared. The increase in VBI-TFSI concentration resulted in a clear broadening of the aromatic peaks (7.3 – 6.5 ppm) of the spiro-OMeTAD, and in a downfield shift of the most acidic proton of VBI-TFSI (9.2 – 9.1 ppm) (Figure 97). The broadening and shifting of the spiro-OMeTAD peaks suggest the formation of a hydrogen bond between the imidazolium and the amine centre of the spiro-OMeTAD. The shift observed for the imidazolium is consistent with an increase in proton dissociation. Both observations therefore confirm the reaction 1 of the mechanism (Figure 95).

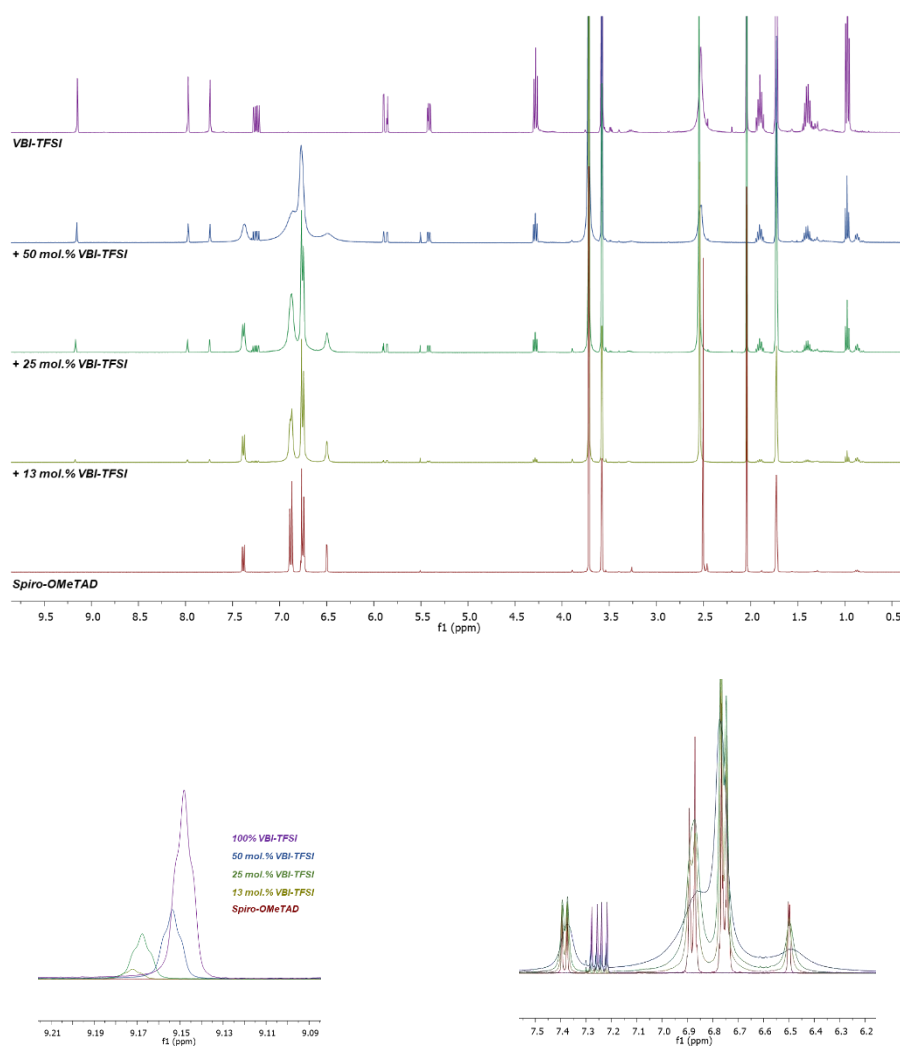


Figure 97. ^1H 400 MHz NMR spectra of spiro-OMeTAD containing different concentrations of VBI-TFSI in d_8 -THF. Focus on the peak of the most acidic proton of VBI-TFSI (bottom left), and on the aromatic peaks of spiro-OMeTAD (bottom right).

Secondly, similar study was carried out to elucidate the possible interactions between VBI-TFSI and tBP (Figure 98). When increasing VBI-TFSI concentration, only a shift of the VBI-TFSI peak in the 9.15 ppm region was observed. The unmodified peaks of tBP suggest that VBI^+ had weaker interactions with tBP than with spiro-OMeTAD. A weak hydrogen bonding is still considered between VBI^+ and the amine of tBP to explain the shift of the VBI-TFSI peak.

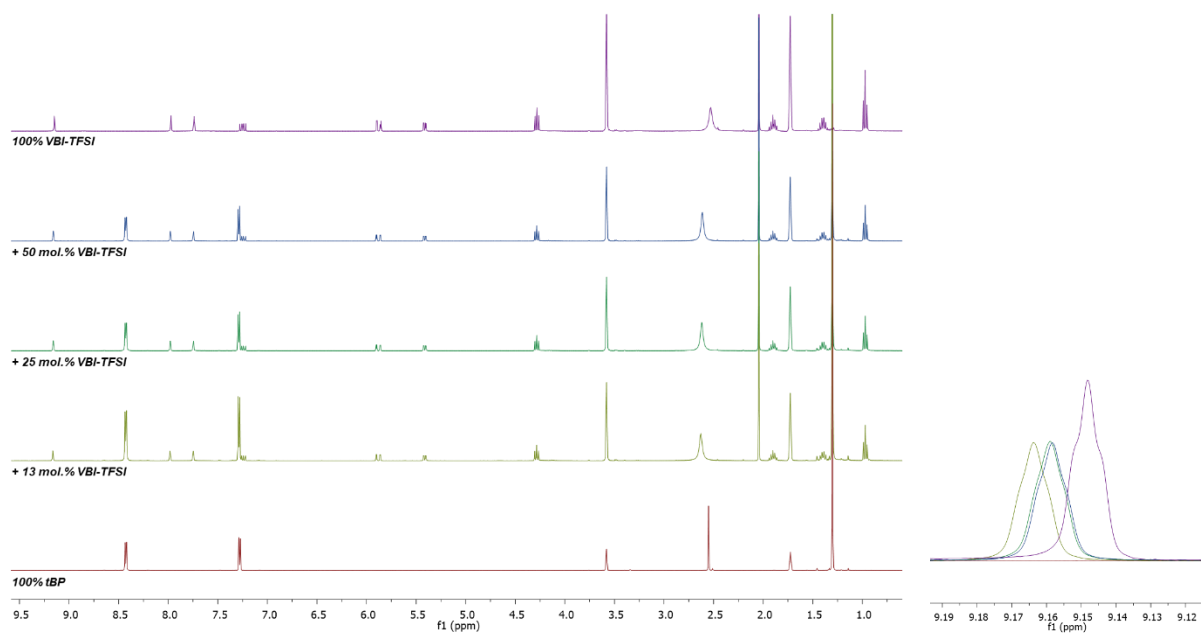


Figure 98. ^1H 400 MHz NMR spectra of tBP containing different concentrations of VBI-TFSI in d_8 -THF (left). Focus on the peak of the most acidic proton of VBI-TFSI (right).

When tBP was added to the spiro-OMeTAD doped with VBI-TFSI, the initial shape of the large peaks of the spiro-OMeTAD were found to be restored. In addition, the most acidic proton of VBI^+ shifted towards upper fields, suggesting that VBI^+ stopped interacting with spiro-OMeTAD in favour of interacting with tBP (Figure 99). This may be explained by the bigger size of spiro-OMeTAD making *VBI-H-spiro-OMeTAD* less stable than *VBI-H-tBP*. In this way, in presence spiro-OMeTAD and tBP, VBI-TFSI preferentially weakly interacts with tBP, confirming the reaction 2 of the mechanism (Figure 95).

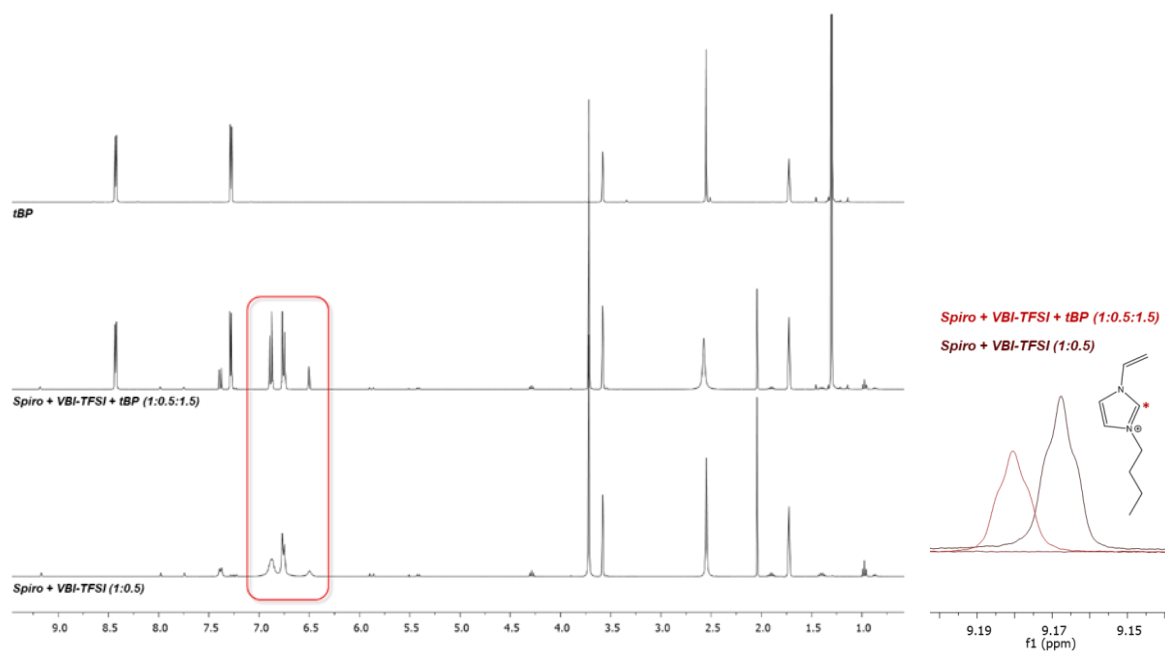


Figure 99. Effects of the addition of $t\text{BP}$ in VBI-spiro solution on ^1H 400 MHz NMR spectrum in d_8 -THF (left). Focus on the most acidic proton of VBI-TFSI (right).

To prove the protonation of spiro-OMeTAD by VBI-TFSI, ^{13}C NMR was performed on the 25 mol.% solution. 1.5 molar equivalent of CS_2 were added to trap the carbenes. Carbenes should be evidenced by a shift of the "h" peak of VBI-TFSI at 136 ppm towards around 250 ppm. However, this peak remains at the same position upon the addition of spiro-OMeTAD (Figure 100). Thus VBI^+ cannot protonate spiro-OMeTAD in solution. It is noteworthy that the reaction 3 of the mechanism is not excluded to happen in thin film, considering the presence of spiro-OMeTAD-NH^+ and $\text{spiro-OMeTAD}^{\cdot+}$ in the absorption spectra.

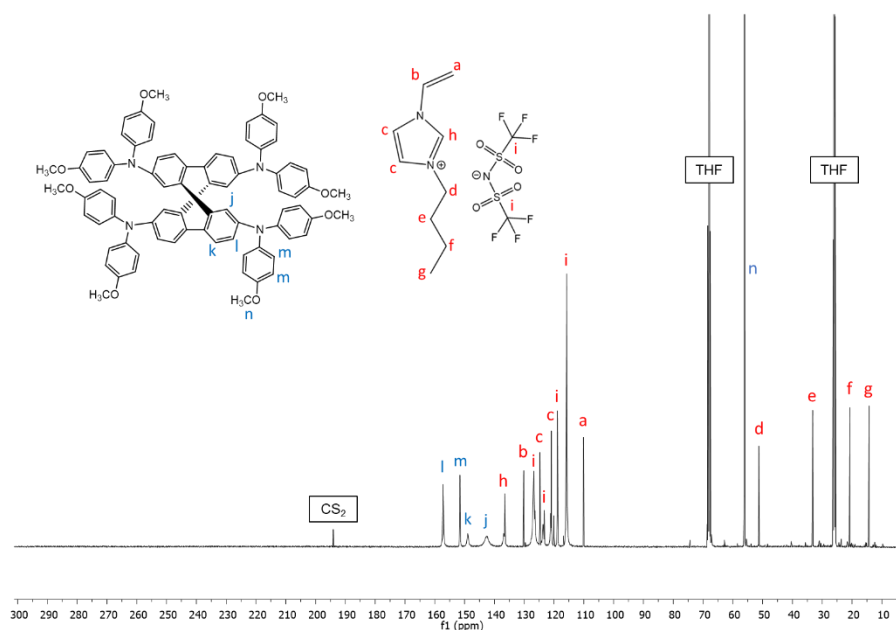


Figure 100. ^{13}C NMR of spiro-OMeTAD doped with 25 mol.% of VBI-TFSI in d_8 -THF.

Furthermore, it is to be noted that reactions 1 and 2 of the mechanism (Figure 95) are more likely to occur in solvents with low dielectric constant (Table 42). Polar solvents, such as DMF and DMSO, with a relatively high dielectric constant, tend to partly cancel the electric field of ionic compounds, improving their solubility. On the contrary, non-polar solvents are less able to solvate ionic compounds. The particular proximity between spiro-OMeTAD and PVBI-TFSI in non-polar solvents should help species to interact. The non-reactivity of spiro-OMeTAD and VBI-TFSI in polar solvent was confirmed by recording their ^1H NMR spectrum in DMSO (Figure 101). As expected, no variation was observed. Therefore, the counter anion of PVBI^+ have to be carefully chosen. Changing TFSI^- for I^- , doping of spiro-OMeTAD doesn't occur, no change in colour is observed in solution and poor PV performances were recorded. Electrostatic force between PVBI^+ and I^- should be stronger than between PVBI^+ and TFSI^- .

Table 42. PVBI-spiro solution coloration according to the solvent.

Solvent	Dielectric constant	Solution coloration
Chlorobenzene	5.62	Red
THF	7.58	Red
DMF	36.7	Transparent
DMSO	46.7	Transparent

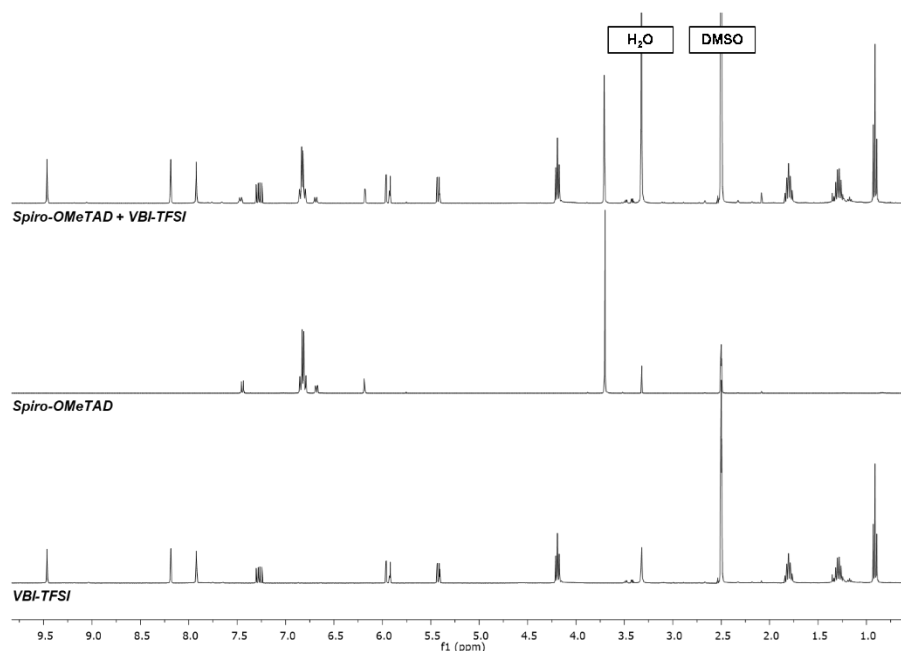


Figure 101. ^1H 400 MHz NMR spectra of VBI-TFSI, spiro-OMeTAD, and a mixture of both (1:2) in d_6 -DMSO.

3.2.3 Thin film properties

Two-probe conductivity measurements were carried out following a previously reported method.⁷ In-plane devices were fabricated as depicted in Figure 102. Different spiro-OMeTAD solutions were spin coated on a 20-nm thick layer of poly(1-vinyl-1,2,4-triazole), a dielectric polymer, to improve the wetting of the solutions. Gold electrodes were evaporated to later record I-V curves. After the process, devices were stored in glove box in the dark. Conductivities were calculated as:

$$\sigma = \frac{L}{Rwt}$$

where L is the channel length (50 μm), w is the channel width (2.5 mm), t is thickness (200 nm) and R is the film resistance, extracted from the slope of I-V curves.

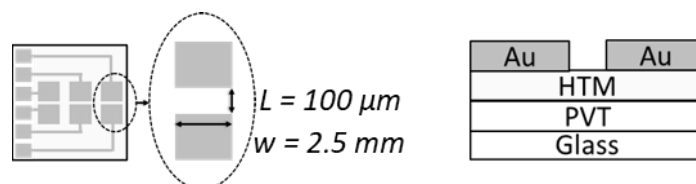


Figure 102. Scheme of the device used to measure the conductivity of the HTM.

The thin film conductivities of spiro-OMeTAD are summarized in Table 43. I-V curves of devices were first recorded after a storage with no light exposure, and repeated after 90 min of exposure under

AM1.5 illumination, 100 mW.cm^{-2} (Figure 103). The conductivity of spiro-OMeTAD was improved from 9.4×10^{-8} to $6.0 \times 10^{-6} \text{ S/cm}$ with LiTFSI as dopant and enhanced to $1.1 \times 10^{-5} \text{ S/cm}$ after 1h30 of irradiation. These results are in accordance with literature data.⁷ Conductivity was improved to $1.6 \times 10^{-5} \text{ S/cm}$ when LiTFSI was replaced by PVBI-TFSI under nitrogen. After light exposure, a highest conductivity of $1.9 \times 10^{-3} \text{ S/cm}$ was recorded for the 1:1:6.6 formulation. According to absorption spectra, oxidized-spiro concentration increases with PVBI-TFSI and irradiance, and decreases with tBP. Irradiance importantly increased the conductivity which reached a maximum for the 1:1:6.6 concentration. This effect can be explained by the morphology of the films, previously noticed on SEM cross sections of PSCs, and observed in Figure 104 by AFM. Rougher films, full of holes, were formed when adding PVBI-TFSI, whereas morphology was improved with increasing the tBP amount. Thus, the film conductivity is either limited by the morphology or by the oxidation level of the spiro-OMeTAD, which are both controlled by the concentration of dopants.

Table 43. Average conductivities (4 films) and standard deviations of spiro-OMeTAD containing different dopant amounts.

HTM		Conductivity dark	Conductivity light
		<i>S/cm</i>	<i>S/cm</i>
Spiro-OMeTAD	1:0:0	$9.4 \pm 2.4 \text{ E-08}$	$2.5 \pm 0.2 \text{ E-06}$
Li-spiro	1:0.5:3.3	$6.0 \pm 0.1 \text{ E-06}$	$1.1 \pm 0.2 \text{ E-05}$
PVBI-spiro	1:0.5:3.3	$1.6 \pm 0.8 \text{ E-05}$	$3.8 \pm 1.0 \text{ E-04}$
	1:1:3.3	$6.1 \pm 2.2 \text{ E-05}$	$9.1 \pm 5.0 \text{ E-04}$
	1:1:6.6	$7.8 \pm 0.3 \text{ E-05}$	$1.9 \pm 0.5 \text{ E-03}$
	1:1:13.2	$2.6 \pm 2.2 \text{ E-05}$	$1.1 \pm 0.3 \text{ E-03}$
	1:1.5:9.9	$1.1 \pm 0.6 \text{ E-04}$	$4.4 \pm 2.4 \text{ E-04}$

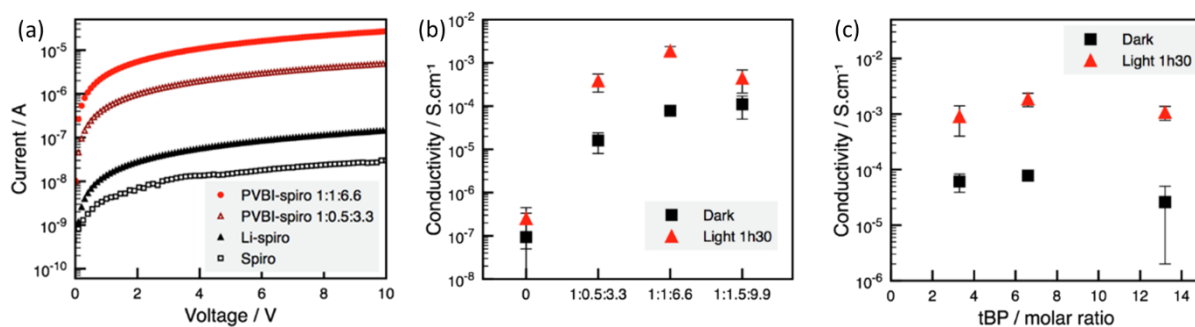


Figure 103. (a) I-V curves of pristine spiro-OMeTAD, Li-spiro (1:0.5:3.3), and PVBI-spiro (1:0.5:3.3 and 1:1:6.6). Conductivities of (b) 1:y:z and (c) 1:1:z PVBI-spiro devices kept in the dark and after 1h30 exposure under AM1.5 illumination, 100 mW.cm⁻².

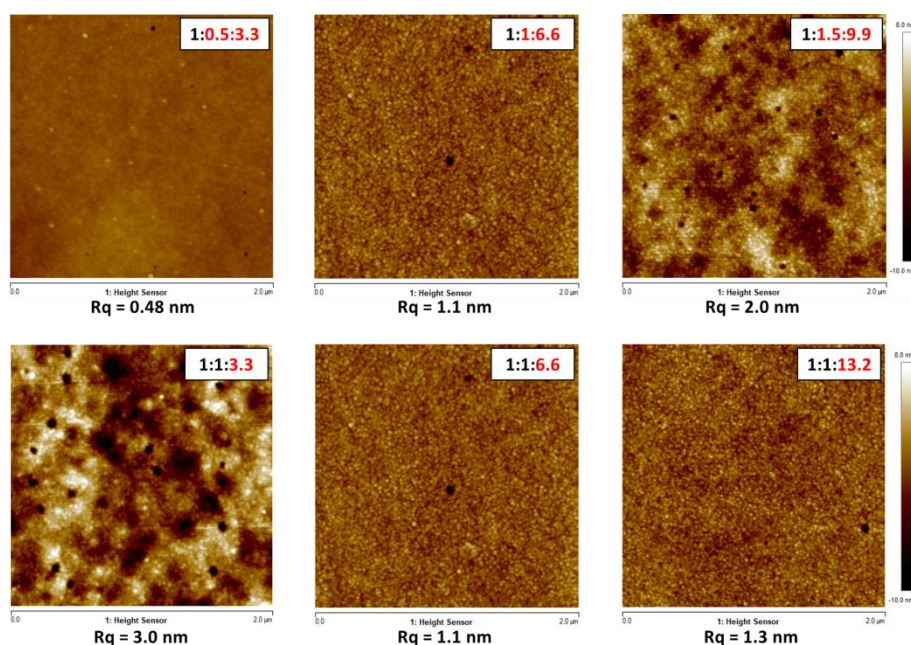


Figure 104. AFM topographic views of PVBI-spiro films with different concentrations of PVBI-TFSI and tBP. Image size = 2 μm x 2 μm. Scale bar from - 10 nm (dark) to 8 nm (light).

HOMO levels of PVBI-spiro were then measured by photoelectron spectroscopy in air (PESA) and reported in Table 44. The pristine spiro-OMeTAD HOMO level was -5.25 eV. Addition of dopants down-shifted the HOMO level to -5.35 eV with LiTFSI and from -5.30 to -5.41 eV with PVBI-TFSI when increasing the concentration. The best PCE of devices containing PVBI-spiro were recorded for the 1:1:6.6 concentration, which corresponds to a HOMO level of -5.35 eV, similar to the one of Li-spiro. So the increase in V_{oc} in PVBI-spiro devices cannot be attributed to a deeper HOMO level of the PVBI-spiro layer, but may be associated to the improved conductivity.

Additionally, despite deeper HOMO levels with higher concentration in dopants, higher V_{oc} were not obtained (Table 44). This may be explained by two reasons. First of all, when the HTM HOMO level is getting closer to the valence band of the perovskite, the probability of recombinations increases. Secondly, the higher amount of defects in the HTL when increasing dopant concentration may create trap states and resistances, reducing the V_{oc} .

Table 44. HOMO levels of pristine spiro, Li-spiro and PVBI-spiro, and the corresponding V_{oc} previously measured in PSCs.

HTM		HOMO level eV	V_{oc} V
Spiro-OMeTAD	1:0:0	- 5.25	
Li-spiro	1:0.5:3.3	- 5.35	1.11
PVBI-spiro	1:0.5:3.3	- 5.30	1.13
	1:1:6.6	- 5.35	1.15
	1:1.5:9.9	- 5.41	1.12

Ultraviolet photoelectron spectroscopy (UPS) measurements were performed to study the changes in the electronic properties of spiro-OMeTAD with the addition of p-dopant PVBI-TFSI and to probe the perovskite/spiro-OMeTAD interface before and after doping. As seen from the secondary electron (S.E) cut-off of the UP spectra (Figure 105), the work function of spiro-OMeTAD was found to be 4.15 eV, which is in good agreement with the literature for comparable solution processed spiro-OMeTAD.⁴⁴ The HOMO of pristine spiro-OMeTAD was measured to be at 0.8 eV relative to the fermi level. Addition of PVBI-TFSI was found to significantly increase the work function of spiro-OMeTAD to 4.5 eV accompanied by a 0.2 eV shift in the HOMO edge towards the fermi level, confirming p-doping of the spiro-OMeTAD.⁴⁴ As a result, the ionization potential of spiro-OMeTAD was increased from 4.95 eV to 5.1 eV.

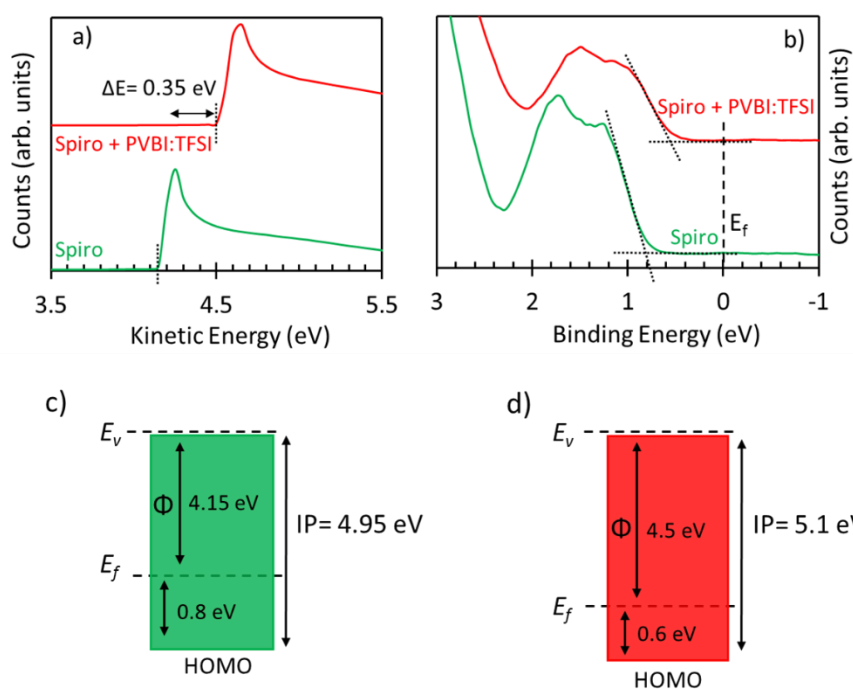


Figure 105. UP spectra depicting the (a) secondary electron cut-off and (b) the HOMO edge of spiro-OMeTAD with and without PVBI-TFSI. The work function and ionisation potential of undoped (c) and doped (d) spiro-OMeTAD is also depicted schematically.

Energy level alignment at the perovskite/spiro-OMeTAD interface was further probed by studying the electronic properties of perovskite as well as that of spiro-OMeTAD deposited over perovskite, identical to that in fully functional devices. The work function of the K^+ doped $MA_{0.15}FA_{0.85}PbI_{2.55}Br_{0.45}+KI$ perovskite was found to be 4.2 eV (Figure 106) whereas the valence band maxima (VBM) was found to be at 1.9 eV. This suggests a strong n-type doping characteristics of the perovskite and agrees well with the values reported in the literature for a comparable system.⁴⁵ The photoemission cutoff was found to have a significant shift from 4.2 eV to 3.5 eV (Figure 106), when a thin layer of spiro-OMeTAD was deposited on the perovskite surface, also accompanied by a shift of 0.3 eV in the valence edge and was found to be at 1.5 eV.^{45b} When spiro-OMeTAD doped with PVBI-TFSI and tBP was deposited on the perovskite surface, the work function increased to 3.8 eV. Importantly, the HOMO edge was found at 1.3 eV, a shift of 0.6 eV away from the VBM of perovskite towards the fermi level.

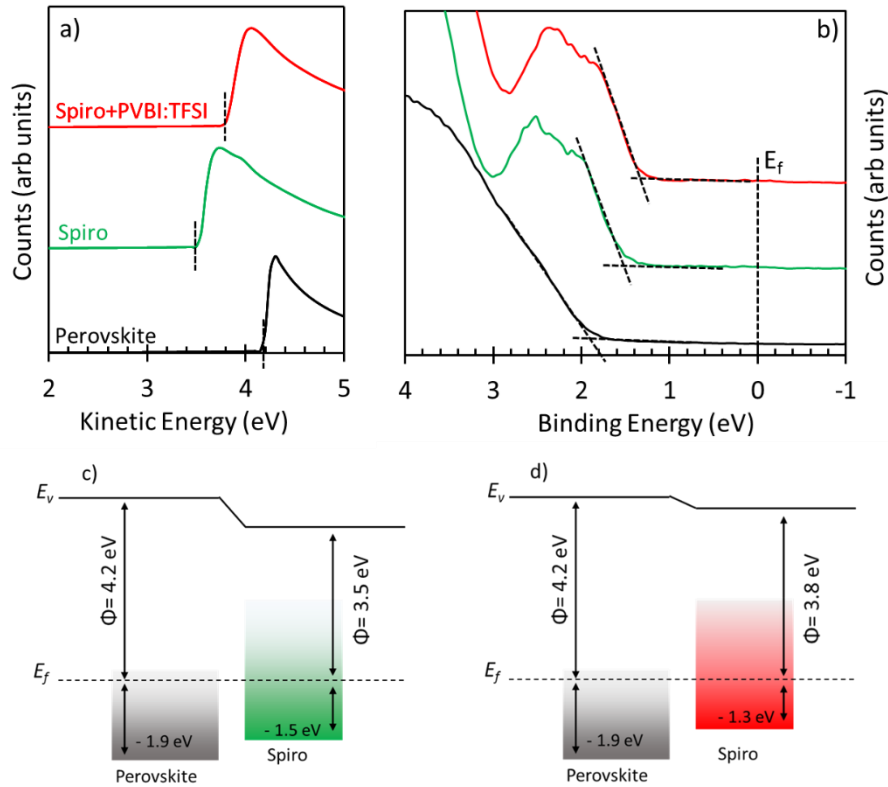


Figure 106. UP spectra depicting the a) S. E. cut-off and b) the VBM edge of perovskite and HOMO of spiro-OMeTAD with and without PVBI-TFSI, deposited over perovskite. The band diagram of the perovskite/spiro-OMeTAD interface with (c) and without (d) PVBI-TFSI is also depicted schematically.

3.2.4 Passivation effect of PVBI-TFSI

In addition to enhanced PCE, PVBI-spiro based PSCs demonstrated significantly reduced hysteresis. This could be due to the passivation of the perovskite surface. This effect was recently discussed by Salado *et. al.*⁴⁶ They evidenced the surface passivation of the perovskite by the imidazolium iodide ionic liquid when coating a thin layer of the IL between the perovskite and the HTL. Improved V_{oc} , FF and lower hysteresis were attributed to a decrease in the number of trap sites. It is suggested that the iodide counter anions passivate halide vacancies and retard superoxide formation. Furthermore, presence of ions at the interface was supposed to reduce charge accumulation. Using this interlayer, maximum PCE of 19.9 % was achieved.⁴⁶

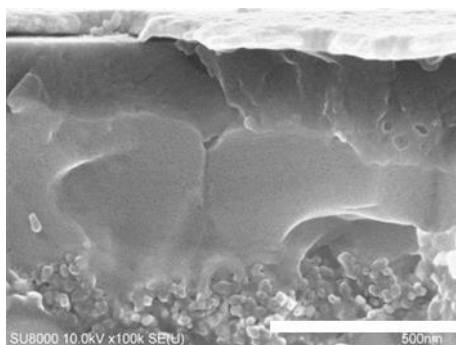


Figure 107. SEM cross section of the PSC containing a thin layer of PVBI-TFSI between the perovskite and Li-spiro. Scale bar = 500 nm.

To investigate the effect of PVBI-TFSI at the interface, an interlayer of PVBI-TFSI was coated in isopropanol on top of the perovskite, and was covered by the standard Li-spiro. Some holes were observed at the perovskite/HTM interface possibly due to the remaining isopropanol (Figure 107). The resulting device exhibited improved V_{oc} and reduced hysteresis, comparable to devices containing PVBI-spiro (Table 45, Figure 108). Although the FF was reduced, the final efficiency was 18.4 %, similar to the Li-spiro PSCs. It is considered that PVBI-TFSI would locally dope spiro-OMeTAD and furthermore, passivate the perovskite/HTM interface leading to hysteresis-free devices. Since in both formulations, TFSI⁻ anion is present, the passivation effect should come from interactions with PVBI⁺.

Table 45. Effect of a PVBI-TFSI interlayer between the perovskite and the HTM on the PV parameters.

	Reverse scan				Forward scan				HI
	J_{sc}	V_{oc}	FF	PCE	J_{sc}	V_{oc}	FF	PCE	
	$mA.cm^{-2}$	V		%	$mA.cm^{-2}$	V		%	
PVBI-spiro	22.80 ^a	1.15	0.77	20.21	23.04	1.16	0.76	20.35	-0.007
Li-spiro	22.45	1.10	0.74	18.44	22.71	1.10	0.71	17.71	0.039
Interlayer	22.31	1.16	0.71	18.41	22.62	1.16	0.70	18.30	0.006
	21.87 ^b	1.16	0.69	17.38	22.21	1.15	0.67	17.24	0.008
	$\pm 0.86^c$	± 0.01	± 0.03	± 1.54	± 0.83	± 0.01	± 0.03	± 1.52	± 0.001

^a Best cell; ^b average on 4 cells; ^c standard deviation of the average.

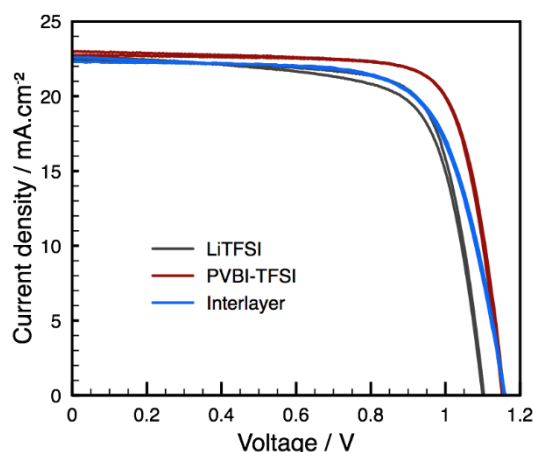


Figure 108. Effect of a PVBI-TFSI interlayer between the perovskite and the HTM on the I-V characteristics.

Secondly, it can be underlined that the hysteresis behaviour was mainly dependent on PVBI-TFSI and tBP concentrations (Figure 109a). In fact, it has been demonstrated that hysteresis behaviour in a device can be easily changed by applying a pre-poling bias to the device. By applying a voltage $V < 0$, positive charges in the perovskite layer accumulate near the perovskite/HTM interface, resulting in an inverted hysteresis (Figure 109b).⁴⁷

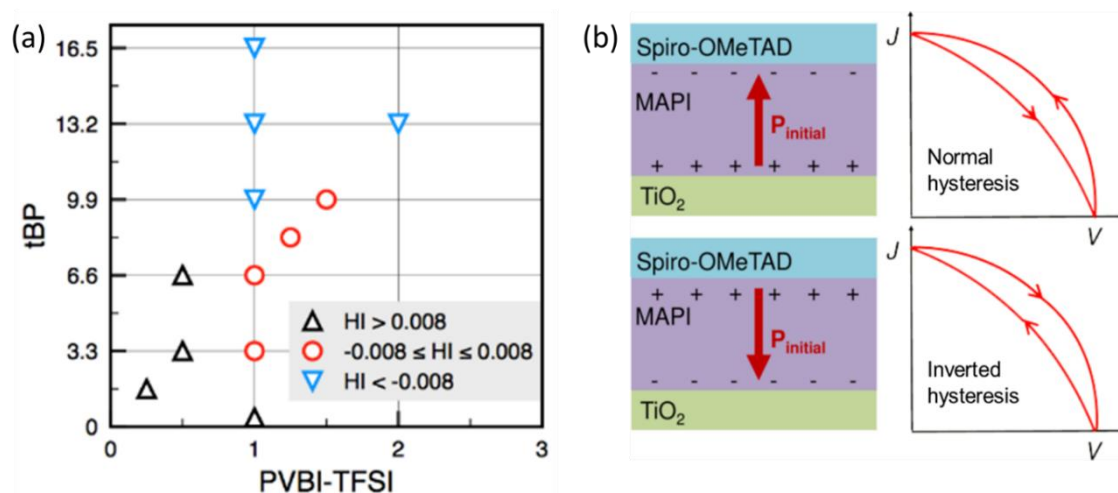


Figure 109. (a) Mapping of the hysteresis behaviour according to the dopants concentration. (b) Hysteresis behaviour according to the pre-poling of the device by Nemnes et.al.⁴⁷

Besides, it has been also shown that tBP could affect polarization of the device (Figure 110a).⁴⁸ It was proposed that tBP was able to deprotonate the methylammonium, creating a local negative perovskite crystal, attracting mobile holes to maintain the neutrality, resulting in the p-doping of the perovskite at the perovskite/HTM interface (Figure 110b). Following on, increasing the tBP concentration in the HTM would locally increase the p-doping of the perovskite, polarizing the

device, and thus would change the hysteresis behaviour. Moreover, additional reactions may occur with PVBI^+ or eventually, PVBI-carbene. Considering the PVBI-TFSI interlayer experiment, the hysteresis-less devices suggest a contribution of the PVBI-TFSI itself. A potential PVBI-carbene may be protonated again to form PVBI^+ , accentuating the polarization of the device (Figure 110c). This could also be due to ionic accumulation at the perovskite/HTM interface which might improve charge extraction and charge transport.⁴⁶ It is noteworthy to mention that these possible reactions induce degradation of the perovskite layer and might affect device stability.

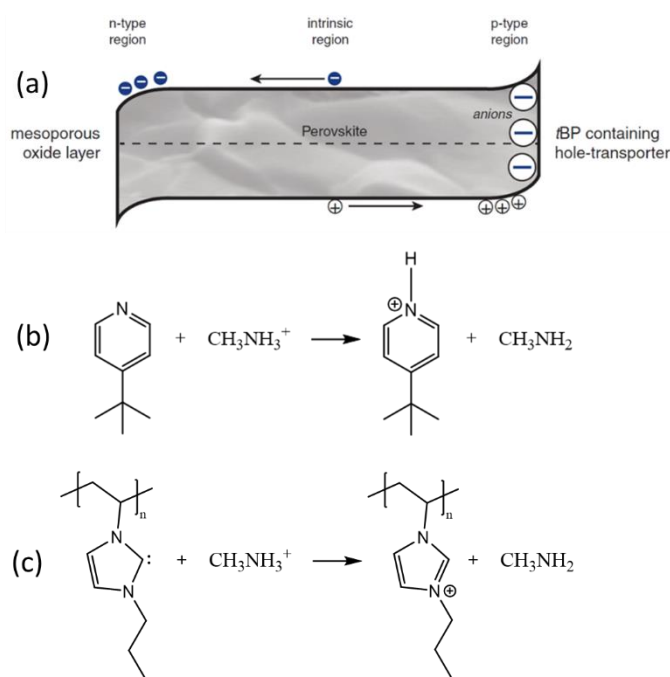


Figure 110. (a) Proposed p-doping mechanism of the perovskite by the tBP by Habisreutinger et.al.⁴⁸ (b) Protonation of tBP by the methyl ammonium. (c) Possible protonation of the PVBI-carbene by the methylammonium.

Photoluminescence (PL) measurements consist in recording light emission of a material induced by photoexcitation. Time resolved photoluminescence (TRPL) gives information on relaxation processes, *i.e.* radiative and non-radiative recombinations. Radiative recombination is a process where charge carriers recombine releasing a photon. Non-radiative recombination occurs when charge carriers recombine to an intermediate energy state created in the bandgap by impurities in the crystal. In this case, a phonon, or lattice vibration, is released instead of a photon. To maximize light generation and thus performance of opto-electronic devices, all recombinations should be radiative. In PSCs, non-radiative losses originate from charge-carrier trap states in the perovskite layer, especially on grain surfaces.⁴⁹ These trap states are possibly due to ionic defects such as halide vacancies.⁵⁰

To investigate charge transfer processes at the interfaces, PL measurements were carried out in PVBI-spiro and Li-spiro PSCs. On Figure 111, perovskite on glass revealed longer charge carrier lifetime than perovskite in PVBI-spiro, meaning that the light emission was quenched by charge separation and non-radiative recombinations at the TiO₂/perovskite and perovskite/HTM interfaces. PL characteristics were measured by exciting the solar cell from both sides, *i.e.* TiO₂ side and HTM side. Since the light absorption of the sample depends on the Beer-Lambert law, light intensity decreases exponentially as the path length increases, following the function:

$$I(x) = I_0 e^{-ax}$$

where $I(x)$ is the intensity of light after passing through a x distance in the semiconductor, I_0 is the intensity of light before passing through the sample and a is the absorption coefficient. The transmission profile according to the path length is given in Figure 111. In other words, device irradiated from TiO₂ side reflects PL processes occurring close to the TiO₂/perovskite interface. Reciprocally, devices excited from HTM side reflects PL processes occurring close to the perovskite/HTM interface.

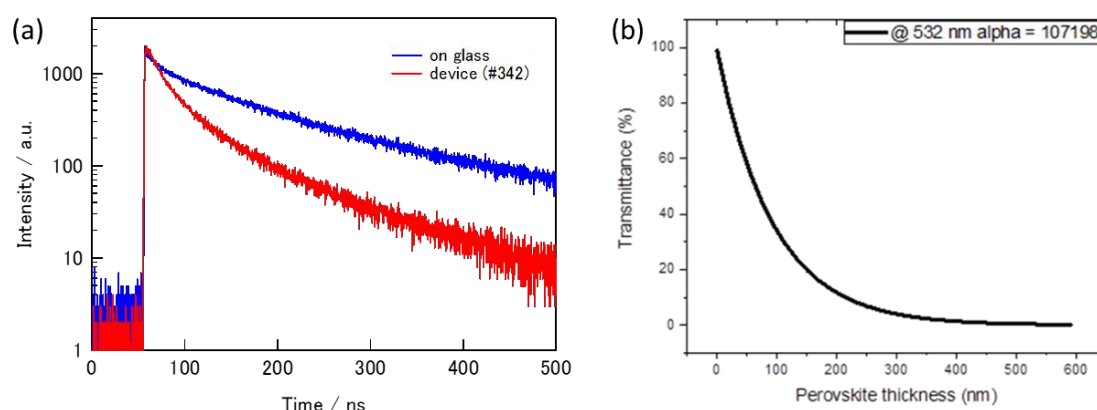


Figure 111. (a) TRPL of the perovskite (blue) and of the perovskite/PVBI-spiro (red). (b) Transmission of the light according to the perovskite thickness.

For PVBI-spiro, PL occurred at 782 nm on both TiO₂ and HTM side (Figure 112a). TRPL on TiO₂ side showed shorter decay than HTM side, suggesting that charge separation occurs more efficiently at the TiO₂/perovskite interface (Figure 112b). On the other hand, in the case of Li-spiro, different emission spectra were recorded for each surface excitation (Figure 112c). The emission spectrum on the TiO₂ side is remarkably red-shifted from 782 to 794 nm. One reason could be the effect of Li⁺ diffusion from the HTL to the TiO₂ surface which have been pointed before to create defects in the perovskite layer, resulting in a red-shift of the perovskite bandgap. Considering emission spectra on HTM side, PL peak appeared at the same position for each dopant suggesting that the local

perovskite bandgap is not affected. It should be noted that emission decay curves irradiated from TiO_2 side are very similar in Li-spiro and PVBI-spiro solar cells (Figure 112d). From HTM side, emission decay of Li-spiro quenched faster than PVBI-spiro, suggesting that hole injection is improved. However, according to deconvolution analysis, at least three decay mechanisms were involved (Table 46). The faster parameter τ_1 is considered to reflect hole injection into the HTM since it is shorter than the emission lifetime of perovskite on glass. Thus, hole injection should be more efficient in PVBI-spiro. Finally, the longer charge carrier lifetime in PVBI-spiro may be due to less non-radiative/more radiative recombinations into the perovskite as compared to Li-spiro, which could also explain the higher V_{oc} and the lower hysteresis in PVBI-spiro PSCs. To confirm this interpretation, PLQE could be performed. If higher PLQE is found in the PVBI-spiro PSC, it would mean that there is less non-radiative recombinations in the PVBI-spiro devices.⁵¹

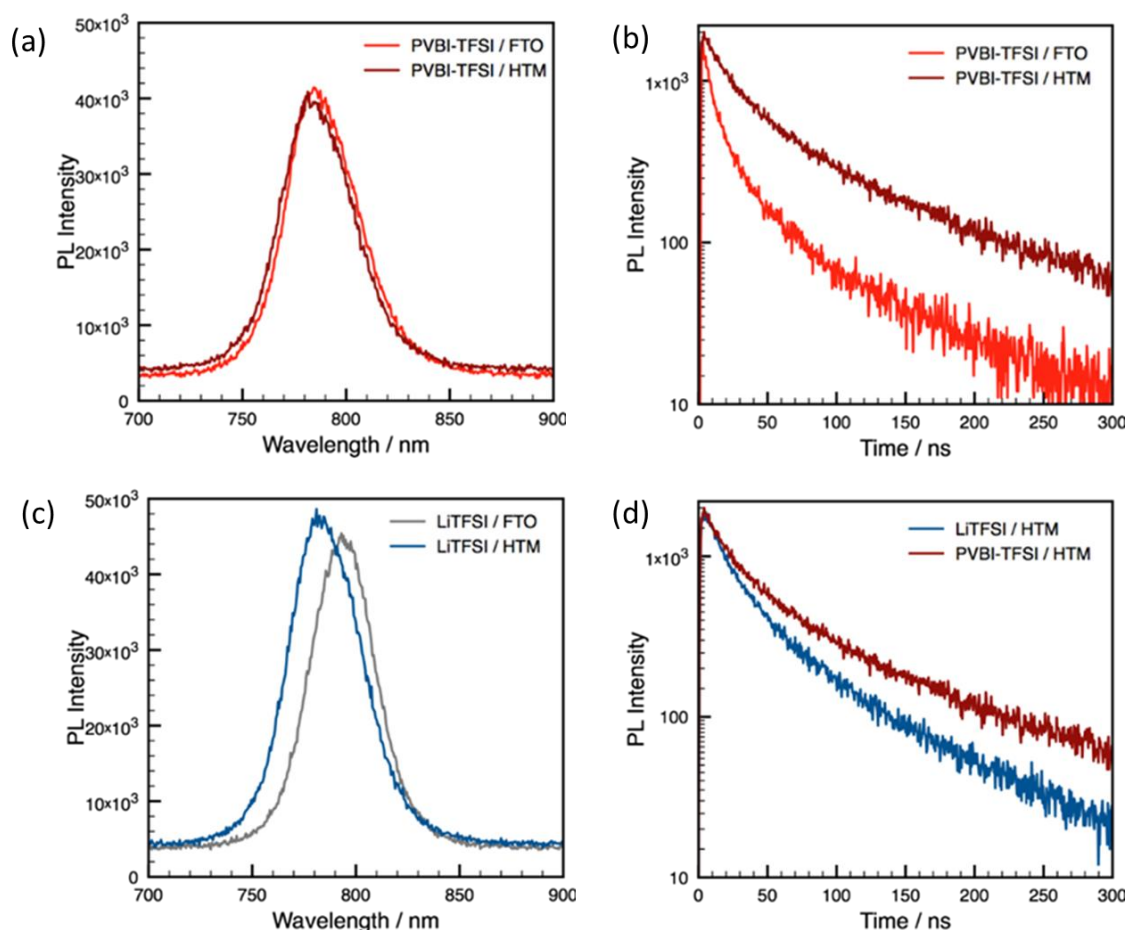


Figure 112. (a) PL and (b) TRPL of PSCs containing PVBI-spiro, irradiated from FTO and from HTM sides. (c) PL and (d) TRPL using Li-spiro as HTM.

Table 46. Calculated convolution parameters from TRPL measurements. The fitting was performed following $A = A_1.e^{-t/\tau_1} + A_2.e^{-t/\tau_2} + A_3.e^{-t/\tau_3}$.

		τ_1	$A_1/(A_1+A_2+A_3)$	τ_2	$A_2/(A_1+A_2+A_3)$	τ_3	$A_3/(A_1+A_2+A_3)$
		ns		ns		ns	
Perovskite on glass		32.7	49	174	51	-	-
FTO-side	LiTFSI	6.85	65	25.1	25	89.2	10
	PVBI-TFSI	6.43	63	24.6	29	103	8
HTM-side	LiTFSI	17.4	65	55.4	29	180	6
	PVI-TFSI	14.8	45	51.8	40	188	15

3.2.5 Stability

The stability of the devices was controlled by regularly measuring I-V curves (Figure 113). PSCs were stored in dry atmosphere in the dark. PVBI-spiro device efficiency was found to slightly decrease from over 20 to 18.5 % within 25 days, due to reduced J_{sc} and FF. The evolution of the V_{oc} was more surprising, decreasing during the first week from 1.15 to 1.08 V, before recovering and stabilizing around 1.13 V. Li-spiro device performance was found to increase between the first and the second measurement. In Li-spiro PSCs, ageing seemed to be beneficial in particular for the V_{oc} with a best PCE of 19.5 % measured 16 days after the device was fabricated. This could be explained by the slow doping mechanism of spiro-OMeTAD by LiTFSI and oxygen. In both devices, hysteresis is a little bit enlarged. After a 25-day ageing, the Li-spiro device was 0.7 % more efficient than the PVBI-spiro one. A longer study would be necessary to understand better the degradation processes in both devices.

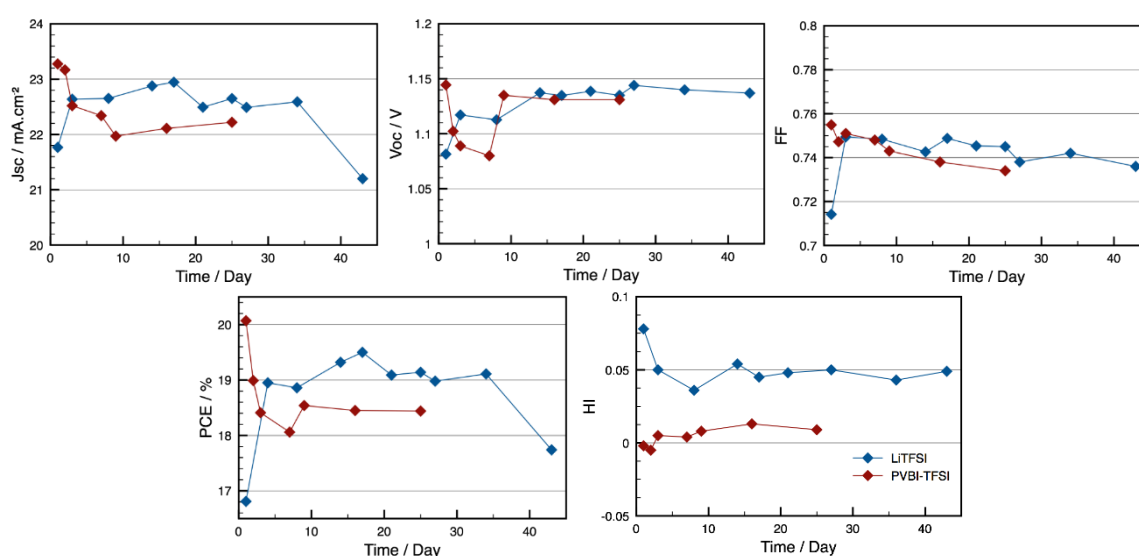


Figure 113. Stability of J_{sc} , V_{oc} , FF, PCE, and HI of spiro-OMeTAD and PVBI-TFSI-based PSCs over time.

Stability of PVBI-spiro devices in operating conditions was less than expected. Maximum power point tracking (MPPT) of PVBI-spiro showed a significant drop in current after a 4-minute experiment as compared to Li-spiro (Figure 114a). However, J_{sc} tracking with alternative switches of light showed smaller variations than Li-spiro (Figure 114b). This may suggest a photo-reversible mechanism in the HTM or at the perovskite/HTM interface affecting the current density of the device. The photo-responsivity was also improved for the PVBI-spiro devices, which is in accordance with the reduced hysteresis found in these devices. Continuous V_{oc} tracking revealed same behaviour in both devices (Figure 114c).

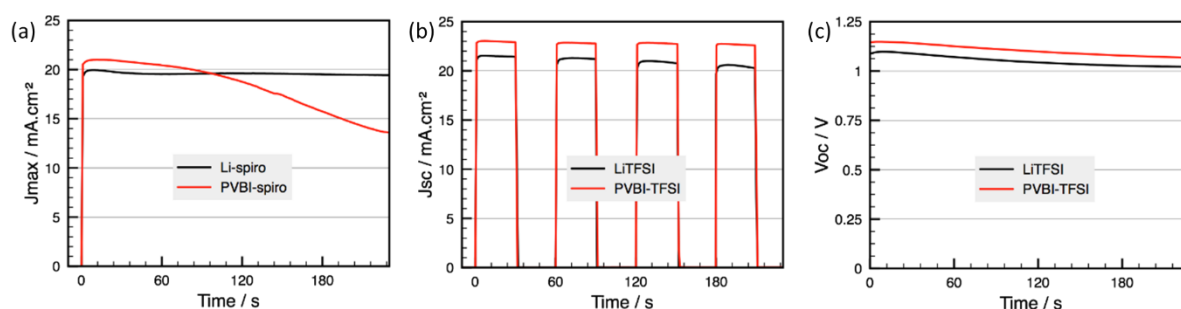


Figure 114. (a) Continuous J_{max} tracking, (b) J_{sc} tracking over alternative light switches, and (c) V_{oc} tracking in operating conditions of Li-spiro and PVBI-spiro PSCs.

To confirm the photo-reversible effect, one PSC was carefully prepared away from light and the other continuously exposed to ambient light. In Figure 115, a first I-V scan showed that the PSC stored in the dark well performed with a high efficiency of 19.5 % while the one over exposed to light only gave 14.0 % efficiency. Second I-V scans were carried out after a 72-h storage in the dark for both cells. The PSC made in dark conditions still exhibited high efficiency of 19.1 %, while the previously light exposed PSC gave enhanced efficiency of 16.3 %, meaning that the cell can partially recover after a while away from light. Moreover, when several I-V curves are performed in a row, we observe a decrease in PV performances and a switch of hysteresis from normal to inverse (Table 47). Going back to the previous paragraph where the possible deprotonation of the methylammonium by either tBP or PVBI was hypothesized, over light exposure or over operating the device may favour these reactions, changing the hysteresis behaviour and creating local defects due to high concentration of negative perovskite crystal and/or protonated PVBI and tBP.

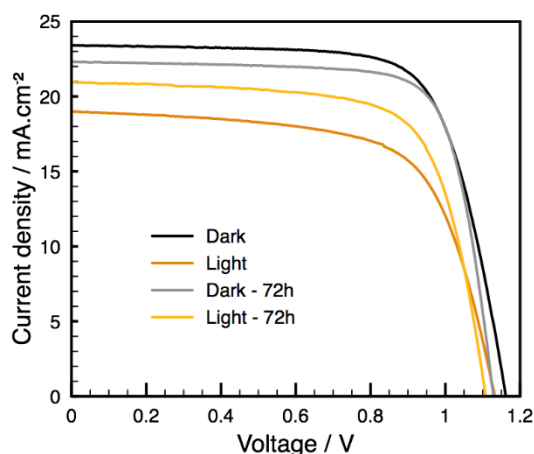


Figure 115. I-V curves of PVBI-spiro PSCs processed either in the dark or under illumination, after fabrication and after a 72-h ageing in the dark.

Table 47. Best PV parameters of PVBI-spiro PSCs processed either in the dark or under illumination, after fabrication and after a 72-h ageing in the dark.

		Reverse scan				Forward scan				HI
		J _{sc}	V _{oc}	FF	PCE	J _{sc}	V _{oc}	FF	PCE	
		mA.cm ⁻²	V		%	mA.cm ⁻²	V		%	
t = 0	Dark	23.21	1.17	0.72	19.33	23.42	1.16	0.72	19.53	-0.01
	Light	18.98	1.13	0.65	13.98	20.80	1.12	0.51	11.99	0.14
t = 72h	Dark	22.31	1.13	0.76	19.10	22.67	1.12	0.73	18.65	0.02
	Light	20.94	1.11	0.70	16.32	21.85	1.10	0.54	12.89	0.21

4 Polyelectrolytes as dopants for the perovskite

The potential of the materials to dope the perovskite was finally explored. As mentioned before, all had a very good solubility in DMF and DMSO. Typically, optimal ionic liquid concentration to dope the perovskite around 2 mol.%. Thus, 1.7 mol.% of PVBI-TFSI, 1.6 mol.% of PVBI-I, 2 mol.% of PSTFSI-K and 2 mol.% of PILS(TFSI)-*b*-PVK were independently added to perovskite precursor solutions. In this experiment, the perovskite was not doped with K⁺ (MA_{0.15}FA_{0.85}PbI_{2.55}Br_{0.45}). No solubility issues were noticed. The process to make the perovskite layers was unchanged.

Table 48. PV parameters of PSCs employing polymers to dope the perovskite.

Dopant	Reverse scan				Forward scan				HI
	J _{sc}	V _{oc}	FF	PCE	J _{sc}	V _{oc}	FF	PCE	
	mA.cm ⁻²	V		%	mA.cm ⁻²	V		%	
Without	22.76 ^a	1.10	0.74	18.33	22.94	1.06	0.53	12.93	0.40
	22.72 ^b	1.09	0.71	17.48	22.82	1.05	0.44	10.63	0.39
	± 0.08 ^c	± 0.01	± 0.03	± 0.93	± 0.10	± 0.02	± 0.10	± 2.63	± 0.12
PVBI-TFSI	21.67	1.07	0.39	8.95	21.90	1.04	0.51	11.60	-0.30
	18.57	0.99	0.42	7.78	20.33	0.96	0.46	9.25	-0.18
	± 3.56	± 0.08	± 0.04	± 1.51	± 1.79	± 0.09	± 0.04	± 2.39	± 0.09
PVBI-I	22.96	1.05	0.61	14.80	23.12	1.02	0.41	9.59	0.35
	22.76	1.04	0.56	13.30	22.92	1.00	0.36	8.32	0.38
	± 0.20	± 0.02	± 0.06	± 1.79	± 0.30	± 0.04	± 0.06	± 1.77	± 0.06
PSTFSI-K	5.89	0.65	0.33	1.27	7.82	0.59	0.32	1.49	-0.17
	6.22	0.62	0.33	1.24	8.04	0.57	0.32	1.48	-0.19
	± 0.46	± 0.04	± 0.01	± 0.03	± 0.31	± 0.03	± 0.02	± 0.01	± 0.02
PILS(TFSI)-b-PVK	21.09	1.14	0.40	9.66	21.91	1.12	0.39	9.61	0.01
b-PVK	20.53	1.14	0.40	9.45	21.70	1.12	0.37	8.92	0.06
	± 0.79	± 0.01	± 0.02	± 0.30	± 0.30	± 0.01	± 0.03	± 0.97	± 0.07

^a Best cell; ^b average on 4 cells; ^c standard deviation of the average.

In devices, the undoped perovskite exhibited a best efficiency of 18.3 % with a large hysteresis (Table 48). Among the doped devices, PVBI-I showed the best PCEs, up to 14.80 % (Figure 116). Hysteresis was slightly reduced but is still important. Lower PCE are mainly due to lower FF. The PILS(TFSI)-b-PVK doped perovskite had a high V_{oc} of 1.14 V, narrower hysteresis, but the FF limited the PCE to 9.7 %. Interestingly, the PVBI-TFSI doped perovskite devices had a reverse hysteresis, with the best PCEs from the forward scans. However, here again, the FF limited the final efficiency to 11.6 %. Finally, the best-looking perovskite doped with PSTFSI-K led to the worst PV performances < 2 % efficiency. Even though the performances of the devices were still fair, this first attempt revealed the potential of the PILs to increase the V_{oc} (PILS(TFSI)-b-PVK) or influence the hysteresis (PVBI-TFSI, PVBI-I, PILS(TFSI)-b-PVK).

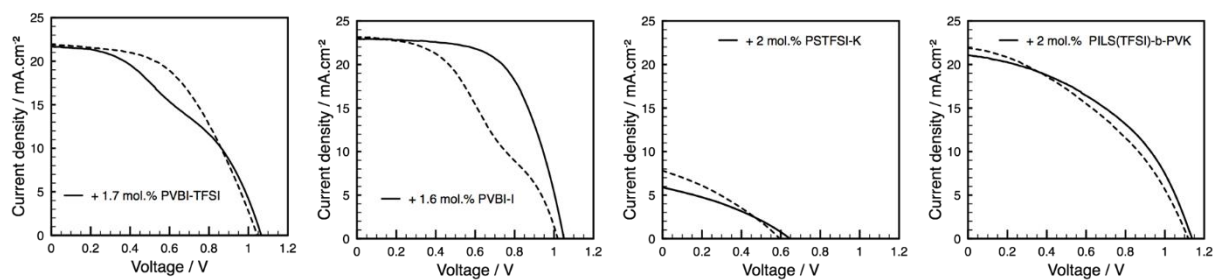


Figure 116. Best I-V curves of PSCs containing perovskite doped with different PILs. Filled lines: reverse scan; dotted line: forward scan.

Conclusion

Polyelectrolytes were incorporated in perovskite solar cells as dopants for HTMs and as dopant for the perovskite. The use of poly(ionic liquid) PVBI-TFSI as dopant for spiro-OMeTAD showed promising results for efficient lithium-free PSCs.

PVBI-TFSI was able to considerably increase spiro-OMeTAD conductivity of four orders of magnitude, up to 1.9×10^{-5} S/cm. In PSCs, PVBI-TFSI-doped spiro-OMeTAD demonstrated record power conversion efficiency as high as 20.4 %, versus 18.4 % for LiTFSI-doped spiro-OMeTAD. This improvement was characterized by a high V_{oc} and a negligible hysteresis, which are suggested to be due to a reduction of recombinations at the perovskite/HTM interface and a good balanced charge extraction, induced by a higher conductivity and a better energy band alignment. Moreover, compared to LiTFSI, the long chains of the polymer dopant are expected to provide phase stability to the PSC, by inhibiting the diffusion of the active components as in the case of low molecular weight additives, which ultimately deteriorates the long term operation of the PSCs. Also, air-free doping mechanism avoids the atmosphere exposure step required in LiTFSI doped spiro-OMeTAD devices that could induce device degradation. Up to now, this is the best PSC performance so far reported with an alternative dopant in spiro-OMeTAD.

The proposed doping mechanism involves a proton transfer from PVBI⁺ to spiro-OMeTAD. Hydrogen bonding between PVBI⁺ and spiro-OMeTAD was evidenced by NMR in solution, while formation of oxidized spiro-OMeTAD species were revealed by absorption spectroscopy in thin film. The doping mechanism was found to be influenced by the solvent, tBP, and light exposure. tBP and light dependency are suspected to induce or encourage undesirable reactions that compromise the device stability in operating conditions.

References

1. Qian, W.; Texter, J.; Yan, F., Frontiers in poly(ionic liquid)s: syntheses and applications. *Chemical Society Reviews* **2017**, *46* (4), 1124-1159.
2. Jeng, J.-Y.; Chiang, Y.-F.; Lee, M.-H.; Peng, S.-R.; Guo, T.-F.; Chen, P.; Wen, T.-C., CH₃NH₃PbI₃ Perovskite/Fullerene Planar-Heterojunction Hybrid Solar Cells. *Advanced Materials* **2013**, *25* (27), 3727-3732.
3. Jung, S.-K.; Heo Jin, H.; Lee Dae, W.; Lee, S.-C.; Lee, S.-H.; Yoon, W.; Yun, H.; Im Sang, H.; Kim Jong, H.; Kwon, O. P., Nonfullerene Electron Transporting Material Based on Naphthalene Diimide Small Molecule for Highly Stable Perovskite Solar Cells with Efficiency Exceeding 20%. *Advanced Functional Materials* **2018**, *28* (20), 1800346.
4. Choi, H.; Mai, C.-K.; Kim, H.-B.; Jeong, J.; Song, S.; Bazan, G. C.; Kim, J. Y.; Heeger, A. J., Conjugated polyelectrolyte hole transport layer for inverted-type perovskite solar cells. *Nature Communications* **2015**, *6*, 7348.
5. Li, X.; Liu, X.; Wang, X.; Zhao, L.; Jiu, T.; Fang, J., Polyelectrolyte based hole-transporting materials for high performance solution processed planar perovskite solar cells. *Journal of Materials Chemistry A* **2015**, *3* (29), 15024-15029.
6. Wang, S.; Yuan, W.; Meng, Y. S., Spectrum-Dependent Spiro-OMeTAD Oxidization Mechanism in Perovskite Solar Cells. *ACS applied materials & interfaces* **2015**, *7* (44), 24791-8.
7. Snaith, H. J.; Grätzel, M., Enhanced charge mobility in a molecular hole transporter via addition of redox inactive ionic dopant: Implication to dye-sensitized solar cells. *Applied Physics Letters* **2006**, *89* (26), 262114.
8. (a) Haque, S. A.; Palomares, E.; Cho, B. M.; Green, A. N. M.; Hirata, N.; Klug, D. R.; Durrant, J. R., Charge Separation versus Recombination in Dye-Sensitized Nanocrystalline Solar Cells: the Minimization of Kinetic Redundancy. *Journal of the American Chemical Society* **2005**, *127* (10), 3456-3462; (b) Dürr, M.; Yasuda, A.; Nelles, G., On the origin of increased open circuit voltage of dye-sensitized solar cells using 4-tert-butyl pyridine as additive to the electrolyte. *Applied Physics Letters* **2006**, *89* (6), 061110.
9. Berhe, T. A.; Su, W.-N.; Chen, C.-H.; Pan, C.-J.; Cheng, J.-H.; Chen, H.-M.; Tsai, M.-C.; Chen, L.-Y.; Dubale, A. A.; Hwang, B.-J., Organometal halide perovskite solar cells: degradation and stability. *Energy & Environmental Science* **2016**, *9* (2), 323-356.
10. Li, Z.; Xiao, C.; Yang, Y.; Harvey, S. P.; Kim, D. H.; Christians, J. A.; Yang, M.; Schulz, P.; Nanayakkara, S. U.; Jiang, C.-S.; Luther, J. M.; Berry, J. J.; Beard, M. C.; Al-Jassim, M. M.; Zhu, K., Extrinsic ion migration in perovskite solar cells. *Energy & Environmental Science* **2017**, *10* (5), 1234-1242.
11. Hawash, Z.; Ono, L. K.; Raga, S. R.; Lee, M. V.; Qi, Y., Air-Exposure Induced Dopant Redistribution and Energy Level Shifts in Spin-Coated Spiro-MeOTAD Films. *Chemistry of Materials* **2015**, *27* (2), 562-569.
12. Li, W.; Dong, H.; Wang, L.; Li, N.; Guo, X.; Li, J.; Qiu, Y., Montmorillonite as bifunctional buffer layer material for hybrid perovskite solar cells with protection from corrosion and retarding recombination. *Journal of Materials Chemistry A* **2014**, *2* (33), 13587-13592.
13. Greijer, H.; Lindgren, J.; Hagfeldt, A., Resonance Raman Scattering of a Dye-Sensitized Solar Cell: Mechanism of Thiocyanato Ligand Exchange. *The Journal of Physical Chemistry B* **2001**, *105* (27), 6314-6320.

14. Xu, B.; Zhu, Z.; Zhang, J.; Liu, H.; Chueh, C. C.; Li, X.; Jen Alex, K. Y., 4-Tert-butylpyridine Free Organic Hole Transporting Materials for Stable and Efficient Planar Perovskite Solar Cells. *Advanced Energy Materials* **2017**, 7 (19), 1700683.
15. Li, Z.; Tinkham, J.; Schulz, P.; Yang, M.; Kim, D. H.; Berry, J.; Sellinger, A.; Zhu, K., Acid Additives Enhancing the Conductivity of Spiro-OMeTAD Toward High-Efficiency and Hysteresis-Less Planar Perovskite Solar Cells. *Advanced Energy Materials* **2017**, 7 (4), 1601451.
16. (a) Koh Teck, M.; Dharani, S.; Li, H.; Prabhakar Rajiv, R.; Mathews, N.; Grimsdale Andrew, C.; Mhaisalkar Subodh, G., Cobalt Dopant with Deep Redox Potential for Organometal Halide Hybrid Solar Cells. *ChemSusChem* **2014**, 7 (7), 1909-1914; (b) Noh, J. H.; Jeon, N. J.; Choi, Y. C.; Nazeeruddin, M. K.; Gratzel, M.; Seok, S. I., Nanostructured TiO₂/CH₃NH₃PbI₃ heterojunction solar cells employing spiro-OMeTAD/Co-complex as hole-transporting material. *Journal of Materials Chemistry A* **2013**, 1 (38), 11842-11847; (c) Krishnamoorthy, T.; Kunwu, F.; Boix, P. P.; Li, H.; Koh, T. M.; Leong, W. L.; Powar, S.; Grimsdale, A.; Gratzel, M.; Mathews, N.; Mhaisalkar, S. G., A swivel-cruciform thiophene based hole-transporting material for efficient perovskite solar cells. *Journal of Materials Chemistry A* **2014**, 2 (18), 6305-6309.
17. Pellaroque, A.; Noel, N. K.; Habisreutinger, S. N.; Zhang, Y.; Barlow, S.; Marder, S. R.; Snaith, H. J., Efficient and Stable Perovskite Solar Cells Using Molybdenum Tris(dithiolene)s as p-Dopants for Spiro-OMeTAD. *ACS Energy Letters* **2017**, 2 (9), 2044-2050.
18. Li, M.; Wang, Z.-K.; Yang, Y.-G.; Hu, Y.; Feng, S.-L.; Wang, J.-M.; Gao, X.-Y.; Liao, L.-S., Copper Salts Doped Spiro-OMeTAD for High-Performance Perovskite Solar Cells. *Advanced Energy Materials* **2016**, 6 (21), 1601156.
19. (a) Nguyen, W. H.; Bailie, C. D.; Unger, E. L.; McGehee, M. D., Enhancing the Hole-Conductivity of Spiro-OMeTAD without Oxygen or Lithium Salts by Using Spiro(TFSI)₂ in Perovskite and Dye-Sensitized Solar Cells. *Journal of the American Chemical Society* **2014**, 136 (31), 10996-11001; (b) Bach, U. Solid-state dye-sensitized mesoporous TiO₂ solar cells. Ph.D. Thesis. Ecole polytechnique fédérale de Lausanne, 2000.
20. Xu, M.; Rong, Y.; Ku, Z.; Mei, A.; Li, X.; Han, H., Improvement in Solid-State Dye Sensitized Solar Cells by p-Type Doping with Lewis Acid SnCl₄. *The Journal of Physical Chemistry C* **2013**, 117 (44), 22492-22496.
21. Chen, D. Y.; Tseng, W. H.; Liang, S. P.; Wu, C. I.; Hsu, C. W.; Chi, Y.; Hung, W. Y.; Chou, P. T., Application of F4TCNQ doped spiro-MeOTAD in high performance solid state dye sensitized solar cells. *Physical chemistry chemical physics : PCCP* **2012**, 14 (33), 11689-94.
22. Ye, T.; Wang, J.; Chen, W.; Yang, Y.; He, D., Improved Performance and Reproducibility of Perovskite Solar Cells by Well-Soluble Tris(pentafluorophenyl)borane as a p-Type Dopant. *ACS applied materials & interfaces* **2017**, 9 (21), 17923-17931.
23. Qiuju Liu, L. F., Qin'e Zhang, An'an Zhou, Baozeng Wang, Hua Bai, Qingyong Tian, Bin Fan, and Tongyi Zhang, Benzoyl Peroxide as an Efficient Dopant for Spiro-OMeTAD in Perovskite Solar Cells. *ChemSusChem* **2017**, (10), 3098-3104.
24. Luo, J.; Xia, J.; Yang, H.; Chen, L.; Wan, Z.; Han, F.; Malik, H. A.; Zhu, X.; Jia, C., Toward high-efficiency, hysteresis-less, stable perovskite solar cells: unusual doping of a hole-transporting material using a fluorine-containing hydrophobic Lewis acid. *Energy & Environmental Science* **2018**.
25. Abate, A.; Hollman, D. J.; Teuscher, J.; Pathak, S.; Avolio, R.; D'Errico, G.; Vitiello, G.; Fantacci, S.; Snaith, H. J., Protic Ionic Liquids as p-Dopant for Organic Hole Transporting Materials and Their Application in High Efficiency Hybrid Solar Cells. *Journal of the American Chemical Society* **2013**, 135 (36), 13538-13548.

26. Zhang, H.; Shi, Y.; Yan, F.; Wang, L.; Wang, K.; Xing, Y.; Dong, Q.; Ma, T., A dual functional additive for the HTM layer in perovskite solar cells. *Chemical Communications* **2014**, 50 (39), 5020-5022.
27. Calìò, L.; Salado, M.; Kazim, S.; Ahmad, S., A Generic Route of Hydrophobic Doping in Hole Transporting Material to Increase Longevity of Perovskite Solar Cells. *Joule* **2018**.
28. Sun, C.; Xue, Q.; Hu, Z.; Chen, Z.; Huang, F.; Yip, H.-L.; Cao, Y., Phosphonium Halides as Both Processing Additives and Interfacial Modifiers for High Performance Planar-Heterojunction Perovskite Solar Cells. *Small* **2015**, 11 (27), 3344-3350.
29. Shahiduzzaman, M.; Yamamoto, K.; Furumoto, Y.; Kuwabara, T.; Takahashi, K.; Taima, T., Ionic liquid-assisted growth of methylammonium lead iodide spherical nanoparticles by a simple spin-coating method and photovoltaic properties of perovskite solar cells. *RSC Advances* **2015**, 5 (95), 77495-77500.
30. Wan, Y.; Dong, S.; Wang, Y.; Yang, L.; Qin, W.; Cao, H.; Yao, C.; Ge, Z.; Yin, S., Ionic liquid-assisted perovskite crystal film growth for high performance planar heterojunction perovskite solar cells. *RSC Advances* **2016**, 6 (100), 97848-97852.
31. Cho, N.; Li, F.; Turedi, B.; Sinatra, L.; Sarmah, S. P.; Parida, M. R.; Saidaminov, M. I.; Murali, B.; Burlakov, V. M.; Goriely, A.; Mohammed, O. F.; Wu, T.; Bakr, O. M., Pure crystal orientation and anisotropic charge transport in large-area hybrid perovskite films. *Nature Communications* **2016**, 7, 13407.
32. Bi, D.; Gao, P.; Scopelliti, R.; Oveisi, E.; Luo, J.; Grätzel, M.; Hagfeldt, A.; Nazeeruddin Mohammad, K., High-Performance Perovskite Solar Cells with Enhanced Environmental Stability Based on Amphiphile-Modified CH₃NH₃PbI₃. *Advanced Materials* **2016**, 28 (15), 2910-2915.
33. Salado, M.; Ramos, F. J.; Manzanares Valentin, M.; Gao, P.; Nazeeruddin Mohammad, K.; Dyson Paul, J.; Ahmad, S., Extending the Lifetime of Perovskite Solar Cells using a Perfluorinated Dopant. *ChemSusChem* **2016**, 9 (18), 2708-2714.
34. Zhang, Y.; Fei, Z.; Gao, P.; Lee, Y.; Tirani Farzaneh, F.; Scopelliti, R.; Feng, Y.; Dyson Paul, J.; Nazeeruddin Mohammad, K., A Strategy to Produce High Efficiency, High Stability Perovskite Solar Cells Using Functionalized Ionic Liquid-Dopants. *Advanced Materials* **2017**, 29 (36), 1702157.
35. Masi, S.; Colella, S.; Listorti, A.; Roiati, V.; Liscio, A.; Palermo, V.; Rizzo, A.; Gigli, G., Growing perovskite into polymers for easy-processable optoelectronic devices. *Scientific Reports* **2015**, 5, 7725.
36. Guo, Y.; Shoyama, K.; Sato, W.; Nakamura, E., Polymer Stabilization of Lead(II) Perovskite Cubic Nanocrystals for Semitransparent Solar Cells. *Advanced Energy Materials* **2016**, 6 (6), 1502317.
37. Zhao, Y.; Wei, J.; Li, H.; Yan, Y.; Zhou, W.; Yu, D.; Zhao, Q., A polymer scaffold for self-healing perovskite solar cells. *Nature Communications* **2016**, 7, 10228.
38. Bi, D.; Yi, C.; Luo, J.; Décoppet, J.-D.; Zhang, F.; Zakeeruddin, Shaik M.; Li, X.; Hagfeldt, A.; Grätzel, M., Polymer-templated nucleation and crystal growth of perovskite films for solar cells with efficiency greater than 21%. *Nature Energy* **2016**, 1, 16142.
39. Lin, Z.; Chang, J.; Zhu, H.; Xu, Q.-H.; Zhang, C.; Ouyang, J.; Hao, Y., Enhanced planar heterojunction perovskite solar cell performance and stability using PDDA polyelectrolyte capping agent. *Solar Energy Materials and Solar Cells* **2017**, 172, 133-139.
40. Li, H.; Liang, C.; Liu, Y.; Zhang, Y.; Tong, J.; Zuo, W.; Xu, S.; Shao, G.; Cao, S., Covalently Connecting Crystal Grains with Polyvinylammonium Carbochain Backbone To Suppress Grain Boundaries for Long-Term Stable Perovskite Solar Cells. *ACS applied materials & interfaces* **2017**, 9 (7), 6064-6071.

41. Xu, J.; Buin, A.; Ip, A. H.; Li, W.; Voznyy, O.; Comin, R.; Yuan, M.; Jeon, S.; Ning, Z.; McDowell, J. J.; Kanjanaboos, P.; Sun, J.-P.; Lan, X.; Quan, L. N.; Kim, D. H.; Hill, I. G.; Maksymovych, P.; Sargent, E. H., Perovskite–fullerene hybrid materials suppress hysteresis in planar diodes. *Nature Communications* **2015**, *6*, 7081.
42. (a) Chiang, C.-H.; Wu, C.-G., Bulk heterojunction perovskite–PCBM solar cells with high fill factor. *Nature Photonics* **2016**, *10*, 196; (b) Li, M.; Chao, Y.-H.; Kang, T.; Wang, Z.-K.; Yang, Y.-G.; Feng, S.-L.; Hu, Y.; Gao, X.-Y.; Liao, L.-S.; Hsu, C.-S., Enhanced crystallization and stability of perovskites by a cross-linkable fullerene for high-performance solar cells. *Journal of Materials Chemistry A* **2016**, *4* (39), 15088-15094; (c) Liu, X.; Lin, F.; Chueh, C.-C.; Chen, Q.; Zhao, T.; Liang, P.-W.; Zhu, Z.; Sun, Y.; Jen, A. K. Y., Fluoroalkyl-substituted fullerene/perovskite heterojunction for efficient and ambient stable perovskite solar cells. *Nano Energy* **2016**, *30*, 417-425.
43. de Frémont, P.; Marion, N.; Nolan, S. P., Carbenes: Synthesis, properties, and organometallic chemistry. *Coordination Chemistry Reviews* **2009**, *253* (7), 862-892.
44. Schölin, R.; Karlsson, M. H.; Eriksson, S. K.; Siegbahn, H.; Johansson, E. M. J.; Rensmo, H., Energy Level Shifts in Spiro-OMeTAD Molecular Thin Films When Adding Li-TFSI. *The Journal of Physical Chemistry C* **2012**, *116* (50), 26300-26305.
45. (a) Schulz, P.; Edri, E.; Kirmayer, S.; Hodes, G.; Cahen, D.; Kahn, A., Interface energetics in organo-metal halide perovskite-based photovoltaic cells. *Energy & Environmental Science* **2014**, *7* (4), 1377-1381; (b) Wang, Q.-K.; Wang, R.-B.; Shen, P.-F.; Li, C.; Li, Y.-Q.; Liu, L.-J.; Duhm, S.; Tang, J.-X., Energy Level Offsets at Lead Halide Perovskite/Organic Hybrid Interfaces and Their Impacts on Charge Separation. *Advanced Materials Interfaces* **2015**, *2* (3), 1400528.
46. Salado, M.; Jodlowski, A. D.; Roldan-Carmona, C.; de Miguel, G.; Kazim, S.; Nazeeruddin, M. K.; Ahmad, S., Surface passivation of perovskite layers using heterocyclic halides: Improved photovoltaic properties and intrinsic stability. *Nano Energy* **2018**, *50*, 220-228.
47. Nemnes, G. A.; Besleaga, C.; Stancu, V.; Dogaru, D. E.; Leonat, L. N.; Pintilie, L.; Torfason, K.; Ilkov, M.; Manolescu, A.; Pintilie, I., Normal and Inverted Hysteresis in Perovskite Solar Cells. *The Journal of Physical Chemistry C* **2017**, *121* (21), 11207-11214.
48. Habisreutinger, S. N.; Noel, N. K.; Snaith, H. J.; Nicholas, R. J., Investigating the Role of 4-Tert Butylpyridine in Perovskite Solar Cells. *Advanced Energy Materials* **2017**, *7* (1), 1601079.
49. Tachikawa, T.; Karimata, I.; Koberi, Y., Surface Charge Trapping in Organolead Halide Perovskites Explored by Single-Particle Photoluminescence Imaging. *The Journal of Physical Chemistry Letters* **2015**, *6* (16), 3195-3201.
50. (a) Kim, J.; Lee, S.-H.; Lee, J. H.; Hong, K.-H., The Role of Intrinsic Defects in Methylammonium Lead Iodide Perovskite. *The Journal of Physical Chemistry Letters* **2014**, *5* (8), 1312-1317; (b) Agiorgousis, M. L.; Sun, Y.-Y.; Zeng, H.; Zhang, S., Strong Covalency-Induced Recombination Centers in Perovskite Solar Cell Material CH₃NH₃PbI₃. *Journal of the American Chemical Society* **2014**, *136* (41), 14570-14575.
51. Abdi-Jalebi, M.; Andaji-Garmaroudi, Z.; Cacovich, S.; Stavrakas, C.; Philippe, B.; Richter, J. M.; Alsari, M.; Booker, E. P.; Hutter, E. M.; Pearson, A. J.; Lilliu, S.; Savenije, T. J.; Rensmo, H.; Divitini, G.; Ducati, C.; Friend, R. H.; Stranks, S. D., Maximizing and stabilizing luminescence from halide perovskites with potassium passivation. *Nature* **2018**, *555*, 497.

Chapter 5

PEDOT:PSTFSI Hole Transporting Material Towards Semi-Transparent Inverted Perovskite Solar Cells

In this last Chapter is studied an alternative hole transporting material to PEDOT:PSS for inverted p-i-n perovskite solar cells. PEDOT:PSTFSI is particularly less acidic and more transparent than PEDOT:PSS, suggesting potential for the development of stable semi-transparent solar cells. The possible integration of semi-transparent perovskite solar cells to perietodynamic windows was also investigated.

1 Introduction

As mentioned in the first Chapter, a largely used HTM for hole transport in inverted PSCs is PEDOT:PSS. This complex is composed of conductive and positively charged PEDOT polymer stabilized by PSS which acts as an aqueous dispersant polymer and as counter ion for the PEDOT. Good opto-electronic properties associated to printable processability from water have made PEDOT:PSS a material of choice for organic electronic devices, including PSCs.

A motivation to develop alternatives to PEDOT:PSS results from the relatively lower V_{oc} generally obtained with this hole transporting materials (0.88 – 0.95 V) compared to other PSCs (1.05 – 1.12 V). In this aim, Jen *et al.* regulated the acidity of PEDOT:PSS to optimize performances and film morphology, resulting a better band alignment, higher V_{oc} and higher PCE.¹ This introduces another drawback of PEDOT:PSS, its high acidity that could induce corrosion of the device.² Therefore, current strategies to improve performances and stability of PEDOT-based PSCs involve adjustment of the pH of PEDOT:PSS as well as optimizations of morphology and charge transport properties through introduction of organic solvents, dopants or surfactants.³

The electronic conductivity of PEDOT:PSS is governed by the ability of charge carriers to travel via polarons and bipolarons of the PEDOT chains. Alternative counter ions to PSS were investigated in order to bring ionic conductivity. This was particularly possible with bistriflimide ions (TFSI) which are more dissociated than sulfonates due to their extended delocalization.⁴ Poly(4-styrenesulfonyl(trifluoromethylsulfonyl)imide) (PSTFSI) is an ionic polymer made of a trifluoromethyl bisulfonfyl imide groups attached to a styrenic backbone. It was first synthesized for lithium battery application.⁴ Associated to PEDOT to form PEDOT:PSTFSI, the complex has comparable conductivity and higher transparency than PEDOT:PSS (Figure 117). PSTFSI does not only act as counter ion and aqueous dispersant but also brings ionic conductivity.

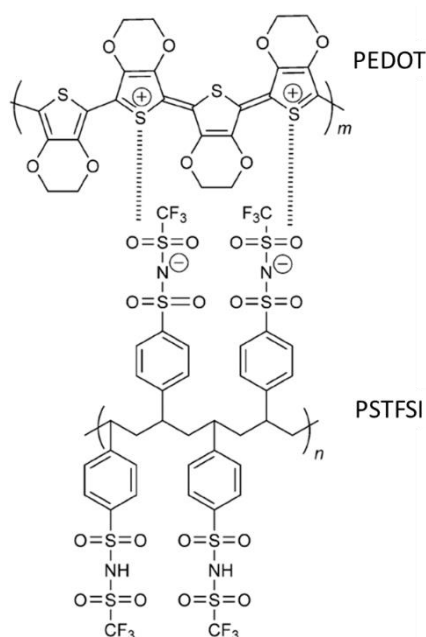


Figure 117. Stabilization of positive charge carriers of the PEDOT by PSTFSI.

Herein is compared commercial PEDOT:PSS (Clevios PH1000) to home-made PEDOT:PSTFSI. The PEDOT:PSTFSI complex was obtained by oxidative polymerization of EDOT in aqueous PSTFSIK (300 kg.mol⁻¹) solution. Charge transport properties and transparency of PEDOT:PSS and PEDOT:PSTFSI formulated with 5 wt.% of DMSO and 0.05 wt.% of Zonyl (FS-300 fluorsurfactant) have been reported in a previous work and are given in Table 49. Zonyl was added in order to improve film formation. Compared to commercial PEDOT:PSS, PEDOT:PSTFSI was also found to be more viscous, to be less acidic, to exhibit a gel-like behaviour which make film processability through doctor blading easier, and to be highly stable.⁵ Greater transparency of PEDOT:PSTFSI and lower acidity are expected to enhance solar light absorption by the perovskite and to improve the stability of inverted PSCs. PEDOT:PSTFSI could also be a promising candidate as HTM in semi-transparent PSCs.

Table 49. Thin film conductivity and transparency of PEDOT:PSS and PEDOT:PSTFSI.

	Conductivity $S.cm^{-1}$	Absorption coefficient at 550 nm $10^{-3} cm^{-1}$
PEDOT:PSS	778 ± 116	5
PEDOT:PSTFSI	224 ± 33	2

2 PEDOT:PSTFSI as an alternative to PEDOT:PSS

2.1 Properties of PEDOT:PSTFSI thin films

Thin film properties of PEDOT:PSTFSI were first compared to those of PEDOT:PSS layers. Both PEDOT:PSS and PEDOT:PSTFSI were formulated with 0.05 wt.% of Zonyl fluorosurfactant and 5 wt.% of DMSO, as it was previously reported to increase thin film morphology and conductivity.⁶

Contact angles of the PEDOT complexes were measured on ITO substrates with and without 15-min UV-ozone treatment of the surface (Table 50). UV-ozone treatment, additional to clean the surface, makes it more hydrophilic, resulting in a decrease in contact angles with the polyelectrolytes. For contact angles below 15° the surface is considered completely wet. Without UV-ozone treatment, PEDOT:PSTFSI showed a slightly higher contact angle on ITO.

Table 50. Contact angle of PEDOT:PSS and PEDOT:PSTFSI on ITO-glass with and without UV-ozone treatment.

	Without UV-ozone treatment	With UV-ozone treatment
PEDOT:PSS	$35.4 \pm 1.9^\circ$	$8.6 \pm 0.4^\circ$
PEDOT:PSTFSI	$38.4 \pm 1.7^\circ$	$13.8 \pm 0.9^\circ$

Homogeneous thin films, about 50 nm, were deposited by spin coating on ITO after UV-ozone treatment. Surface morphology and roughness were controlled by AFM (Figure 118). Roughness was measured on $5 \times 5 \mu\text{m}^2$ surfaces. Slightly smoother films of $R_q = 3.9 \pm 0.8 \text{ nm}$ were formed with PEDOT:PSTFSI, vs. $5.3 \pm 0.9 \text{ nm}$ for PEDOT:PSS films.

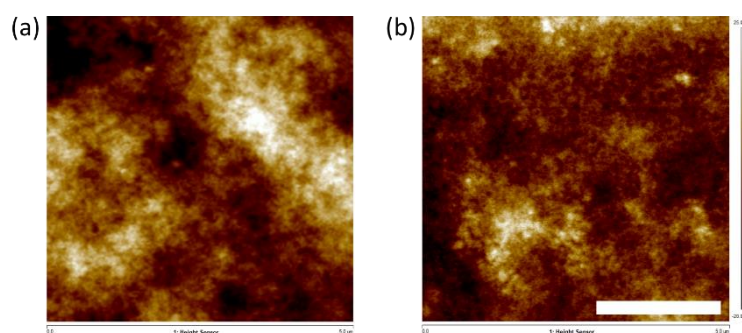


Figure 118. AFM topographic images of (a) PEDOT:PSS and (b) PEDOT:PSTFSI thin films. Scale bar = 2 μm. Colour range from - 20 to 25 nm.

As PEDOT:PSS and PEDOT:PSTFSI were dispersed in water, water content of dried films was evaluated by FTIR spectroscopy. PEDOT:PSS and PEDOT:PSTFSI films were dried 10 min at 150°C. Water is usually identified by a large band between 3100 and 3600 cm^{-1} , which was not found on the FTIR spectra Figure 119. Therefore, no water residues should alter the perovskite layer deposited on top of these films.

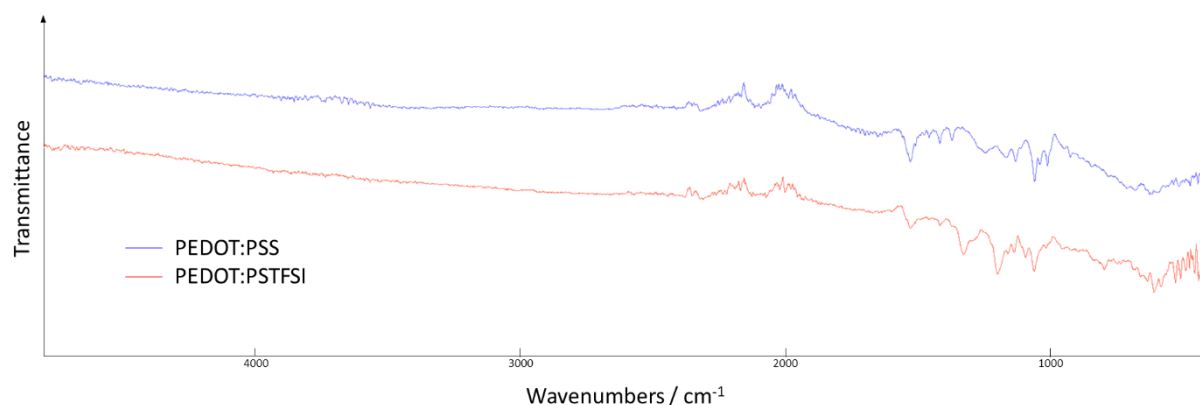


Figure 119. FTIR spectra of PEDOT:PSS and PEDOT:PSTFSI thin films.

Surface tension of similar films of PEDOT:PSS and PEDOT:PSTFSI were measured by the Owens-Wendt method (Table 51). Interfacial tension can be dissociated in two components. The dispersive part represents temporary variations in the electron density which are not permanently localized in the material while the polar part represents interactions in material having a dipole moment. Surface tension of PEDOT:PSS was higher than PEDOT:PSTFSI, suggesting that the PEDOT:PSTFSI film is more hydrophobic. This is also characterized by the lower polar component in PEDOT:PSTFSI.

Table 51. Interfacial tension of PEDOT:PSS and PEDOT:PSTFSI thin films.

	Interfacial tension	Dispersive component	Polar component
	mN/m	mN/m	mN/m
PEDOT:PSS	66.2 ± 0.6	22.3 ± 0.3	43.9 ± 0.3
PEDOT:PSTFSI	62.7 ± 0.3	23.9 ± 0.2	38.8 ± 0.1

HOMO levels of PEDOT:PSS and PEDOT:PSTFSI were measured by PESA on thin films coated on glass (Figure 120). PEDOT:PSS HOMO level was found to be -5.20 eV which is consistent with literature.⁷ PEDOT:PSTFSI showed a deeper HOMO level, about -5.35 eV, closer to the -5.43 eV perovskite valence band.

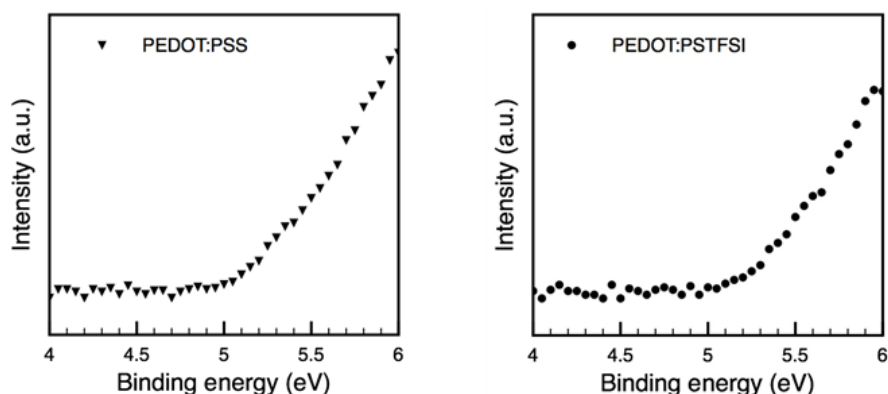


Figure 120. UPS spectra of PEDOT:PSS and PEDOT:PSTFSI thin films.

Absorption of PEDOT:PSS and PEDOT:PSTFSI thin films were measured by UV-vis spectroscopy on ITO substrates using ITO-glass substrate as reference (Figure 121). Both films had low absorbance in the visible range, which is suitable for an application in inverted solar cells. The negative absorption of the films under 500 nm is actually the result of an increase in the transmittance and a decrease in the reflectivity of the film compare to the ITO-glass reference substrate. This effect was observed for both PEDOT:PSS and PEDOT:PSTFSI films.

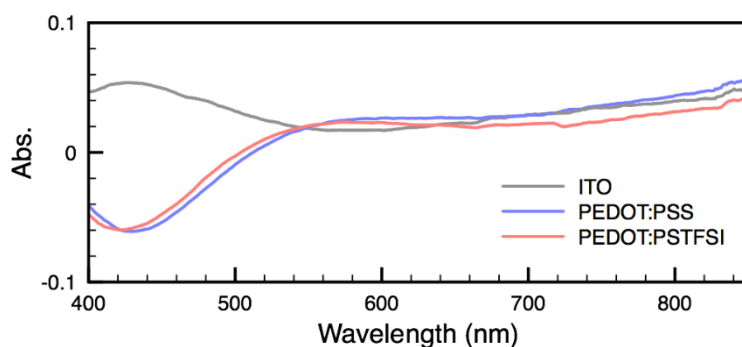


Figure 121. Absorption spectra of PEDOT:PSS and PEDOT:PSTFSI films on ITO-glass substrates.

Contact angles of DMF and of the perovskite precursor solution were measured on PEDOT:PSS and PEDOT:PSTFSI thin films (Table 52). The perovskite precursor solution had a good wetting on both films. PEDOT:PSS which was more hydrophilic had a slightly lower contact angle than PEDOT:PSTFSI.

Table 52. Contact angle of DMF and the perovskite precursor solution on PEDOT:PSS and PEDOT:PSTFSI films.

	DMF	Perovskite precursor solution
PEDOT:PSS	$6.5 \pm 0.9^\circ$	$17.2 \pm 0.8^\circ$
PEDOT:PSTFSI	$6.0 \pm 0.8^\circ$	$20.4 \pm 2.4^\circ$

Perovskite layers were deposited by spin coating using the anti-solvent method. The impact of the nature of the anti-solvent, chlorobenzene or toluene, on the perovskite morphology was controlled by AFM. As well, the perovskite thickness was measured with a profilometer (Table 53). All perovskite layers were shiny and no pinholes were found on AFM images (Figure 122). Perovskite layers had the same 400 nm thickness on top of PEDOT:PSS. Smaller grains about 150 nm were obtained using toluene instead of chlorobenzene where the grains were almost 200 nm large. On PEDOT:PSTFSI films, thinner perovskite layers were formed, especially using chlorobenzene, where a thickness of about 340 nm was measured. This thinner film revealed small grain size of only 65 nm. Larger grains of about 115 nm were formed using toluene. Perovskite surface roughness was around 6 nm on top of PEDOT:PSTFSI made with chlorobenzene. Other films showed the same roughness around 9 nm.

Table 53. Perovskite thin film characteristics according to the HTM and the anti-solvent.

	PEDOT:PSS		PEDOT:PSTFSI	
	Chlorobenzene	Toluene	Chlorobenzene	Toluene
Thickness nm	406 ± 6	404 ± 5	341 ± 13	388 ± 24
Roughness nm	9.2 ± 1.9	9.2 ± 0.8	6.5 ± 0.6	9.5 ± 2.1
Grain diameter nm	193 ± 74	145 ± 58	65 ± 30	116 ± 47

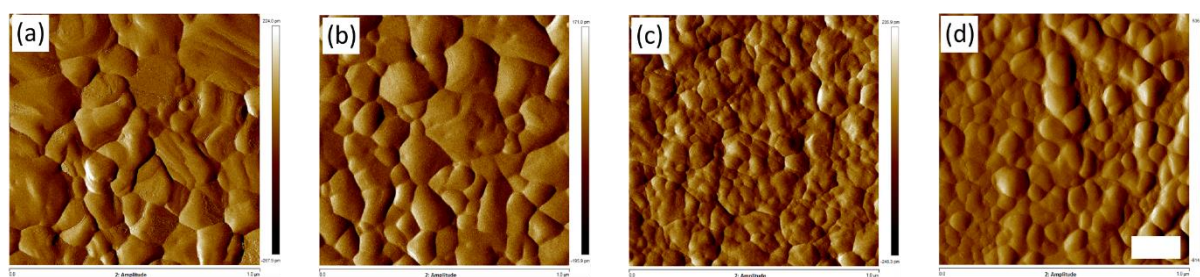


Figure 122. AFM amplitude images of perovskite thin films coated on (a,b) PEDOT:PSS and (c,d) PEDOT:PSTFSI using (a,c) chlorobenzene or (b,d) toluene as anti-solvent. Scale bar = 200 nm.

Chlorobenzene as anti-solvent led to large grains with reasonable surface roughness of the perovskite film coated on top of PEDOT:PSS. In the case of PEDOT:PSTFSI, replacing chlorobenzene by toluene resulted in larger perovskite grains. Although small differences in the perovskite morphology were observed, similar absorption spectra with the typical shape of the MAPbI₃ perovskite material were recorded on top of both polyelectrolytes (Figure 123). The lower absorption detected for MAPbI₃ processed on PEDOT:PSTFSI can be attributed to its thinner thickness.

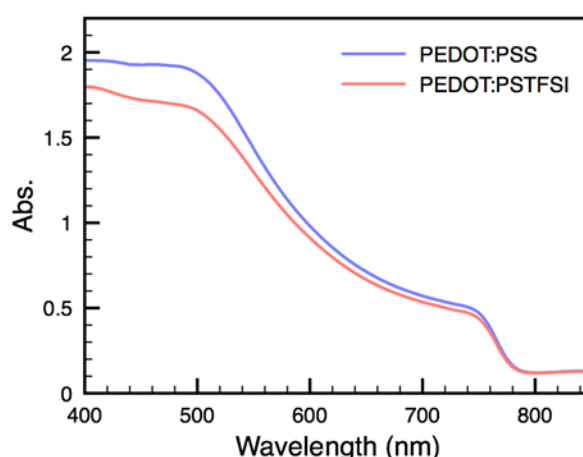


Figure 123. Absorption spectra of perovskite coated on PEDOT:PSS and PEDOT:PSTFSI.

To summarize, PEDOT:PSTFSI present good properties to be applied as HTM in inverted PSCs. Homogeneous thin films were easily processed by spin coating. The HOMO level of PEDOT:PSTFSI was measured at -5.35 eV, close to the perovskite valence band. Pinhole-free perovskite layers were formed on top of PEDOT:PSTFSI. However the lower interfacial tension of the film led to smaller perovskite grains than perovskite on PEDOT:PSS.

2.2 Integration of PEDOT:PSTFSI in perovskite solar cells

PEDOT:PSS and PEDOT:PSTFSI were finally compared as HTM in ITO/HTM/MAPbI₃/PC₆₀BM/BCP/Ag inverted PSCs. The device process is detailed in Chapter 2. PEDOT:PSTFSI and perovskite thickness layers have been optimized by adjusting respectively spin coating parameters and concentration of the precursor solution (Figure 124). Best PV performances were obtained for a PEDOT:PSTFSI thickness of 60 nm and a perovskite precursor solution concentration of 47 wt.%.

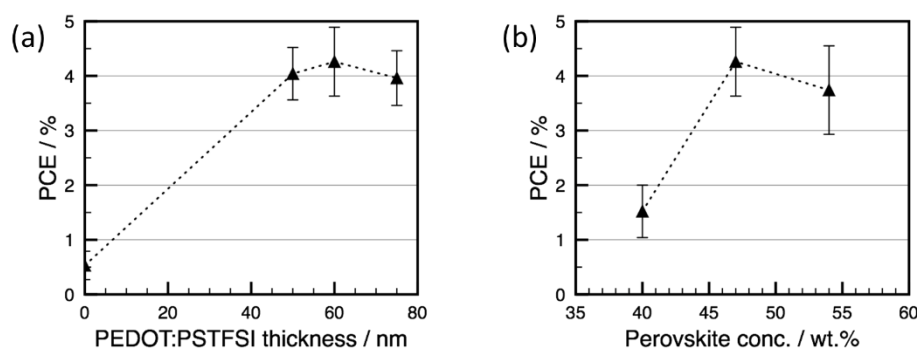


Figure 124. Average PCE of PEDOT:PSTFSI PSCs depending on (a) PEDOT:PSTFSI thickness and (b) the perovskite precursor solution concentration.

Performances of PEDOT:PSS and PEDOT:PSTFSI-based PSCs are reported in Table 54. Hysteresis was evaluated by the hysteresis index (HI) defined as $(PCE_{\text{reverse}} - PCE_{\text{forward}}) / PCE_{\text{reverse}}$. The best efficiency reached with PEDOT:PSTFSI was 5.26 % compared to 12.23 % using PEDOT:PSS (Figure 125). The difference in efficiency is mainly due to the lower J_{sc} for PEDOT:PSTFSI. Hysteresis and standard deviations are in the same range for both devices. These lower PV performances could be due to the lower conductivity of PEDOT:PSTFSI compared to PEDOT:PSS. This could also be due to smaller perovskite grains inducing more grain boundaries and higher recombination rate.

Table 54. Best and average (20 cells) PV parameters of devices based on PEDOT:PSS and PEDOT:PSTFSI.

HTM	Reverse scan				Forward scan				HI
	J_{sc}	V_{oc}	FF	PCE	J_{sc}	V_{oc}	FF	PCE	
	mA.cm^{-2}	V		%	mA.cm^{-2}	V		%	
PEDOT:PSS	21.95 ^a	0.87	0.56	10.86	21.68	0.88	0.63	12.23	-0.13
	18.23 ^b	0.83	0.50	7.72	19.36	0.87	0.59	10.09	-0.35
	$\pm 2.69^c$	± 0.05	± 0.07	± 1.77	± 1.88	± 0.03	± 0.04	± 0.91	± 0.20
PEDOT:PSTFSI	9.89	0.86	0.54	4.66	10.24	0.86	0.58	5.26	-0.13
	8.73	0.79	0.50	3.50	8.84	0.85	0.57	4.26	-0.29
	± 1.62	± 0.14	± 0.07	± 0.91	± 1.68	± 0.03	± 0.06	± 0.63	± 0.38

^a Best cell; ^b average on 8 cells; ^c standard deviation of the average.

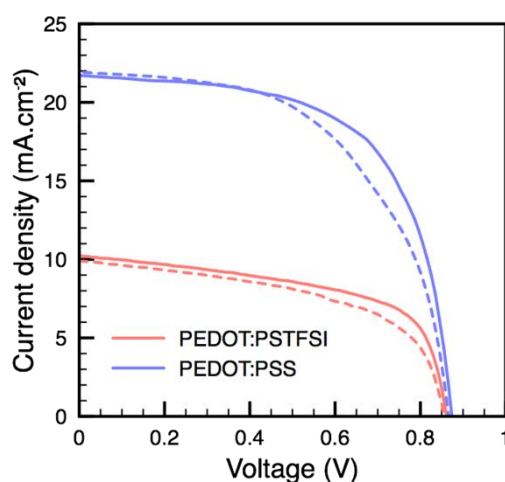


Figure 125. Best I-V curves of PEDOT:PSS and PEDOT:PSTFSI based PSCs. Full line = forward scan ; dotted line = reverse scan.

Two other formulations of PEDOT:PSTFSI were tested: one containing more PEDOT, and the other containing more PSTFSI. Increasing PEDOT proportion in PEDOT:PSTFSI decreased the transmittance. Optimal conductivity was measured for the standard PEDOT:PSTFSI formulation, where a compromise between the amount of conductive PEDOT and the doping ability of PSTFSI was found (Table 55). The pH of solutions was not affected and remained at 7.3.

Table 55. Characteristics of PEDOT:PSTFSI inks.

Formulation	Mol. ratio of PEDOT unit/PSTFSI unit	Absorption coefficient (550 nm) 10^{-3} cm^{-1}	Conductivity $S.\text{cm}^{-1}$
PEDOT rich PEDOT:PSTFSI	0.72	2.5	190 ± 28
Standard PEDOT:PSTFSI	0.60	2.1	224 ± 33
PSTFSI rich PEDOT:PSTFSI	0.48	1.4	146 ± 22

Same process as the original formulation was employed. Surprisingly, an improved PCE of 6.27 % was recorded for the PSTFSI rich PEDOT:PSTFSI, which is the less conductive formulation. Interpretation of these results is quite fastidious considering the large hysteresis of PSTFSI rich PEDOT:PSTFSI PSCs and the lack of reproducibility between solar cells (Table 56, Figure 126). Considering the poor PV performances recorded compared to PEDOT:PSS, PEDOT:PSTFSI was not further employed in the next experiments.

Table 56. Best and average (8 cells) PV parameters of PSCs based on different formulations of PEDOT:PSTFSI.

HTM	Reverse scan				Forward scan				HI
	J_{sc}	V_{oc}	FF	PCE	J_{sc}	V_{oc}	FF	PCE	
	$mA.cm^{-2}$	V		%	$mA.cm^{-2}$	V		%	
PEDOT rich	10.21 ^a	0.83	0.53	4.62	10.61	0.74	0.61	4.87	-0.05
PEDOT:PSTFSI	8.27 ^b	0.63	0.39	2.24	8.56	0.72	0.45	2.88	-0.48
	$\pm 1.26^c$	± 0.20	± 0.07	± 1.26	± 1.31	± 0.11	± 0.09	± 1.09	± 0.57
PSTFSI rich	11.22	0.69	0.44	3.51	11.71	0.82	0.64	6.27	-0.79
PEDOT:PSTFSI	10.07	0.68	0.41	2.94	10.41	0.78	0.51	4.26	-0.57
	± 1.52	± 0.16	± 0.09	± 1.13	± 1.58	± 0.08	± 0.10	± 1.26	± 0.48

^a Best cell; ^b average on 8 cells; ^c standard deviation of the average.

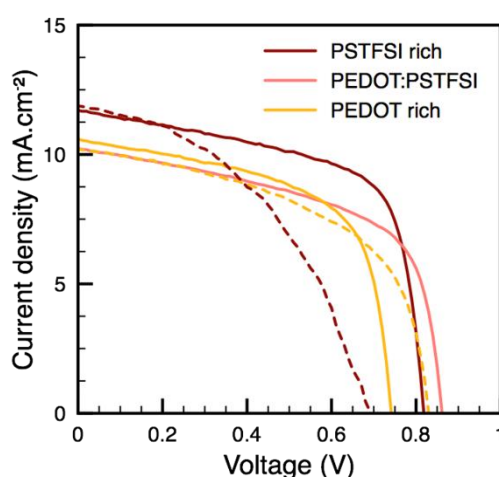


Figure 126. Best I-V curves of PSCs fabricated using different formulations of PEDOT:PSTFSI. Full line = forward scan, dotted line = reverse scan.

3 Towards semi-transparent perovskite solar cells

In this last part is studied the possibility for inverted PSCs to be integrated to windows. This work was realized in collaboration with the company Ridoret located in La Rochelle (France). Ridoret has developed parietodynamic windows acting like heat exchangers to reduce thermal losses. Thereby, during winter, outside air is warmed by heat losses and solar energy through greenhouse effect (Table 58).⁸ In summer, inversed process occurs to cool down incoming air. The objective was to determine how much energy is possible to harvest incorporating PSCs to the system, and how does it affect transparency and performances of the parietodynamic windows. Inverted p-i-n PSCs were chosen for this study due to their potential compatibility to industrial printing and cheapest estimated price compared to n-i-p architectures.⁹

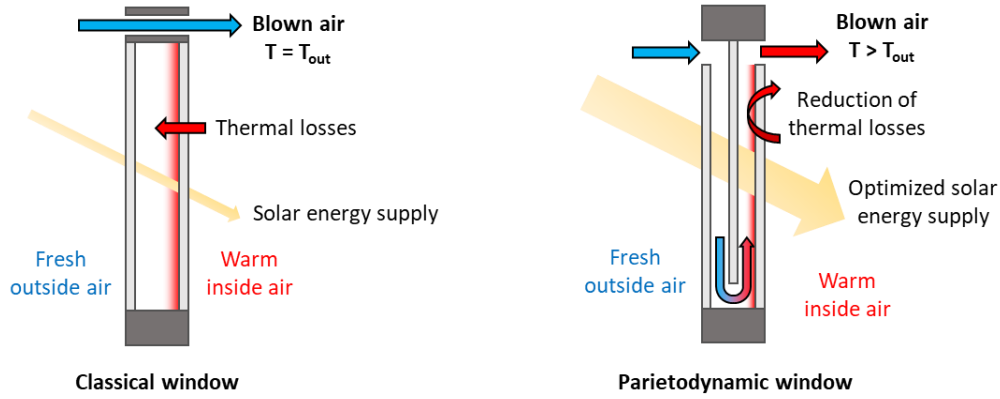


Figure 127. Parietodynamic window principle in summer.

The device architecture was ITO/PEDOT:PSS/MAPbI₃/PC₆₀BM/BCP/Ag. To increase the transparency of the device and determine how does it affect PCE, perovskite layer thickness was reduced by decreasing the concentration of the perovskite precursor solution. Obviously for semi-transparent solar cells, silver would have to be replaced by a transparent top electrode. However, this issue is not addressed in the following. Transparency of the device was determined by the light transmittance τ_L and calculated as:

$$\tau_L = \frac{\sum_{380\text{ nm}}^{780\text{ nm}} D_\lambda V(\lambda) \tau(\lambda) \Delta\lambda}{\sum_{380\text{ nm}}^{780\text{ nm}} D_\lambda V(\lambda) \Delta\lambda} \quad (1)$$

where D_λ is the relative spectral distribution of illuminant D65, $V(\lambda)$ is the spectral luminous efficiency, $\tau(\lambda)$ is the experimental spectral transmittance of the device and $\Delta\lambda$ the wavelength interval. Solar direct transmittance τ_S , ruling part of performances of the parietodynamic window, was defined as:

$$\tau_S = \frac{\sum_{300\text{ nm}}^{2500\text{ nm}} S_\lambda \tau(\lambda) \Delta\lambda}{\sum_{300\text{ nm}}^{2500\text{ nm}} S_\lambda \Delta\lambda} \quad (2)$$

where S_λ is the relative spectral distribution of solar radiation. The product $D_\lambda V(\lambda)$ and S_λ are given in tables.¹⁰

Not surprisingly, transmission of the devices increases, and efficiency decreases together with the decrease in the perovskite thickness (Table 57). As well, the reproducibility of the devices dramatically decreases when the perovskite got thinner. The transmission of the full device with the silver electrode dropped close to 0 %, confirming the necessity of using transparent top electrodes. Perovskite films from solution ≥ 28 wt.% were macroscopically homogeneous. Lower concentrations

were not further studied. Detailed PV performances are given in Table 58. V_{oc} and FF decreased with the perovskite thickness and the hysteresis was enlarged. The hysteresis is characterized by lower FF and V_{oc} for the reverse scan. Lower PV performances when reducing perovskite thickness might be related to a loss in the quality of the perovskite film (smaller grain size, higher number of pinholes...) increasing the recombination rate.

Table 57. Characteristics of the semi-transparent PSCs.

Perovskite sol. conc. <i>wt. %</i>	Perovskite thickness <i>nm</i>	τ_L w/o Ag %	τ_L with Ag %	τ_s w/o Ag %	Best PCE %	Average PCE (8 cells) %
54	585	1.1	0.04	22	12.23	10.09 ± 0.91
47	465	2.4	0.13	22	11.20	8.93 ± 1.10
43	355	4.0	0.07	25	10.37	7.97 ± 1.18
37	290	11	0.20	25	8.52	6.78 ± 1.37
28	190	22	0.18	33	8.36	3.70 ± 3.38
20	155	37			2.02	1.46 ± 0.46
10	80	47			0.15	0.10 ± 0.03

Table 58. PV parameters of semi-transparent PSCs.

Perovskite solution conc.	Reverse scan				Forward scan				HI
wt. %	J_{sc} $mA.cm^{-2}$	V_{oc} V	FF	PCE %	J_{sc} $mA.cm^{-2}$	V_{oc} V	FF	PCE %	
54	21.95 ^a	0.87	0.56	10.86	21.68	0.88	0.63	12.23	-0.13
	18.23 ^b	0.83	0.50	7.72	19.36	0.87	0.59	10.09	-0.35
	$\pm 2.69^c$	± 0.05	± 0.07	± 1.77	± 1.88	± 0.03	± 0.04	± 0.91	± 0.20
47	19.23	0.92	0.53	9.64	20.05	0.93	0.59	11.20	-0.16
	17.21	0.72	0.46	6.04	17.32	0.85	0.60	8.93	-0.63
	± 1.60	± 0.21	± 0.10	± 2.52	± 1.98	± 0.04	± 0.05	± 1.20	± 0.49
43	22.53	0.77	0.47	8.34	22.49	0.81	0.56	10.37	-0.24
	18.42	0.60	0.38	4.44	18.58	0.76	0.56	7.97	-0.84
	± 2.59	± 0.18	± 0.06	± 2.18	± 2.38	± 0.07	± 0.04	± 1.18	± 0.69
37	19.75	0.57	0.48	5.53	20.72	0.67	0.60	8.52	-0.54
	18.00	0.52	0.38	3.95	18.69	0.69	0.51	6.78	-0.73
	± 1.89	± 0.13	± 0.08	± 1.97	± 1.33	± 0.07	± 0.09	± 1.37	± 0.59
28	18.72	0.51	0.39	3.80	18.19	0.78	0.58	8.36	-1.20
	15.77	0.37	0.34	2.80	16.77	0.46	0.40	3.70	-0.69
	± 2.50	± 0.33	± 0.08	± 2.64	± 1.61	± 0.31	± 0.12	± 3.38	± 0.55

^a Best cell; ^b average on 4 cells; ^c standard deviation of the average.

Pictures of the final devices without the top silver electrode are displayed in Figure 128 to give an idea of the transparency of the devices.

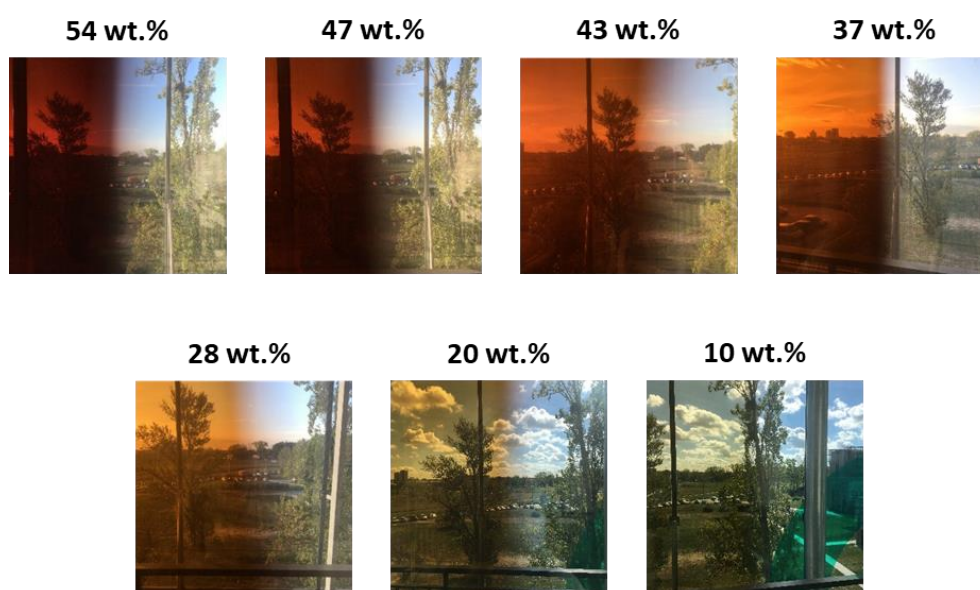


Figure 128. Pictures of semi-transparent devices without the top silver electrode (left) compared to device-free view (right).

The spectral transmittances of all the layers were recorded independently in Figure 129. As expected the perovskite is responsible for the low transmittance in the visible range. The transmittance in the infrared was limited by the ITO-glass substrate.

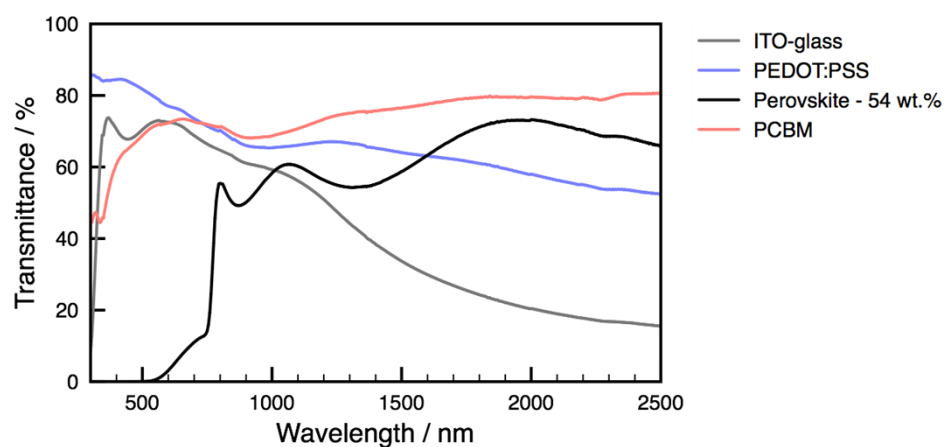


Figure 129. Spectral transmittance of the components of the devices.

Spectral transmittances of the whole devices are represented in Figure 130. Above 800 nm several transmittance peaks can be distinguished, shifting towards shorter wavelengths. They are suggested to be interferences, observable when several layers of materials with different refractive indexes are stacked.

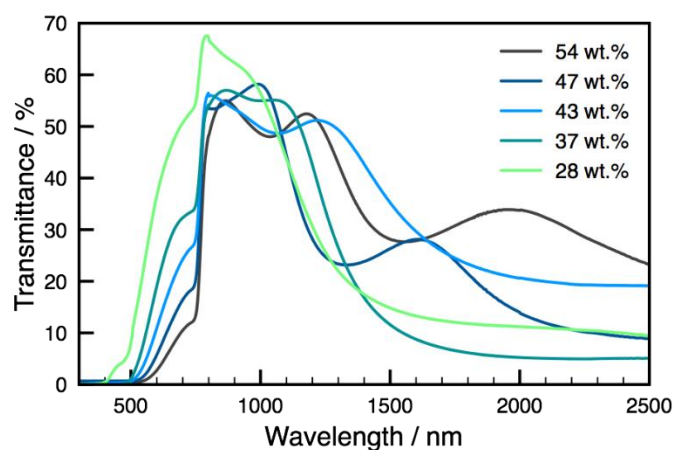


Figure 130. Spectral transmittance of devices according to the perovskite precursor concentration.

Finally, the stability of the devices was estimated by measuring regularly I-V curves (Figure 131). PSCs were stored in the dark in the atmosphere with a relative humidity of 20 %. After two weeks, the two devices with the thickest layers exhibited PCEs close to their initial values above 7 % while the

efficiency of the thinnest one dropped to 2 % efficiency after only 3 days. This result indicated that in our case the thicker the perovskite layer, the more stable is the device.

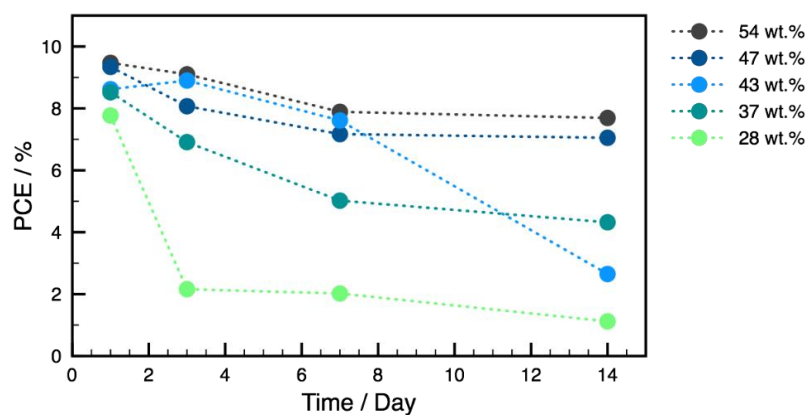


Figure 131. PCE of PSCs versus time.

In this study, it was evidenced that a compromise between efficiency, stability and transparency has to be found for window application. Both top and bottom electrodes materials commonly employed in devices should be replaced by relatively more transparent from visible to infrared regions for preserving performances of the parietodynamic window.

Conclusion

In the line with the development of semi-transparent PSCs, the highly transparent PEDOT:PSTFSI complex was compared to PEDOT:PSS as HTM in inverted PSCs. Despite good film-forming and suitable HOMO level, PEDOT:PSTFSI exhibited low PV performances and in particular low J_{sc} . This was suggested to be due to the lower conductivity of PEDOT:PSTFSI compared to PEDOT:PSS and to the smaller grains of perovskite layer, inducing greater recombination rate and limiting light-harvesting of the solar cells. As for PEDOT:PSS, incorporation of additives should be considered to improve conductivity and modify surface properties to enhance perovskite formation. PEDOT/PSTFSI ratio was found to affect PV performances in an unexpected way. Better understanding of the properties of PEDOT:PSTFSI thin films and their behaviour into PSCs would be necessary to improve PSCs performances.

Finally, problematics relative to the integration of semi-transparent inverted PEDOT-based PSCs to parietodynamic windows were pointed. A relation between efficiency, transparency and stability was experimentally evidenced. Beyond performances, technical issues and cost, it was experienced that perovskite toxicity could be the limiting parameter for the integration of PSCs.

References

1. Wang, Q.; Chueh, C.-C.; Eslamian, M.; Jen, A. K. Y., Modulation of PEDOT:PSS pH for Efficient Inverted Perovskite Solar Cells with Reduced Potential Loss and Enhanced Stability. *ACS applied materials & interfaces* **2016**, *8* (46), 32068-32076.
2. Huang, J.; Wang, K.-X.; Chang, J.-J.; Jiang, Y.-Y.; Xiao, Q.-S.; Li, Y., Improving the efficiency and stability of inverted perovskite solar cells with dopamine-copolymerized PEDOT:PSS as a hole extraction layer. *Journal of Materials Chemistry A* **2017**, *5* (26), 13817-13822.
3. (a) Thomas, J. P.; Zhao, L.; McGillivray, D.; Leung, K. T., High-efficiency hybrid solar cells by nanostructural modification in PEDOT:PSS with co-solvent addition. *Journal of Materials Chemistry A* **2014**, *2* (7), 2383-2389; (b) Dimitriev, O. P.; Grinko, D. A.; Noskov, Y. V.; Ogurtsov, N. A.; Pud, A. A., PEDOT:PSS films—Effect of organic solvent additives and annealing on the film conductivity. *Synthetic Metals* **2009**, *159* (21), 2237-2239; (c) Alemu Mengistie, D.; Wang, P.-C.; Chu, C.-W., Effect of molecular weight of additives on the conductivity of PEDOT:PSS and efficiency for ITO-free organic solar cells. *Journal of Materials Chemistry A* **2013**, *1* (34), 9907-9915.
4. Meziane, R.; Bonnet, J.-P.; Courty, M.; Djellab, K.; Armand, M., Single-ion polymer electrolytes based on a delocalized polyanion for lithium batteries. *Electrochimica Acta* **2011**, *57*, 14-19.
5. (a) Hofmann, A. Aqueous dispersions of conducting polymers for opto-electronic applications. University of Bordeaux, 2016; (b) Hofmann, A. I.; Smaal, W. T. T.; Mumtaz, M.; Katsigiannopoulos, D.; Brochon, C.; Schütze, F.; Hild, O. R.; Cloutet, E.; Hadziioannou, G., An Alternative Anionic Polyelectrolyte for Aqueous PEDOT Dispersions: Toward Printable Transparent Electrodes. *Angewandte Chemie International Edition* **2015**, *54* (29), 8506-8510.
6. Lim, K.; Jung, S.; Lee, S.; Heo, J.; Park, J.; Kang, J.-W.; Kang, Y.-C.; Kim, D.-G., The enhancement of electrical and optical properties of PEDOT:PSS using one-step dynamic etching for flexible application. *Organic Electronics* **2014**, *15* (8), 1849-1855.
7. Zhao, X.; Wang, M., Organic hole-transporting materials for efficient perovskite solar cells. *Materials Today Energy* **2018**, *7*, 208-220.
8. EnR Fenêtre Energie Renouvelable. <http://fenetre-enr.fr/> (accessed October 2018).
9. Cai, M.; Wu, Y.; Chen, H.; Yang, X.; Qiang, Y.; Han, L., Cost-Performance Analysis of Perovskite Solar Modules. *Advanced Science* **2016**, *4* (1), 1600269.
10. 129, C. T., NF EN 410 - Verres dans la construction. *NF EN 410 - Verres dans la construction* **April 2011**.

General Conclusion & Perspectives

This work was in line with one of the current challenges motivating the development of perovskite solar cells (PSCs), *i.e.* improving the power conversion efficiency while insuring the device lifetime. The objective was to propose new hole transporting systems based on polymers, suitable for each of the main PSC architectures: n-i-p planar, n-i-p mesoscopic and p-i-n inverted.

Thereby, the first step consisted in fabricating relatively efficient, reproducible and stable PSCs from commonly used materials. The n-i-p planar configuration was based on a $\text{MAPbI}_{3-x}\text{Cl}_x$ perovskite and was found to exhibit a large hysteresis, as described in the literature. The areas of improvement explored concerned the TiO_2 blocking layer processing, the TiO_2 surface treatments and their impact on the perovskite formation, and the perovskite process, including the incorporation of additives into the precursor solution. In optimal conditions, a best power conversion efficiency (PCE) of 15.99 % was reached. Secondly, n-i-p mesoscopic PSCs were fabricated. The maximum PCE achieved was 18.44 % with a significantly reduced hysteresis. The better performances compared to n-i-p planar devices are attributed to the mesoscopic TiO_2 layer that helps for the electron extraction, to the mixed $\text{MA}_{0.15}\text{FA}_{0.85}\text{PbI}_{2.55}\text{Br}_{0.45}$ perovskite properties and to the doping of the materials. Doping TiO_2 with LiTFSI and $\text{Mg}(\text{TFSI})_2$, and the perovskite with K^+ tune the energetic properties of the materials in a favourable way for the solar cell operation. The last device shows the p-i-n inverted structure. The optimization of the PEDOT:PSS/MAPbI₃/PC₆₀BM/BCP stack allowed to attain a PCE of 12.23 % with reasonable hysteresis. These three architectures have been used as reference cells to introduce new hole transporting systems.

A first project was dedicated to poly(9-vinylcarbazole)- (PVK-) based materials. Widely used in organic electronics, PVK benefits from good charge transport properties, hydrophobicity, and commercial availability. Our strategy was to post-functionalize PVK with moieties of interest to tune the electronic properties, and improve the film forming, the solubility or the conductivity. In a cost-effective approach, the synthetic routes include a maximum of 3 steps, a simple purification procedure through Soxhlet extraction and involve commercially available materials. Among the synthesized polymers, PVK-[N(PhOCH₃)₂]₂ exhibited a best PCE of 14.04 % in n-i-p planar PSCs and comparable average PCE to spiro-OMeTAD, which was attributed to the superior hole mobility of PVK-[N(PhOCH₃)₂]₂. Furthermore, the device lifetime was considerably extended thanks to the better film forming of PVK-[N(PhOCH₃)₂]₂, that provides a hydrophobic barrier preventing the perovskite from degradation induced by moisture present in the atmosphere. Introduced in mesoscopic PSCs,

the V_{oc} was considerably reduced. This issue was overcome by locally modifying the perovskite composition to reduce recombination rate at the interface through the deposition of MAI, FAI or MABr salts. Resulting PSCs reached PCE up to 17.17 % with small hysteresis using the MAI salt. The modification of the perovskite composition is expected to slightly shift energy levels of the perovskite in a more favourable way for the hole extraction. Finally, dopant-free PVK-[N(PhOCH₃)₂]₂-based PSCs were elaborated from n-i-p planar devices. The polymer layer thickness was reduced for a shorter hole-transporting pathway, and an extra molybdenum oxide layer was deposited on top of the polymer to facilitate the charge extraction. A comparable PCE to pristine spiro-OMeTAD of 10.63 % was achieved. The lower PV performances are attributed to the limited hole mobility of the pristine materials. To conclude, it was shown that doping remains essential in PVK-[N(PhOCH₃)₂]₂ to enhance charge transport properties of the polymer and thus, PSC efficiency. The molecular weight (M_n) was found to further improve efficiency and stability of PSCs. It could be interesting to pursue the study with higher M_n polymers. Finally, a careful investigation of the energetic properties of the perovskite could be performed to better understand the effects of the perovskite surface modification.

A second project was dedicated to polyelectrolytes for mesoscopic PSCs. The new synthesized polyelectrolytes include two imidazolium based poly(ionic liquid)s (PVBI-I and PVBI-TFSI), a polyanion (PSTFSI-K) and a block copolymer composed of PVK and imidazolium-based blocks (PILS(TFSI)-*b*-PVK). The properties of the above polymers were carefully studied to be used as hole charge transport materials, hole charge transport dopants or perovskite dopants. From the preliminary studies, PVBI-TFSI showed promising results as dopant for spiro-OMeTAD. The spiro-OMeTAD oxidation was first evidenced in inert atmosphere in solution through colour change upon the addition of PVBI-TFSI. The doping mechanism proposed involves a proton transfer from the imidazolium of the PVBI to the one the nitrogen of spiro-OMeTAD. Interactions between PVBI and spiro-OMeTAD have been evidenced in solution by NMR, formation of oxidized spiro-OMeTAD species was revealed by absorption spectroscopy in thin films, and p-doping of spiro-OMeTAD by PVBI-TFSI in inert atmosphere was demonstrated by UPS. PVBI-TFSI greatly enhanced spiro-OMeTAD conductivity by about four orders of magnitude. Therefore, PSC efficiency was improved from 18.44 % using LiTFSI to 20.35 % using PVBI-TFSI. PVBI-TFSI PSCs were characterized by a high V_{oc} and a negligible hysteresis, which are suggested to be due to a reduction of recombinations at the perovskite/HTM interface and a good balanced charge extraction, induced by a higher conductivity and a better energy band alignment. Moreover, compared to LiTFSI, the poly(ionic liquid) material, due to the long chains character, is expected to provide to the PSCs phase stability by inhibiting the diffusion of the active components as in the case of low molecular weight additives, which ultimately deteriorates the long term operation of the PSCs. Also, air-free doping mechanism avoids the atmosphere exposure step

required in LiTFSI doped spiro-OMeTAD devices that could induce device degradation. In a future study, it would be important to consider the mechanical properties of PVBI-TFSI-doped spiro-OMeTAD compared to the small molecule-doped spiro-OMeTAD. The perspectives would also concern the understanding of the *t*BP and irradiance dependency of the doping mechanism, and the possible relation with the photo-reversible effects observed during solar cell operation.

The last project dealt with the use of inverted perovskite solar cells as semi-transparent devices and their introduction to window panels for solar energy capture. Here we considered the use of transparent electrodes based on PEDOT:X complexes. The usual PSS counter ion (X) of PEDOT:PSS complex was replaced by the PSTFSI ionic polymer in order to bring ionic conductivity in addition to electronic conductivity. PEDOT:PSTFSI has the further advantage to be highly transparent, easy to process, and had suitable energy level to be integrated into inverted PSCs. The used PEDOT:PSTFSI was unfortunately less conductive than PEDOT:PSS and the quality of the MAPbI₃ perovskite on top of PEDOT:PSTFSI was not as good as on top of PEDOT:PSS, resulting in no improvement of PCE. However, it is possible in future study to improve the surface and the charge transport properties of PEDOT:PSTFSI through introduction of additives. On this project, we had the opportunity to consider the compromise between efficiency, transparency and stability, for a useful PSC semi-transparent window panel, and the industrially relevant parameters such as large-scale fabrication, cost and toxicity of components, important to the end producers and users with whom we have shortly discussed and worked.

With the present work we have shown that the use of functional polymer materials in the field of perovskite based solar cells can improve their performance and sustainability through high efficiency, good stability, low cost and easy processability. Herein, the focus was on hole transporting polymers and hole transporting polymer dopants. The possibilities of further progress are infinite considering the various precisely controlled functional properties, relevant to perovskite based PSCs, accessible via polymer synthesis.

Experimental Details

1 Syntheses of polymers

1.1 Materials

9-Vinylcarbazole (Aldrich, 98%) and AIBN (azobisisobutyronitrile, Acros 98%) were recrystallized from methanol. O-ethyl-S-(1-ethoxycarbonyl) ethyldithiocarbonate ($C_8H_{14}S_2O_3$) was synthesized according to literature and used as the RAFT Chain Transfer Agent (CTA).¹ Tetrahydrofuran and toluene were purified through an MB-SPS-800 solvent purification system and were stored under inert atmosphere before use. N,N-dimethylformamide (DMF, 99.8%), dichloromethane (CH_2Cl_2 , $\geq 99.9\%$), methanol (CH_3OH , 99.8%), ethanol (CH_3CH_2OH , 99.8%), acetonitrile (CH_3CN , 99.8%), dimethylsulfoxide ($(CH_3)_2SO$, 99.8%), *tert*-butyl chloride (C_4H_9Cl , 99%), ethyl acetate ($CH_3COOC_2H_5$, 99.8%), diethyl ether ($(C_2H_5)_2O$, 99 %), and bis(trifluoromethane)sulfonimide lithium salt (LiTFSI, 99.95%) were purchased from Aldrich and used as received. 4,4'-Dimethoxydiphenylamine ($C_{14}H_{15}NO_2$, 98%) and sodium *tert*-butoxide (*t*-BuONa, 97%) were purchased from ABCR, tri-*tert*-butylphosphine ($(tBu)_3P$, 98%) and tris(dibenzylideneacetone)dipalladium(0), ($Pd_2(dba)_3$) and copper(I)iodide (CuI, 99.99%) from Strem Chemicals, N-bromosuccinimide ($C_4H_4BrNO_2$, 99%) and sodium methoxide (CH_3NaO , 95%) from Acros, aluminium chloride ($AlCl_3$, 99%), 1-vinylimidazole ($C_5H_6N_2$, 99%), and 1-iodobutane (C_4H_9I , 99%) from Alfa Aesar. All were used as received.

1.2 Syntheses and characterizations

1.2.1 Synthesis of poly[N3,N3,N6,N6-tetrakis(4-methoxyphenyl)-9-vinylcarbazole-3,6-diamine] (PVK-[N(PhOCH₃)₂]₂)

Two batches of PVK-[N(PhOCH₃)₂]₂ were synthesized: one with a theoretical molecular weight of 8.0 kg.mol⁻¹ and another with a molecular weight of 11.7 kg.mol⁻¹, where the synthesis is described below.

1.2.1.1 Synthesis of poly(9-vinylcarbazole) (PVK, 7.0 kg/mol):

In a typical experiment similar to literature, 12 g of 9-vinylcarbazole (VK, 62 mmol, 50 equ.), 0.27 g of O-ethyl-S-(1-ethoxycarbonyl) ethyldithiocarbonate (CTA, 1.2 mmol, 1 equ.) and 0.1 g of 2,2'-Azobis(2-methylpropionitrile) (AIBN, 0.6 mmol, 0.5 equ.) were mixed in 31 mL of tetrahydrofuran (THF, 40% w/v) in a 100 mL schlenk flask equipped with a magnetic stirrer.² After 3 freeze-vacuum-thaw cycles,

the mixture was stirred under nitrogen atmosphere at 60°C and the polymerization was stopped after 20h by dipping the polymerization flask into liquid nitrogen. The polymer was precipitated in methanol, recovered by filtration and dried at 40°C for 24h to give 12 g of PVK (100 % yield).

^1H NMR (Figure 132) (400 MHz, CHCl_3) δ (ppm) 7.8 – 5.7 (m, 7H), 5.3 – 4.5 (m, 1H), 3.5 – 2.9 (m, 1H), 2.1 – 0.9 (m, 2H), identified from the literature.³

FTIR (Figure 136) (ATR, 32 scans, cm^{-1}) 3100-3000 ar. C-H stretch, 3000-2890 al. C-H stretch, 2300-1700 ar. C-H overtones, 1640-1070 skeletal vibrations al. and ar. C-C, C=C stretch, 1060-860 C-H in-plane bending, and 800-650 C-H out-of-plane.

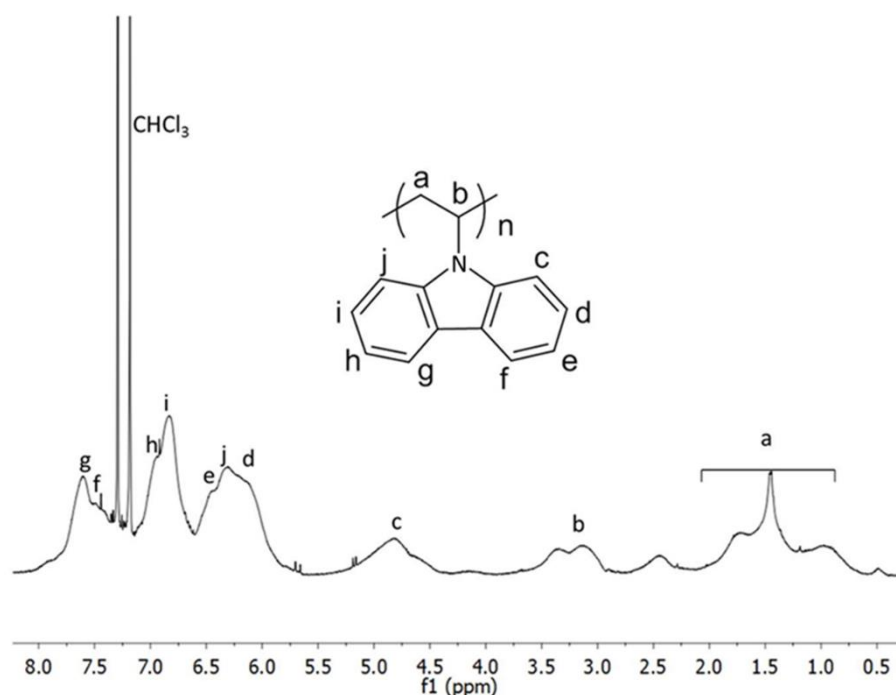


Figure 132. ^1H NMR of PVK in chloroform- d .

A similar procedure was used to prepare PVK of $3.0 \text{ kg} \cdot \text{mol}^{-1}$.

1.2.1.2 Synthesis of poly[(3,6-dibromo)-9-vinylcarbazole] (PVK- Br_2)

2 g of PVK ($7.0 \text{ kg} \cdot \text{mol}^{-1}$, 10 mmol, 1 equ.) were stirred with 103 mL of DMF (1.9 % w/v) in a 250 mL round bottom flask until complete dissolution. 4.6 g of N-bromosuccinimide ($\text{C}_4\text{H}_4\text{BrNO}_2$, 25 mmol, 2.5 equ.) in 26 mL of DMF (17.8 %w/v) were added dropwise to the polymer solution after cooling at 0°C. After addition, the mixture was stirred for 24h at room temperature under inert atmosphere and then was precipitated in an excess of ethanol. Finally, the final product, PVK- Br_2 , was isolated through filtration and dried at 50°C under vacuum for 20h. The final mass was 3.55 g (97.6% yield).

FTIR (Figure 136) (ATR, 32 scans, cm^{-1}) 3100-3000 ar. C-H stretch, 3000-2820 al. C-H stretch, 2100-1600 ar. C-H overtones, 1600-1000 skeletal vibrations al. and ar. C-C, C=C stretch, 1470 asymmetric and 1270 symmetric, 1070-980 C-H in-plane bending, 900-540 C-H out-of-plane bending, 770-840 ar. C-H bend characteristic for aromatic substitution, and 650 C-Br stretch.

A similar procedure was used to prepare PVK-Br₂ from PVK of 3.0 kg.mol⁻¹.

1.2.1.3 Synthesis of PVK-[N(PhOCH₃)₂]₂ (11.7 kg/mol)

Synthesis of poly[(3,6-diamine(N3,N3,N6,N6-tetrakis(4-methoxyphenyl)))9-vinylcarbazole] (PVK-[N(PhOCH₃)₂]₂) is based on Buchwald-Hartwig coupling reaction.⁴ In a typical experiment, 0.6 g of PVK-Br₂ (from PVK of 7.0 kg.mol⁻¹, 1.7 mmol, 1 equ.) was stirred in a 250 mL round bottom flask with 21.3 mL of toluene (2 wt.%) until dissolution under inert atmosphere. Then 0.05 g of tri-tert-butylphosphine [(t-Bu)₃P, 0.3 mmol, 0.15 equ.], 0.12 g of tris(dibenzylideneacetone)dipalladium(0) [Pd₂(dba)₃, 0.1 mmol, 0.07 equ.], 1.2 g of 4,4'-dimethoxydiphenylamine (C₁₄H₁₅NO₂, 5.3 mmol, 3 equ.) and 0.5 g of sodium tert-butoxide (t-BuONa, 5.3 mmol, 3 equ.) were added and the mixture was refluxed for 20h under N₂ atmosphere. The mixture was then poured over water and the final product was extracted into dichloromethane. After removal of dichloromethane using a rotary evaporator, product was diluted in small quantity of DMSO before precipitation in methanol. The obtained crude product was purified through a Söxhlet procedure by washing with methanol, acetonitrile and toluene. All Söxhlet fractions were dried at 50°C under vacuum for 24h. The final mass of **PVK-[N(PhOCH₃)₂]₂** was 0.5 g (45 % yield).

¹H NMR (Figure 133) (400 MHz, CHCl₃) δ 7.2 – 5.6 (m, 22H), 3.9 – 2.7 (m, 13H), 1.7 – 1.4 (m, 2H).

FTIR (Figure 136) (ATR, 32 scans, cm^{-1}) 3130-3000 ar. C-H stretch, 3000-2770 al. C-H stretch (increased at 2800 because of –OCH₃ groups), 2300-1890 ar. C-H overtones, 1640-1070 skeletal vibrations al. and ar. C-C, C=C stretch, 1260-1000 C-O stretch, 1000-860 C-H in-plane bending, and 800-650 C-H out-of-plane bending.

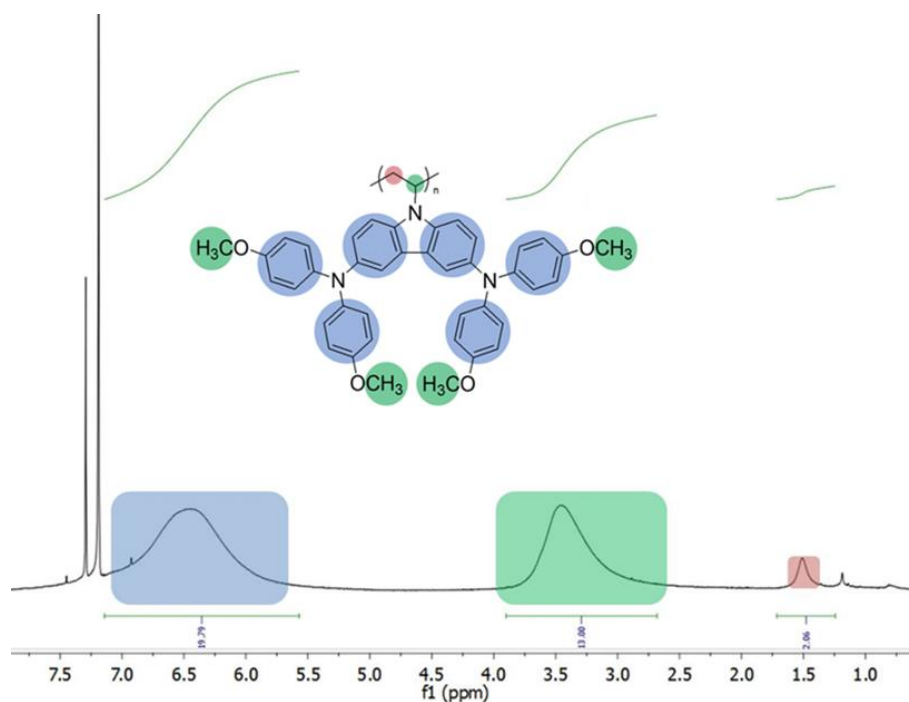


Figure 133. ^1H NMR spectrum of $\text{PVK}-[\text{N}(\text{PhOCH}_3)_2]_2$ in chloroform-d .

A similar procedure was used to prepare $\text{PVK}-[\text{N}(\text{PhOCH}_3)_2]_2$ of 8.0 kg/mol from PVK (3.0 kg/mol).

1.2.2 Synthesis of poly[(3,6-di-*tert*-butyl)-9-vinylcarbazole] ($\text{PVK}-(\text{tBu})_2$, 8.5 kg/mol)

Poly[(3,6-di-*tert*-butyl)-9-vinylcarbazole] was synthesized by Friedel-Crafts alkylation. 2 g of PVK (7.0 kg.mol⁻¹, 0.2 mmol, 1 equ.) and 1.38 g of aluminum chloride (11 mmol, 1 equ.) were stirred in dichloromethane (11 wt.%) in a 250 mL round bottomed flask at 0°C. 2.4 g of *tert*-butylchloride (26 mmol, 2 eq.) were added within 90 min. The mixture was warmed to room temperature and stirred overnight. Then, the reaction was cooled to 0°C in order to add 8 mL of hydrochloric acid (37 %). The mixture was diluted with 28 mL of dichloromethane and extracted twice with water and brine. The organic phase was dried over sodium sulfate. After evaporation of the solvent, the polymer was dried overnight at 50°C to yield 2.4 g of **PVK-(tBu)₂** (78 % yield).

^1H NMR (Figure 134) (400 MHz, CDCl_3) δ 8.30 – 5.65 (m, 7H), 3.74 (dd, $J = 14.2, 7.5$ Hz, 1H) and 2.13 – 0.24 (m, 14H).

FTIR (Figure 136) (ATR, 32 scans, cm^{-1}) 3100-3000 ar. C-H stretch, 3000-2890 al. C-H stretch, 2300-1700 ar. C-H overtones, 1640-1070 skeletal vibrations al. and ar. C-C, C=C stretch, 1060-860 C-H in-plane bending, and 800-650 C-H out-of-plane bending.

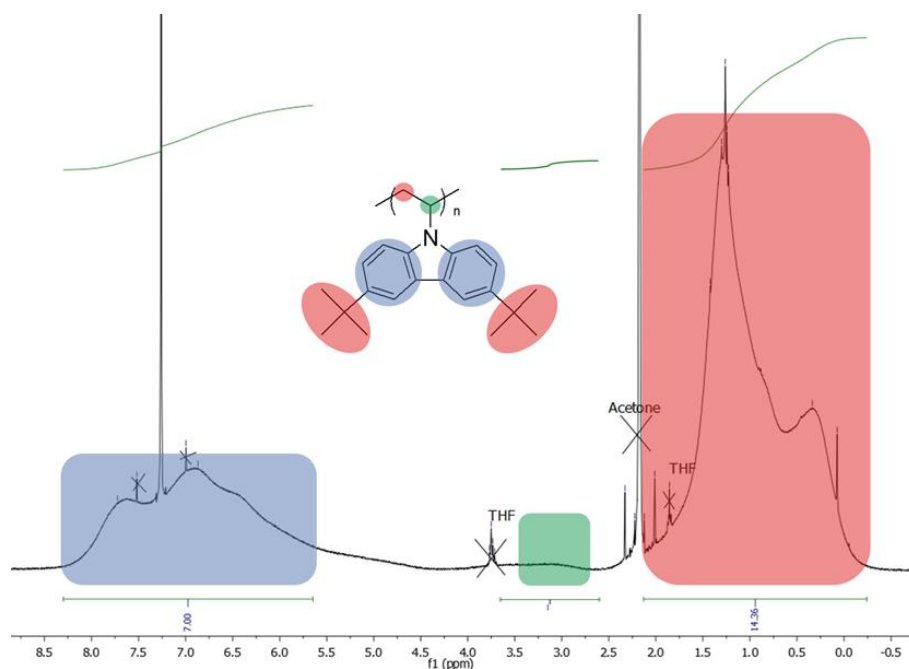


Figure 134. ^1H NMR spectrum of PVK-(tBu) $_2$ in chloroform- d .

1.2.3 Synthesis of poly[(3,6-dimethoxy)-9-vinylcarbazole] (PVK-(OCH $_3$) $_2$, 12.4 kg/mol)

Poly[(3,6-di-methoxy)-9-vinylcarbazole] was synthesized from **PVK-Br $_2$** by direct methoxide displacement of bromine. First, 32 mL of sodium methoxide in methanol (25 wt.%) and 4.05 g of copper bromide (28 mmol, 4 equ.) were added to 2 g of PVK-Br $_2$ (from PVK 7.0 kg.mol $^{-1}$) in 10 mL of DMF, 20 mL of ethyl acetate and 20 mL of toluene in a 250 mL round bottomed flask. The reaction was carried in inert atmosphere at 80°C for 24h. Then the mixture was poured over water, filtered and washed with THF. Excess of solvents was evaporated. The left powder was resolubilized in THF and precipitated by addition of ethanol. Finally, filtration and drying overnight at 50°C led to 1.7 g of **PVK-(OCH $_3$) $_2$** (75 % yield).

^1H NMR (Figure 135) (400 MHz, THF) δ 8.89 – 5.40 (m, 7H), 3.76 (s, 3H) and 2.92 – 1.01 (m, 2H).

FTIR (Figure 136) (ATR, 32 scans, cm $^{-1}$) 3100-3000 ar. C-H stretch, 3000-2890 al. C-H stretch, 2300-1700 ar. C-H overtones, 1640-1070 skeletal vibrations al. and ar. C-C, C=C stretch, 1260-1000 C-O stretch, 1060-860 C-H in-plane bending, and 800-650 C-H out-of-plane bending were found.

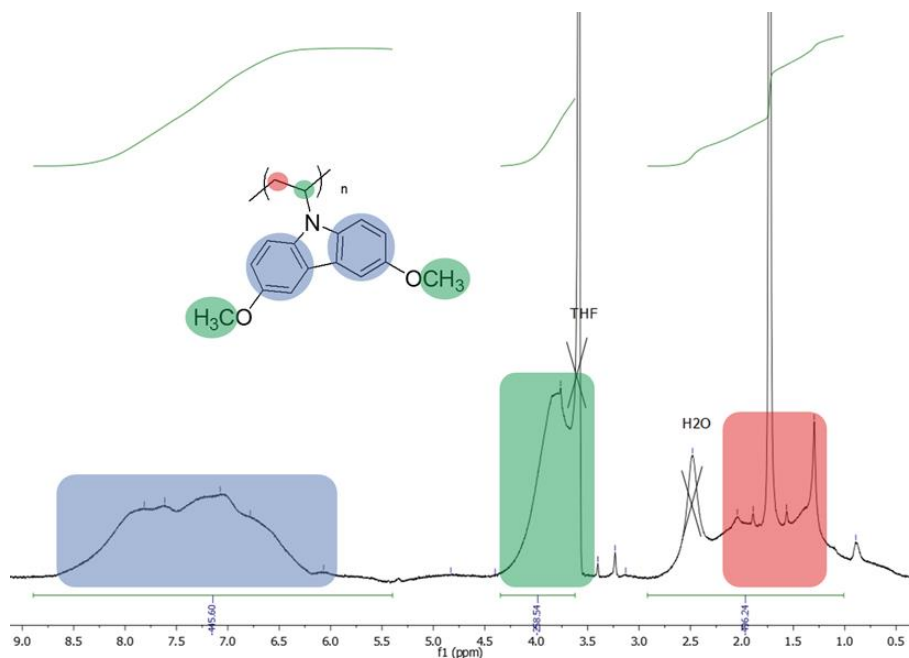


Figure 135. ^1H NMR spectrum of $\text{PVK}-(\text{OCH}_3)_2$ in chloroform- d .

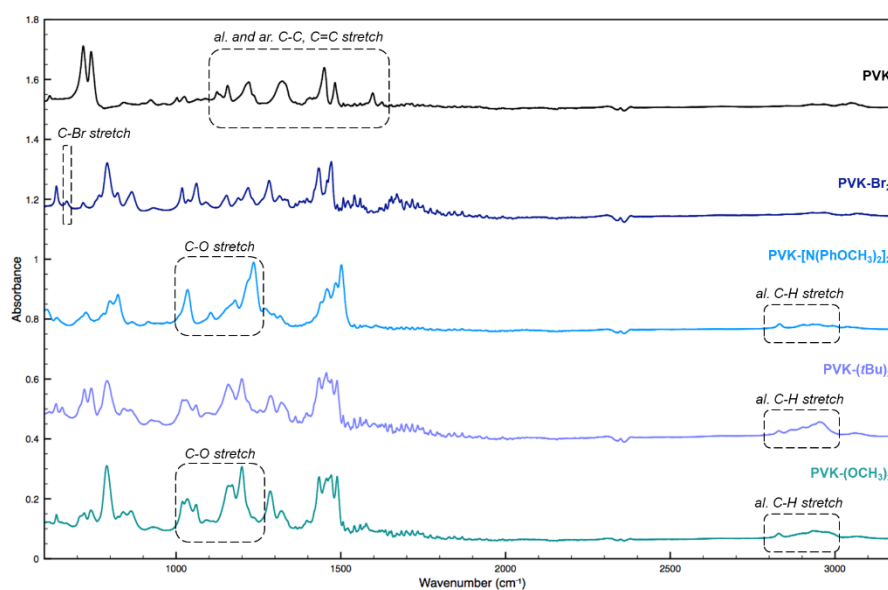


Figure 136. FTIR spectra of PVK (black), $\text{PVK}-\text{Br}_2$ (dark blue), $\text{PVK}-[\text{N}(\text{PhOCH}_3)_2]_2$ (light blue), $\text{PVK}-(\text{tBu})_2$ (purple), and $\text{PVK}-(\text{OCH}_3)_2$ (green).

Molecular weights of the polymers were experimentally determined by SEC/GPC (Figure 137) and the corresponding results are summarized in Table 59.

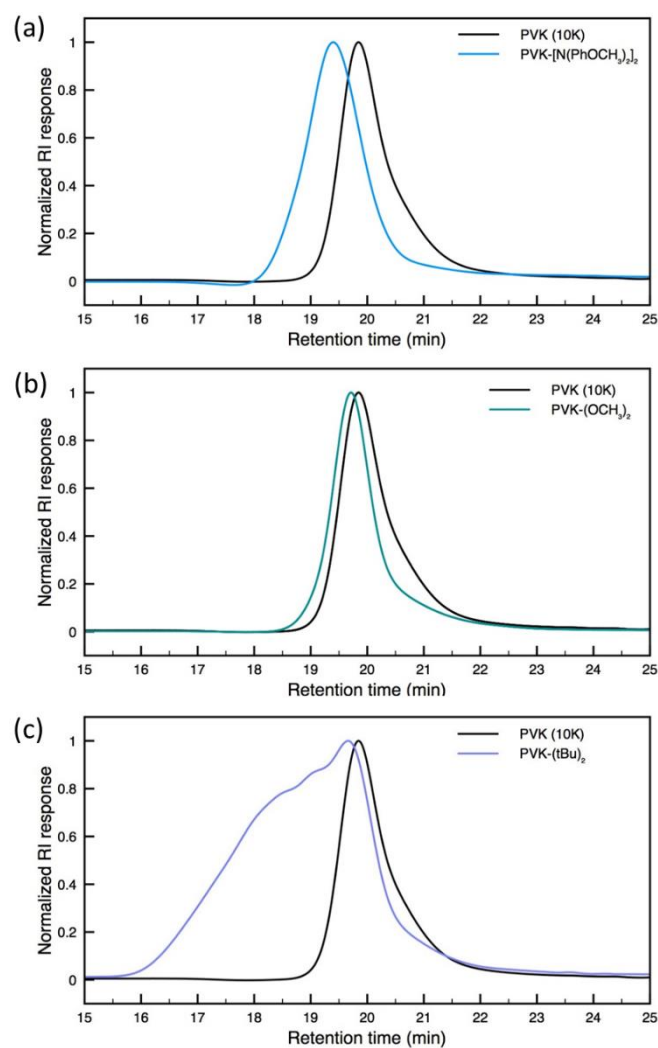


Figure 137. SEC chromatograms (RI detector) in chloroform of PVK compared to (a) PVK-[N(PhOCH₃)₂]₂, (b) PVK-(OCH₃)₂, and (c) PVK-(tBu)₂.

Table 59. Macromolecular characteristics of the synthesized polyvinylcarbazole derivatives.

Polymer	Theoretical M _n ^a	Experimental M _n ^b	Đ
	kg.mol ⁻¹	kg.mol ⁻¹	
PVK	9.880	6.980	1.4
	5.250	2.990	1.3
PVK-Br ₂	17.770		
	9.350		
PVK-[N(PhOCH ₃) ₂] ₂	32.610	11.730	1.4
	17.760	8.030	1.3
PVK-(tBu) ₂	15.050	8.500	1.6
PVK-(OCH ₃) ₂	12.440	8.500	1.2

^a Theoretical calculation from M_n=[VK]/[CTA]*M_n(VK)+M_n(CTA). ^b vs. PS narrow standard calibration SEC in chloroform/1% trimethylamine at 30°C.

1.2.4 Synthesis of poly(1-butyl-3-vinylimidazolium iodide) (PVBI-I)

1.2.4.1 Synthesis of 1-vinyl-3-butyl-imidazolium iodide synthesis (VBI-I)

10.4 g of 1-vinyl-imidazole (0.11 mol, 1 equ.) were mixed to 255 mL of ethyl acetate (20 % w/v) in a 500 mL 3-necked flask cooled with an ice bath under nitrogen. Then, 40.7 g of 1-iodo-butane (0.22 mol, 2 equ.) were added slowly through a septum. The solution was refluxed at 85°C for 20h. The obtained **VBI-I** was washed by triturations with diethylether and dried at 50°C under vacuum overnight.

^1H NMR (Figure 138) (400 MHz, THF) δ 9.1, 8, 7.7 ppm CH protons of imidazolium moieties, 7.2, 6.8, 5.4 ppm vinylic protons of the monomer, 4.3, 1.9, 1.4, 1 ppm butyl protons.

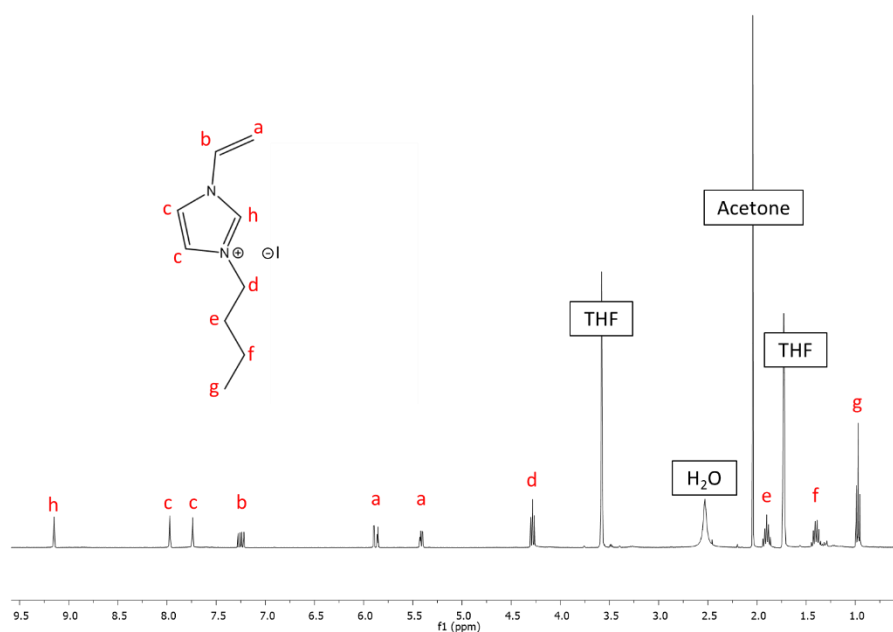


Figure 138. ^1H NMR spectrum of VBI-TFSI in THF- d_8 .

1.2.4.2 Synthesis of poly(1-butyl-3-vinylimidazolium iodide) (PVBI-I)

Poly(1-butyl-3-vinylimidazolium iodide) (PVBI-I) was then prepared through RAFT polymerization of VBI-I. 2 g of VBI-I (7.2 mmol, 1 equ.), 93 mg of O-ethyl-S-(1-ethoxycarbonyl) ethyldithiocarbonate (CTA, Sigma Aldrich, 0.42 mmol, 0.06 equ.) and 34 mg of 2,2'-azobis(2-methylpropionitrile) (AIBN, 98% Sigma Aldrich, 0.21 mmol, 0.03 equ.) were mixed in 10.5 mL of anhydrous N,N-dimethylformamide (DMF, 20 % w/v) in a 50 mL round bottom flask equipped with a magnetic stirrer. After 3 freeze-vacuum-thaw cycles, the mixture was stirred under nitrogen atmosphere at 60°C and the polymerization was stopped after 24h by dipping the polymerization flask into liquid nitrogen. The final mass was 1.62 g (81% yield).

1.2.5 Synthesis of poly(1-butyl-3-vinylimidazolium bis(trifluoromethylsulfonyl)-imide) (PVBI-TFSI)

PVBI-TFSI was prepared by anion exchange from PVBI-I. In a 100 mL flask, 4 g of PVBI-I (14 mmol, 1 equ.) were solubilized in methanol (20 % w/v). A solution of LiTFSI in THF (31 mmol, 2.2 equ., 75 % w/v) was then slowly added to the mixture under nitrogen. The solution was stirred for 24h. After evaporating methanol and THF, the obtained solid was immersed in water at 40°C for 1h and rinsed three times to remove the excess of LiTFSI and iodide. The anion exchange was evidenced by a change in solubility of the polyelectrolyte, which became insoluble in water when I⁻ is exchanged with TFSI⁻. The final mass was 3.97 g (100 % yield).

¹H NMR (Figure 139) (400 MHz, THF-d₈) δ 8.5 – 9 and 7 – 8 ppm CH protons of imidazolium moieties, 4 – 4.3 ppm and 2.4 – 2.8 ppm vinylic protons of the polymer, 4.4 – 4.6 and 0.7 – 2 ppm butyl protons.

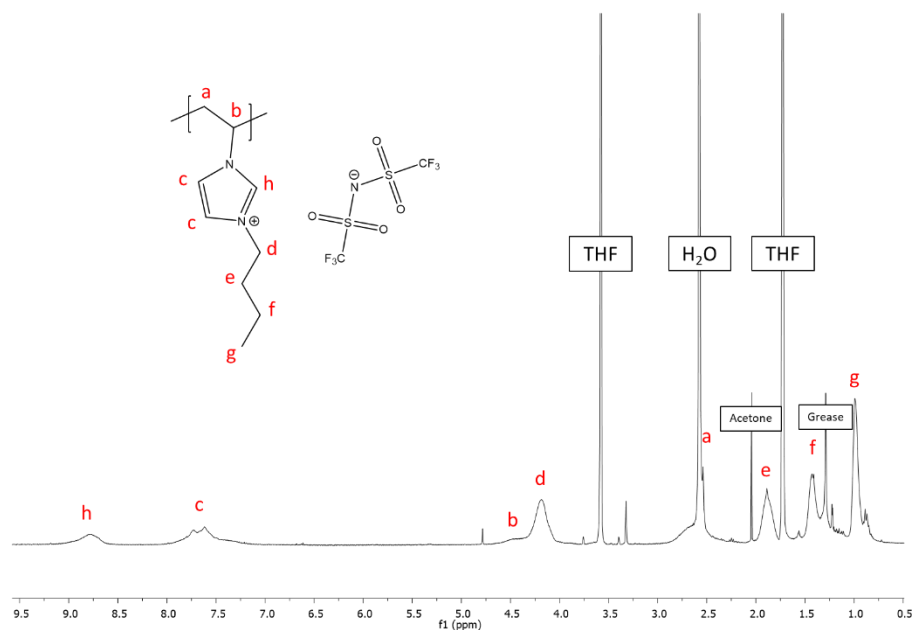


Figure 139. ¹H NMR spectrum of PVBI-TFSI in THF-d₈.

The experimental M_n was calculated to be 7350 g/mol by SEC/GPC in DMF vs. PS narrow standard calibration, with a polydispersity of 1.1 (Figure 140).

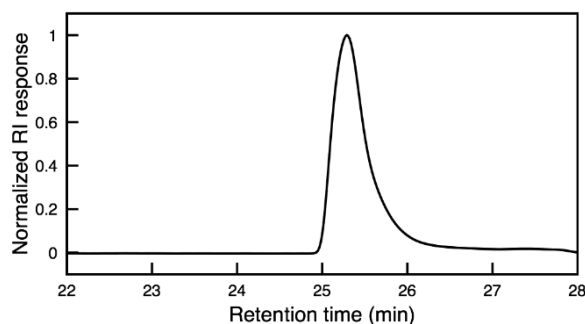


Figure 140. SEC chromatogram (RI detector) of PVBI-TFSI in DMF.

1.2.6 Synthesis of Poly(1-butyl-3-vinylimidazolium bis(trifluoromethylsulfonyl)imide)-*b*-poly(9-vinylcarbazole) (PILS(TFSI)-*b*-PVK)

PVBI-TFSI, referring here to PILS(TFSI) (7 kg.mol⁻¹, 3.5 g) and PVK (3 kg.mol⁻¹, 1.5 g) were introduced together with AIBN (7 mg) in DMF (10 g) in a 50 mL schlenk. The reaction mixture was degassed by three freeze thaw cycles. The flask was placed in an oil bath pre-heated at 60°C and left stirring for 24h. The reaction was quenched using liquid nitrogen and precipitated in acetone. The obtained white powder was dried in an oven at 45°C overnight. The final mass was 4.88 g (about 100% yield). The NMR spectra is given Figure 139.

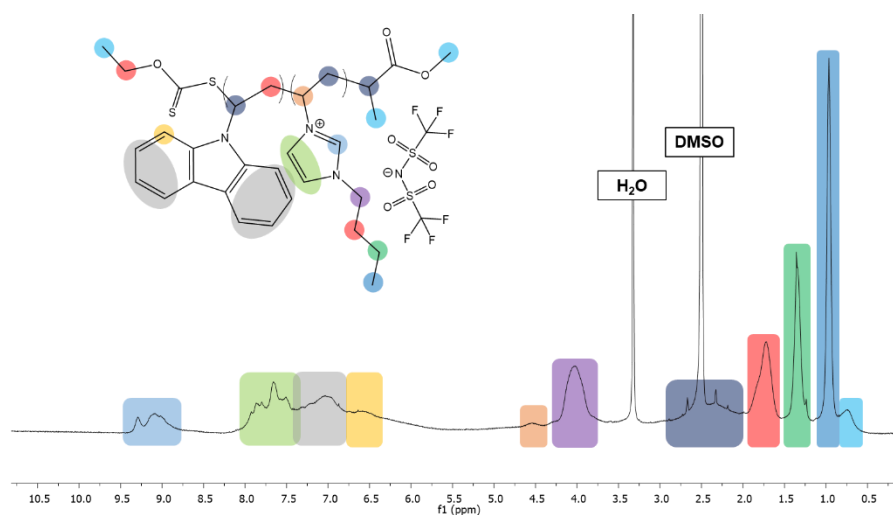


Figure 141. ¹H NMR spectrum of PILS(TFSI)-*b*-PVK in DMSO-d₆.

The experimental M_n was estimated to be 10720 g/mol by SEC/GPC in THF vs. PS narrow standard calibration, with a polydispersity of 1.6 (Figure 143).

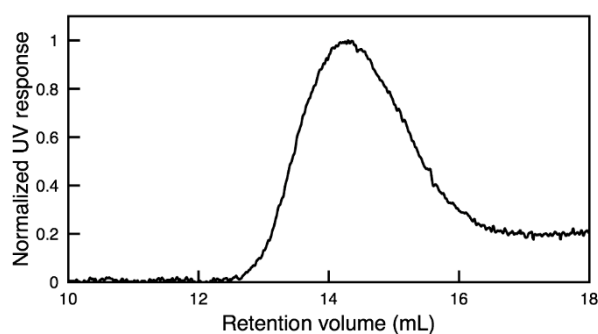


Figure 142. SEC chromatogram (UV detector) of PILS-b-PVK in THF.

1.2.7 Synthesis of poly[4-styrenesulfonyl(trifluoromethylsulfonyl) imide] potassium salt (PSTFSI-K)

PSTFSI-K was synthesized by RAFT polymerization of the STFSI-K monomer in presence of a chain transfer agent and AIBN, as described by Mumtaz *et. al.*⁵

¹H NMR (Figure 143) (400 MHz, DMF) δ 7.5 – 8.2 ppm and 6.3 – 7.7 ppm aromatic protons of the polystyrene moities, 3 – 3.2 and 0.5 – 2.4 ppm, vinylic protons and protons of the ending groups.

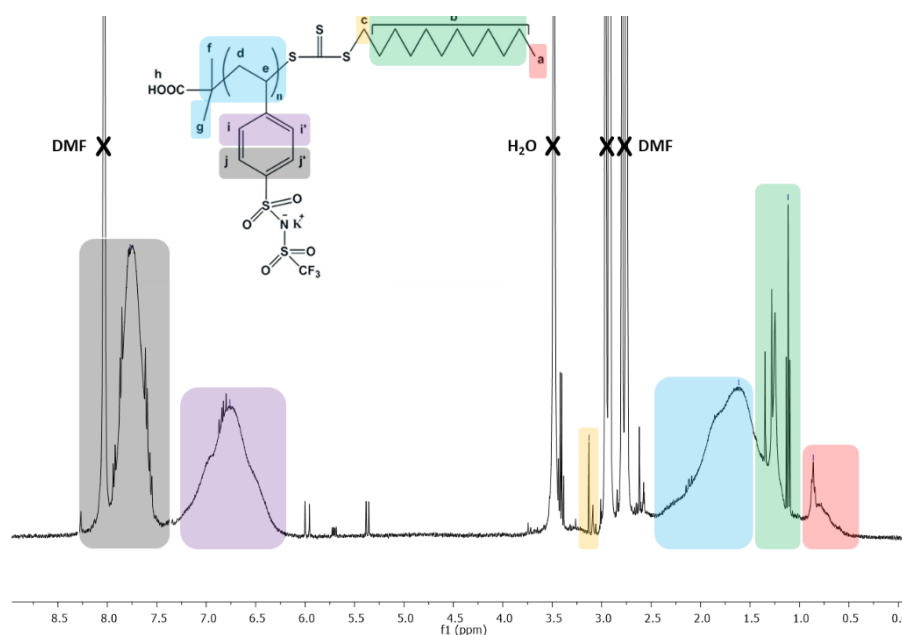


Figure 143. ¹H NMR spectrum of PSTFSI-K in DMF-d₇.

The experimental M_n was estimated to be 6000 g/mol by SEC/GPC in DMF vs. PS narrow standard calibration, with a polydispersity of 1.3 (Figure 144).

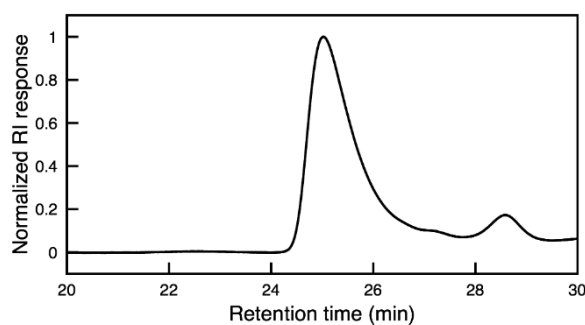


Figure 144. . SEC chromatogram (RI detector) of PSTFSI-K in DMF.

1.2.8 Synthesis of PEDOT:PSTFSI

The PEDOT:PSTFSI complex was synthesized by oxidative polymerization of EDOT in aqueous PSTFSI solution in water, as described by Hofmann *et. al.*⁶

1.3 Methods

¹H-NMR and ¹³C-NMR spectra were recorded using a Bruker AC-400 NMR at room temperature. Chemical shifts (δ) for protons are reported in parts per million (ppm) downfield and are referenced to residual proton in the NMR solvent.

SEC was performed on a Malvern Viscotek TDA 305 instrument equipped with viscometer, light scattering (LS) and refractive index (RI) detectors with a 100A guard column and two PLgel Mixed C bead columns assembled in series. The molecular weights of the polymers were calculated through standard polystyrene (PS) calibration.

FTIR spectroscopy was performed on a Shimadzu IRAffinity-1S, using the attenuated total reflection (ATR) method.

DSC was performed on TA Instruments Q100 DSC system under helium flow (25 mL/min) at a scan rate of 10°C/min, between 0°C and 250°C.

TGA data were recorded on a TGA Q500 of TA Instruments using a heating rate of 10°C/min either in atmosphere or inert atmosphere.

2 Fabrication of perovskite solar cells

2.1 n-i-p planar perovskite solar cells

2.1.1 Materials

Zinc powder, hydrochloric acid (HCl, 37 %), titanium diisopropoxide bis(acetylacetonate) (TiAcAc, 75 wt.% in IPA), titanium(IV) chloride (99.9 %), spiro-OMeTAD (99 %), LiTFSI (99 %), tBP (96 %), and 3-aminopropyltriethoxysilane (APTES, 99 %) were purchased from Sigma Aldrich. Lead(II) chloride (PbCl₂, ultra dry, 99.999 %) was obtained from Alfa Aesar. All solvents were obtained from Sigma Aldrich.

2.1.2 Fabrication steps

The FTO-glass substrates (sheet resistance of $\approx 15 \Omega/\square$, Solaronix) were patterned with zinc powder and HCl. Then, they were subsequently washed in ultrasonic bath in water and ethanol before being treated with a UV-ozone cleaner. An about 50 nm-TiO₂ compact layer from a solution of TiAcAc in ethanol was deposited by spin-coating and calcinated at 475°C for 30 min. The substrates were further immersed in a TiCl₄ solution in ethanol at 70°C before being calcinated at 500°C for 30 min. The following steps were then realized in nitrogen glovebox. MAI and PbCl₂ (3:1) were mixed in anhydrous DMF, stirred for 3h at 70°C and kept at this temperature during the deposition by spin coating. The obtained layer was annealed at 120°C for 45 min. The spiro-OMeTAD solution doped with LiTFSI and tBP was deposited by spin coating and let overnight in dry air before finally evaporating the 80 nm-gold electrode on top of the device. The active area of the cells was 0.1 cm². Perovskite and HTM layers were scratched between the gold electrodes to avoid electrical contact issues. Compositions of the solutions and detailed deposition conditions are described in Table 60 and Table 61.

Table 60. Composition of the solutions to prepare regular planar PSCs.

Solution	Material	Concentration	Solvent
bl-TiO ₂	TiAcAc	10.3 vol.%	Ethanol
TiCl ₄	TiCl ₄	8.8 mM	Ethanol
Perovskite	MAI:PbCl ₂	3:1 mol. ratio 40 wt.%	DMF
HTM-LiTFSI	LiTFSI	1.5 M	Acetonitrile
Spiro-OMeTAD	Spiro-OMeTAD	13.2 wt.%	Chlorobenzene
	+ LiTFSI	0.08 M	Acetonitrile
	+ tBP	0.11 M	

Table 61. Spin coating parameters to prepare regular planar PSCs.

Solution	Volume	Spin Coating			Annealing	
		Speed	Slope	Time	Temperature	Time
	μL	rpm	s	s	$^{\circ}\text{C}$	min
bl-TiO₂	70	5000	2.5	30	475	30
Perovskite	100	0	0	60	120	45
		2000	2	30		
Spiro-OMeTAD	70	0	0	30		
		3000	1	30		

2.1.3 APTES grafting to TiO₂ surface

APTES and toluene were first distilled. 250 mL of toluene and 115 μL of APTES were introduced in a schlenk. TiO₂ substrates were cleaned with 20 min of UV-ozone treatment before being placed in the closed reactor under N₂. The APTES solution was slowly introduced into the reactor via a cannula and the grafting was carried out for 1h. The substrates were then rinsed in ultrasonic bath for 5 min in toluene, water and finally chloroform.

2.2 Mesoscopic perovskite solar cells

2.2.1 Materials

All materials were employed as received. Perovskite materials, including FAI (> 99 %) and MABr (> 98 %) were purchased from Diesol, and PbI₂ (99.99 %) and MABr (> 98 %) from Kojundo Chemical Laboratory Co. KI (> 99.5 %) and magnesium(II) bis(trifluoromethanesulfonyl)imide (Mg(TFSI)₂) were obtained from TCI. Titanium diisopropoxide bis(acetylacetonate) (TiAcAc, 75 wt. % in isopropanol), lithium bis(trifluoro methanesulfonyl)imide (LiTFSI) and 4-tert-butylpyridine (tBP) were bought from Sigma-Aldrich. The 24 nm nano-TiO₂ paste (PST-24NR) was purchased from JPG C&C and the spiro-OMeTAD from Merck. All solvents were obtained from Wako Pure Chemical Industries.

2.2.2 Fabrication steps

First, FTO glass substrates (sheet resistance of $\approx 10 \Omega/\square$, Nippon Sheet Glass Co.) were etched by a laser to be able in the end to connect top gold electrode. Before any deposition, substrates were successively cleaned 10 min in ultrasonic bath in water, detergent, acetone and ethanol, and by excimer UV cleaning. Then, a solution made of TiAcAc mixed with LiTFSI and Mg(TFSI)₂ in ethanol was deposited by spray pyrolysis at 430°C and annealed 10 min at the same temperature to form a 40-nm

compact-TiO₂ layer. The next steps were performed in a drying room with dew point temperature at -30°C. A mesoporous-TiO₂ layer of 150 nm was made by spin coating a solution of TiO₂ paste (PST-24NR) diluted in ethanol, followed by a 2-step annealing, at 125°C and 550°C. The layer was then doped with a LiTFSI solution deposited by spin coating and annealed at 100°C and 430°C. Perovskite precursor solution was made by dissolving MABr, PbBr₂, PbI₂ and FAI in a mixture of DMSO and DMF. 5 mol.% of KI were then added to the solution. 5-minute sonication was performed before spin coating to insure good solubility of all materials. Anti-solvent spin-coating method was carried out to make a dark, smooth and homogeneous perovskite layer by dropping 500 µL of chlorobenzene after 33 s of spin coating. Substrates were then rapidly transferred to the hot plate at 160°C. After cooling down, doped spiro-OMeTAD with LiTFSI and tBP was spin coated and the layer was annealed at 70°C. Substrates were left overnight in the dry room. Finally, the 80-nm top gold electrode was evaporated. Compositions of solutions and deposition conditions are respectively detailed in Table 62 and Table 63.

Table 62. Formulation of the solutions for the fabrication of mesoscopic PSCs.

Solution	Material	Concentration	Solvent
c-TiO₂	TiAcAc	6.6 vol.%	Ethanol
	+ Mg(TFSI) ₂	3 mol.%	
	+ LiTFSI	3 mol.%	
mp-TiO₂	PST-24NR	14.3 wt.%	Ethanol
mp-LiTFSI	LiTFSI	0.1 M	Acetonitrile
KI	KI	1.5 M	DMSO
Perovskite	MABr	0.20 M	DMSO:DMF (1:4 vol. ratio)
	PbBr ₂	0.20 M	
	PbI ₂	1.15 M	
	FAI	1.09 M	
	+ KI	5 mol.%	DMSO
HTM-LiTFSI	LiTFSI	1.85 M	Acetonitrile
Spiro-OMeTAD	Spiro-OMeTAD	0.06 M/6.6 wt.%	Chlorobenzene
	+ LiTFSI	0.03 M	Acetonitrile
	+ tBP	0.20 M	

Table 63. Deposition conditions of spin coated solution for the fabrication of mesoscopic PSCs.

Solution	Volume	Spin Coating			Annealing	
		Speed	Slope	Time	Temperature	Time
	μL	rpm	s	s	$^{\circ}\text{C}$	min
mp-TiO ₂	100	6000	5	30	125	5
					550*	15
mp-LiTFSI	100	3000	3	25	100	5
					450	30
Perovskite	100	1000	1	10		
	+ 500 of CB	4000	4	30	160	15
Spiro-OMeTAD	70	4000	2	30	70	10

2.3 p-i-n Inverted perovskite solar cells

2.3.1 Materials

All materials were used as received. PEDOT:PSS (Clevios PH1000) was purchased from Heraeus. Lead(II) iodide (PbI₂, 99%) and 2,9-dimethyl-4,7-diphenyl-1,10-phenanthroline (bathocuproine), and ammonium bis[2-(perfluoroalkyl)ethyl] phosphate (zonyl) fluorsurfactant were obtained from Sigma Aldrich. PC₆₀BM (> 99.5 %) was purchased from Solenne BV. All solvents were obtained from Sigma Aldrich and used as received.

2.3.2 Fabrication steps

ITO-glass substrates (10 Ω/\square) were purchased patterned. They were successively washed in water, ethanol and isopropanol in ultrasonic baths and finally by UV-ozone treatment. PEDOT:PSS solution was filtered with a PTFE filter 1 μm to remove biggest aggregates, and formulated with 5 % of DMSO and 0.04 % of zonyl. The following steps were carried out in nitrogen glovebox. A thin layer of PEDOT:PSS was deposited by spin coating and annealed at 135°C for 15 min. The perovskite layer was made of MAI (previously synthesized) and PbI₂ mixed in DMSO and DMF. The solution was stirred at 70°C for 1h. It was deposited by spin coating employing the anti-solvent method (drop of chlorobenzene after 5 s of spin coating) and dried at 100°C for 10 min. After cooling down, the perovskite layer was covered by a thin layer of PC₆₀BM deposited by spin coating in chlorobenzene. As well, a bathocuproine (BCP) layer was spin coated from isopropanol. The device was annealed at 70°C for 15 min. Finally, a 100-nm top electrode of silver was evaporated. All the layers were scratched between the silver electrodes to avoid electrical contact issues. The active area was 0.1

cm². Detailed composition of the solutions and deposition conditions are specified in Table 64 and Table 65.

Table 64. Composition of the solutions to fabricate inverted PSCs.

Solution	Material	Concentration	Solvent
Perovskite	MAI:PbI ₂	1:1 mol. ratio	DMF
		54 wt. %	+ 10 vol. % DMSO
PC ₆₀ BM	PC ₆₀ BM	12 wt. %	Chlorobenzene
BCP	BCP	1 mg/mL	Isopropanol

Table 65. Deposition conditions of solutions to prepare inverted PSCs.

Solution	Volume	Spin Coating			Annealing	
		Speed	Slope	Time	Temperature	Time
	μL	rpm	s	s	$^{\circ}\text{C}$	min
PEDOT:PSS	100	5000	2.5	30	135	15
Perovskite	70	4000	1	30	100	10
	+ 200 of CB					
PC ₆₀ BM	70	0	0	30		
		2000	1	30		
BCP	70	4000	1	30	70	15

2.4 Methods

CF₄ surface treatment was operated by a reactive ion etching plasma from Plasma Etch (40 W, 17 sscn, 15 s).

ALD of TiO₂ was realized using a G2 Savannah system from Ultratech at 250°C. The deposition rate was 0.4 Å/cycle.

UV-Vis absorption spectra were recorded using a Shimadzu UV3600 UV/VIS/NIR spectrometer.

Emission spectra were measured using a Horiba Scientific Fluoromax-4 spectrofluorometer.

Surface energies were determined from contact angles of water, diiodomethane and ethylene glycol on the films, and calculated using the Owens-Wendt model (Krüss DSA-100).

AFM (AFM Dimension FastScan Bruker) was used in tapping mode to characterize surface morphology of thin films. Silicon cantilevers (Fastscan-A) with a radius of 5 nm, a spring constant of 18 N.m^{-1} and a cantilever resonance frequency of 1.4 MHz were employed.

SEM images were recorded with a Jeol 7800 prime microscope.

Photoelectron spectroscopy in air (PESA) was performed on a Riken Keiki AC-3 spectrometer. **UPS measurements** were performed in an ultra-high vacuum chamber built by SPECS (Germany), using a low intensity UV light (He I line) with an excitation energy of 21.21 eV. The samples were prepared in a nitrogen glovebox and transferred to the analysis chamber via a mechanized linear transfer line (10^{-9} mbar range) connected to the nitrogen glovebox, with no exposure to ambient air atmosphere. The spectra of photo-emitted electrons were recorded at a pass energy of 2 eV with a hemispherical analyzer (Phoibos 100). The work function of the sample is determined as the difference between the excitation energy and the length of the spectrum.

I-V curves for **conductivity** and **hole mobility** measurements were carried out with a Keithley 2400 SMU. Data from I-V curves for the hole mobility were recorded and treated as followed: 4 J-V curves were acquired in this order: $0 \rightarrow V_{\text{max}} \rightarrow 0 \rightarrow -V_{\text{max}} \rightarrow 0$. V_{max} varied according to the materials and the formulation. Scans were repeated if hysteresis was estimated to be too large. Scans from 0 V to positive or negative voltage with the highest current was selected to avoid bias stress effect and injection-limited behaviour of the electrode. As thin-film electrodes can behave as ohmic resistors, voltage should be corrected with an external series resistance, typically of the order of 10-100 Ω . In Chapter 3, equivalent model has allowed to estimate series resistance to be around 15 Ω for each device. Voltage should also be corrected for built-in voltage. Usually the amount of built-in voltage is unknown in a device, and can vary depending on preparation conditions. Reasonable value should be $< 0.5 \text{ V}$. To estimate the built-in voltage, data were plotted on a double-logarithmic scale and V_{BI} was adjusted in order to straighten the I-V curve. V_{BI} were typically between 0.05 V and 0.15 V depending on the device. Finally, $V_{\text{corrected}} = V - R_s \cdot I - V_{\text{BI}}$. The upper part of the curve corresponds to the SCLC domain and is selected for the fitting.

The **photoluminescence** spectra were recorded at a pass energy of 2 eV with a hemispherical analyser (Phoibos 100).

Specific for n-i-p planar and inverted PSCs: **I-V curves** of solar cells were characterized using a K.H.S. Solar Cell test-575 solar simulator with AM 1.5G filters set at 100 mW.cm^{-2} with a calibrated radiometer (IL 1400BL). Labview controlled Keithley 2400 SMU enabled I-V measurements. The scan was carried out between -0.2 V and 1.2 V at 100 mV.s^{-1} . The active area was defined by a black mask

of 0.1 cm^2 . **IPCE** spectra were recorded on the IQE 200 system from New Port. One part of the cell was spotted (without mask).

Specific for mesoscopic PSCs: **I-V curves** of solar cells were recorded under AM 1.5G (100 mW.cm^{-2}) illumination using a 450-W xenon as the light source (YSS-80A, Yamashita Denso). The light intensity was calibrated using a standard Si photodiode of BS-520 (Bunkoukeiki Co). The scan was also carried out between -0.2 V and 1.2 V at 100 mV.s^{-1} . The active area was defined by a black mask of 0.181 cm^2 . **IPCE** spectra were recorded on an EQE system (CEP-2000MLQ, Bunkoukeiki Co.).

References

1. Mori, H.; Yahagi, M.; Endo, T., RAFT Polymerization of N-Vinylimidazolium Salts and Synthesis of Thermoresponsive Ionic Liquid Block Copolymers. *Macromolecules* **2009**, *42* (21), 8082-8092.
2. Limburg, W. W.; Williams, D. J., Variation in Inter-Ring Interactions in a Series of Carbazyl Group Containing Polymers. *Macromolecules* **1973**, *6* (5), 787-788.
3. Karali, A.; Dais, P.; Heatley, F., Carbon-13 Nuclear Magnetic Relaxation Study of Solvent Effects on Chain Local Dynamics of Poly(N-vinylcarbazole) in Dilute Solution. *Macromolecules* **2000**, *33* (15), 5524-5531.
4. Xu, B.; Sheibani, E.; Liu, P.; Zhang, J.; Tian, H.; Vlachopoulos, N.; Boschloo, G.; Kloo, L.; Hagfeldt, A.; Sun, L., Carbazole-Based Hole-Transport Materials for Efficient Solid-State Dye-Sensitized Solar Cells and Perovskite Solar Cells. *Advanced Materials* **2014**, *26* (38), 6629-6634.
5. Mumtaz, M.; Aissou, K.; Katsigiannopoulos, D.; Brochon, C.; Cloutet, E.; Hadziioannou, G., A well-defined polyelectrolyte and its copolymers by reversible addition fragmentation chain transfer (RAFT) polymerization: synthesis and applications. *RSC Advances* **2015**, *5* (119), 98559-98565.
6. Hofmann, A., Aqueous dispersions of conducting polymers for opto-electronic applications. . *PhD Thesis, Université de Bordeaux* **2016**.

Systèmes hybrides pour cellules solaires à pérovskite stables à haut rendement

Résumé : Les cellules solaires comprenant comme matériau actif une pérovskite organométallique hydride sont apparues récemment comme une technologie de haute performance et bon marché pour la conversion de l'énergie solaire. Les efforts mobilisés pendant cette thèse se sont concentrés sur un composant clé des cellules solaires à pérovskite, le transporteur de trous, qui assure à la fois les performances et la stabilité des cellules. Les avantages des polymères semi-conducteurs pour cette fonction se retrouvent dans leur stabilité, leurs bonnes propriétés de transport de charge et leur caractère filmogène. Ainsi, la stabilité des cellules solaires à pérovskite planes a pu être améliorée en intégrant un polyvinylcarbazole fonctionnalisé, tout en conservant de bonnes efficacités. Le potentiel de polyélectrolytes à base de PEDOT a pu être évalué dans les cellules de type inverses. Et enfin, une nouvelle méthode de dopage par un polyélectrolyte à base d'imidazole a démontré des efficacités remarquables, supérieures à 20%.

Mots clés : photovoltaïque, pérovskite, polymère.

Hybrid systems for highly efficient and stable perovskite solar cells

Abstract: Perovskite solar cells based on hybrid organometal perovskite recently appeared as a cost-effective and highly efficient technology for the conversion of sunlight. Efforts undertaken during this PhD thesis focused on one component of the perovskite solar cells, the hole transport material, which rules both, performance and stability of the devices. Advantages of semiconducting polymers result in their thermal and chemical stability, their good charge transport properties and their ability to form homogeneous thin films. Thereby, through synthesis of novel polyvinylcarbazole and incorporation into devices, stability of planar perovskite solar cells has been enhanced while conserving good efficiency. The potential of PEDOT-based polyelectrolytes has been investigated in inverted perovskite solar cells. Finally, a new strategy to efficiently dope hole transporting materials has been demonstrated through the introduction of *N*-heterocyclic imidazolium-based polyelectrolytes. Thereby, efficiency of solar cells has been promoted to over 20%.

Keywords : photovoltaics, perovskite, polymer.

Laboratoire de Chimie des Polymères Organiques

UMR 5629, Allée Geoffroy Saint-Hilaire, 33615 Pessac, France.